UNIVERSITY OF SOUTHAMPTON

On the Mechanism of Carbon Nanotube Formation by Means of Catalytic Chemical Vapour Deposition

by

Gregory N. Ayre

A thesis submitted in partial fulfillment for the
degree of Doctor of Philosophy

in the
Faculty of Physical and Applied Sciences
School of Physics and Astronomy

October 2011

UNIVERSITY OF SOUTHAMPTON

ABSTRACT

FACULTY OF PHYSICAL AND APPLIED SCIENCES
SCHOOL OF PHYSICS AND ASTRONOMY

Doctor of Philosophy

by Gregory N. Ayre

Despite enormous strides in the synthesis of carbon nanotubes (CNTs), the mechanism for growth is still a highly debated issue. It is generally accepted that the model for carbon filament growth [1, 2], derived from concepts of vapour-liquid-solid theory, also applies to CNT growth. However, this model fails to account for the growth of CNTs from noble metal [3–7], ceramic [8, 9] and semiconducting nanoparticles [10–13], all of which are regarded as unable to catalyse the dissociation of hydrocarbons. In addition, in their bulk form, these materials do not have a catalytic function to produce graphite.

This work examines non-traditional catalyst assisted chemical vapour deposition of CNTs with a view to determine the essential role of the catalyst in nanotube growth. CNT synthesis based upon noble metal and two approaches using germanium nanoparticles are presented. Extensive characterisation has been undertaken of each step of the growth process, and the synthesized carbon nanotubes are analysed by atomic force microscopy, electron microscopy and Raman spectroscopy. The results indicate that good densities of high quality single-walled carbon nanotubes are produced by these techniques. Additionally, the effects of different catalyst support interactions were explored by testing combinations of metal catalysts and support media. This study showed that the support has a strong effect on the chemical activity and morphology of the catalyst.

The results presented show that the commonly utilised model of carbon filament growth is inadequate to describe CNT growth from non-traditional catalysts. A model for CNT growth consistent with the experimental results is proposed, in which the structural reorganisation of carbon to form CNTs is paramount.

Contents

List of Figures

List of Tables

List of Symbols

CVD	**C**hemical **V**apour **D**eposition
CNT	**C**arbon **N**ano**T**ube
SWNT	**S**ingle **W**alled Carbon **N**ano**T**ube
MWNT	**M**ulti **W**alled Carbon **N**ano**T**ube
EM	**E**lectron **M**icroscope
SEM	**S**canning **E**lectron **M**icroscope
TEM	**T**ransmission **E**lectron **M**icroscope
EBIC	**E**lectron **B**eam **I**nduced **C**urrent
EELS	**E**lectron **E**nergy **L**oss **S**pectroscopy
SAED	**S**elected-**A**rea **E**lectron **D**iffraction
EDS	X-Ray **E**nergy **D**ispersive **S**pectroscopy
AFM	**A**tomic **F**orce **M**icroscope
STM	**S**canning **T**unnelling **M**icroscope
KPFM	**K**elvin **P**robe **F**orce **M**icroscope
DOS	**D**ensity **O**f **S**tates
vHs	**v**an **H**ove **s**ingularities
RBM	**R**adial **B**reathing **M**ode
HiPco	**Hi**gh **P**ressure **C**arbon **O**xygen Coversion
PL	**P**hoto**L**uminescence
XPS	**X**-ray **P**hotoelectron **S**pectroscopy
FIB	**F**ocussed **I**on **B**eam
VLS	**V**apour-**L**iquid-**S**olid
FRC	**F**ree **R**adical **C**ondensate
PAH	**P**olycyclic **A**romatic **H**ydrocarbon
UHV	**U**ltra **H**igh **V**acuum
SLS	**S**olid-**L**iquid-**S**olid
SMSI	**S**trong **M**etal **S**upport **I**nteraction

Declaration of Authorship

I, Gregory N. Ayre, declare that this thesis titled, 'On the Mechanism of Carbon Nanotube Formation by Means of Catalytic Chemical Vapour Deposition' and the work presented in it are my own. I confirm that:

- This work was done wholly or mainly while in candidature for a research degree at this University.
- Where any part of this thesis has previously been submitted for a degree or any other qualification at this University or any other institution, this has been clearly stated.
- Where I have consulted the published work of others, this is always clearly attributed.
- Where I have quoted from the work of others, the source is always given. With the exception of such quotations, this thesis is entirely my own work.
- I have acknowledged all main sources of help.
- Where the thesis is based on work done by myself jointly with others, I have made clear exactly what was done by others and what I have contributed myself.

Signed:

Date: October 2011

List of Publications

1. G. N. Ayre, D. C. Smith, B. Mazumder, A. L. Hector, T. Uchino, C. H. de Groot, and P. Ashburn, "CMOS Compatible Synthesis of Carbon nNnotubes." In: *Materials Research Society Conference*, 24th-28th March 2008, San Francisco, USA.

2. T. Uchino, G. N. Ayre, D. C. Smith, J. L. Hutchison, C. H. de Groot, and P. Ashburn, "Growth of Single-Walled Carbon Nanotubes Using Germanium Nanocrystals Formed by Implantation." *J. Electrochem. Soc.*, 156 (8). K144-K148. 2009.

3. T. Uchino, G. N. Ayre, D. C. Smith, J. L. Hutchison, C. H. de Groot, and P. Ashburn, "Growth of Carbon Nanotubes on HfO2 towards Highly Sensitive Nano-Sensors." *Jpn. J. Appl. Phys*, 49 . 04DN11-1-04DN11-4. 2010.

4. G. N. Ayre, T. Uchino, B. Mazumder, A. L. Hector, J. L. Hutchinson, D. C. Smith, P. Ashburn, and C. H. de Groot "Chemical Vapour Deposition of CNTs Using Structural Nanoparticle Catalysts." In: *Carbon Nanotubes*, pp. 19-39, INTECH. ISBN 978-953-307-054-4. 2010.

5. T. Uchino, G. N. Ayre, D. C. Smith, J. L. Hutchison, C. H. de Groot, and P. Ashburn, "Metal-Catalyst-Free Growth of Carbon Nanotubes and Their Application in Field-Effect Transistors." *Electrochem. Solid-State Lett.*, 14 (4). K21-K23. 2011.

6. T. Uchino, J. L. Hutchison, G. N. Ayre, D. C. Smith, C. H. de Groot, and P. Ashburn, "Metal-Catalyst-Free Growth of Silica Nanowires and Carbon Nanotubes Using Ge Nanostructures." *Jpn. J. Appl. Phys*, 50 (4). 04DN02. 2011.

7. G. N. Ayre, T. Uchino, B. Mazumder, A. L. Hector, J. L. Hutchison, D. C. Smith, P. Ashburn and C. H. de Groot, "On the Mechanism of Carbon Nanotube Formation: The Role of the Catalyst." *J. Phys.: Condens. Matter* 23. 394201. 2011.

Acknowledgements

Today's research involves the effort of specialists with different backgrounds and different points of view. This work would be impossible without the collaboration of numerous sources. Hereby, I would like to acknowledge their input.

First and foremost, I would like to convey my gratitude to my supervisor, Dr. David C. Smith, for his continual support and valuable guidance throughout the project. His assistance and advice were crucial. I would also like to thank him for the opportunity to work in his research group under excellent conditions (especially considering that my working hours were "non-conventional").

I would also like to thank Professor Peter Ashburn for his patience, support and guidance since the days of my undergraduate studies. I am very grateful for the help and advice he has given me over the years, and for opening many sources of opportunities throughout my university education. I wish him all the best in his retirement.

Many thanks to Dr. Kees de Groot, who was immensely helpful in working with me towards publishing a large body of my work. I owe him much for his patience, numerous discussions and general good humour.

Furthermore, I would like to thank Dr. Takashi Uchino for his help with the practical aspects of the project, in particular with the FE-SEM and the CNT furnace. His advice, useful suggestions and discussions were invaluable. I would also like to acknowledge his role in conceiving the idea of carbon nanotube growth on Ge nanoparticles and undertaking Raman and TEM measurements for the implanted Ge nanocrystals, shown in Section 5.7.

I would also like to acknowledge John M. Nesbitt for his part in undertaking the RBM resonance measurements of HiPCo nanotubes (Figure 2.7) and for the normalisation and plotting of the spectra. This work was especially complex and time consuming as it required normalisation of power and spectrometer grating efficiency in addition to re-optimising the system alignment for each wavelength utilised. I am very grateful for his help and friendship.

I would also like to thank Dr. Shuncai Wang for his assistance in this work with electron microscopy. In addition, I am grateful to Zondy Webber for the useful suggestions,

training and advice regarding the use of clean room equipment. A large debt of gratitude (and beer) is owed to Dr. Harold Chong for allowing me to use the Nano Group Raman System for the characterisation of all my nanotube samples.

Finally, I would like to thank my family and friends for their support of so many years. In particular I would like to thank my parents, Izaura and Robert Ayre for everything they have done and sacrificed for me over the years. As my father likes to point out, I wouldn't even be able to tie my shoes if it wasn't for them. Michael Pollard and Matthew Forse also deserve a special mention for their friendship and for keeping me sane all these years.

Thank you to everyone who shared all the pleasures and troubles of these years.

Chapter 1

Introduction

Carbon nanostructures, such as fullerenes [38], nanotubes [39], nano-onions [40] and nano-horns [41] have attracted much interest recently. In particular, the mechanical and electronic properties of carbon nanotubes are the subject of intensive studies [42]. Beside the fundamental interest in their physical, electronic and chemical properties; there is a strong drive in application development for devices based on carbon nanotubes. Nanotubes can be produced using arc discharge [39], laser ablation [43] or chemical vapour deposition (CVD) techniques [44]. CVD is currently the most promising and flexible method with regard to applications, but our understanding of the role of the catalyst and deposition parameters on nanotube growth is still fragmentary.

1.1 Motivation

Applications for single walled carbon nanotubes (SWNTs) range from nanoelectronics, sensors, field emitters to composites [45]. These require reliable synthesis techniques capable of generating large quantities of high purity material. In addition, applications in the field of nanoelectronics and photonics may require controlled growth at precise lithographically patterned areas. Understanding how to control the synthesis of SWNTs is vital in order to deterministically integrate such nanostructures into various technologies.

Of the various methodologies developed for carbon nanotube (CNT) synthesis, those based upon catalyst-assisted chemical vapour deposition (CCVD) appear to be best suited to satisfy these requirements. Traditionally, $3d$ transition metal nanoparticles, such as Fe, Co and Ni, are used to catalyze CNT growth. These catalysts are thought to work in accordance with the model for carbon filament growth, derived by Baker et al. [1, 2, 46], from concepts of vapour-solid-liquid theory [47]. In this model, hydrocarbons adsorbed on the metal nanoparticle are catalytically decomposed resulting in atomic

carbon dissolving into the liquid catalyst particle, and when a supersaturated state is reached, carbon precipitates in a tubular, crystalline form.

Recently, several groups have reported successful growth of CNTs from noble metal [3–7], ceramic [8, 9] and semiconducting nanoparticles [10–13], all of which are regarded as unable to catalyse the dissociation of hydrocarbons. In addition to this, in their bulk form, these materials do not have a catalytic function to produce graphite. This implies that given enough energy, carbon atoms on a nanoparticle are capable of a structural reorganisation into CNTs. This leads to a new interpretation of the role of the catalyst in nanotube growth in which only a nanoscale curvature and carbon adsorption sites are necessary.

This work explores non-traditional paths of catalytic chemical vapour deposition of carbon nanotubes with a view to determine the essential role of the catalyst in nanotube growth.

1.2 Organisation

Chapter 2 covers the characterisation methods which are used throughout this work, and provides a brief overview of other techniques commonly used in carbon nanotube research. The structure of carbon nanotubes is briefly summarised, followed by a description of the various characterisation techniques. The most interesting features of each technique are noted and practical considerations addressed.

Chapter 3 presents a review of the literature highlighting the more interesting methodologies for carbon nanotube synthesis by thermal chemical vapour deposition. Catalyst and supporting material for nanotube deposition, carbon precursor, operating conditions are discussed as the important parameters affecting the quality and yield of carbon nanotube synthesis by chemical vapour deposition. A model for catalytic growth of single-walled carbon nanotubes is presented and discussed.

In Chapter 4, single-walled carbon nanotubes growth catalysed by noble metal nanoparticles has been studied. Au, Cu and Ag nanoparticles have been synthesized and investigated as potential catalysts. Au and Cu nanoparticles have shown to be adequate catalysts for CNT growth and extensive characterisation of each stage of the growth process is presented. The results presented show that the commonly utilised model of carbon filament growth is inadequate to describe SWNT growth from noble metal catalysts. A new interpretation of the role of the catalyst is presented and discussed.

Chapter 5 presents a novel technique to synthesize single-walled carbon nanotubes from germanium nanoparticles. The Ge nanoparticles are synthesized by ion implantation into a SiO_2 followed by an anneal step in N_2 and hydrofluoric acid vapour etch. This

process affords good control over nanoparticle size and density, which allows the investigation of the effect of catalyst size on growth of carbon nanotubes. The process used is compatible with silicon complementary metal oxide semiconductor process and is amenable for application in hybrid silicon-nanoelectronics.

In Chapter 6 research on the use of colloidal Ge nanoparticles for carbon nanotube growth is presented. Colloidal Ge nanoparticles are fabricated by an inverse micelle technique, which offered good control over the nanoparticle sizes. The colloidal Ge catalyst is shown to be a viable catalyst for the formation of single-walled carbon nanotubes on a SiO_2 support. The effect of pretreatment on the catalyst is studied in order to ascertain its effect on the yield of carbon nanotubes. The synthesized nanotubes were examined by Raman spectroscopy and transmission electron microscopy and were found to be of a good quality. This chapter also presents a mechanism for the formation of SiO_x nanowires frequently grown in conjunction with nanotubes.

Finally, in Chapter 7, the factors affecting the activity of a metal catalyst-support system are investigated. To explore these interactions, combinations of catalyst metals (Fe, Ni and Co) and support mediums (SiO_2, Al_2O_3 and HfO_2) are tested for nanotube growth under similar conditions in a high temperature furnace. AFM, SEM and Raman analysis were employed to characterise the synthesized nanotubes and the morphology of the catalyst nanoparticles at various stages in the growth process.

Chapter 2

Characterisation Techniques in Carbon Nanotube Research

This chapter covers the characterisation methods which are utilised throughout this work, and provides a brief overview of other techniques commonly used in carbon nanotube research. The structure of carbon nanotubes is briefly summarised, followed by a description of the various characterisation techniques. The most interesting features of each technique are noted and practical considerations addressed.

2.1 Structure and Properties of Carbon Nanotubes

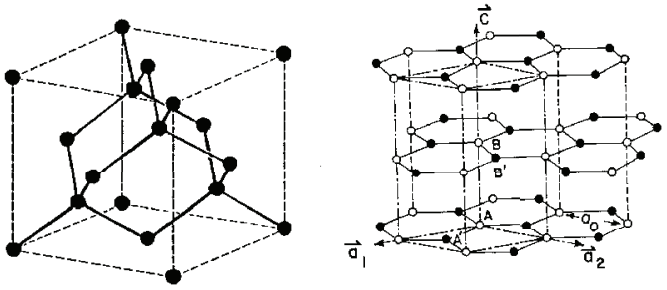

FIGURE 2.1: Structure of the two main modifications of carbon: Diamond (left) and Graphite (right). Modified from Dresselhaus et al. [14].

Pure carbon exists in the solid form mainly in two allotropes (Figure 2.1). In diamond, the orbitals of the carbon atom are in a state of sp^3 hybridisation. The four valence electrons create four equivalent σ bonds to connect four other carbons in the four tetrahedral directions. This three dimensional interlocking structure is very rigid, stable and hard. The solid has a band gap of 5.5 eV and is thus an insulator. The second configuration is graphite, with sp^2 hybridised orbitals. In this configuration, three outer shell electrons of each carbon atom form three in-plane σ bonds with an out-of-plane π orbital (bond),

forming a hexagonal network parallel with each other with a spacing of 0.34 nm. The bonding strength in-plane is very strong, whereas between the layers the bonding is mediated by relatively weak van-der-Waals forces. In addition, the out-of-plane π electron is delocalised over a graphite plane making it thermally and electrically conductive in this orientation.

In 1985, Kroto et al [38] discovered a new allotrope of carbon, fullerenes. These are ball-like molecules which consist of e.g. 60, 70 or 80 carbon atoms. The bonding is mainly sp^2, although due to a high curvature this is mixed with sp^3 character. The special bonded structures in fullerene molecules have provided several surprises such as metal-insulator transition [48], unusual magnetic correlations [49] and very rich electronic and optical band structures and properties [50]. For the discovery of fullerenes Kroto, Smalley and Curl obtained the Nobel Prize for Chemistry in 1996.

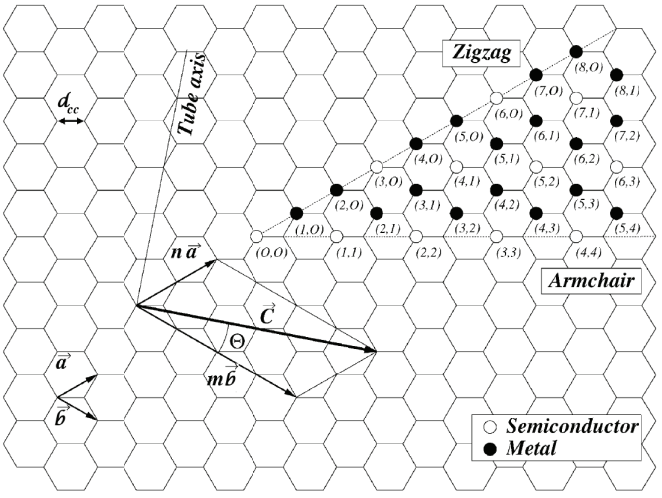

FIGURE 2.2: Chiral vector $\vec{C}$ and chiral angle θ definition for a $(2,4)$ nanotube on a graphene sheet. $\vec{a}$ and $\vec{b}$ are the unit cell vectors of the two dimensional hexagonal graphene sheet. The circumference of the nanotube is given by the length of the chiral vector. The chiral angle θ is defined as the angle between the chiral vector and and the zig-zag axis. Modified from McGuire and Rao [15].

A carbon nanotube can be described as a hollow cylinder formed by rolling graphite sheets. Bonding in nanotubes is essentially sp^2. However, the circular curvature will cause quantum confinement and $\sigma-\pi$ rehybridisation, in which three σ bonds are slightly out of plane. For compensation, the π orbital is delocalised outside the tube. This makes nanotubes mechanically stronger, electrically and thermally more conductive, and chemically more reactive than graphite. A single-walled carbon nanotube (SWNT)is therefore a single graphene plane rolled into a cylindrical shape so that the structure is one dimensional, and in general exhibiting a spiral conformation, called chirality.

Any SWNT is completely described, except for their length, by a single vector $\vec{C}$ (called the chiral vector). Two atoms in a planar graphene sheet are chosen and one is used as the origin. The chiral vector $\vec{C}$ is pointed from the first atom towards the second one

(Figure 2.2) and is defined by the relation, $\vec{C} = n\vec{a} + m\vec{b}$, where n, m are integers, and $\vec{a}$, $\vec{b}$ the unit vectors of the two-dimensional lattice formed by the graphene sheet. The direction of the nanotube axis is perpendicular to this chiral vector. Thus, the SWNT is constructed by rolling up the sheet such that the two end-points of the vector $\vec{C}$ are superimposed.

One can derive, by geometric considerations, that the diameter D of the tube (n, m) and the conformation angle θ, with equal C-C bond length (d_{C-C}), are given by:

$$D = \frac{\sqrt{3}d_{C-C}}{\pi}\sqrt{n^2 + nm + m^2} \tag{2.1}$$

$$\theta = \arccos\left(\frac{2n + 2m}{2\sqrt{n^2 + nm + m^2}}\right) \quad (0 \leq \theta \leq \frac{\pi}{6}) \tag{2.2}$$

Simple tight-binding methods predict that SWNTs with $2n+m = 3i$ are metallic (where i is a positive integer) and with $2n + m \neq 3i$ are semiconducting. However, in most cases this view is overly simplistic. A more complete description can be found in [51], which shows that the armchair ($n = m$) tubes are metallic, zigzag tubes $(3n, 0)$ are narrow-gap semiconductors, helical tubes (n, m) with $2n + m = 3i$ are also narrow-gap semiconductors and all other tubes are wide-gap semiconductors. This behaviour is caused by periodic boundary conditions for the component of momentum along the circumference of the tube, which results in quantisation.

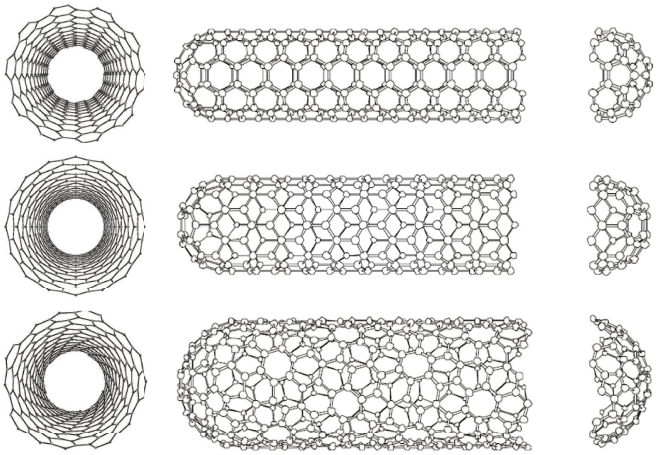

FIGURE 2.3: Models of single walled carbon nanotubes and termination caps: $(5, 5)$ armchair nanotube, $(9, 0)$ zig-zag nanotube and $(10, 5)$ chiral nanotube.

The terminating cap of a nanotube is formed from pentagons and hexagons (Figure 2.3). It has been shown that the formation of this cap plays an important role in determining the nanotube chirality when fabricated by chemical vapour deposition. The smallest cap that fits to the cylinder of the carbon tube seems to be the well known C_{60} hemisphere. The smallest experimental value of nanotube diameter, 0.7 nm, is in good agreement with

this cap [52]. However, recently there have been studies of nanotubes at the theoretical limit of 0.4 nm in diameter [53–59]. These nanotubes are sometimes capped with a C_{20} dodecahedron [54]. According to Liang et al. [55], these nanotubes have only three possible chiralities; $(4, 2)$, $(5, 0)$ and $(3, 3)$.

2.2 Electron Microscopy

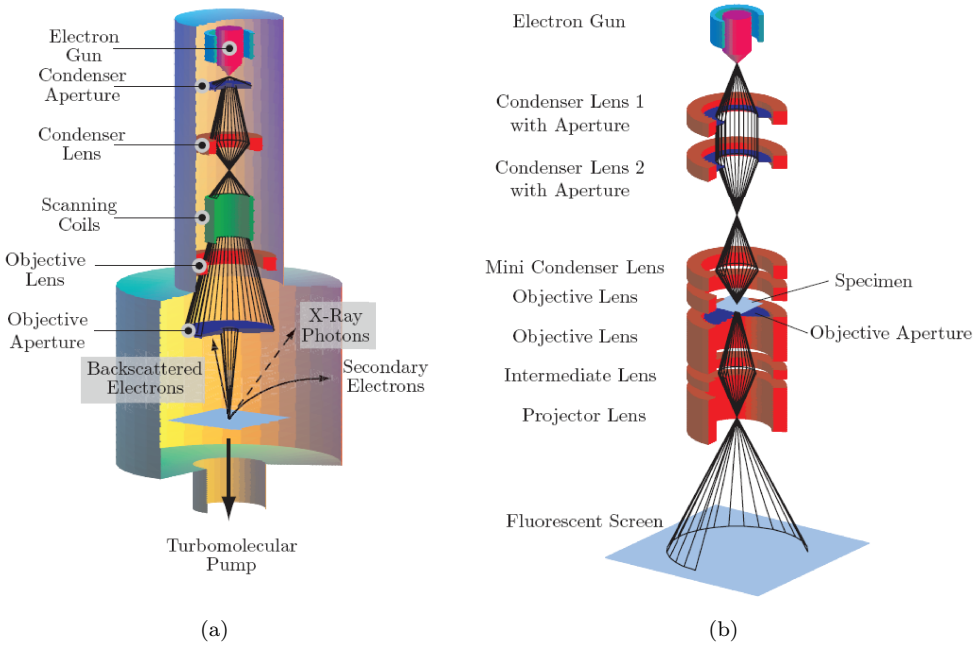

FIGURE 2.4: Electron path in a scanning (a) and transmission (b) electron microscope.

Due to their small diameter, typically around 1 nm, imaging SWNTs requires high-resolution microscopy techniques. Electron microscopes (EMs) function as their optical counterparts except that they use a particle beam of electrons instead of light to create an image of the specimen. Due to the shorter wavelength of electrons (cf. visible light), EMs are capable of higher magnifications and have a greater resolving power than a light microscope. In addition, owing to the dual wave-particle nature of electrons, EMs also yield a wealth of secondary signals such as x-rays, Auger electrons and light [60, 61]. These secondary signals can provide topography, morphology, chemical composition and crystallographic information.

2.2.1 Scanning Electron Microscopy

The scanning electron microscope (SEM) is used to study the surface of materials rather than their internal arrangement. The typical resolution of this technique is approximately 2 to 5 nm, and thus does not allow for individual SWNTs to be imaged within

a rope [15], however due to charging effects it is possible to resolve isolated SWNTs on an insulating substrate [62]. This instrument differs from all other conventional microscopes, using light or electrons (with exception to Scanning Transmission Electron Microscopes and Confocal Optical Microscopes), in forming its image progressively.

In a typical SEM (Figure 2.4(a)), electrons generated by the electron gun, are condensed by the first condenser lens to form a beam. Together with the condenser aperture, this stage eliminates high angle electrons from the beam. The second condenser lens then forms the electrons into a thin, tight collimated beam. Further high angle electrons are eliminated from the beam at this point by an objective aperture. The beam passes through pairs of scanning coils, which deflect the beam in the x and y axes so that it scans in a raster fashion over a rectangular area of the sample surface. The final lens, the objective lens, focuses the scanning beam onto the desired part of the specimen.

A number of phenomena occur at the surface when the primary beam interacts with the specimen. The most important for scanning microscopy are the emission of secondary electrons, originated from specimen atoms by collisions with high energy electrons, and the re-emission or reflection of high-energy backscattered electrons from the primary beam. The intensity of the secondary and backscattered electrons are very sensitive to the angle at which the electron beam strikes the surface, i.e. to topological features on the specimen. The emitted electron current is collected and amplified. Variations in the resulting signal strength as the electron probe is scanned across the specimen are used to vary the intensity of a corresponding spot of a raster image synchronous with the probe.

Individual SWNTs exhibit remarkable contrast on an insulating substrate when imaged using a low-energy electron beam. SWNTs appear as bright and rather thick (typically $10 - 15$ nm) lines in the secondary electron image. It has been reported that nanotube contrast on an insulator stems from the local potential difference between the nanotube and the substrate [62]. This may be the case when nanotubes are charged, on a thick insulator. However, Homma et al. [63] report that the imaging mechanism can be explained by an electron-beam-induced current (EBIC). The EBIC from the nanotube (or nanotube network) affects the charging state of the insulating substrate, thereby increasing secondary electron emission from the surface. Images typically reflect the EBIC range round the nanotubes, and thus SWNTs appear much thicker than their actual diameter.

Scanning electron microscopy was performed to analyse the nanostructures in plan view. A JEOL JSM-6500F microscope, equipped with a thermionic field emission gun, operating between 2 and 10 kV at a typical working distance of 10 mm in secondary electron imaging mode was used.

2.2.2 Transmission Electron Microscopy

Figure 2.4(b) shows the electron path in a typical transmission electron microscope (TEM). In the TEM, the sample is illuminated with an electron beam using condenser lenses. The beam is restricted by the condenser aperture, removing high angle electrons. After striking the specimen, parts of the beam are transmitted. The objective lens then forms an inverted image. The resulting image, representing a 2-D projection of the sample is magnified by the projector lens before striking a CCD or fluorescent screen.

Although SEM can be useful in imaging CNTs on a substrate surface, transmission electron microscopy is a more powerful technique, with a higher resolution that allows one to image the number of walls in a multi-walled carbon nanotube [16, 64–66], or image isolate SWNTs residing inside a bundle [17]. This allows for careful measurement of tube diameters as well as investigation of structural defects in CNTs. Many studies have been done on nanotubes involving TEM, and Figure 2.5 illustrates the results of some of those studies.

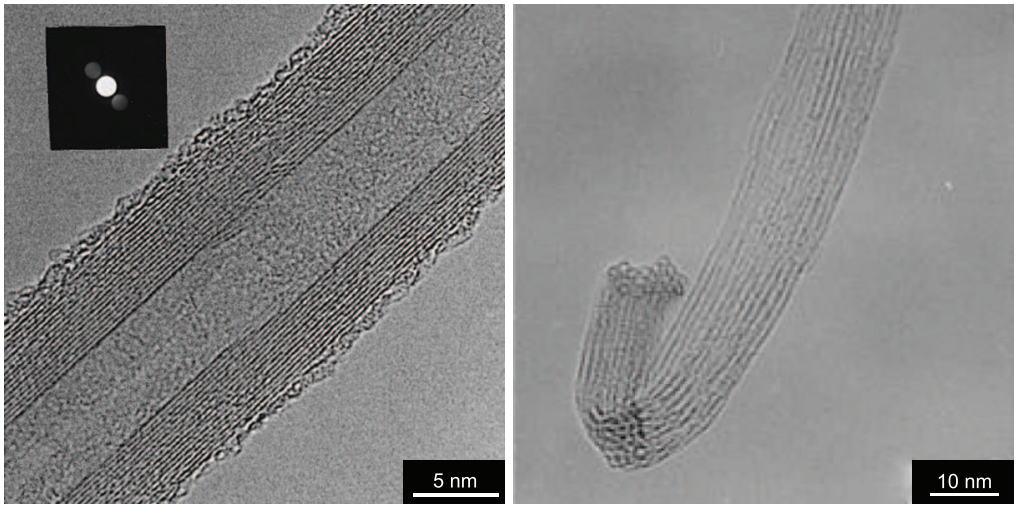

(a) (b)

FIGURE 2.5: TEM images of: (a) a MWNT showing concentric stacking of several nanotubes with concentric diameters, inset shows observed electron diffraction spots (modified from Andrews et al. [16]), (b) a single bundle containing $\sim$ 40 SWNTs as it bends throught the image plane of the microscope (modified from Thess et al. [17]).

The inter-shell spacing of multi-walled carbon nanotubes (MWNTs) have been studied by Kiang et al. [64] using high resolution TEM images. The inter-shell spacing is found to range from 0.34 to 0.39 nm varying with tube diameter. These values are greater than the graphite inter-planar distance (0.336 nm) [65], although this increase can be explained by the curvature of the graphene sheets which is modified by the tube radius.

Another benefit that comes with using TEM is the use of electron diffraction and electron energy loss spectroscopy (EELS). Qin [67] has demonstrated that the true helicity of CNTs can be deduced from electron diffraction patters. A curvature correction factor

is determined by a Bessel function calculated from the tube indices (n,m). The chiral indices of CNTs can be measured by the selected-area electron diffraction (SAED) technique. Then, the true chiral indices can be retrieved for SWNTs or MWNTs up to radii of 4 nm. Contrary to spectroscopic techniques, no empirical fitting parameter such as C-C bond length is required to determine the helicity of the tube. In addition, the determination of CNT structures within nanotube bundles can also be obtained using TEM coupled with electron diffraction [68]. EELS has been particularly beneficial in the area of doped nanotubes [69, 70]. It has allowed researchers to determine the amount of dopant present in the nanotube structure. In conjuction with x-ray energy dispersive spectroscopy (EDS), TEM has also enabled the identification of the catalyst composition responsible for nanotube nucleation [71].

In this work, TEM was used to obtain high-resolution images of several nanostructures and catalysts. A JEOL JEM-3010 microscope, operating between 200 and 300 kV was primarily used (point resolution 0.21 nm). Additional TEM imaging was undertaken at the Materials Department of Oxford University, utilising a range of microscopes.

2.3 Scanning Probe Microscopy

The previous section demonstrated the usefulness of the EM techniques applied to nanotube research. However, there are two other microscopic methods that are indispensable in nanotube research. These methods are atomic force microscopy (AFM) and scanning tunnelling microscopy (STM). Both methods have provided useful information of nanotube structure and properties. Although not explicitly used in this work, STM and a brief overview of the advances in Kelvin probe force microscopy of carbon nanotubes are presented for completeness.

2.3.1 Atomic Force Microscopy

The AFM consists of a cantilever with a sharp tip (probe) at its end that is used to scan the specimen surface. The cantilever is typically silicon or silicon nitride with a tip radius of curvature on the order of a few nanometers. When the tip is brought into proximity of a sample surface, forces between the tip and the sample lead to a deflection of the cantilever according to Hooke's law. Typically, the deflection is measured using a laser spot reflected from the top surface of the cantilever into an array of photodiodes.

In order to prevent damage to the sample, a feedback mechanism is employed to adjust the tip-to-sample distance to maintain a constant force between the tip and the sample. Traditionally, the sample is mounted on a piezoelectric tube, that can move the sample in the z direction for maintaining a constant force, and the x and y directions for scanning

the sample. The resulting map of the area $s = f(x, y)$ represents the topography of the sample.

The AFM can be operated in a number of modes, depending on the application. In general, possible imaging modes are divided into static (also called contact) modes and a variety of dynamic (non-contact or tapping) modes where the cantilever is vibrated. In tapping mode, the cantilever is deliberately vibrated at near its resonant frequency in either amplitude modulation mode or frequency modulation. Very weak van der Waals attractive forces are present at the tip-sample interface. The surface topography is measured by laterally scanning the sample under the tip while simultaneously measuring the separation-dependent force or force gradient between the tip and the surface. The force gradient is obtained by vibrating the cantilever and measuring the shift in the resonant frequency of the cantilever. To obtain topographic information, the interaction force is either recorded directly, or used as a control parameter for a feedback circuit that maintains the force or force derivative at a constant value.

AFM has been very useful in imaging isolated SWNTs that have been grown directly on silicon substrates via a chemical vapour deposition process [72–74] or prepared by processing SWNT bundles [75]. Although the resolution is not as high as that found in the TEM, diameter estimates as well as the length measurements of the nanotubes within a sample are possible. It should be noted that the finite size and shape of the tip poses a considerable obstacle in the accurate imaging of nanostructures, as in the general case the acquired image is a convolution of the sample and the probe shape. In most cases this is not problematic as the sample will dominate the image, however when the size of the sample is smaller than the probe this is problematic and will require a deconvolution procedure [76, 77].

In this work, AFM was primarily used to characterise the size of the nanoparticle catalysts before and after thermal treatment. As the size of the nanostructures typically were smaller than the probe size, height data (z-axis) was predominantly used in the subsequent analysis. A Veeco Multi-Mode AFM was used for all imaging in this work, utilising a super-sharp silicon cantilever (typical tip radius of 2 nm, resonant frequency of 300 kHz). The AFM was operated in tapping mode, using a minimum resolution of 512×512 points per μm^2.

2.3.2 Scanning Tunnelling Microscopy

The scanning tunnelling microscope (STM) is based on the concept of quantum tunnelling. When a conducting probe is brought very near to the surface to be examined, a bias applied between the two can allow electrons to tunnel through the vacuum between them. The resulting tunnelling current is a function of probe position, applied voltage, and the local density of states (LDOS) of the sample [78]. Information is acquired by

monitoring the current as the probe's position scans across the surface, and is usually displayed in image form. STM can be a challenging technique, as it requires extremely clean and stable surfaces, sharp tips, excellent vibration control, and sophisticated electronics.

To use this technique, carbon nanotubes must be deposited on a flat conducting substrate such as highly-orientated pyrolytic graphite [79, 80] or gold [20, 81]. STM images give directly the three dimensional morphology of tubes and are consistent with the structure inferred from SEM [79]. Moreover, STM can resolve simultaneously both the atomic structure and the density of states (DOS), making this a powerful tool for nanotube characterisation. Experiments to determine the atomic structure of of SWNTs at low temperature were conducted by several groups [80, 81]. The atomic structure of SWNTs in a rope was also shown by various authors [20, 82]. These studies confirmed the predicted behaviours of SWNTs [83, 84] and revealed the sensitivity of the electronic properties to the helicity and tube diameter.

2.3.3 Kelvin Probe Force Microscopy

Kelvin probe force microscopy (KPFM) is a non-contact variant of AFM. With KPFM, the work function of surfaces can be observed at atomic or molecular scales. The work function relates to many surface phenomena, including catalytic activity, doping and band-bending of semiconductors, charge trapping in dielectrics and corrosion.

KPFM is a scanning probe method where the potential offset between a probe tip and a surface can be measured using the same principle as a macroscopic Kelvin probe. The cantilever acts as a reference electrode that forms a capacitor with the surface, over which it is scanned laterally at a constant separation. The cantilever is not piezoelectrically driven at its resonant frequency, although an alternating current is applied. When there is a potential difference between the cantilever and the surface, the AC+DC voltage offset will cause the cantilever to vibrate. The resulting vibration is detected as in AFM and feedback systems drive a DC potential to null this vibration. As a result a map of the nulling potential versus the lateral position is formed.

Recent research using KPFM on carbon nanotubes has shown that it is possible to differentiate metallic and semiconducting nanotubes by measuring the low-frequency dielectric polarization of individual nanotubes [85]. A measurement methodology is described by Lu et al. [86] which allows quantitative differentiation between metallic and semiconducting nanotubes by KPFM. For further details, please refer to references [85–89].

2.4 Raman Spectroscopy

Over the past 20 years, Raman spectroscopy has proven to be one of the most powerful tools in the characterisation of carbon-based materials. It has been used extensively to study the bonding and properties of pristine, metallic and superconducting phases of graphite intercalation compounds and fullerene-based solids [14, 18, 21, 33, 90–94]. Naturally, this technique is equally useful to characterise carbon nanotubes. This section provides a brief overview of the Raman effect, its application to carbon nanotubes and some highlights of recent Raman studies on these nanostructures.

2.4.1 The Raman Effect

Raman scattering is an optical process involving inelastic scattering of a photon. This can be considered a three stage process. The first stage is the excitation of a real or virtual electron-hole pair, caused by an incoming photon. The electron or hole is then scattered by a phonon, either emitting or absorbing a phonon. This results in a decrease or increase in the energy of the electron-hole pair, respectively. In the final stage the electron-hole pair recombines, emitting an outgoing photon with its energy shifted relative to that of the incoming photon by one phonon energy lower (Stokes shift) or higher (anti-Stokes shift). This energy shift is known as a Raman shift. Typically, only 1 in 10^6 photons scattered will have been Raman scattered.

Using classical considerations, the Stokes and Anti-Stokes lines should possess the same intensity. However, experimental data has shown that this is not the case. In addition, the classical treatment is not able to provide any information on the relation between derived polarizability and the properties of the scattering system, such as transition frequencies. For this, a quantum mechanical treatment is required (for further details please refer to [95–100]).

The scattering rate for this process, calculated from the light-semiconductor dipole Hamiltonian for incoming light ($\hat{H}_{\text{in}}$), scattered light ($\hat{H}_{\text{scat}}$), and the carrier-phonon Hamiltonian ($\hat{H}_{\text{phonon}}$) is given by:

$$\Gamma \propto |M|^2 \begin{cases} \delta\omega_{\text{scat}} - \omega_{\text{in}} + \omega_{\text{phonon}}(N_{\text{phonon}} + 1) & \text{Stokes} \\ \delta\omega_{\text{scat}} - \omega_{\text{in}} - \omega_{\text{phonon}}(N_{\text{phonon}}) & \text{anti-Stokes} \end{cases} \tag{2.3}$$

where

$$|M|^2 = \left| \sum_{k,l} \frac{\langle 0| \hat{H}_{\text{scat}} |k\rangle \langle k| \hat{H}_{\text{phonon}} |l\rangle \langle l| \hat{H}_{\text{in}} |0\rangle}{(E_k + i\Gamma_k - \eta\omega_{\text{scat}})(E_l + i\Gamma_l - \eta\omega_{\text{in}})} \right|^2 \tag{2.4}$$

and ω_{in}, ω_{scat} are the frequencies of the incoming and scattered light, respectively. $|k\rangle$ and $|l\rangle$ are the intermediate electron-hole pairs states, N_{phonon} is the phonon occupancy and the delta functions indicate energy conservation. The relative intensities of Stokes and anti-Stokes scattering depend on the population of the system. These populations can be calculated using Bose-Einstein statistics;

$$N_{\text{phonon}} = \frac{1}{e^{\frac{E}{kT}} - 1} \tag{2.5}$$

where E is the phonon excitation energy given by $\hbar\omega_{\text{phonon}}$.

When the incoming and outgoing light is not resonant with any intermediate states, all of the intermediate states give similar contributions to the overall scattering rate, and so the matrix element can be approximated by;

$$|M|^2 \propto \langle 0| \hat{H}_{\text{scat}} \hat{H}_{\text{phonon}} \hat{H}_{\text{in}} |0\rangle^2 \tag{2.6}$$

It is in the form of Equation 2.6 that the polarisation selection rules and wavevector conservation during Raman scattering are derived ($k_{\text{phonon}} = k_{\text{in}} - k_{\text{scat}}$).

2.4.2 Resonance Raman Scattering

Typically Raman spectra only involves phonons explicitly, being independent of the electronic structure of the material and the laser energy used to excite the Raman spectra. Furthermore, the usual Raman scattering signal is very weak. However, the scattering efficiency is greatly enhanced when the laser excitation energy matches the energy between optically allowed electronic transitions in the material. This enhancement process is called resonance Raman scattering [97]. The resonance Raman intensity depends on the density of electronic states (DOS) available for optical transitions, and this property is very important for one-dimensional systems.

In the case that the incoming or outgoing light is close to, or in resonance with any of the intermediate states, these states dominate the Raman scattering rates shown in Equations 2.3 and 2.4. This results in a breakdown of the general polarisation selection rules and wavevector conservation (shown in Equation 2.6). The resonance conditions;

$$\begin{aligned} E_{\text{laser}} &= E_l &&= E_{ii} && \text{(Incoming)} \\ E_{\text{laser}} &= E_k &&= E_{ii} + E_{\text{phonon}} && \text{(Outgoing)} \end{aligned} \tag{2.7}$$

are then derived from Equation 2.4, where E_{ii} is an allowed optical transition.

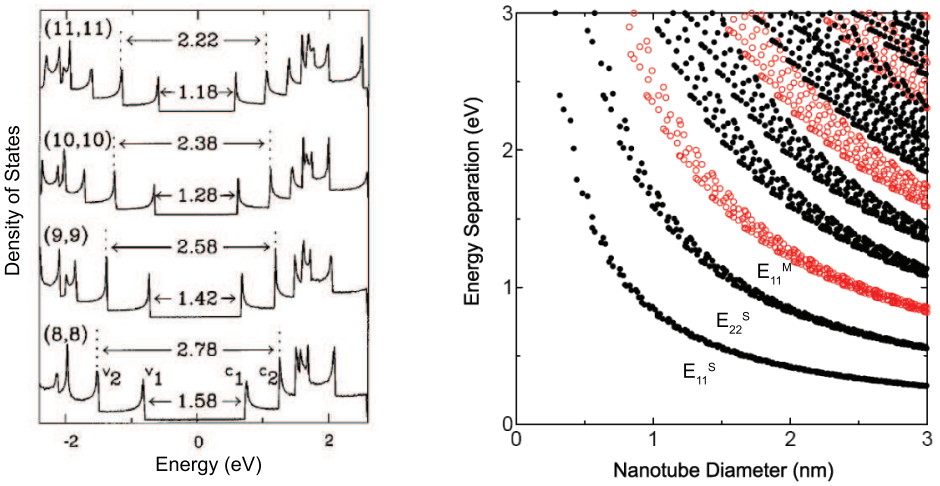

(a) (b)

FIGURE 2.6: (a) Calculated electronic DOS for several SWNTs, modified from Rao et al. [18]. (b) Kataura plot generated for SWNTs in a diameter range of 0.4 to 3 nm, after Kataura et al. [19].

Figure 2.6(a) shows the DOS for four different armchair SWNTs; $(8,8)$, $(9,9)$, $(10,10)$ and $(11,11)$. Depending on tube diameter and chiral vector of the nanotube, the DOS will vary from tube to tube. As one-dimensional systems, the DOS of SWNTs are characterised by sharp, narrow peaks referred to as van Hove singularities (vHs). The sharp vHs define narrow energy ranges where the DOS intensity becomes very large, as such a single carbon nanotube exhibits a molecular-like behaviour with well defined energy levels at each vHs. A resonance enhancement of the spectrum can be obtained when the laser excitation energy is equal to the energy separation between vHs in the valence and conduction bands (e.g. $E_{11}^S = v_1c_1$ and $E_{22}^S = v_2c_2$ in Figure 2.6(a)) in the DOS plot. It should be noted that this is restricted by the selection rules for optically allowed electronic transitions [101–103].

As the energy transitions between vHs are diameter dependent, the resonance condition will vary depending on tube diameter and chirality. Calculations have been undertaken to correlate nanotube diameter with the diameter-dependent transition energies of vHs in SWNTs [19]. The result of these calculations is the Kataura plot, shown in Figure 2.6(b). Each point in this plot represents one optically allowed electronic transition energy (E_{ii}) from a given (n,m) SWNT. In practical terms this indicates that a change in the laser excitation frequency will bring into resonance a different SWNT with a different diameter that satisfies the new resonance condition. This is called diameter-selective Raman spectroscopy and led in 1997 to the first use of Raman spectroscopy to differentiate between metallic and semiconducting nanotubes [18]. This effect is illustrated in Figure 2.7. Figure 2.7(a) shows the radial breathing mode (see Section 2.4.4) resonance plot of High Pressure Carbon Monoxide Conversion (HiPco) carbon nanotubes dispersed on a SiO_2 substrate. This plot shows the intensity of the radial breathing mode (RBM)

for various tubes increasing and decreasing as the resonance conditions are altered by varying the laser excitation energy. Figure 2.7(b) shows the change in Raman intensity for a single SWNT, RBM = 257.1 cm^{-1} as laser excitation energy is varied. The width of the resonant Raman window and energy of the transition can also be calculated from this information.

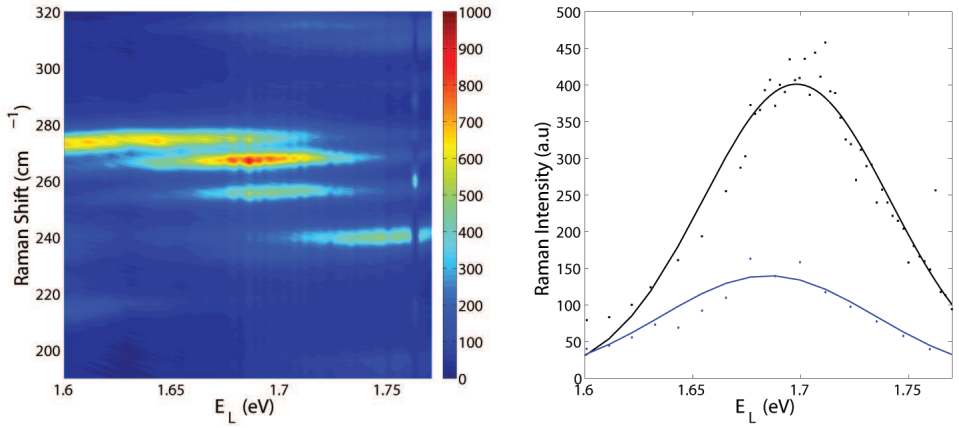

(a) (b)

FIGURE 2.7: (a) Radial breathing mode resonance plot of HiPco carbon nanotubes dispersed on a SiO_2 substrate, measured with 55 different laser energies (E_L) in Stokes. Colours (see scale on the right) indicate Raman intensity. (b) Raman intensity vs. laser excitation energy for the RBM = 257.1 cm^{-1} peak in the Stokes (black) and anti-Stokes (blue) Raman processes for one SWNT on a SiO_2 substrate. Stokes and anti-Stokes intensities have been normalised for power and spectrometer grating efficiency. The curves show the resonant Raman windows from which E_{ii} = 1.697 eV and a width for the window γ = 9 meV were determined.

2.4.3 Active Modes in Carbon Nanotubes

Upon rolling a graphene sheet into a tube, numerous vibrational modes are made Raman active by the cyclic boundary condition. Experimentally measured Raman spectrum is shown in Figure 2.8. The most characteristic features are summarised as following:

(i) a low frequency peak $\leq$ 350 cm^{-1} characteristic of single walled carbon nanotubes assigned to a A_{1g} mode of the tube. This is refered to as a radial breathing mode and corresponds to the atomic vibration of the C atoms in the radial direction, its frequency essentially depends on the diameter of the tube.

(ii) a large structure (1340 cm^{-1}) assigned to residual, ill-organised graphite, referred to as the defect modes, or D-band. This is not wavevector conserving.

(iii) a high frequency band between approximately 1550 and 1650 cm^{-1} characteristic of nanotubes, called the G band. This is assigned to a splitting of the E_{2g} stretching mode of graphite [104], corresponding to atomic vibrations in the axial

and circumferential directions. The line shape of this band is composed of up to 6 peaks, but only the two most intense peaks are useful for analysis [28].

(iv) a second order peak observed between 2450 and 2650 cm^{-1} assigned to the first overtone of the D mode and often called G' mode.

(v) a combination mode of the D and G bands between 2775 and 2950 cm^{-1}.

An in-depth description of Raman frequencies and symmetries can be found in Kuzmandy et al. [105]. For comparison with experiment, calculated Raman peak positions are shown in the bottom of Figure 2.8 for $n = 8$ to 11 armchair symmetry tubes. The calculated spectra are for a range of diameters consistent with those determined through TEM studies, and the vibrational frequencies are calculated with the same C-C force constants used to fit Raman, neutron and electron energy loss data for a flat graphene sheet. The small effect of curvature on the force constants was not taken into account, and theoretical Raman intensities were calculated using a bond polarizability model. The theoretical peak positions closely match the experimental peaks. Additionally, it can be noticed that certain experimentally obtained features are broader than others. This difference in width is attributed to an inhomogeneous line-broadening mechanism, which stems from the fact that certain mode frequencies exhibit a strong diameter dependence.

2.4.4 Radial Breathing Modes

The radial breathing mode can be used to determine the nanotube diameter (d_t) through its frequency (ω_{RBM}), to probe the electronic structure through its resonance (I_{RBM}, described in Section 2.4.2) and to perform a (n, m) assignment of a single isolated SWNT from analysis of both d_t and I_{RBM}. The status of research on these topics is summarised below.

The radial breathing mode (RBM) Raman features correspond to the coherent vibrations of the C atoms in the radial direction. These features are unique to carbon nanotubes and occur with frequencies between $120 \leq \omega_{RBM} \leq 350$ cm^{-1} for SWNTs within $0.7 \leq d_t \leq 2.0$ nm. These RBM frequencies are therefore very useful for identifying whether a given carbon material contains SWNTs, and for characterising the nanotube diameter distribution in the sample.

The RBM is directly dependent of the nanotube diameters through the relation $\omega_{RBM} = \frac{A}{d_t} + B$; where A and B are parameters determined experimentally [28]. However, the frequency of the RBM is not related to the chiral angle of the nanotubes [106–108]. For isolated SWNT bundles on an oxidised Si substrate, the experimental value of A is found to be 248 nm cm^{-1} and $B = 0$ nm cm^{-1} [21]. Using a force constant model with interactions to the fourth neighbour, Bandow et al. [22] calculated the value $A = 224$

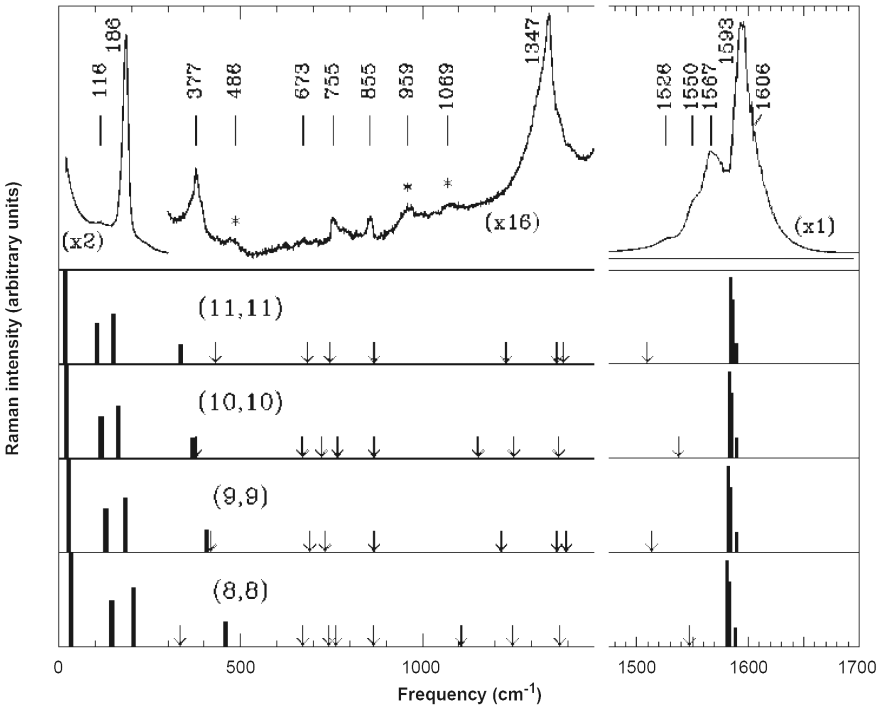

FIGURE 2.8: Experimentally measured Raman spectrum compared with theoretically determined Raman peak positions and intensities for several armchair nanotubes, from Rao et al. [18]. The calculated spectra are for a range of diameters consistent with the same C-C force constants used to fit Raman, neutron and electron energy loss data for a flat graphene sheet. The small effect of curvature on the force constants was not taken into account, and theoretical Raman intensities were calculated using a bond polarizability model.

nm cm^{-1}. Summarised in Bandow et al. [23], other values of the parameter A are given according to the models used. Figure 2.9 illustrates the dependence of the RBM on the nanotube diameter as described by some authors.

It should be noted that this phenomenological relationship is only valid over the range 1 nm $\leq d_t \leq$ 2 nm. With nanotube diameters below 1 nm, a chirality dependence of ω_{RBM} appears due to a distortion in the nanotube lattice. In addition, with diameters greater than 2 nm, the intensity of the RBM is weak [28]. The direct environment of the nanotubes also causes a modification of the RBM, due to van der Waals interactions. For instance, tube-tube interactions (bundling) result in an up-shift of the RBM by 14 cm^{-1} for $(9, 9)$ nanotubes [109].

The natural linewidths for the RBM feature are $\gamma_{\mathrm{RBM}} = 3$ cm^{-1}, although larger Γ_{RBM} values are usually observed due to broadening effects [110]. This broadening has been observed to increase monotonically with increasing diameter, and $\Gamma_{\mathrm{RBM}} \geq 20$ cm^{-1} values have been observed for $d_t \geq 2$ nm [110]. In SWNT bundles, the linewidth will not reflect Γ_{RBM}, but the ensemble of tubes in resonance with the excitation laser energy.

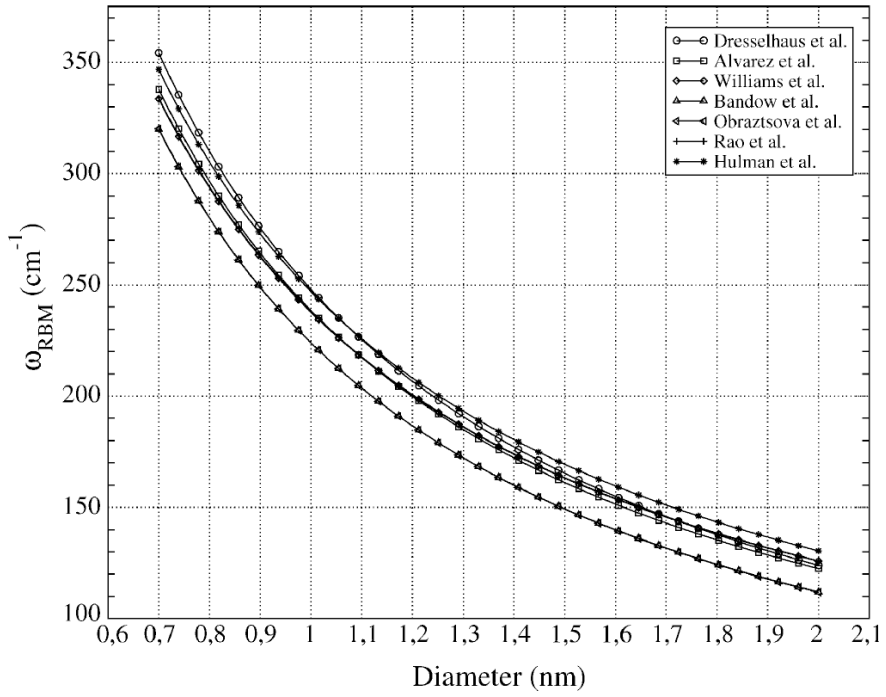

FIGURE 2.9: Phenomenological relations between radial breathing mode (ω_{RBM}) and the nanotube diameter as determined by several authors [20–26]. Modified from Belin and Epron [27].

The RBM spectra for SWNT bundles will contain a contribution from different SWNTs in resonance with the excitation laser line. It should be noted that a single Raman measurement would give an idea of the tubes that are in resonance with that laser line, but does not give a complete diameter characterisation of the sample. However, by taking Raman spectra using many laser lines, a good diameter characterisation can be obtained [111].

2.4.5 Tangential Modes

The Raman-allowed tangential mode, G-band, in graphite involves an optical phonon mode between the two dissimilar carbon atoms (A and B) in the unit cell. The corresponding mode in SWNTs bears the same name. In contrast to the graphite Raman G-band, which exhibits one single Lorentzian peak at 1582 cm^{-1} related to the tangential mode vibrations of the C atoms, the SWNT G-band is composed of several peaks due to the phonon wave vector confinement along the circumferential direction and due to symmetry-breaking effects associated with nanotube curvature. For chiral tubes, the G-band is composed of six modes with symmetry A_{1g}, E_{1g} and E_{2g} [110, 112]. However, for achiral tubes the G-band consists of only three modes [113]. This multi-peak feature can be used for diameter characterisation, to distinguish between metallic and semiconducting SWNTs and to probe charge transfer arising from doping.

A simple analysis can be carried out considering the two most intense peaks that originate due to the symmetry-breaking effects associated with nanotube curvature. The higher frequency peak around 1590 cm^{-1}, G^+, corresponds to atomic displacements along the tube axis and its frequency (ω_{G^+}) is sensitive to charge transfer from dopant additions. The lower frequency peak around 1570 cm^{-1}, G^-, is associated with atomic displacement along the circumferential direction and its lineshape is highly sensitive to the metallicity of the nanotube.

The Raman lineshape differs between metallic and semiconducting nanotubes thus allowing to distinguish between the two types. For semiconducting nanotubes, the profile of the two components is narrow [29] and fits to a Lorentzian lineshape [21, 28]. For metallic tubes, the ω_{G^-} component is located at a lower frequency compared to semiconducting tubes, resulting in a broader lineshape. This is related to the presence of free electrons in nanotubes with a metallic character [114, 115]. Figure 2.10(a) shows the difference in lineshape for semiconducting, metallic and multi-walled carbon nanotubes.

For metallic tubes, the tangential mode typically contains two main components: a Lorentzian component at high frequency, ω_{G^+}, and a Breit-Wigner-Fano (BWF) component at low frequency [19, 114, 115]. Surface-enhanced Raman scattering results show that the phonon BWF coupling is to an electronic continuum [116], the plasmons being the electronic excitations involved in this coupling. Kempa [117] showed that the quasi-acoustic plasmon mode in SWNTs forms hybrid excitations with the phonon mode. In this model, there is an enhancement of the BWF component in a bundle due to the formation of the plasmon band which reduces the minimum required momentum for the photonic excitation of the hybrid plasmon-phonon mode. Recent experimental findings by Paillet et al. [118] support this model, and show that the BWF component vanishes in isolated metallic SWNTs. Therefore, the presence of the BWF component in the tangential mode is an intrinsic feature of the metallic SWNT bundle.

Figure 2.10(b) shows the diameter dependence of the frequency of the G^+ and G^- features, ω_{G^+} and ω_{G^-} respectively, for semiconducting and metallic nanotubes. While ω_{G^+} is independent of tube diameter, ω_{G^-} decreases quadratically with decreasing d_t as a result of the increasing curvature of the nanotube. Therefore, the difference $\Delta\omega_G = \omega_{G^+} - \omega_{G^-}$ can be used for diameter characterisation. The relation describing this dependence is given, for semiconducting tubes by $\Delta\omega_G = \frac{47.7}{d_t^2}$ and for metallic tubes by $\Delta\omega_G = \frac{79.5}{d_t^2}$ [21, 28].

G-band measurements on a single, isolated nanotube have shown this is a first order process [119, 120]. This implies that ω_{G^+} is independent of d_t or chiral angle, while ω_{G^-} is dependent on d_t but not on chiral angle. It is important to note that G-band diameter dependent measurements can only be done at the single, isolated nanotube level, and the results can be used along with other Raman measurements to corroborate (n, m) assignments. However, it should be noted that there are recent works that argue that

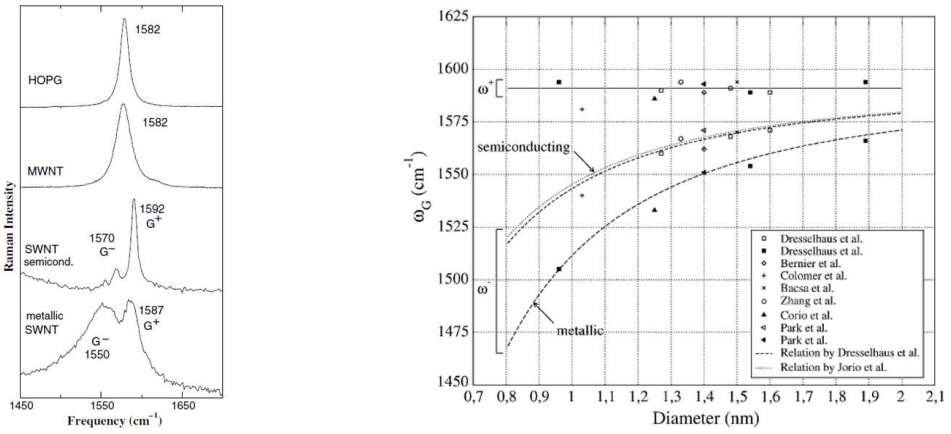

(a) (b)

FIGURE 2.10: (a) G-band lineshape for highly ordered pyrolytic graphite, MWNT bundles, one isolated semiconducting and metallic SWNT. Two peaks can be clearly distinguished in the cases of SWNT, while for MWNTs the multi-peak G-band feature is not present due to larger tube diameters. Modified from Jorio et al. [28]. (b) Dependence of G-band frequency components ω_{G^+} and ω_{G^-} on nanotube diameter for SWNTs. Data obtained from several authors [28–34], after Belin and Epron [27].

the G-band Raman signal originates from a double resonance mechanism [121, 122]. In such a case, the G-band intensity would depend on defects and is sensitive to the excitation laser energy, making it difficult to accurately use this information for SWNT characterisation.

2.4.6 Double Resonance Features

The presence of disorder in sp^2-hybridized carbon systems leads to rich and intriguing phenomena in their Raman spectra. A feature which occurs in the Raman spectra around 1350 cm^{-1} is the disorder induced mode, or D-band. This is a dispersive mode, originating from a double resonance process in which scattering from both a phonon and a defect is needed to conserve momentum [123, 124]. This feature occurs in graphene, and in the case of nanotubes the corresponding shift is dependent on chirality and diameter [125]. This is due to a strong dependence of the double resonance process on how the 2-D electronic and phonon structure is folded into a 1-D structure. The D-band can be used as a first evaluation of the quality of the nanotubes, however it is not yet fully understood which type of defects lead to the D-band feature [28].

A first overtone of the D-band appears between 2450 and 2650 cm^{-1} and is called the G' mode. This is a double resonance second order process, in which two phonons are involved [123]. Due to momentum conservation, the phonons involved in this process are of opposite wave vector and therefore there is no need for defect scattering for this mode to occur. For similar reasons as the D-band, the frequency of this mode is chirality and diameter dependent.

The disorder induced D-band and G' mode show, for graphene or nanotubes, a strong dispersion as a function of laser excitation energy [21, 126]. Graphite-like forms present a strong linear scatter coefficient with energies of approximately 53 $\text{cm}^{-1}\text{eV}^{-1}$ for D-band [21, 28] and approximately 106 $\text{cm}^{-1}\text{eV}^{-1}$ for G' mode [127]. However, the various forms of carbon can be distinguished by the position and linewidth of the D-band [127]. Amorphous carbon has a very broad linewidth (≥ 100 cm^{-1}) and a position at approximately $1285-1300$ cm^{-1} [128], SWNTs typically exhibit D-band position at $1285-1300$ cm^{-1} with a narrow linewidth ($10-30$ cm^{-1}) [128, 129], and crystalline graphite-like forms (including MWNTs [128]) have a typical position of $1305-1330$ cm^{-1} and a width of $30-60$ cm^{-1} [130].

Quantifying disorder in a carbon nanotube or graphene monolayer is usually made by analysing the intensity ratio between the disorder induced D-band and the Raman allowed G-band (I_D/I_G). Experiments by Dresselhaus et al. [131] show that the I_D/I_G ratio has a non-monotonic dependence on the average distance between defects (L_D), increasing with increasing L_D up to $L_D \approx 4$ nm where I_D/I_G has a peak value, and then decreasing for $L_D \geq 4$. This behaviour has been explained by the existence of two disorder-induced competing mechanisms contributing to the Raman D-band. These mechanisms are basis for a phenomenological model for L_D dependence of I_D/I_G, described by Lucchese et al. [132].

2.5 Other Techniques

This section will provide a brief overview of other useful characterisation techniques for carbon nanotubes. Although not explicitly used in this work, these techniques can provide useful information on the electronic, mechanical and morphological characteristics of synthesized carbon nanotubes.

2.5.1 Photoluminescence Spectroscopy

Photoluminescence (PL) in carbon nanotubes occurs as follows: an electron in a nanotube absorbs excitation light via a S_{22} transition, creating an electron-hole pair (exciton). Both electron and hole rapidly relax, via phonon-assisted processes, from c_2 to c_1 and from v_2 to v_1 states, respectively. The electron-hole pair recombine through a $c_1 - v_1$ (E_{11}) transition resulting in light emission. The PL emission is dominated by the E_{11} transition, while a wide range of wavelengths are useful for the PL excitation. As the energies of the vHs maxima (and thus the transition energies) are dependent on nanotube diameter and chirality [133], different (n, m) SWNTs in a sample will show various superpositions of distinct E_{xx} transitions which will appear at different PL emission wavelengths [134]. As a consequence, the nature, geometries and the diameters of

the carbon nanotubes are accessible via the PL technique. Moreover, the luminescence spectra is sensitive to the presence of chemical defects and to the purity of the samples [135].

It should be noted that no excitonic luminescence can be produced in metallic tubes. In addition, interactions between semiconducting and metallic nanotubes in a bundle will quench PL. For this reason, bundles are typically separated into individual tubes prior to characterisation. This is typically achieved by ultrasonic treatment of the nanotubes with surfactants in water suspension, such as sodium dodecyl sulfate [133, 135].

2.5.2 X-Ray Photoelectron Spectroscopy

X-Ray Photoelectron Spectroscopy (XPS) is a quantitative spectroscopic technique that measures the elemental composition, empirical formula, chemical state and electronic state of the elements that exist within a material. XPS spectra are obtained by irradiating a material with a beam of X-rays while simultaneously measuring the kinetic energy and number of electrons that escape from the top 1 to 10 nm of the material being analysed. XPS requires ultra high vacuum conditions.

XPS can give information on the chemical structure of carbon nanotubes and the catalysts used for synthesis. But the most widely used data refers to the structure modification of the CNT walls due to the chemical interaction with organic compounds or gas adsorption. Droppa Jr. et al. [136] studied the incorporation of nitrogen in carbon nanotubes and determined that when compared to non-nitrogenated tubes, the C1s peak exhibits both a shift and asymmetric broadening to higher binding energies. Research by Pham-Huu et al. [137] compared XPS C1s data obtained from highly ordered pyrolytic graphite and carbon nanofibres. The findings indicated a graphitic nature of carbon nanofibres and a broadening of the C1s peak attributed to C-H terminating surfaces. In addition the presence of a peak at 289.5 eV indicate the presence of carbon-oxygen bonds. By studying the sidewall functionalization of SWNTs by fluorination, Lee et al. [138] have shown that the C1s peak of undoped SWNTs is composed of three peaks: sp^2 carbon at 284.3 eV, sp^3 carbon at 285 eV and oxygen related groups (carboxyl) at about 288.5 eV.

2.5.3 X-ray and Neutron Diffraction

Local details such as size, diameter can be obtained by Raman or local electron diffraction, but to investigate CNTs at a larger scale X-ray or Neutron diffraction is needed. Neutron diffraction is widely used for determination of structural features such as bond length and possible distortion of hexagonal network [139]. Neutron diffraction allows a wide range of scattering vectors due the weak decrease of the atomic factor with scattering vector [140]. In addition, many Bragg reflections and the use the radial distribution

function allow one to obtain structural features; for the smallest diameters a distinction between nanotube type can be achieved thanks to the effect of curvature on the powder diffraction pattern.

X-ray diffraction can be used to obtain information on the interlayer spacing, the structural strain and impurities of the CNTs. However, CNTs typically have multiple orientations in compared to the incident beam, so care is needed in the analysis. Diameter and chirality distributions are obtainable, which allow a statistical characterisation of CNTs. In addition, the number of layers in MWNTs are measurable. Due to their intrinsic nature, the main features of X-ray diffraction pattern are close to those of graphite [27]. Consequently, the X-ray diffraction profile is not useful to differentiate microstructural details between CNTs and graphite structures [141] but can help determine sample purity.

Chapter 3

Carbon Nanotube Synthesis by CVD

Applications for carbon nanotubes range from nanoelectronics, sensors and field emitters to composites [142–145]. These require reliable synthesis techniques capable of generating large quantities of high purity material. In addition, applications such as nanoelectronics and field emission may require controlled growth at precise lithographically patterned areas [146]. Of the various methodologies developed for CNT synthesis, chemical vapour deposition (CVD) is the best suited technique to satisfy these requirements [147–149].

This review examines some of the more interesting methodologies for carbon nanotube synthesis by thermal chemical vapour deposition (CVD). Catalyst and supporting material for nanotube deposition, carbon precursor, synthesis temperature, atmosphere and reaction time are discussed as the important parameters affecting the quality and yield of carbon nanotube synthesis by CVD.

3.1 Overview of CNT Synthesis by Thermal CVD

Chemical vapour deposition (CVD) involves the formation of a non-volatile solid material on a substrate by the reaction of vapour phase chemicals (reactants) that contain the required constituents. For nanotube growth by thermal CVD, this is achieved by decomposing a carbon source in the gas phase by using a high temperature furnace and catalyst nanoparticles. Nanotube growth on catalyst nanoparticles has similarities to traditional gas-solid interaction processes such as thin film deposition on substrates by CVD. This proceeds according to the following steps:

1. Transport of precursors by forced convection to the main deposition region.

2. Diffusion of precursors through a thin boundary layer to the substrate.
3. Adsorption of reactants onto the nanoparticle surface.
4. Surface processes leading to nanotube formation and gaseous by-products. These processes include chemical deposition, reaction, surface migration and site incorporation.
5. Desorption of gaseous product species from the surface
6. Transport of outgassing species through the boundary layer and back to the main gas stream.
7. Transport of outgassing species by forced convection away from the deposition region.

The synthesis of CNTs by thermal CVD is normally a two-step process consisting of an initial catalyst preparation step, followed by the actual growth of CNTs. The initial catalyst preparation step acts to ensure the deposited catalyst is in the optimum morphology and composition to support CNT growth. Indeed, there have been several studies correlating CNT diameter to particle size [150–159]. The consensus is that the dimensions of the catalyst are critical. Large particles may produce multi-wall CNTs (MWNTs), however if these are too large, carbon fibres and filaments can be obtained. The composition of the catalyst is of equal importance. In the process described by Park et al. [160], NH_3 was required to reduce the catalyst to generate nanoparticular iron. Wang et al. [161] also claimed that H_2, which acts to reduce iron oxides to metallic iron, is critical to obtain CNTs. However, dedicated chemical pretreatment steps are not always necessary, as Delzeit et al. [162, 163] have shown that the use of different support materials may be used to influence the morphology and composition of the deposited catalyst.

The CNT synthesis step requires the presence of a gaseous phase containing carbon. This is achieved by utilizing a flow reactor for the thermal decomposition of carbon compounds, as shown in Figure 3.1(a). Commonly used gaseous precursors include methane, acetylene, ethylene, carbon monoxide, benzene, toluene and short chain alcohols. Synthesis temperatures are typically between 600 and 1200 °C. Studies in which the reaction zone has been monitored have shown that most of the free carbon is either atomic or aggregated in dimers and trimers [43, 164, 165]. This suggests that the mechanism for nanotube growth is likely to occur by addition of elemental carbon into (on to) catalyst nanoparticles followed by precipitation into nanotubes.

3.1.1 Growth Apparatus & Procedure

The typical thermal CVD apparatus reported in the literature [164, 166, 167] consists of a quartz tube (1 to 2 in. diameter) inserted in a tubular furnace. The furnace temperature

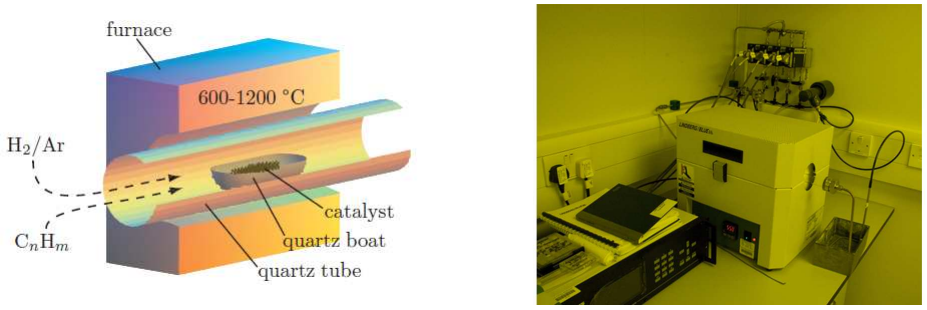

(a) (b)

FIGURE 3.1: Thermal CVD apparatus for the synthesis of CNTs. (a) Sketch of the furnace reaction area; the sample is introduced into the furnace in a quartz boat. Nanotubes grow over the catalyst via the decomposition of a hydrocarbon. (b) Photograph of the apparatus used in this work. Shown in the photograph are a mass flow controller unit (lower left), furnace (centre) and individual mass flow controllers for each reactant gas (top right).

can be maintained within ±1 °C over a 5 cm central area. This is a hot-wall system, which generally operates at atmospheric pressure and does not require pumping. The gas flow is metered through a number of mass flow controllers, as shown in Figure 3.1. The outlet gases are cooled by a water bath and vented into a fume extract. The length of the quartz tube and the flow rate of the gases prevent the back flow of oxygen. At present, CNT research is primarily done in small pieces ($\approx$ 1 in) of wafers using low-throughput batch reactors [45]. As the market for CNT-based products begin to emerge, this will undoubtedly change to satisfy the need for large-scale commercial reactors.

A typical growth run would involve first purging the reactor with an inert gas, reducing agent (such as H_2) or a mixture of the two until the reactor reaches the desired temperature. The choice of gas is dictated by the catalyst type in use. Then the gas flow is switched to a hydrocarbon and H_2 mixture, metered through a mass flow controller, for the specified growth period. At the end, the gas flow is switched back to an inert gas while the reactor cools, before exposing the nanotubes to air. In general, the sample must not be exposed to air at temperatures above 300 °C as this can cause damage to the CNTs due to oxidation.

3.1.2 Pyrolysis

Organic materials undergo a thermochemical decomposition at elevated temperatures in the absence of oxygen. This process is called pyrolysis, with pure carbon as the end product. Various allotropes of carbon can form due to pyrolysis, these include carbon nanotubes, highly-oriented pyrolytic graphite, graphite whiskers and glassy and amorphous carbon [168]. The other elements present in the carbon feedstock form gaseous products and diffuse away.

The growth of CNTs by CVD is a controlled pyrolysis of a gaseous carbon feedstock. Hydrocarbon molecules decompose when heated and become activated [169]. The activated molecules are either adsorbed by the catalyst and used to form nanotubes or precipitated on the sample surface forming amorphous carbon. Amorphous carbon is a constant by-product of CVD deposition of carbon. This has no long-range order but some short-range order (≈ 1 nm), depending on the carbon bond type and the hydrogen content. In the growth of CNTs this is detrimental as it is thought that amorphous carbon leads to the deactivation of catalyst nanoparticles [170]. Moreover, the quality of the synthesized nanotubes is reduced due to amorphous carbon coating.

3.1.3 Radicals

Hydrocarbon pyrolysis begins with the breaking of carbon-hydrogen or carbon-carbon bond with each fragment keeping one electron to form two free radicals. The formation of radicals requires energy which can be provided by impact processes (i.e. an increase in kinetic energy created by an increase in temperature) [171, 172]. However, the rate of radical formation is not solely dependent on temperature, the type of chemical bond is important. In order to break a chemical bond a characteristic bond dissociation energy needs to be provided. This is dependent on the atoms that form the bond, the chemical environment of the bond [173] and the temperature [174]. The presence of a radical in a hydrocarbon molecule permits rapid rearrangement of carbon bonds due to their high reactivity. Free radicals undergo rapid addition to form larger free radicals. The selectivity of propagation reactions are very low [175] and this results in an efficient mechanism for mass growth. In fact, free radical addition is a useful method for forming polymers [176]. Termination of free radicals results from recombination of two free radicals.

Reilly and Whitten [176] argue that hydrocarbon CVD of CNTs does not follow simple gas phase kinetic principles. In its most basic form, the hydrocarbon CVD process ($C_mH_n + C_s \leftrightarrow C_s + (n/2)H_2$) should lead to an increased rate of CNT formation with increasing hydrocarbon concentration and decrease with increasing hydrogen concentration. However, the CVD process works best when the reactor is run at some empirically derived lean fuel condition. Increasing hydrocarbon concentration above this optimum level leads to reduced CNT growth and leads to amorphous carbon deposition. The authors suggest that the process has an intermediate, which was previously reported as precursor soot in flame pyrolysis of hydrocarbons [177–179] and during the commercial production of carbon black [180]. Precursor soot is a condensate of free radicals in a background of neutral hydrocarbons that require an energetic medium to be maintained. A more accurate term is free radical condensate (FRC), as it is descriptive of the properties of the medium.

Mass growth in pyrolysis of hydrocarbons proceeds by the formation of polycyclic aromatic hydrocarbons (PAHs) by radical addition. PAHs are the most thermodynamically stable forms of hydrocarbons in high temperature environments [181]. PAHs can undergo rapid rearrangement, and this is more facile than bond cleavage [176]. Further addition of other hydrocarbons and radicals increases the mass of the hydrocarbon species. At some point the condensing PAHs and hydrocarbons become a medium where hydrogen exchange, carbon skeletal rearrangement and mass growth become facile processes due to the presence of radicals. This medium is considered a FRC.

FRCs are dehydrogenated to form various carbon allotropes. Rearrangement of carbon skeletal structure is easiest when a leaving group is present. The rate of hydrogen loss is the differentiating factor in whether amorphous carbon, fullerenes or nanotubes are formed [176, 182, 183]. If dehydrogenation/rearrangement process is allowed to occur so that the minimum energy form of carbon can be achieved then fullerenes or CNTs are formed [176, 182]. In the case of CNTs, the presence of a catalyst prevents the carbon cage from closing so that a continuous tube of six-membered rings can be formed. Due to the rapid exchange of hydrogen it is possible to establish equilibrium between the hydrogen in the gas phase with the hydrogen in the FRC. This allows control over the carbonisation temperature and consequently the rate of of hydrogen loss. This can be seen in the flow tube pyrolysis work of Miki et al. [184].

3.2 Models of Catalytic Growth

The model for carbon filament growth, derived by Baker et al [1, 2, 46], is based on the concepts of the VLS (vapour-liquid-solid) theory developed by Wagner and Ellis [47]. It is commonly believed in the CNT community that this mechanism for filament growth also applies, to nanotube growth [73]. This belief arises from the observation by TEM of catalyst particles on the ends of nanotubes, as was the case with carbon filaments. In this section, a brief overview of this mechanism is presented.

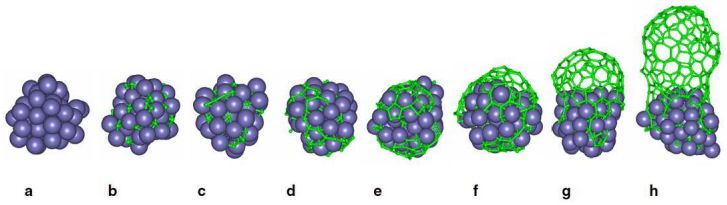

FIGURE 3.2: SWNT nucleation and growth according to the VLS mechanism. Modified from Ding and Bolton [35]. (a) Pure Fe cluster. (b) Initial dissolution of C into the Fe cluster. (c-e) As the cluster becomes highly supersaturated, C diffuses across the particle and coalesces into strings, polygons and islands. Under certain conditions, the island lifts off the surface to form a graphitic cap (f-g) and forms a CNT (h).

In the VLS model, hydrocarbons are adsorbed on the catalytic particle and release carbon upon decomposition. Carbon dissolves and diffuses into the liquid catalytic particle

(Figure 3.2(b)). According to this model, molecular decomposition and carbon solution are assumed to occur at one side of the catalytic particle, which then becomes supersaturated [185] (Figure 3.2(c-d)). Carbon diffuses from the side where it has been decomposed to another side where it is precipitated from solution [46] (Figure 3.2(e)). It is unclear whether the diffusion within the particle is driven by a concentration gradient [186] or a temperature gradient created by the exothermic decomposition of the hydrocarbon at the exposed front faces and the endothermic deposition of carbon at the rear faces [46, 187]. Due to a much lower surface energy of the basal planes of graphite compared with the prismatic planes, it is energetically favourable for the filament to precipitate with the basal planes, resulting in a tubular crystalline form [185] (Figure 3.2(f-h)). Finally, if the particle support interactions are weak, tip growth mode prevails whereas strong interactions lead to base-growth mechanism.

However, due to their nanometer dimensions the mechanics of growth of nanotubes on nanoparticles are markedly different from the growth of carbon filaments. The energetic argument of the precipitation of carbon on its low-energy basal planes is no longer valid since the curving of the graphite layers introduces an extra elastic term into the free-energy equation of nucleation and growth, leading to a lower limit of 10 nm [146, 185]. Other mechanisms are therefore required to explain the nucleation of CNTs from nanoparticular catalysts smaller than this lower size limit. One such model is the Yarmulke mechanism proposed by Dai et al [188].

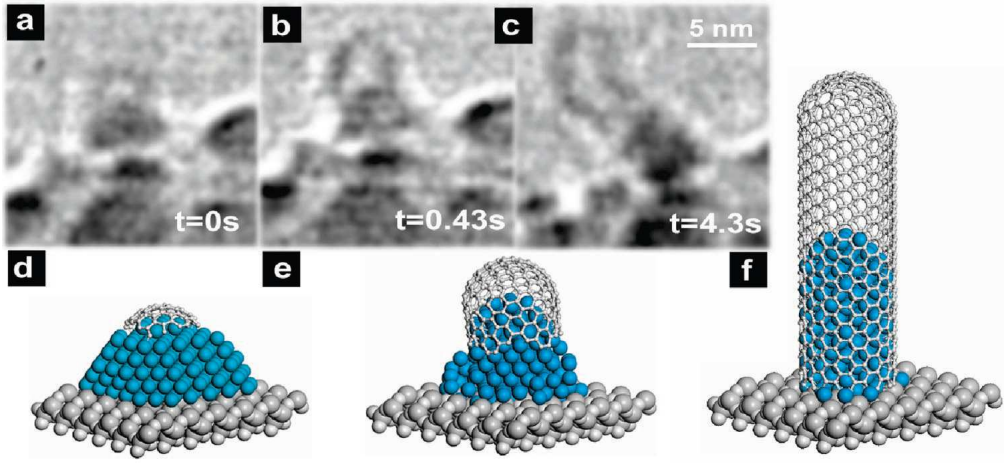

FIGURE 3.3: (a-c) Atomic-scale environmental TEM image sequence of a Ni-catalysed CNT base growth recorded in 8×10^{-3} mbar C_2H_2 at 615 °C. The time of the respective stills is indicated. (d-f) Schematic ball-and-stick model of different growth stages. From Hofmann et al. [36].

In the Yarmulke mechanism, a graphene cap is assembled on the particle surface with its edges strongly chemisorbed to the catalyst (Figure 3.3(c)). As additional carbon atoms are added, the hemifullerene cap formed on the particle surface lifts off (Figure 3.3(d)), creating a hollow tube with constant diameter which grows away from the particle [189] (Figure 3.3(e)). This model was supported by molecular dynamics simulation studies

by Shibuta and Maruyama [190]. This mechanism is illustrated in Figure 3.3. The formation of the graphene cap on the nanoparticle surface acts to reduce the total surface energy of the nanoparticle-carbon system. The driving force for the lifting process is believed to originate from the free energy release due to relaxation of the strain built up in the carbon cap around the spherical surface of the catalyst nanoparticle when carbon fragments assemble to form a CNT [189, 191]. Recent works in high-resolution *in-situ* TEM observation of the catalytic growth of CNTs have verified this mechanism on nickel nanoparticles [36, 192]. These studies have also shown that cap stabilisation and nanotube growth involve reshaping of the catalyst nanocrystal.

3.3 Catalyst Preparation Techniques

A brief overview is provided here on two routes to supported-catalyst preparation, followed by an approach for large scale synthesis (floating catalyst approach).

3.3.1 Solution Based Approaches

The literature contains various methodologies for the synthesis of catalysts from solutions. The main techniques utilized in the literature are the sol-gel method [146, 193, 194], incipient wetness impregnation [195–198], ion-exchange [199, 200], ion-adsorption [201] and inverse micelle [202].

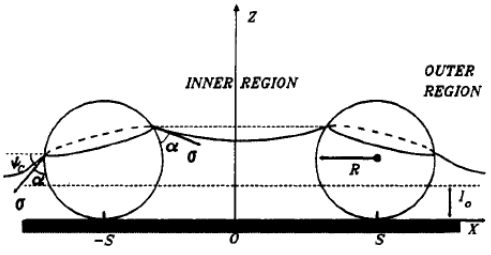

FIGURE 3.4: Depiction of two nanospheres during evaporation, depicting the attractive capillary forces acting as a result of the menisci formed during evaporation. From Denkov et al. [37].

In general, solution based approaches are time consuming [45]. A typical preparation would include steps such as dissolution, stirring, precipitation, refluxing, separating, cooling, gel formation, reduction, calcinations, etc. Other problems include difficulty in confining the deposited catalyst to specific patterns, and catalyst aggregation due to lateral capillary forces [37, 203] (depicted in Figure 3.4).

3.3.2 Physical Techniques

This approach involves deposition of the catalyst using some physical technique. Typically, a thin catalyst film is deposited using this methodology. There is some correlation between film thickness and tube diameters, with thinner films leading to smaller particles and diameters [159, 204]. However, it is believed that the catalyst on the surface must be in the form of particles instead of smooth, continuous films (which do not appear to yield nanotubes). As the deposited films do not guarantee a small grain size, it is necessary to include a preparation step in order to reduce the catalyst films into particles of the desired morphology.

Several different physical techniques have been successfully employed for catalyst preparation. These include electron gun evaporation [159, 205–207], thermal evaporation [204, 208], pulsed laser deposition, ion-beam sputtering [162, 163, 167, 209–213] and magnetron sputtering [161, 214–216]. These techniques have the advantage that they are quick, low cost, and amenable to disperse catalysts in small lithographically defined patterns, which is difficult to do using solution based techniques.

3.3.3 Floating Catalyst Approach

CVD can also be used to grow large quantities of nanotubes using a floating catalyst approach. In this case, a catalyst is injected into the flowing hydrocarbon precursor by a nozzle system. A second furnace may be required to heat the catalyst to its dissociation temperature.

This approach was first reported by Sen et al [217], who used either ferrocene or nickolecene as their catalyst source, with benzene as a carbon precursor. The process initially yielded MWNT growth, but after some process optimisation their later work reported SWNT growth [218]. However using this approach, it is difficult to obtain catalyst particles of the correct size for SWNT growth. It was found that transition metal sources vaporise at temperatures much lower than that of the gas phase pyrolysis of the carbon precursor. In utilising ferrocene, the iron particles condensed and formed clusters. Clusters smaller than $40 - 50$ atoms (0.7 nm in diameter) tended to evaporate, while very large clusters favoured graphitic over coating. By fine tuning the process conditions and obtaining a correct balance between the competing evaporation and clustering mechanisms [219], it is possible to obtain clusters of the correct dimensions for CNT growth.

3.4 Transition Metal Catalysts

Metals used to catalyse CNT formation are usually transition metals. In particular, iron, nickel and cobalt are commonly used. It is no coincidence that these metals are the most common catalysts for CNT growth; long before the discovery of fullerenes [38] and later nanotubes [39] researchers had been investigating the formation of graphitic carbon deposits on metal substrates [1]. The most effective metal substrates for the formation of ordered carbon were iron, nickel and cobalt [220]. These metals were known for their catalytic ability for decomposing carbon compounds and forming metastable carbides. Table 3.1 summarises the most commonly used catalysts in CNT fabrication, citing the literature that supports them.

Catalyst	CNT Type	References
Fe	SWNT	[147, 150, 157, 189, 221]
Fe	MWNT	[193, 194, 198, 199, 217]
Co	SWNT	[218, 222, 223]
Co	MWNT	[199, 202, 212, 224, 225]
Ni	SWNT	[222, 223]
Ni	MWNT	[199, 225–230]
Fe-Co Alloys	SWNT	[149]
Fe-Ni Alloys	MWNT	[231]
Mg-Co Oxides	SWNT	[232]
Mg-Co Oxides	MWNT	[233]

TABLE 3.1: Overview of commonly utilised transition metal catalysts and supporting work.

Experimental comparisons between Fe, Co and Ni catalysts have been undertaken in the literature. Klinke et al. [225] determined that Fe yields the highest density of carbon structures at any considered growth temperature between 580 °C and 1000 °C. However, in terms of graphitization and structure, an improvement to the quality of the CNTs obtained on silica is achieved when Co is used [224]. Both these findings are supported by the study conducted by Fonseca et al. [201]. Groups utilising Ni based catalysts generally report the growth of MWNTs, many of them with bamboo structure or fibres. Ivanov et al. [199] observed that the crystallinity of CNTs grown on Ni is inferior to those on Fe and Co.

3.4.1 Catalysts Containing Structuring Agents

Research by Colomer et al. [222, 223] and Nagy et al. [234] studied the synthesis of SWNTs from Fe, Co and Ni catalysts from methane. The findings presented agree with

the work of Klinke et al. [225] and Hernadi et al. [224]. The supported catalysts were prepared from metal nitrates; by impregnation of the support with ethanol, followed by sonication, solvent evaporation and finally reduction under a N_2/H_2 atmosphere. SiO_2, MgO and Al_2O_3 were used as supports. With SiO_2, large amounts of amorphous carbon are produced. MgO and Al_2O_3 on the other hand, gave rise to pure SWNTs. The authors reported that for higher metal loadings a loss of selectivity is observed with the formation of MWNTs and nanofibres. This is a result of the formation of large nanoparticles by phase coarsening. The production of SWNTs begins at a temperature of 800 °C and an optimum in productivity is achieved between $900 - 950$ °C. At higher temperatures, the production of amorphous carbon starts.

There is a high sensitivity of SWNT growth to the processing conditions. Li et al. [235] used the same processing conditions cited above to fabricate CNTs using a Co/MgO catalyst between $900 - 1000$ °C. Due to a lower gas velocity, the synthesized nanotubes were exclusively double-walled CNTs, which is markedly different that the work of Nagy et al. [234] and Colomer et al. [222, 223]. Additionally, the work of Hu et al. [236] using a Co/MgO catalyst and similar processing conditions produced 90% $0.7 - 2.0$ nm SWNT ropes together with few isolated $2 - 5.5$ nm SWNTs.

Cassel et al. [166] compared the catalytic activities of iron, ruthenium, molybdenum and various bimetallic combinations and reported a synergetic effect between iron and molybdenum. The authors prepared different Fe-Mo supported catalysts from aqueous solutions of $Fe_2(SO_4)_3$ and $[NH_4]_6[Mo_7O24 \cdot 4H_2O]$ to impregnate alumina and alumina-silica hybrid supports. These catalysts led to the production of SWNT at 900 °C using methane as the carbon source. The carbon material produced was constituted of SWNT bundles and a few amounts of DWNTs, both free of amorphous carbon. The authors argue that the higher yields obtained were due to the presence of acidic sites on the support medium. Several other authors have also reported similar improvements in SWNT yield when using a Fe-Mo catalyst [237–239].

A synergistic effect between cobalt and molybdenum has also been reported by Resasco et al. [240] [241–243]. The synthesis of SWNTs is performed between $600 - 900$ °C, from carbon monoxide. Under these conditions, Mo is quite inactive and Co has been reported to produce only MWNTs [244]. The catalyst was prepared by simultaneous impregnation of $Co(NO_3)_2$ and $[NH_4]_6[Mo_7O_{24} \cdot 4H_2O]$ dissolved in water on a silica support. Evaporation of water and calcination in air at 500 °C provide a mixed Co-Mo oxide [241]. During the activation of this catalyst in hydrogen well-dispersed Co^{2+} entities are formed, as evidenced by X-ray absorption. This interaction between Co and Mo prevents the sintering of Co at the CNT synthesis temperature [242]. In contrast, when cobalt reacts with the silica surface, Co_3O_4 is formed which converts into large metallic Co particles during the reduction step [243]. The best results in terms of activity and selectivity were observed for growth temperatures of 700 °C, and a low Co:Mo molar ratio (1 : 4) [242]. There is also a clear relationship between SWNT

diameter and temperature, $0.6 - 1.2$ nm diameter tubes are formed at 750 °C, $0.7 - 1.4$ nm at 850 °C and $0.92 - 2.0$ nm at 950 °C.

Solid solutions of metal oxides have been explored in much depth for growing CNTs. Such catalysts, in which ions of one metal substitute ions of the other metal, are mainly prepared by coprecipitation or combustion methods. Peigney et al. [245] [246–248] prepared solid solutions based on α-Al_2O_3 by substitution of Al^{3+} with Fe ions, introduced as oxalate salts. After precipitation, the resulting powder is decomposed at 400 °C and subjected to further calcination at 1100 °C. The material is reduced by a mixture of hydrogen and methane at $900 - 1000$ °C. During this step, iron migrates toward the surface and, due to the high dispersion of the initial oxide the size of the iron particles remain below 10 nm. It should be noted that this technique is not adapted to high metal loadings since the solubility limit of Fe^{3+} in the alumina lattice is around 10%. These catalysts lead to the formation of mixtures of SWNT and MWNT with diameters ranging between $1.5 - 15$ nm, along with amorphous carbon. SWNT with diameters of $0.7 - 1.0$ nm have also been produced using solid solutions of Ni-MgO catalysts [249] at 800 °C from acetylene. In this case, $Ni(C_2H_3O_2)_2$ and $Mg(NO_3)_2$ are used as precursors and K_2CO_3 is used as a precipitation agent. Calcinations at 850 °C and reduction in H_2/Ar mixtures at 750 °C provide an active catalyst that contains $3 - 10$ wt% nickel. Very high selectivity of SWNTs have also been reached with coprecipitated catalysts produced by a modified synthesis of MCM-41 [250–252] using carbon monoxide as feedstock. In this case, $CoSO_4{\cdot}7H_2O$ is mixed with HiSil-915 and $(CH_3)_4N(OH){\cdot}2SiO_2$ in the presence of $C_{14}H_29(CH_3)3NBr$ as surfactant.

Another method to produce solid solutions of metal oxides is combustion. In this process, transition metal nitrates are mixed with $Mg(NO_3)_2$ and/or $Al(NO_2)_3$ in a minimum amount of water [253–255]. The addition of urea (or citric acid in the case of Co-Mo) followed by decomposition in air at $550 - 600$ °C allows the production of an oxide powder. This material is ball-milled in aqueous solutions of dispersants, followed by a calcination at 500 °C to obtain a thin powder. In situ reduction occurs during the CNT growth process using CH_4/H_2 mixtures around 1000 °C [254]. Regardless of the catalyst loading, Fe is the most catalytically active followed by Co and then Ni. In terms of selectivity, Co represents the most effective catalyst for producing SWNTs as observed by TEM.

3.4.2 Catalysts on a Planar Support

For some applications, such as nanoelectronics, direct growth of SWNT on a flat substrate may be required. In these conditions, the preparation of highly dispersed catalysts is more difficult to achieve due to the low surface area of the support [244]. To overcome this difficulty, alternate preparation techniques have been developed. Spin coating of nanoparticles from colloidal solutions [150, 256–258], physical vapour deposition

[159, 161–163, 167, 204–216] and nanolithography [73, 166, 205] have been successfully used.

Low densities of SWNT have been synthesized from nickel nanoparticles, supported on SiO_2 at temperatures between $750 - 950$ °C in $Ar/H_2/C_2H_2$ mixtures [256]. In this case, the catalyst was prepared by decomposition of $1,5$-cyclooctadiene (COD) complex, $Ni(COD)_2$, under H_2 in the presence of polyvinylpyrrolidone (PVP). The nanoparticles are suspended in an ethanol solution solution and deposited by spin coating. The synthesized nanotubes showed a narrow size distribution, 1.4 ± 0.5 nm. The use of CH_4 rather than C_2H_2 resulted in the production of MWNTs in conjuction with the SWNTs.

Colloidal iron nanoparticles, synthesized by a variety of precursors, showed a good propensity for CNT formation. Precursors typically utilised are $Fe(CO)_5$ [150], $FeCl_3$ [258, 259] or $Fe(C_2H_3O_2)_3$ [257] . Iron nanoparticles with diameters of 3, 9 and 13 nm were synthesized from the decomposition of $Fe(CO)_5$ in the presence of carboxylic acids in dioctyether [150]. The nanoparticles were deposited on SiO_2, activated at 800 °C under H_2/Ar mixtures and nanotubes were grown using CH_4 or C_2H_4 as the carbon feedstock. In all cases the average CNT diameter correlated well with the nanoparticle diameter. A close correlation between SWNT diameter and catalyst was also observed in the case of nanoparticles synthesized from $Fe(C_2H_3O_2)_3$ [257]. In this experiment the nanoparticles were prepared by decomposition of the precursor in a mixture of phenyl ether, $1,2$-hexadecandiol, oleic acid and oleylamine. The catalyst was deposited by spin coating on SiO_2 and CNTs were grown at 900 °C using CH_4 as the carbon feedstock. Finally, low densities of SWNT ($0.9 - 2.4$ nm) were reported from colloidal nanoparticles synthesized from $FeCl_3$ [259]. The nanoparticles were synthesized by a surface mediated reaction between $FeCl_3 \cdot 6H_2O$ and a hydroxylamine reducing agent and deposited by dip coating on SiO_2. This process resulted in a high density of highly dispersed nanoparticles of 1.5 ± 0.6 nm.

Bimetallic nanoparticles have been prepared from chloride salts and reduction in a glycol solution of ammonia in the presence of PVP [260]. The synthesized nanoparticles were spin coated onto SiO_2 substrates and SWNT growth was performed using CH_4 at 900 °C. Although the SWNT yield is modest, the performance of bimetallic catalysts are superior to those of the single component nanoparticles. Various other groups have explored the performance of bimetallic nanoparticles; Fe-Ru [260], Fe-Pt [260], Fe-Mo [261, 262], Fe-Mo-Al_2O_3 [263].

An alternate approach, often used to prepare catalysts on model supports, consists of the direct evaporation of a metal onto a planar support. Indeed, there have been many reports in the literature citing this approach [159, 161–163, 167, 204–216]. In this methodology, a thin catalyst film is deposited and is subjected to a pretreatment step to cause dewetting of the catalyst film to form nanoparticles. This process is highly dependent on the support material used [167, 210], the thickness of the deposited

layer [159, 216] and the pretreatment gas [204, 206, 208]. A comparison of different metal catalysts (Ni, Co/Fe, Co, Fe/Mo and Fe) deposited by high ion beam coating on SiO_2 substrates has been performed by Seidel et al. [264]. This work reported that the optimum catalyst material for dense SWNT network synthesis from CH_4 at low temperature was nickel. A reasonable hypothesis to explain this behaviour is the lower bulk melting point of nickel.

3.5 Non-Traditional Routes to SWNT Synthesis

3.5.1 Catalyst Free Methods

CNT synthesis from SiC has been the most widely used catalyst free technique. The synthesis techniques involving this catalyst have produced high densities of carbon nanostructures by annealing either SiC particles [265], amorphous SiC films [266] or hexagonal SiC (6H-SiC) [266] in a vacuum. In these methodologies, the nanotube formation can be explained by the mechanism proposed by Kusonoki et al. [266]. Owing to the low vacuum in the chamber when annealing, the SiC oxidises forming SiO_2. As a consequence, the carbon atoms are free to bond with other atoms. If they bond to neighbouring carbon atoms, graphite fragments are formed containing dangling bonds. Thermodynamics drives the folding of graphitic fragments so that the dangling bonds of opposite edges are saturated. The as-formed nanotube segments act as seeds for the attachment of new carbon atoms, leading to CNT growth. However, these techniques require high temperature annealing at approximately 1650 °C.

An alternate approach involves using carbon nanoparticles. This technique also depends on the structural reorganization of carbon aggregates into nanotubes upon annealing. Botti et al. [267] report a dense array of CNTs grown on silicon by spraying amorphous hydrogenated carbon nanoparticles on a Si substrate and annealing. Other similar approaches have been reported in the literature [268].

These techniques, although not strictly classed as chemical vapour deposition (CVD) of CNTs, provide some insight into the behaviour of carbon aggregates at elevated temperatures without the influence of an external catalyst with a function to produce graphite. These results also demonstrate that regardless of the catalyst, the formation of CNTs involves two important processes: (i) the diffusion of carbon and (ii) the nucleation of a graphitic cap or fragment followed by the further incorporation of carbon into the growing nanotube. It has been reported that the diffusion process on a nanoparticle surface or across its interior is a rate limiting step [269], while the chirality of the growing CNT is decided upon the formation of the graphitic cap [270, 271].

3.5.2 Noble Metal Catalysts

Nanosized iron-group metals (Fe, Co, Ni) are known for their ability to catalyse SWNT growth in chemical vapour deposition. It has been generally accepted that these metals and their alloys consistently show the highest catalytic activity [272, 273]. This is attributed to the solubility of carbon in the metal-solid solution [274]. However, noble metals such as Au, Ag or Cu have both negligible carbon solubility and negligible carbide formation and have recently been identified as catalysts for the growth of CNTs. Takagi et al. [3] have found that the yield of SWNTs from noble metals is comparable to that of iron-group metals. Moreover noble metals, in particular Cu, are thought to favour CVD growth of CNT nanotubes at low temperatures with a narrow chirality distribution [270].

The first demonstration of CNT growth from Au nanoparticle catalysts by Lee et al. [6], involved the decomposition of acetylene over nanoparticles supported on SiO_2-Al_2O_3. This support showed a good propensity for the decomposition of acetylene and demonstrated strong interactions between the Au nanoparticles and its surface. The synthesized products were predominantly MWNTs, with average diameters of $\leq$ 20 nm. The first reports of the formation of SWNTs from small Au nanoparticle catalysts were by Takagi et al. [3] and Bhaviripudi et al. [275]. XPS measurements in both publications showed that CNT growth was only possible from contaminant-free catalyst nanoparticles, once the residual shell of gold oxides or gold chlorides were reduced by H_2. The findings of Liu et al. [276] correborate this finding. Interestingly, neither paper detected any radial breathing modes in the low ω region, corresponding to large diameter nanotubes.

Metallic Cu, long considered to be a contaminant in the growth of SWNTs, has also been reported as an efficient catalyst for SWNT formation in several studies [3–5]. It has been reported that the carbon solubility in a metallic catalyst should be in the range of $0.5 - 1.5$ wt% carbon in order to efficiently form CNTs [274]. Therefore, it is surprising that Cu can be catalytically active, as its carbon solubility is extremely low. However, Zhou et al. [4] argue that the low solubility of carbon in Cu results in an increased rate of carbon precipitation.

Interestingly, Zhou et al. [4] reported a higher ratio of metallic SWNTs in Cu catalysed samples, determined from Raman analysis. Simulations by Yazyev and Pasquarello [270] also found that the nucleation of graphitic fragments bound to the Cu nanoparticle catalyst favours the formation of metallic nanotubes. In addition, the low melting point and low carbon diffusion barriers suggest that CVD synthesis could take place at much lower temperatures. In these conditions, the chirality preference would be further enhanced.

There are few reports in the literature of Ag nanoparticles catalysing SWNT growth. The first demonstration of CNT growth from Ag nanoparticles by Takagi et al. [3] involved the decomposition of ethanol vapour over nanoparticles supported on SiO_2. In this experiment, nanoparticles were formed by annealing an ultra-thin metal film in air at $800 - 900$ °C. To the authors knowledge, the only other report of Ag nanoparticles used to synthesize CNTs was by Kang et al. [277]. In this paper, MWNTs were formed by directly reducing C_2Cl_4 with Na at 140 °C in the presence of Ag nanocrystals.

3.5.3 Ceramic Catalysts

Ceramic materials, such as Al_2O_3, have typically been used as a buffer layer to disperse metallic catalyst particles and enhance their catalytic properties in CNT growth [11]. However, the simplistic view that the support only plays a catalytically passive role in the formation of carbon nanotubes requires some examination. Rummeli et al. [278] demonstrated that under typical conditions for CVD growth of CNTs, nanoparticles of difficult-to-reduce metal-oxides are exceedingly good at promoting ordered carbon (graphene) growth. As was expected, there was no observation of ordered carbon formation in bulk/film samples. This difference was attributed to the presence of surface defect sites on the nanoparticle oxides, and it was argued that in the substrate-based CNT synthesis routes, the interface between the catalyst particle and the surface behaves as an annular defect site. These sites would then promote the formation of cylindrical graphene structures, or nanotubes.

A recent study by Liu et al. [8] reports the formation of dense CNT layers catalysed by Al_2O_3 nanoparticles. Raman spectra of the synthesized nanotubes indicated that the nanotubes were predominantly single walled and of a good quality. Interestingly, the authors surmise that the mechanism of formation is different from the traditional VLS mechanism as the nanoparticles are likely to be in the solid state during growth. This finding reinforces the argument of Rummeli et al. [278], and additionally indicates that the growth of single-walled carbon nanotubes (SWNTs) on flat Al_2O_3 substrates may be possible by nanostructuring their surfaces. This hypothesis was partially confirmed by Liu et al. [279] using a nanostructured SiO_2 substrate to grow SWNTs.

Another ceramic catalyst reported in the literature is ZrO_2 [9]. In this publication, dense growth of either multi-walled carbon nanotubes (MWNTs) or SWNTs was possible, depending on the carbon feedstock used. ZrO_2 was typically deposited on either Al_2O_3 capped SiO_2 supports or Si substrates with an oxynitride support through a chloride salt solution. Samples were pretreated in H_2 prior to the introduction of the carbon feedstock. ZrO_2 is known to not be reduced by H_2 [280] and additionally, carbothermic reduction of ZrO_2 does not yield Zr metal, but results in the formation of ZrC [281]. In-situ x-ray photoelectron spectroscopy (XPS) revealed that the state of the catalyst after H_2 pretreatment showed two phases; a stoichiometric and an oxygen deficient

phase of zirconia. The role of the H_2 pretreatment in this work, while shown not to result in the formation of Zr metal, is thought to introduce surface defect sites into zirconia nanoparticles that aid in enhancing catalytic ability. It should be noted that, as observed by in-situ XPS, CNT growth seems to begin only after the introduction of both the hydrocarbon and hydrogen. It is speculated that the introduction of hydrogen aids in the transformation of the hydrocarbon into other organic precursors which can then be uptaken and catalysed into CNTs.

3.5.4 Semiconducting Catalysts

The first reports of CNT growth from semiconducting catalysts were by Uchino et al. [10] at the University of Southampton. In this experiment carbon doped SiGe islands, deposited by CVD on Si, form nanoscale clusters through various mechanisms which act as a seed for SWNT growth. These results were supported by the work of Takagi et al. [11], who showed that CNT growth from Ge, Si and SiC nanoparticles was possible. More recently, there have been various reports of CNT growth from SiO_2 nanoparticles [279, 282], which are thought to be promising catalysts owing to their ability to maintain a narrow size distribution at CNT growth temperatures.

In this section, research on the use of semiconductor materials for carbon nanotube growth is reviewed. Three different techniques to synthesize CNTs based upon semiconductor catalysts are discussed. These are based on SiGe islands, Ge Stranski-Krastanow dots, and semiconductor nanoparticles. It is shown that in all cases, high quality, SWNTs can be grown using these approaches.

3.5.4.1 SiGe Islands

A 50 nm thick $Si_{0.7}Ge_{0.3}$ layer was deposited by CVD on Si(001) wafers after the growth of a thin Si buffer layer. To accommodate the stress resulting from the lattice mismatch between Si and Ge, the SiGe layer forms islands on top of a thin wetting layer. The heights of the islands ranged from 20 to 50 nm. Subsequently, the islands were implanted with carbon ions (energy 30 keV, dose of 3×10^{16} cm^{-2}). This heavy ion implantation is thought to induce damage and form an amorphous layer at the surface [283]. The substrates were then dipped in buffered HF solution to remove the native oxide. Chemical oxidation was performed using a 30% hydrogen peroxide (H_2O_2) solution at room temperature. This step was followed by a pretreatment step in a mixture of Ar and H_2 for 10 minutes at 900 °C, followed by the CNT growth step in a mixture of CH_4 and H_2 at 850 °C.

Figure 3.5(a) shows a SEM image of the as-synthesized products on SiGe islands. In this image, two distinct types of nanostructures are visible. The short and thick nanofibres,

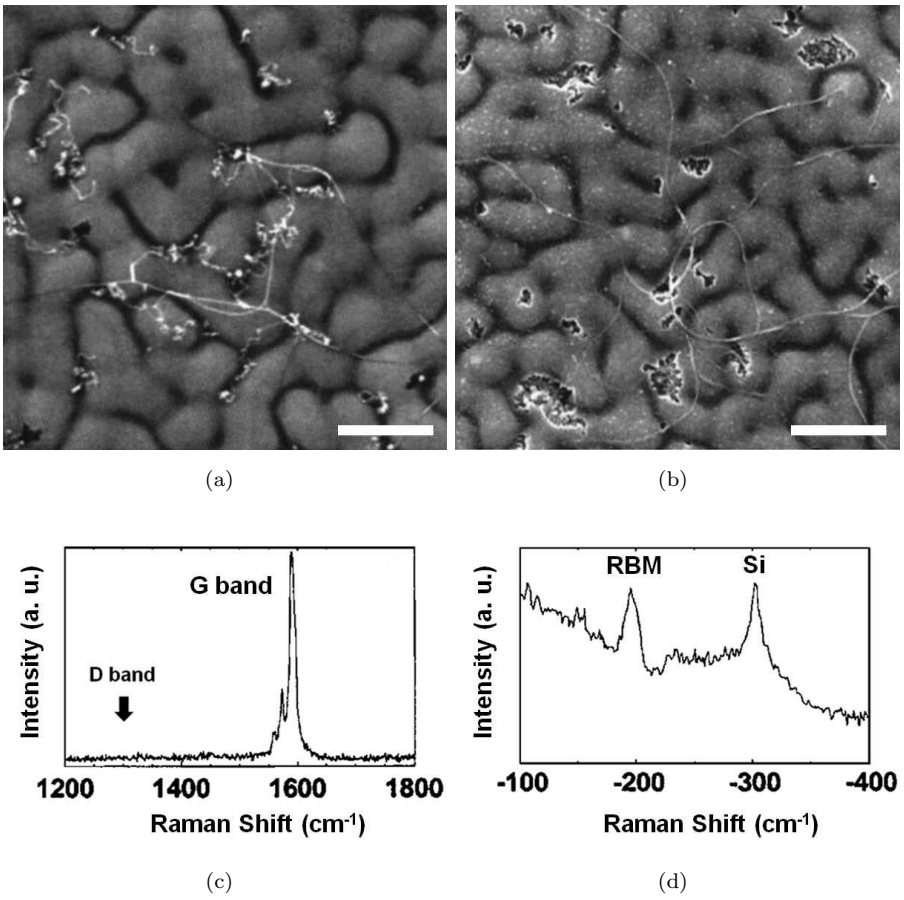

FIGURE 3.5: SEM images of as grown CNTs and SiO_x nanowires synthesized from C implanted SiGe islands (a) before and (b) after HF vapour etching, showing that only carbon nanotubes remain. Scale bar corresponds to 500 nm. Typical Raman spectra of the as-grown CNTs showing (c) G-band characteristic and (d) anti-Stokes spectra showing the radial breathing mode characteristic.

approximately 20 nm in diameter and 1 μm in length, are formed during the pretreatment step. These nanostructures were identified as SiO_x nanowires by TEM, Raman and photoluminescence measurements, and are formed by the carbothermic reduction of SiO_2 [284, 285]. These fibres were easily removed by an HF vapour etch, as shown in Figure 3.5(b). The second type of nanostructure forms during the growth step and comprises straight and thin fibres of less than 10 nm diameter and approximately 5 μm in length. Raman measurents, shown in Figures 3.5(c) and 3.5(d), confirm that these fibres are SWNTs. Despite considerable effort, the disorder induced D-band feature that is normally seen at 1350 cm^{-1} [125] could not be detected. This indicates that the nanotubes have a low defect density, and thus could be described as high quality.

In this experiment, nanoscale Ge clusters are formed following the chemical oxidation and annealing of the SiGe layers. The oxidation behaviour of SiGe layers has been studied to a great extent [286, 287]. Si is known to have a stronger thermodynamic tendency to be oxidised in comparison to Ge. Therefore, the dry oxidation of SiGe alloys, with a low Ge content, results in the formation of SiO_2 and the segregation of Ge clusters

from the growing oxide [288]. It should be noted that this effect is less pronounced with wet oxidation, and the oxide layer typically contains a mixture of Si-O and Ge-O bonds. However, upon an anneal in a reducing atmosphere, the Ge-O bonds are preferentially broken owing to a lower stability, resulting in the formation of nanoscale Ge clusters [289]. These clusters are thought to act as the catalyst for the growth of CNTs in this methodology.

3.5.4.2 Ge Stranski-Krastanow Dots

Figure 3.6(a) shows a TEM image of a bundle of SWNTs grown from Ge Stranki-Krastanow dots. In this experiment, Ge Stranski-Krastanow dots are formed by CVD deposition of Ge atop a thin Si buffer layer. This step forms Ge dots in the forms of cones with diameters from 20 to 250 nm and heights between 10 and 25 nm. Subsequently, the islands were implanted with carbon ions (energy 30 keV, dose of 3×10^{16} cm^{-2}). The substrates were then dipped in buffered HF solution to remove the native oxide and subjected to a chemical oxidation using a 30% hydrogen peroxide (H_2O_2) solution at room temperature. This step is expected to produce a 0.5 nm thick oxide on the Si and a 2 nm thick oxide on the Ge [290, 291]. The substrates were then transfered to an atmospheric CVD furnace and pretreatmented in a mixture of Ar and H_2 for 10 minutes at 1000 °C, followed by the CNT growth step in a mixture of CH_4 and H_2 at 850 °C. Raman measurements on the synthesized CNTs, Figure 3.6(b), clearly show the radial breathing mode feature and tangential G band mode expected for SWNTs. The radial breathing modes indicate that the diameters of the synthesized CNTs are in the range 1.6 to 2.1 nm, which are slightly larger than those on SiGe islands [10]. Again, the disorder induced D-band could not be detected, indicating that these CNTs are of a high quality.

It is believed that the mechanism of formation is very similar to that of the CNTs grown from SiGe islands. Upon chemical oxidation of the Ge Stranski-Krastanow dots, an thin layer of SiGe oxide film is formed. Following the subsequent anneal in a reducing atmosphere, Ge clusters are nucleated and it is believed that these act as catalysts in this growth technique. Sass et al. [288] reported that after the oxidation of Ge islands on Si(001), recovery of the original dot structure was not possible. Instead, a reduction of the the GeO_2 around the single crystalline core of the non-oxidized Ge dot materials results in only Ge-enriched clouds, surrounded by a matrix of non-reductable material. This assertion is supported by SEM images taken after each stage in the process (not shown), which indicate a definite change of morphology after the chemical oxidation and reduction steps [12]. In fact, there have been reports of the formation of ultrahigh density Ge nanodots, with approximate diameters of 4 nm, from the oxidation/reduction of Ge/Si surfaces [292], which further supports this hypothesis.

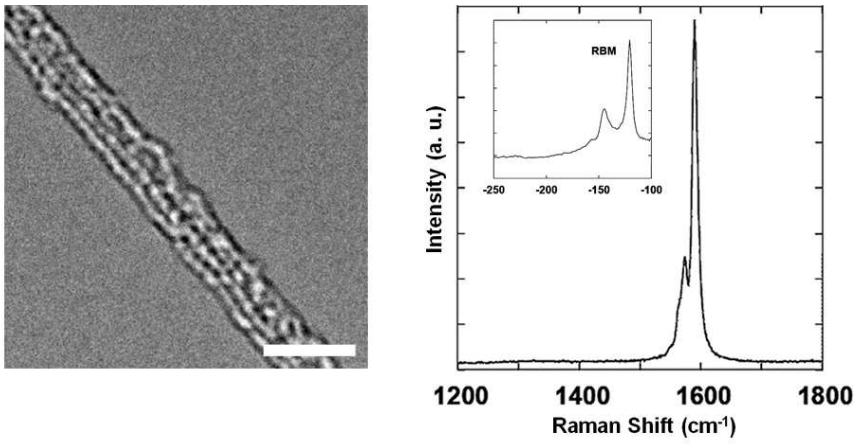

(a) (b)

FIGURE 3.6: (a) TEM image of a bundle of SWNTs synthesized from C implanted Ge Stranski-Krastanow dots. Scale bar corresponds to 10 nm. The TEM sample was prepared by scraping the substrate surface with a surgical blade and collecting the material on a holey-carbon TEM grid. (b) Typical Raman spectra of the as-grown CNTs showing the G-band characteristic. Inset shows anti-Stokes spectra displaying the radial breathing mode characteristic.

3.5.4.3 Semiconductor Nanoparticle Catalysts

Takagi et al. [11] fabricated SiC, Ge and Si nanoparticles for synthesis of CNTs from ethanol vapour. The SiC nanoparticles were synthesized by soaking a Si(111) substrate in ethanol (C_2H_5OH) solution for 3 minutes and then heating the substrate in an ultra-high vacuum (UHV) at around 1000 °C. This led to the formation SiC crystalline nanoparticles with the epitaxial relationship of (111)/(111), using carbon bearing molecules desorbed from the sample surface as the carbon source. The Ge and Si nanoparticles were formed on 6H-SiC(0001) substrates by evaporation in UHV followed by an anneal at 400 °C. This process formed crystalline nanoparticles with the epitaxial relationships of both (111/0001) and (110)/(0001). The synthesized nanoparticles were pretreated in air at atmospheric pressure for up to 10 minutes at 900 °C, followed by a reduction anneal in Ar/H_2 for 10 minutes at the same temperature. Following the pretreatment step, CNTs were formed by bubbling liquid ethanol using Ar/H_2 for $10-30$ minutes at $5-7\times10^2$ Pa (flow rate was approximately 50 sccm).

TEM analysis of the synthesized nanotubes confirmed the formation of SWNT and DWNTs with diameters ranging from $3-4$ nm. However, the nanotubes were typically curved and looped, indicating that these were highly defective. For Ge and Si nanoparticle catalysts, the authors were able to observe the catalyst nanoparticles at the tip of the nanotubes, however lattice fringes could not be observed to confirm the composition of the nanoparticles. The yield of CNTs from the Ge nanoparticles was found to be higher than those from SiC and Si nanoparticles. This was attributed to the lower melting point of Ge and it is expected that the Ge nanoparticles would be liquid at the growth

temperature. In contrast, both Si and SiC nanoparticles are expected to remain solid. The authors hypothesize that CNT form on semiconductor catalysts by a mechanism of cap formation. In the case of Ge, carbon is soluble in the catalyst and is dissolved and then precipitated forming a graphene cap. In the case of a solid catalyst, carbon is adsorbed on the nanoparticle surface and may assemble by surface diffusion to form a graphene cap.

Recently, there have been reports of CNT formation from SiO_2 nanoparticles [279, 282]. In these reports, high quality CNTs were synthesized from SiO_2 nanoparticles formed by thermal pretreatment of a sputtered SiO_2 layer [279] or by scratching a SiO_2 substrate with a diamond blade [282]. In both cases CNT growth was performed at 900 °C with CH_4 used as the carbon feedstock. Huang et al. [282] ascribe the growth of SWNTs using this catalyst due to oxygen vacancies formed during the growth process, which are thought to be capable of causing hydrocarbon dissociation. The SiO_2 catalyst is thought to be in a molten state at growth temperature and the high fluctuation of the liquid-like state allows Si and O atoms to move around quickly, creating s vacancy or dislocation. The deposited carbon is thought to assemble into a graphene cap on the nanoparticle surface due to the high curvature of the catalyst, and subsequent addition of carbon atoms leads to the formation of CNTs.

3.6 Parameters Affecting Catalytic Properties

Since the discovery of CNTs by Iijima [39], an enormous number of studies have been devoted to the growth and processing of MWNT and SWNTs. From these studies, some interconnected key parameters have been taken into consideration for the control of SWNT growth. In this section, experimental results from the literature are analysed in order to ascertain the influence of the operating conditions, catalyst composition, morphology and the support on the ability of certain materials to catalyse CNT growth.

3.6.1 Operating Conditions

Several carbon sources have been used for SWNT synthesis, including methane, acetylene, carbon monoxide, benzene, toluene and short chain alcohols. Thus, the process appears to show a low selectivity to the carbon supply. However, Yazyev and Pasquarello [270] reported different activation energies for the surface diffusion of C dimers and adatoms on noble metal catalysts, and argued that appropriate choice of a diatomic or monatomic carbon gas-phase source could significantly accelerate diffusion. Considering that carbon penetration inside small nanoparticles is unlikely [293], the growth of CNTs is most likely a process primarily controlled by surface diffusion [269, 294, 295]. Therefore, the choice of an appropriate carbon source should significantly affect the growth rates and yield of CNTs.

The carbon supply rate is determined primarily by the choice of carbon feedstock and the partial pressure of the gas. At a given temperature, close to the optimised conditions, too low a supply rate will cause the yield of SWNT to decrease dramatically compared to its optimised value. It should be noted that the selectivity of the process towards SWNT remains unchanged for certain catalysts [296]. For too high a supply rate, even when the carbon yields increase, the selectivity towards SWNT is lost and poorly organised carbon or carbon encapsulated metal particles appear. This fact highlights the importance of achieving the optimum balance between decomposition rate of the carbon source, the diffusion rate of carbon and the carbon precipitation rate.

The synthesis of SWNT in the literature is typically undertaken in a process window centred around 900 °C. This finding is in agreement with Lamouroux et al. [244], who presented several reports from the literature in order to obtain a process window for several carbon feedstock gases. An increase in the temperature above $900 - 950$ °C results mainly in the sintering of the metal nanoparticles that induces a decrease in selectivity with formation of fibres, encapsulated particles and an increase in amorphous carbon deposition. Temperatures below 900 °C are frequently associated with larger amounts of deposited carbon, using more reactive carbon feedstock gas, so that the selectivity of the process decreases with formation of MWNT and fibres.

This overview of the operating conditions shows that SWNT growth is an extremely sensitive process, in which most parameters are interconnected. A temperature range between $850 - 950$ °C is often used and should correspond to the best compromise between carbon decomposition rate, carbon solubility in the metallic phase and carbon precipitation rate. The carbon supply rate is also identified as a key parameter, although no recommendations can be made due to the complexity of the system.

3.6.2 Composition

Transition metals already used for catalytic reforming (iron, cobalt and nickel) have been used successfully for SWNT growth in their oxide or metallic form, or as bimetallic mixtures [272, 273]. Beyond the ability of a metal to catalytically decompose the carbon source, other important properties should be taken into account such as their melting point, vapour pressure, carbon solubility and carbon diffusion rate inside the nanoparticles. When starting with an oxide, it should be stressed that a reduction step should take place prior to the decomposition of the carbon source. Moisala et al. [174] presents several important physico-chemical properties of the mostly used transition metals in their bulk form.

Conventional catalysts are thought to first bond the hydrocarbon molecules at its surface. The hydrocarbon, now in an adsorbate form, interacts with the catalyst by transferring an amount of electron density to the catalyst. Normally, simultaneous back-donation

takes place; electron transfer from the catalyst to the non-occupied, antibonding orbitals of the adsorbate molecule. The electronic structure of the adsorbate is changed in such a manner that dissociation of the molecule can occur. Therefore the ability of a metal to catalyse dissociation of a hydrocarbon molecule is intimately linked to its electronic structure. This may explain the reason why iron is found to be more efficient than nickel and cobalt by hydrocarbon decomposition [253, 254, 297]. Some papers also show that an added component can lower the activation energy for dissociation and thus the growth temperature by changing the electronic structure of the catalyst [298, 299]. However, it is not clear whether differences in electronic structure between different catalyst materials can account for the observed differences in the quality of CNT in terms of graphitisation.

Considering the growth model presented in Section 3.2, the electronic interaction between the catalyst and hydrocarbon may play an essential role in the initial stage of the CNT growth process since it allows chemisorption of the carbon cap edges to the catalyst nanoparticle. Kim et al. [300] studied the formation of carbon filament structures on copper-nickel catalysts and found that the wetting behaviour of the metal on graphite is extremely sensitive to the chemical nature of the nanoparticles. The author supposed that materials that will readily wet graphite will produce ordered carbon filament structures. The wetting behaviour is determined by the interaction between the catalyst and carbon, which can originate from Van der Waals forces, overlap of orbitals, and others [301]. This factor could explain the growth from non-traditional catalysts, which do not show a strong electronic interaction with hydrocarbon molecules. The high curvature of such catalysts may be sufficient to initiate CNT growth.

In the VLS growth mechanism, once a hydrocarbon has decomposed, carbon atoms are believed to diffuse into the catalyst particle leading to supersaturation of carbon in the metal. This indicates that the finite solubility of carbon in the catalyst plays an important role in the growth process. There is some controversy in the literature over the role of the carbon solubility of a catalyst. Some studies have claimed that prior to nucleation, the formation of carbides are required. Fe_3C has been detected in iron catalysed CNT growths [302]. Yoshida et al [303] identified Fe_3C as the catalyst particle at the end of nanotubes, and suggested that this may be the real catalyst. However, Hernadi et al [304] tested Fe_3C nanoparticles and did not detect any catalytic activity. Another study by Herreyre et al [305] detected an Fe_3C phase when the Fe catalyst was entirely deactivated, and attributed this phase as the cause of catalyst poisoning. However, it should be noted that the Yarmulke mechanism proposed for SWNT growth does not imply carbon diffusion into the metal nanoparticle and thus carbide formation.

3.6.3 Morphology

There is a consensus in the literature concerning the correlation between the catalyst size and the CNT diameter. Many groups have observed a direct dependence of the

two quantities [150–159]. Nikolaev et al [189] observed that the catalyst particle tends to be slightly larger than CNT diameter, suggesting a change in morphology due to carbon absorption. This is supported by high-resolution in-situ TEM observation of the catalytic growth of CNTs [36, 192]. Both studies have shown that upon CNT nucleation and growth, the catalyst particle is reshaped due to the precipitation of carbon.

The size of a particle appears to have an effect on its catalytic properties. The Yarmulke mechanism, described in Section 3.2, is only valid for small nanoparticular catalysts, which exhibit a high surface energy. In this mechanism, the graphene cap assembled on the particle surface lowers the total surface energy due to the extremely low surface energy of the basal planes of graphite. This makes the particle favourable for CNT nucleation. This is reinforced by Hafner et al. [182], who supposed that the supply-limited growth of CNTs allows more time to anneal to the lowest-energy structure, so that smaller particles produce CNTs, while larger particles are encapsulated. Dai et al [188] also observed that larger particles always appear to be encapsulated by amorphous carbon, rendering them inactive for CNT catalysis

There is some difficulty in producing well-dispersed nanoparticles of a small enough size on the support surface in order to obtain CNTs of desired diameters. This is mainly due to problems controlling particle agglomeration. A widely employed solution is the use of a porous support. In this technique, particle agglomeration is prevented by trapping the catalyst particles in the pores of the substrate. Commonly used porous supports include porous silicon [306], anodic aluminium oxide [307] and zeolites [167]. Another approach to this problem is increasing the surface roughness of the substrate in order to hinder surface diffusion of the catalyst and thus its coalescence into larger particles [167].

3.6.4 Support

The role played by the support in the CVD of CNTs is not yet fully understood. The simplistic view that the support only plays a catalytically passive role in the formation of CNTs requires examination. The work of Rummeli et al. [278] demonstrated that under typical CVD growth conditions, nanoparticles of difficult-to-reduce metal oxides were capable of promoting ordered carbon growth. The authors attributed this to the presence of surface defect sites on the nanoparticle oxides. However, the interface between the catalyst nanoparticle and the support is thought to act as a annular defect site. This would indicate that the nature of the support-nanoparticle interface may be very important to the behaviour of the catalyst.

In the supported catalyst method of metal catalysed carbon nanotube synthesis, the support can interact both chemically and physically with the catalyst nanoparticle [308–312]. The support can control the size of the catalyst nanoparticle by affecting the

kinetics of nanoparticle formation. The support can also act to disperse the metal catalyst particles formed upon decomposition of metal salt precursors by physically holding the particle in place [299]. Additionally, the support can interact chemically with the catalyst nanoparticle and dramatically affect its catalytic ability. For instance, acquisition of negative charge by the catalyst nanoparticle from the support can enhance its catalytic activity by strengthening back donation of electron density into anti-bonding orbitals of the adsorbate. This electron sharing between the catalyst and adsorbate sufficiently weakens the bonding within the adsorbate, resulting in its dissociation [311, 312].

The catalyst nanoparticle can acquire negative charge through the interaction between either the metal cation or oxygen anion sites in the support [309–312]. A strong interaction between the catalyst nanoparticle and the cationic sites on the support is known as strong-metal support interaction (SMSI). SMSI arises from partial reduction of the oxide, which enables the metal cation of the support to donate partial negative charge to the supported metal nanoparticle [299]. For support oxides that are not readily reduced, another interaction involves the catalyst nanoparticle and an exposed oxygen anion sites on the support [309, 310]. The anions can act as Lewis base sites donating negative charge to the metal nanoparticle. In a similar manner, the partial negative charge it does accept from the oxide can enhance its catalytic activity.

In addition to these site-specific interactions, other processes such as Ostwald ripening and sintering can also occur during the metal nanoparticle formation steps [313, 314]. For instance, dramatic structural changes occur when metals supported on TiO_2 are heated in H_2 to 500 °C. The oxide becomes partially reduced to Ti_4O_7 and the metal assumes the form of hexagonal plates. In other systems, a compound may form between the support and metal nanoparticle [314]. Changes in the phase and crystalline structure of the support may also affect the nature of its interaction with the catalyst [299]. Consequently, the physical and electronic structure of the supported catalyst nanoparticle will also be affected.

3.7 Conclusions

In this chapter a review of the methodologies for carbon nanotube synthesis by catalytic chemical vapour deposition has been presented. The material reviewed in this chapter is by no means exhaustive, however it discusses the literature relevant to the work undertaken in this thesis. This review contains an summary of CNT synthesis by thermal CVD, the apparatus used and the growth process kinetics. The role of pyrolysis and radicals in this process has also been discussed, and it has been argued that hydrocarbon CVD of CNTs does not follow simple gas phase kinetics. In its most basic form, the hydrocarbon CVD process ($C_mH_n + C_s \leftrightarrow C_s + (n/2)H_2$) should lead to an increased rate

of CNT formation with increasing hydrocarbon concentration and decrease with increasing hydrogen concentration. However, the CVD process works best when the reactor is run at some empirically derived lean fuel condition. Increasing hydrocarbon concentration above this optimum level leads to reduced CNT growth and leads to amorphous carbon deposition. Therefore, it is suggested that the CNT growth process proceeds by the formation of an intermediate medium, a free radical condensate, where hydrogen exchange, carbon skeletal rearrangement and mass growth become facile processes due to the the presence of radicals.

In this medium, hydrocarbons and radicals are dehydrogenated to form various carbon allotropes. The rate of hydrogen loss is the differentiating factor in whether amorphous carbon, fullerenes or nanotubes are formed [176, 182, 183]. If dehydrogenation/rearrangement process is allowed to occur so that the minimum energy form of carbon can be achieved then fullerenes or CNTs are formed [176, 182]. In the case of CNTs, the presence of a catalyst prevents the carbon cage from closing so that a continuous tube of six-membered rings can be formed. A model for catalytic growth consistent with these findings is presented.

Several catalyst preparation techniques are presented, and a brief overview is provided of each technique. Several transition metal catalysts are reviewed, and approaches for their application in CNT synthesis are discussed. The synthesis of CNTs using structural agents and on a planar support are two prevailing techniques for CNT synthesis using transition metal catalysts discussed in this chapter. Additionally, a review of CNT synthesis using non-conventional catalysts, such as ceramic, noble metal and semiconducting nanoparticles, is also presented. Techniques reliant on the reorganisation of carbon to form CNTs is also provided. Finally, the operating conditions, catalyst composition, morphology and supporting material are discussed as important parameters affecting the quality and yield of carbon nanotubes by CVD.

Chapter 4

SWNT Synthesis from Noble Metal Nanoparticle Catalysts

Nanosized iron-group metals (Fe, Co, Ni) are known for their ability to catalyse SWNT growth in chemical vapour deposition. It has been generally accepted that these metals and their alloys consistently show the highest catalytic activity [272, 273]. This is attributed to the solubility of carbon in the metal-solid solution [274]. However, noble metals such as Au, Ag or Cu have both negligible carbon solubility and negligible carbide formation, and have recently been identified as catalysts for the growth of CNTs. Takagi et al. [3] have found that the yield of SWNTs from noble metals is comparable to that of iron-group metals. Moreover, noble metals, in particular Cu, are thought to favour CVD growth of CNT nanotubes at low temperatures with a narrow chirality distribution [270].

In this chapter, single-walled carbon nanotube growth catalysed by noble metal nanoparticles is studied. A novel technique for synthesizing carbon nanotubes using narrow size distribution Au nanoparticles is presented. Additionally, Cu and Ag nanoparticles were synthesized by decomposing a metal nitrate and investigated as potential catalysts. The effect of pretreatment temperature and dilution on the size distribution of the nanoparticles was studied by atomic force microscopy. The nanoparticle size distribution has been correlated to carbon nanotube yield and quality. Au and Cu nanoparticles have shown to be adequate catalysts for CNT growth and extensive characterisation of each stage of the growth process is presented. The results presented show that the commonly utilised model of carbon filament growth is inadequate to describe SWNT growth from noble metal catalysts. A new interpretation of the role of the catalyst is presented and discussed.

4.1 Experimental Details

Au nanoparticles, purchased from *Nanoprobes, Inc*, were suspended in isopropanol at three concentrations; 0.03 mM, 0.006 mM and 0.003 mM. The nanoparticles were specified to be approximately 1.4 nm in diameter, with a narrow size distribution, and were supplied as solid lyophilized form methanol solution. Unlike colloidal gold products, these solutions are stable for several months at $2 - 8$ °C and do not aggregate. They are purified by gel filtration and stable under a wide range of pH conditions.

A Cu nitrate catalyst solution was prepared using highly pure salt (99.995% Copper(II) nitrate hemi-pentahydrate from Sigma Aldrich) and isopropyl alcohol (Chromasolv, absolute, 99.9% from Sigma-Aldrich). The Ag nitrate catalyst solution was prepared using highly pure salt (99.995% Silver nitrate from Sigma Aldrich) and isopropyl alcohol (Chromasolv, absolute, 99.9% from Sigma-Aldrich). Three concentrations were prepared for both Cu and Ag catalysts, 1 mM, 2 mM and 4 mM and the solutions were sonicated for 20 minutes. The catalyst was deposited by dip-coating the supports in the solution at a speed of 3 mm/s . Samples were then subjected to a 100W O_2 plasma for 10 minutes to remove any residual organic left from deposition. The samples were then annealed in air at 400 °C for 30 minutes to thermally decompose the deposited metal nitrate. This step was found to be crucial in obtaining a satisfactory yield.

$< 001 >$ oriented, p-type silicon ($17 - 33$ Ωcm resistivity) with a 300 nm SiO_2 layer were used as substrates. All supports were cut to 10×10 mm pieces to suit a one-inch diameter furnace tube. The Au catalyst was deposited by spin-coating 40 μL of the Au solution at a rotation speed of 4000 RPM for 45s. Samples were then subjected to a 100W O_2 plasma for 10 minutes to remove any residual organic left from deposition.

Carbon nanotubes were grown in a one-inch tube furnace using a two step process. The first step was a hydrogen pretreatment performed at a temperature between 850 and 1000 °C for 10 minutes and the second step was a CNT growth step by thermal CVD in a hot-wall reactor at atmospheric pressure. The CNT growth was carried out using a mixture of methane (1000 sccm) and hydrogen (300 sccm) at a temperature of 850 °C. A new quartz tube was used exclusively for this work to avoid contamination.

The catalysts were characterised using a Veeco Multi-Mode atomic force microscope, using super sharp Si cantilevers (typical tip radius of 2 nm). The synthesized CNTs were observed by field-emission scanning electron microscope (JEOL 6500F). The chemical compositions of SEM samples were analysed by energy-dispersive X-ray spectroscopy (Oxford Instruments INCA Microanalysis System). Particle height distributions for each sample were determined using a minimum of ten 1 μm^2 AFM images utilising the Veeco Nanoscope software package. Images were first flattened using a three point levelling technique, and a threshold height of 0.4 nm was set in the particle detection software. The area densities of CNTs were evaluated using FE-SEM images using ImageJ

to determine the total contour length of CNTs [315]. For quantitative analysis, several images taken from the same sample were used, with overlapping regions being discarded. Raman spectra were obtained using a Renishaw micro-Raman system with He-Ne (632.8 nm) laser excitation with a power of 12 mW and a spot size of 1 μm.

4.2 Gold Nanoparticle Catalysts

Bulk Au is considered a noble metal, as it is highly unreactive and catalytically inactive. Au is the only metal with an endothermic chemisorbtion requirement, and in addition it has *d*-states so low in energy that the interaction with oxygen 2*p*-states is net repulsive. Nevertheless, in its nanoparticle form, Au is capable of catalysing a wide variety of reactions. These include the oxidation of CO [316], the selective hydrogenation of acetylene [317], hydrogenation of halogen compounds, reduction of nitrogen oxides and photocatalytic hydrogen production [318]. The origin of this effect is believed to be the increase in the fraction of low-coordinated Au atoms as the size of the Au cluster is reduced. In some cases, the catalytic nature of supported Au clusters can be explained by assuming the Au-support perimeter interface acts as a site for activating at least one of the reactants.

The first demonstration of CNT growth from Au nanoparticle catalysts by Lee et al. [6], involved the decomposition of acetylene over nanoparticles supported on SiO_2-Al_2O_3. This support showed a good propensity for the decomposition of acetylene and demonstrated strong interactions between the Au nanoparticles and its surface. The synthesized products were predominantly MWNTs, with average diameters of $\leq$ 20 nm. The first reports of the formation of SWNTs from small Au nanoparticle catalysts were by Takagi et al. [3] and Bhaviripudi et al. [275]. XPS measurements in both publications showed that CNT growth was only possible from contaminant-free catalyst nanoparticles, once the residual shell of gold oxides or gold chlorides were reduced by H_2. The findings of Liu et al. [276] corroborate this finding. Interestingly, neither paper detected any radial breathing modes in the low Raman shift region, corresponding to large diameter nanotubes.

4.2.1 Catalyst Characterisation

To determine the particle size distributions of the Au nanoparticles, AFM analysis was performed after spin coating and O_2 plasma treatment of the 0.03 *m*M, 0.006 *m*M and 0.003 *m*M concentrated solutions on SiO_2 substrates. Figure 4.1(a)–(c) show typical AFM topography images of fabricated samples from each concentration, respectively. Figure 4.1(a) (0.03 *m*M concentrated solution) shows a high density of local maxima in the topography scan, and each peak is believed to be an individual particle. The measurements indicate a density of 2500 ± 790 (mean $\pm$ standard deviation)

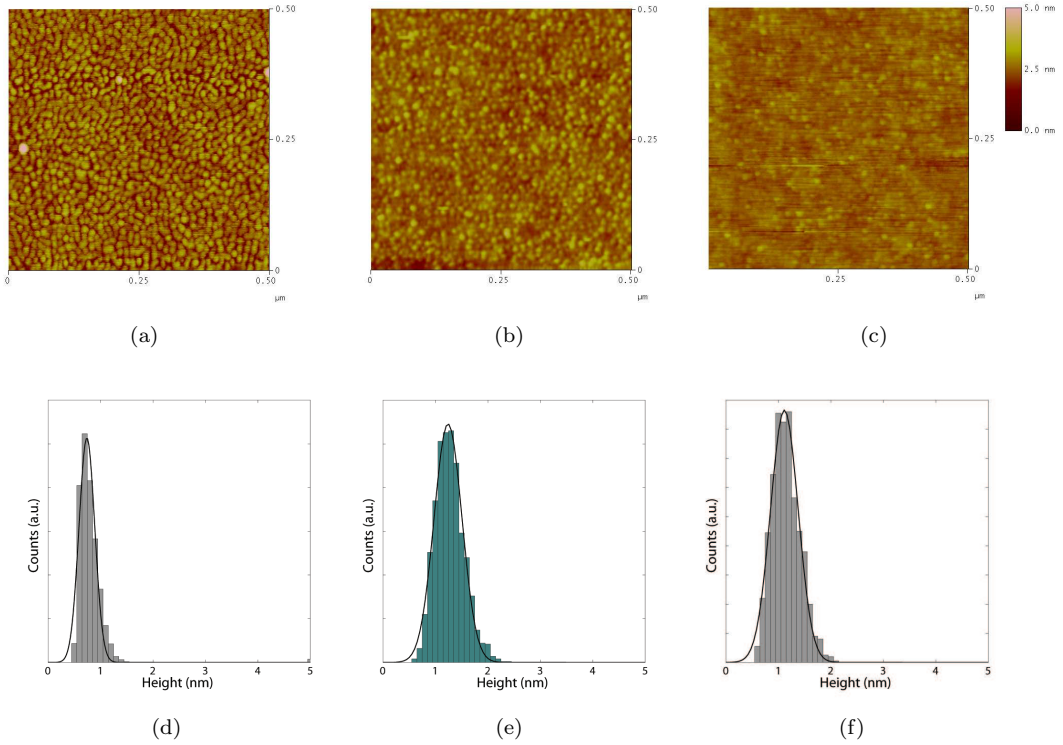

FIGURE 4.1: Atomic force microscope topography image of Au catalyst dispersed on a SiO_2 support at three dilutions; (a) 0.03 mM, (b) 0.006 mM and (c) 0.003 mM. Corresponding particle size distributions are shown in (c), (d) and (e), respectively. Particle size distributions have been fitted with a non-centred, normalised Gaussian.

particles/μm^2, which corresponds to an interparticle separation of approximately 20 ± 3 nm. Figure 4.1(b) (0.006 mM concentrated solution) shows a lower density of particles, 1100 ± 400 particles/μm^2, corresponding to an interparticle separation of approximately 31 ± 7 nm. Finally, Figure 4.1(c) (0.003 mM concentrated solution) shows the lowest density of particles, 210 ± 96 particles/μm^2, corresponding to an interparticle separation of approximately 72 ± 17 nm. It is clear that the density of particles of the substrate has decreased linearly with dilution of the solution. Additionally, the distribution of the Au nanoparticles on the substrate is very homogeneous which indicates that spin coating is a suitable method for deposition of the catalyst on the substrate.

Figure 4.1(d) shows the particle height distribution for several images taken from the 0.03 mM concentrated solution sample. This distribution has been fitted with a normalised, non-centred Gaussian, which shows a modal height of 0.7 nm with a standard deviation of 0.15 nm. This curve showed a good fit, with a minimal variance ($R_2 = 0.978$, using non-linear regression). Figure 4.1(e) shows the particle height distribution for several images taken from the 0.006 mM concentrated solution sample, also fitted with a normalised, non-centred Gaussian ($R_2 = 0.996$, using non-linear regression). This distribution shows a modal height of 1.3 nm and a standard deviation of 0.2 nm, matching the specifications provided by the supplier. Finally, the particle height distribution for the 0.003 mM concentrated solution sample is shown in Figure 4.1(f), also also fitted with a normalised,

non-centred Gaussian ($R_2 = 0.993$, using non-linear regression). This distribution shows a modal height of 1.2 nm and a standard deviation of 0.3 nm, closely matching the supplier specifications.

Normally, regardless of dilution, the deposited Au nanoparticles should have demonstrated the same particle height distribution. However, the distribution for the 0.03 mM concentrated solution sample is considerably sharper than the diluted samples and the modal height does not match the supplier specifications (1.4 nm). A possible explanation for this could be found in the accuracy of the measurement. Owing to the high density of particles on the sample surface and the shape of the scanning probe tip, the nanoparticles may not have been sufficiently dispersed to allow for an accurate measurement of particle height. This argument is supported by the fact that Figure 4.1(a) appears as a porous film, in contrast to discrete nanoparticles in the diluted samples. Finally, the slight difference between our measurements of particle height of the 0.006 mM and 0.003 mM concentrated solution samples with the supplier specification can be explained by the roughness of the SiO_2 substrates used, which is of the order of 0.1 nm ($R_A = 0.11$ nm).

4.2.2 Effect of Catalyst Density

Figure 4.2 shows SEM images of CNTs synthesized from the Au catalyst solution dispersed on a SiO_2 support for each dilution. The samples were fabricated at the optimum growth condition for the catalyst, H_2 pretreatment at 1000 °C for 10 minutes, followed by the CNT growth step for 20 minutes at 850 °C in a mixture of H_2 and CH_4 (1 : 3 gas ratio). Figure 4.2(a) shows a representative SEM image of the 0.03 mM concentrated solution sample after the CNT growth step. Two types of nanostructures are present in this sample and have been labelled for clarity. The first type comprises of shorter, thicker fibres, approximately 20 nm in diameter and 250 nm in length. These fibres are present after the pretreatment step, and photoluminescence and TEM measurements on similar samples have shown that these are composed of amorphous silicon oxide (SiO_x). The second type comprises of long, thin and straight fibres which were found to be CNTs. This sample shows a good density of CNTs, 3.4 ± 0.8 μm in length/μm^2, and a fairly homogeneous coverage across the sample. Figure 4.2(b) shows an SEM image of the 0.006 mM concentrated solution sample after the CNT growth step. In this sample no CNTs were detected, only amorphous silicon oxide fibres were present. The same case occurred for the 0.003 mM concentrated solution sample after the CNT growth step, shown in 4.2(b).

In order to determine why CNT growth is only possible from the high density Au nanoparticle sample, AFM was performed on the 0.003 mM concentrated solution sample after pretreatment at several temperatures. The results indicated that with a increase

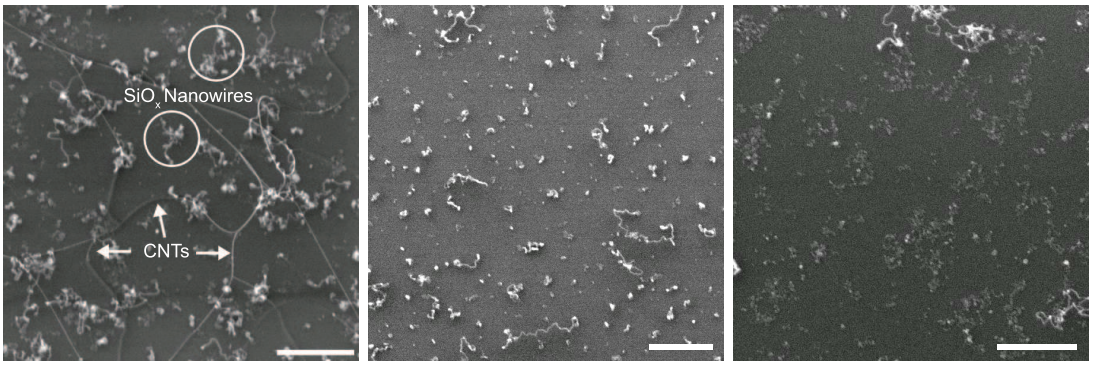

(a) (b) (c)

FIGURE 4.2: Scanning electron microscope image of CNTs synthesized from Au catalyst dispersed on a SiO_2 support at three dilutions; (a) 0.03 mM, (b) 0.006 mM and (c) 0.003 mM. Scale bar corresponds to 500 nm. CNTs were grown at the optimum growth condition, H_2 pretreatment at 1000 °C for 10 minutes, followed by the CNT growth step for 20 minutes at 850 °C in a mixture of H_2 and CH_4 (1 : 3 gas ratio).

in pretreatment temperature there is a change in the morphology of the Au nanoparticles. On average, the measured nanoparticles show a reduction in modal height as pretreatment temperature increases; from 0.8 nm for pretreatment at 850 °C to 0.7 nm for pretreatment at 1000 °C. Furthermore, there is a linear reduction in nanoparticle density as pretreatment temperature increases. Indeed, the initial density of 210 ± 96 particles/μm^2 is reduced to 84 ± 22, 54 ± 20, 12 ± 5 and 7 ± 4 particles/μm^2 after pretreatment at 850 °C, 900 °C, 950 °C and 1000 °C respectively. This drastic reduction in nanoparticle density could be explained by evaporation of the Au nanoparticles or diffusion into the support medium. This reduction would account for the inability to synthesize CNTs from the low density samples.

4.2.3 Effect of Catalyst Pretreatment

Figure 4.3 shows SEM images of the 0.03 mM diluted Au catalyst on a SiO_2 support after a 850 °C CNT growth step. Figure 4.3(b) shows the topography of a sample without a catalyst pretreatment anneal prior to the CNT growth step. This image shows large aggregations of Au particles throughout the sample surface. This sample showed no evidence of CNTs. Figure 4.3(a) shows the topography of a sample subjected to a 1000 °C pretreatment in H_2 prior to growth. This sample showed a good density of CNTs, in addition to some amorphous silicon oxide nanowires. Additionally, the Au particles on the surface appear smaller and well dispersed (in comparison to Figure 4.3(b)), indicating that a catalyst preparation anneal is necessary. Reports from the literature state that this is due to the need to reduce the catalyst particles prior to growth. Indeed, the work of Takagi et al. [3], Bhaviripudi et al. [275] and Liu et al. [276] showed that CNT growth was only possible from contaminant-free catalyst nanoparticles, once the residual shell of gold oxides or gold chlorides were reduced by H_2. However, the results presented in

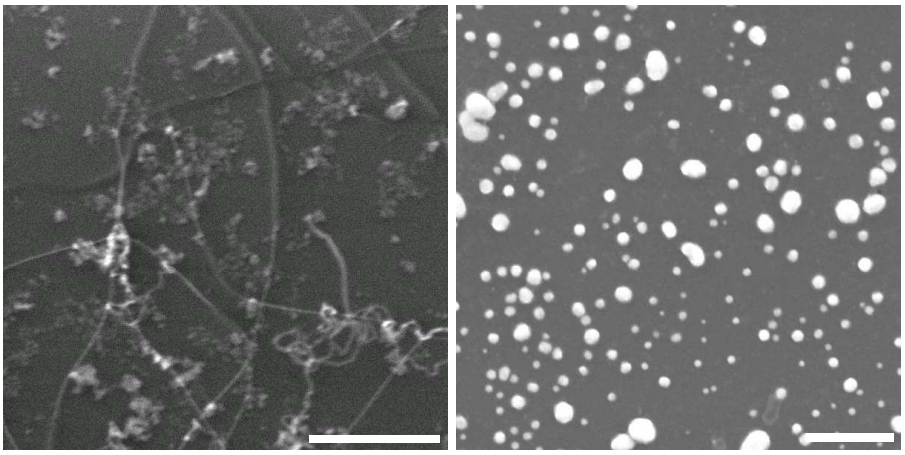

(a) (b)

FIGURE 4.3: Scanning electron microscope image of CNT growth on a SiO_2 support from 0.03 mM diluted Au catalyst, (a) with and (b) without a catalyst pretreatment step (1000 °C in H_2 for 10 minutes). The CNT growth step was 850 °C in a mixture of H_2 and CH_4 (1 : 3 gas ratio) for 20 minutes in both cases. Scale bar corresponds to 500 nm.

this work suggest that the catalyst pretreatment step also affects the morphology of the supported catalyst. The effect of pretreatment on catalyst morphology will be discussed in further detail in Section 4.2.4.

Figure 4.4 shows SEM images of the 0.03 mM diluted Au catalyst on a SiO_2 support after a 850 °C CNT growth step following a catalyst pretreatment anneal in H_2 at various temperatures for 10 minutes. The pretreatment anneal temperatures shown in Figure 4.4(a)–(d) are 1000, 950, 900 and 850 °C, respectively. These images establish the optimal growth condition of the Au nanoparticle catalyst and provide an insight to the importance of the catalyst pretreatment anneal. Figure 4.4(a) shows a typical sample after pretreatment at 1000 °C, this sample showed a good density of CNTs (3.4 ± 0.8 μm in length/μm^2) and a fairly homogeneous coverage across the sample. Figure 4.4(b) shows a typical sample after pretreatment at 950 °C, this sample showed a slightly lower density of CNTs, 2.1 ± 0.9 μm in length/μm^2. After pretreatment at 900 °C, shown in Figure 4.4(c), there was an even lower density of CNTs, 1.1 ± 1.2 μm in length/μm^2 and the coverage of CNTs across the sample was not as uniform as for the higher pretreatment temperatures. Finally, no CNTs were found at the lowest pretreatment temperature, 850 °C. This sample also did not exhibit any of the typical features seen the higher pretreatment temperatures indicating that the catalyst required a higher temperature pretreatment in H_2 prior to growth.

CNTs were found in samples pretreated at a temperature in the range from 900 °C to 1050 °C, however the highest area density was found in samples pretreated at 1000 °C as shown in Figure 4.4(a). For all samples pretreated in this temperature range we see both CNTs and amorphous silicon oxide nanowires. At pretreatment temperatures

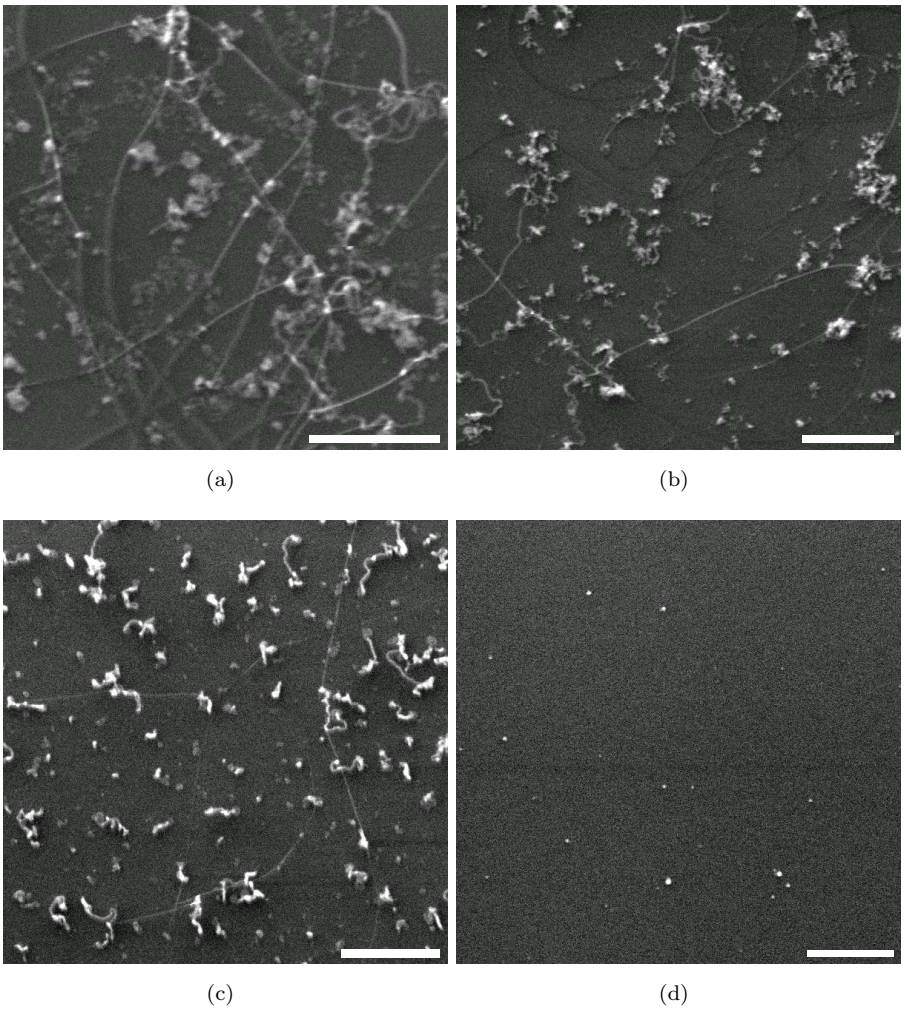

FIGURE 4.4: Scanning electron microscope image of CNT growth on a SiO_2 support from 0.03 *m*M diluted Au catalyst, at four different pretreatment temperatures; (a) 1000 °C, (b) 950 °C, (c) 900 °C and (d) 850 °C. The samples were pretreated in H_2 for 10 minutes. The subsequent CNT growth step was kept constant at at 850 °C in a mixture of H_2 and CH_4 (1 : 3 gas ratio) for 20 minutes. Scale bar corresponds to 500 nm.

below 900 °C, the only features present in the SEM images are large dots, which are believed to be large aggregations of Au nanoparticles, observed in Figure 4.4(d). It is believed that there are smaller Au nanoparticles also present in this sample, however due to the resolution of the SEM these are not visible. These results indicate that the H_2 pretreatment is essential for the synthesis of CNTs, which is in agreement with the literature [3, 275, 276]. These authors argue that there is a requirement for contaminant-free catalyst nanoparticles, achieved by the pretreatment in H_2. However, without XPS measurements taken in-situ we cannot reach the same conclusions. In this work, it is evident that the pretreatment of the catalyst affects the morphology of the samples, as shown in Figure 4.3. Interestingly, there is also no formation of amorphous silicon oxide nanowires without pretreatment in H_2 at temperatures higher than 900 °C. It is believed that these nanowires are formed by the carbothermal reduction of the SiO_2 substrate

[284, 319], this formation mechanism will be discussed in detail in the upcoming chapters of this work.

In order to confirm that the CNT growth is catalysed by the Au nanoparticles and not any systematic contaminant, a control sample was fabricated at the optimum growth condition. The control sample was subjected to the same deposition and cleaning process as the Au nanoparticle samples, however no Au nanoparticles were deposited. This sample was pretreated at 1000 °C in H_2 for 10 minutes and exposed to the CNT growth step at 850 °C in a mixture of CH_4 and H_2 (3 : 1 ratio). No CNTs were found in this sample. Additionally, EDS analysis has been undertaken in all the sample regions which showed CNTs, and regions which showed contaminants were discarded from subsequent analysis. However, it should be noted that at this scale, the sensitivity of EDS is low.

4.2.4 Evolution of the Catalyst

The different CNT area densities observed in Figure 4.4 suggest that the pretreatment temperature has a great effect on the yield of the process. Presumably, this is owing to a change in the nature of the catalyst during the pretreatment step. In order to understand the effect this has on the morphology of the catalyst, AFM characterisation of the 0.03 mM diluted Au catalyst samples has been undertaken for the range of pretreatment temperatures discussed in in Section 4.2.3.

From typical AFM images on samples after a pretreatment step at temperatures between 1000 and 850 °C, the mean density of particles has been determined. The initial particle density of 2500 ± 790 (mean $\pm$ standard deviation) particles/μm^2 is reduced to 495 ± 220, 421 ± 190, 343 ± 170 and 293 ± 170 particles/μm^2 after pretreatment at 850 °C, 900 °C, 950 °C and 1000 °C respectively. It is evident that with an increase in pretreatment temperature there is an associated reduction in nanoparticle density. It is likely that the reduction in nanoparticle density is due to nanoparticle evaporation or ripening. Additionally, in several AFM images, there were pits found in the oxide substrate and it is believed that these were caused by diffusion of the Au catalyst into the substrate. The high propensity of silicon-metal interdiffusion [320] supports this hypothesis.

Figure 4.5(a)–(d) show the particle height distribution for samples pretreated in H_2 for 10 minutes at 1000 °C, 950 °C, 900 °C and 850 °C respectively. Each distribution has been fitted with a non-centred, normalised Gaussian. All distributions showed a close fit to a Gaussian curve, with a lowest value of $R_2 = 0.929$ by non-linear regression for the sample pretreated at 900 °C. Figure 4.5(e) shows a normalised overlay of each fitted Gaussian curve for comparison. The particle height distribution for a sample pretreated at 1000 °C is shown in Figure 4.5(a). This distribution showed an excellent fit with a non-centred Gaussian ($R_2 = 0.989$ using non-linear regression) and has a modal height of 1.2 nm with a standard deviation of 0.37 nm. After pretreatment at 950 °C (Figure 4.5(b)),

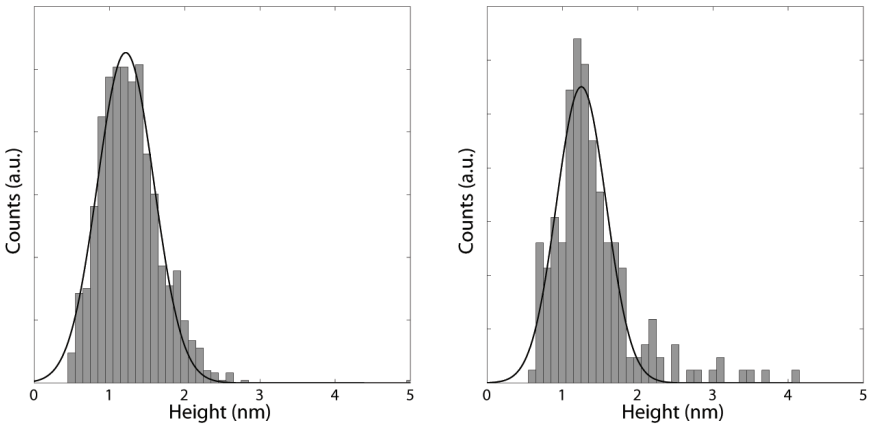

(a)

(b)

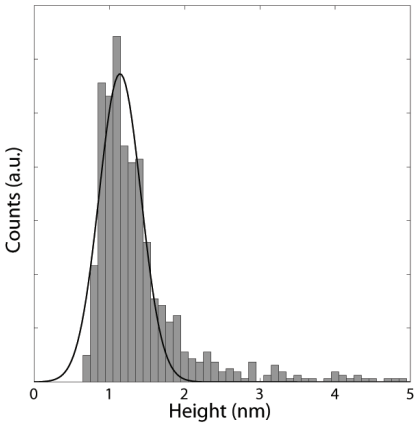

(c)

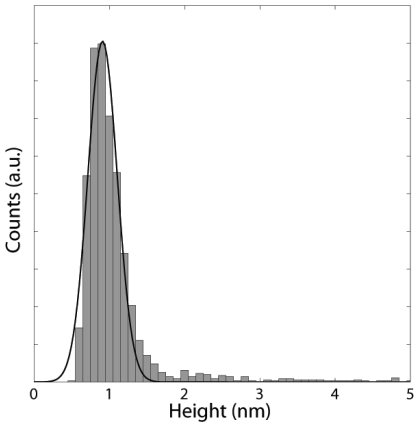

(d)

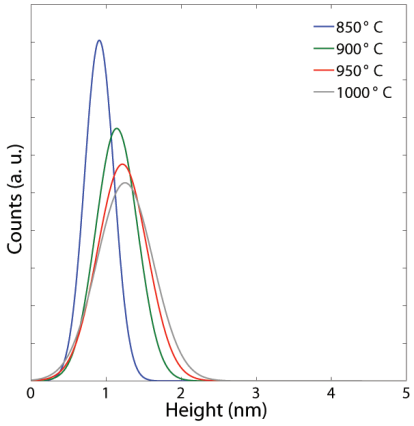

(e)

FIGURE 4.5: Particle size distribution for 0.03 mM diluted Au catalyst dispersed on a SiO_2 support after pretreatment in H_2 for 10 minutes at; (a) 1000 °C, (b) 950 °C, (c) 900 °C and (d) 850 °C. Particle size distributions have been fitted with a non-centred, normalised Gaussian. (e) Normalised particle size distribution Gaussian curve fits for each pretreatment temperature.

Pretreatment		Distribution Statistics		Nanoparticle Density
Temperature (°C)	Time (min)	Mode (nm)	R_2	(particles/μm^2)
1000	10	1.2 ± 0.37	0.989	293 ± 170
950	10	1.3 ± 0.33	0.964	343 ± 170
900	10	1.1 ± 0.28	0.929	421 ± 190
850	10	0.9 ± 0.19	0.978	495 ± 220

TABLE 4.1: Particle size distribution fit parameters and nanoparticle densities for 0.03 mM diluted Au catalyst dispersed on a SiO_2 support after pretreatment in H_2 at various temperatures.

the distribution has a modal height of 1.3 nm and a standard deviation of 0.33 nm. The particle height distribution for the sample pretreated at 900 °C is shown in Figure 4.5(c) and has a modal height of 1.1 nm and a standard deviation of 0.28 nm. Finally, after pretreatment at 850 °C (Figure 4.5(d)), the distribution has a modal height of 0.9 nm and a standard deviation of 0.19 nm. This information is summarised in Table 4.1.

This data shows that there is an increase in the modal height of the particles as the pretreatment temperature increases. There is also a broadening of the distribution as the pretreatment temperature increases, shown by the increasing standard deviations and Figure 4.5(e). As pretreatment temperatures increase, the distributions show a reduction in the number of small particles and an increase in the mean particle size. This behaviour suggests phase coarsening, which occurs at the expense of small particles within a system, which shrink and finally disappear [321]. This is a thermodynamically-driven spontaneous process occurring because larger particles are more energetically favoured than smaller particles [322]. This may account for the reduction in nanoparticle density as pretreatment temperature increases. This behaviour is in contrast to the 0.003 mM diluted Au catalyst samples after pretreatment, which showed a reduction in nanoparticle modal height as pretreatment temperature increased. However, this difference could be explained by the low initial particle density and consequently large inter-particle separation, which may have been too large to allow coarsening to take place. Interestingly, at the lowest pretreatment temperature (850 °C), the nanoparticle modal height is 0.9 nm which is significantly lower than the value specified by the supplier and measured by AFM. The density of nanoparticles suggests that this measurement is not an artefact. This suggests that there must be a competing process occurring to account for the reduction of nanoparticle size from the initial, specified size. Indeed, due to the temperatures involved, nanoparticle evaporation or diffusion into the substrate seem likely. This competing loss process could explain why measured shape of the distributions do not match the shape of distributions found using multiparticle diffusion simulations seen in the literature [323, 324].

There is a consensus in the literature concerning the correlation between the catalyst size and the CNT diameter. Many groups have observed a direct dependence of the two quantities [150–159]. Nikolaev et al. [189] observed that the catalyst particle tends to be slightly larger than CNT diameter, suggesting a growth mechanism involving graphene cap formation. This has been supported by high-resolution in-situ TEM observation of the catalytic growth of CNTs [36, 192]. To date, the smallest experimental value of nanotube diameter detected has been 0.7 nm [52]. The results presented in this section demonstrate that the size of the Au nanoparticle catalyst after pretreatment is within the possible range to seed CNT growth. However, these results do not allow us to determine the reason for the higher CNT yield in samples pretreated at 1000 °C. One possibility may be that the slightly larger nanoparticles are more efficient at forming the graphene cap required to seed a CNT. Yet it is more likely that pretreatment at higher temperatures are more effective at removing residual contaminants or reducing the nanoparticles.

4.2.5 Raman Spectroscopy

In Figure 4.6, representative Raman spectra are shown from samples synthesized using a 0.03 mM diluted Au catalyst dispersed on a SiO_2 support. The measured CNTs were grown using a pretreatment in H_2 for 10 minutes at 1000 °C, followed by a growth step at 850 °C in a mixture of H_2 and CH_4 (1 : 3 gas ratio) for 20 minutes. The Raman measurements were undertaken utilising a Renishaw in-Via system, consisting of an Olympus Microscope, a monochromator with a 1200 groves/mm grating, a Peltier cooled CCD, holographic notch filter and a He-Ne (632.8 nm) laser excitation. The signal is collected via a backscatter geometry, with the holographic notch filter tuned so that the frequency cut-off was a shift of approximately 110 cm^{-1}. For this reason, the system is not able to detect RBMs from CNTs with diameters larger than 2.3 nm.

The Raman spectra obtained from areas of relatively high CNT area density typically exhibited an asymmetric double peak at approximately 1590 cm^{-1} (Figure 4.6(a)). This double peak can be attributed to the Raman-allowed tangential mode of CNTs, G-band. In the representative spectrum shown in Figure 4.6(a), this feature could be fitted with four Lorentzian oscillators located at 1539, 1554, 1589 and 1598 cm^{-1}. Group theory predicts that there are six Raman-active modes within the tangential G-band spectral region (1600 cm^{-1}) for general chiral SWNTs [112, 325]. The symmetry assignments used to fit the four Lorentzian features (in this case 1539, 1554, 1589 and 1598 cm^{-1}) have been reported [112, 325], and are believed to be characteristic of a semiconducting tube. Indeed, assuming that the signal originates from a single, isolated nanotube, we can determine the signal to originate from a semiconducting tube of 1.15 nm diameter (using the relation $\Delta\omega_G = \omega_{G^+} - \omega_{G^-}$, as described in Section 2.4.5).

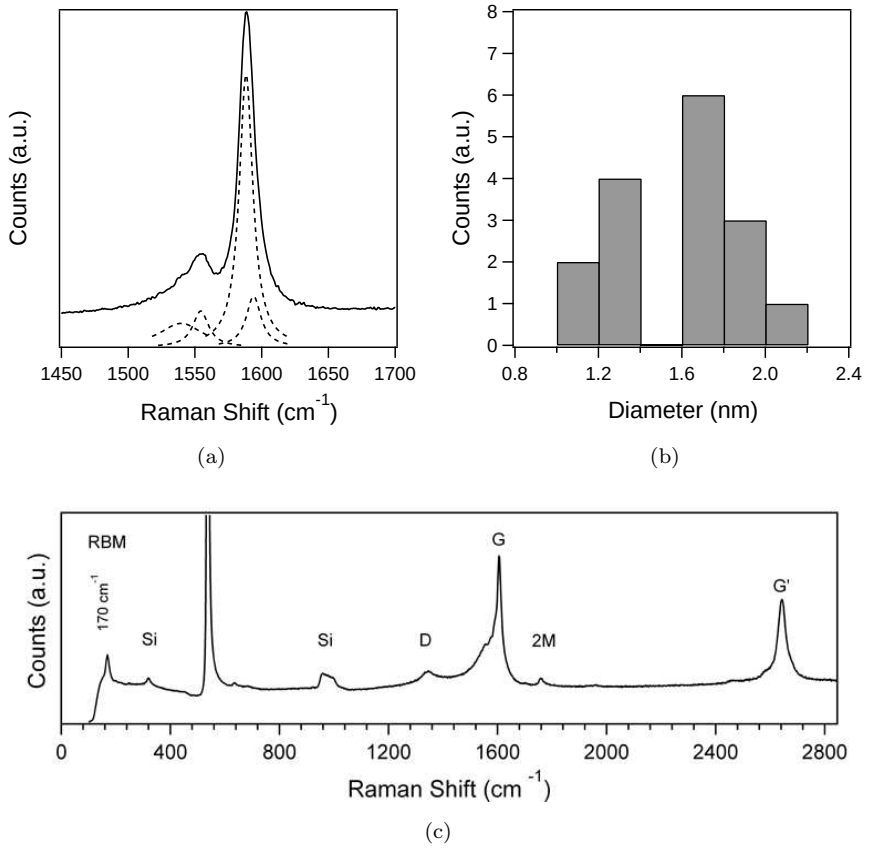

FIGURE 4.6: Raman spectra for the carbon nanotubes synthesized using 0.03 mM diluted Au catalyst dispersed on a SiO_2 support after pretreatment in H_2 for 10 minutes at 1000 °C, followed by a growth step at 850 °C in a mixture of H_2 and CH_4 (1 : 3 gas ratio) for 20 minutes. (a) Typical G-band characteristic, fitted with four Lorentzian curves. (b) Histogram of the SWNT diameters obtained via RBM. (c) Typical Raman spectra of the synthesized nanotubes.

Figure 4.6(c) shows a typical Raman spectrum obtained from the Au catalyst sample. This spectrum shows five characteristic features of CNTs; the RBM, D-band, G-band, 2M band and G' mode. The G-band feature in this spectrum is broader than that show in in Figure 4.6(a), and its lower frequency component (ω_{G^-}) is asymmetric and can be fit by a Breit-Wigner-Fano lineshape. This gives an indication that the Raman signal nanotube originates from bundle of nanotubes. In general, the measured spectra showed a good intensity ratio between the disorder induced D-band and the Raman allowed G-band ($I_D/I_G = 0.12$) indicating that the nanotubes are of a high quality in terms of structure and graphitisation. This spectrum shows an overtone of the D-band, the G' mode at approximately 2650 cm^{-1}. Additionally, there is a combination mode present, the 2M mode which results from the G-band and the RBM. Finally, in many cases spectra exhibiting peaks in the region between 110 to 250 cm^{-1} were obtained. These peaks are attributed to the RBM feature of SWNTs [125] and appear only at points from the sample from which a strong G-band feature is obtained. Therefore, it can be concluded that this spectral feature is indicative of the presence of SWNTs in

the sample. In the typical spectrum shown in Figure 4.6(c), there is a low-frequency peak at 170 cm^{-1} which is attributed to a RBM. This breathing mode corresponds to a metallic nanotube of 1.45 nm diameter, which is in agreement with the results of the G-band analysis.

A histogram of the SWNT diameters observed in the measurements via the RBM spectral feature is shown in Figure 4.6(b). It should be noted that since the measurements were only undertaken using a 632.8 nm He-Ne excitation these results do not provide a full diameter characterisation of the sample. This histogram indicates that the majority of the SWNTs observed had a large diameter. Although no strong conclusions can be drawn from this fact, this result correlates with the higher CNT yield found in samples pretreated at higher temperatures, which showed a larger nanoparticle modal size. It is feasible that the slightly larger nanoparticles are more efficient at seeding SWNT growth, however further experimental work is required to confirm this.

4.3 Copper Nanoparticle Catalysts

Nanosized particles containing a high surface area and reactive morphologies have been considered as effective catalysts for organic reactions such as hydrogenation, oxidation, cross-coupling, etc [326–329]. The main benefits associated with nanomaterials are based on their high atom efficiency and their high reaction rate, ease for catalyst recovery and the recyclability of catalysts. Cu nanoparticles, in particular, can be active catalysts for various processes. For instance, CuO and Cu immobilized on polymer resins have been used in alcohol oxidation [330]. CuO nanoparticles were studied for C-N, C-O and C-S bond formation via cross-coupling reactions [331] and for the removal of organic pollutants in aqueous solutions [332]. Generally, Cu nanoparticles are cheap and require only mild reaction conditions for high yields of products in short reaction times as compared to traditional catalysts [333].

Metallic Cu, long considered to be a contaminant in the growth of SWNTs, has also recently been reported as an efficient catalyst for SWNT formation in several studies [3–5]. However, in comparative experiments and theoretical predictions Cu shows the poorest catalytic efficiency for CNT growth [274, 334]. The experimental results presented in this section will show that Cu has a good catalytic activity and can act as a new type of catalyst for the synthesis of CNTs.

4.3.1 Catalyst Characterisation

To determine the particle size distributions of the Cu nanoparticles, AFM analysis was undertaken after subjecting the dip coated samples to a O_2 plasma clean and an anneal at 400 °C in air. Figure 4.7(a)-(c) show typical AFM topography images for the 1, 2

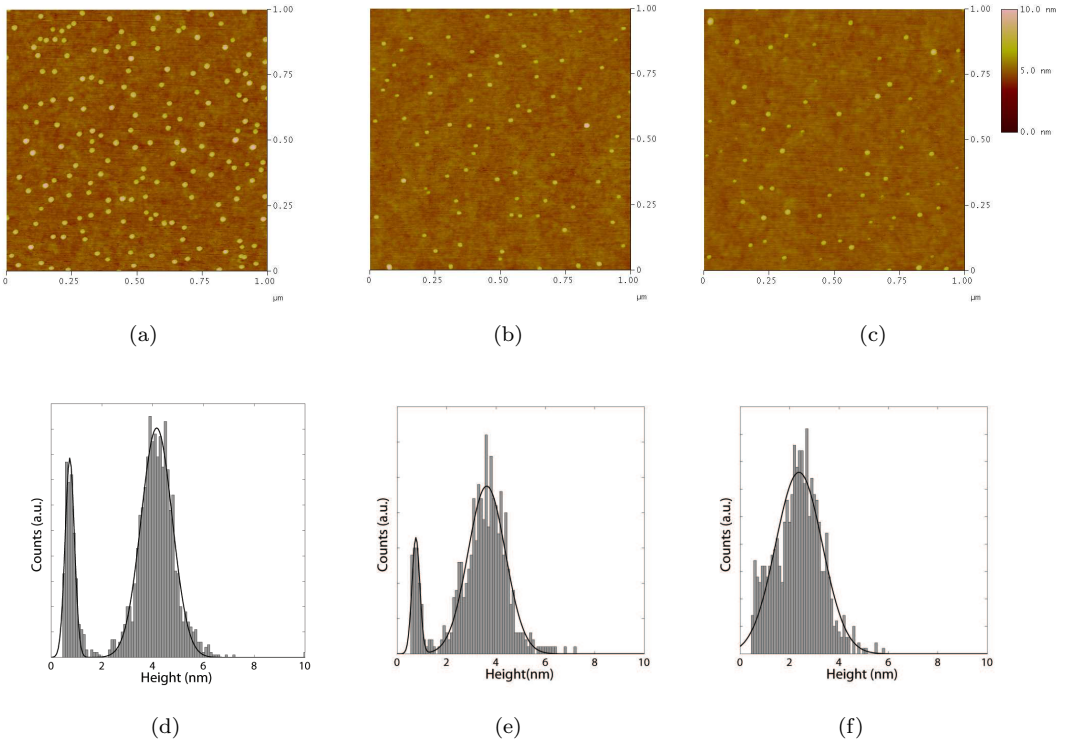

FIGURE 4.7: Atomic force microscope topography image of Cu catalyst dispersed on a SiO_2 support at three dilutions; (a) 1 mM, (b) 2 mM and (c) 4 mM. Corresponding particle size distributions are shown in (c), (d) and (e), respectively. Particle size distributions have been fitted with a non-centred, normalised Gaussian.

and 4 mM Cu nitrate solution samples, respectively. All samples showed a reasonable density of local maxima in the topography scan, and each peak is believed to be an individual particle. Figure 4.7(a) (1 mM Cu nitrate solution) showed the highest density of nanoparticles, 180 ± 27 particles/μm^2, corresponding to an interparticle separation of 75 ± 5 nm. The 2 mM Cu nitrate solution, shown in Figure 4.7(b), showed a slightly lower density of nanoparticles, 105 ± 18 particles/μm^2 which corresponds to an interparticle separation of 98 ± 9 nm. The highest concentration, 4 mM Cu nitrate solution, showed the lowest density of nanoparticles. The measurements indicate a a density of 81 ± 7 particles/μm^2, which corresponds to an interparticle separation of 111 ± 5 nm. The distribution of the Cu nanoparticles on the substrate is very homogeneous which indicates that dip coating is a suitable method for deposition of the catalyst on the substrate. Additionally, the density of nanoparticles on the substrate has decreased as the concentration of the metal-nitrate solution increased. This behaviour is in contrast to that seen with the Au nanoparticles, however this is most likely due to the requirement of nucleation and growth from the metal-nitrate solution to form nanoparticles.

The particle height distribution, obtained from several images from the 1, 2 and 4 mM Cu nitrate solution samples is shown in Figure 4.7(d)-(f), respectively. These distributions have been fitted with normalised, non-centred Gaussian curves, which in all cases showed a reasonable fit. The 1 and 2 mM Cu nitrate solution samples, shown

in Figure 4.7(d) and 4.7(e), exhibited a bimodal distribution. Figure 4.7(d) showed two modes, with heights of 0.7 ± 0.2 nm and 4.2 ± 0.6 nm, which was determined by fitting two non-centred, normalised Gaussian curves ($R_2 = 0.986$, using non-linear regression). Figure 4.7(e) also exhibited two modes with heights of 0.8 ± 0.1 nm and 3.6 ± 0.8 nm, also determined by two non-centred, normalised Gaussian curves ($R_2 = 0.964$, using non-linear regression). The 4 mM Cu nitrate solution sample could be fit by a mono-modal Gaussian distribution. This distribution showed a good fit ($R_2 = 0.963$, using non-linear regression) and showed a modal height of 2.4 nm and a standard deviation of 0.9 nm.

The bimodal particle size distributions, seen in the 1 and 2 mM Cu nitrate solution samples, suggest a formation mechanism involving either breakup of large particles or variable growth mechanisms in the system. Such distributions usually result from two different generation processes: the smaller mode is a result of molecular condensation, while the larger one is a result of breakup or redispersion [335]. It should be noted that a bimodal particle distribution is considered to be less thermodynamically stable than a mono-modal distribution owing to a requirement for minimization of surface energy [336, 337]. It is apparent from these three distributions that there is a transformation from bimodal to mono-modal distribution as the concentration of the Cu nitrate solution is increased. This behaviour may be due to the nitrate reduction anneal in air, which results in the formation of CuO [338]. It is believed that the free surface of the particles would be oxidized, and that the interior would remains as metal. This structure is expected to affect the particle size distribution by promoting splitting until the entire particle is converted to oxide [339]. Thus, the bimodal distribution may arise due to the complete oxidation of smaller particles, leading to a segregation in the distributions. It should also be noted that the mono-modal particle size distribution shown in Figure 4.7(f) most likely conceals a bimodal distribution, however due to measurement accuracy this could not be resolved.

4.3.2 Effect of Catalyst Concentration

Figure 4.8 shows SEM images of CNTs synthesized from the Cu nitrate solution dispersed on a SiO_2 support for each concentration. The samples were fabricated at the optimum growth condition for the catalyst, H_2 pretreatment at 1000 °C for 10 minutes, followed by the CNT growth step for 20 minutes at 850 °C in a mixture of H_2 and CH_4 (1 : 3 gas ratio). Figure 4.8(a) shows a representative SEM image of the 1 mM Cu nitrate solution sample after the CNT growth step. Unlike with the Au nanoparticles, only one type of nanostructure is present; the long, thin and straight fibres believed to be CNTs. No amorphous SiO_x nanowires were found in the samples, regardless of concentration, and it is believed that the nitrate reduction anneal in air is responsible for this difference. This sample showed a reasonable density of CNTs, 2.1 ± 1.1 μm in length/μm^2, and a fairly

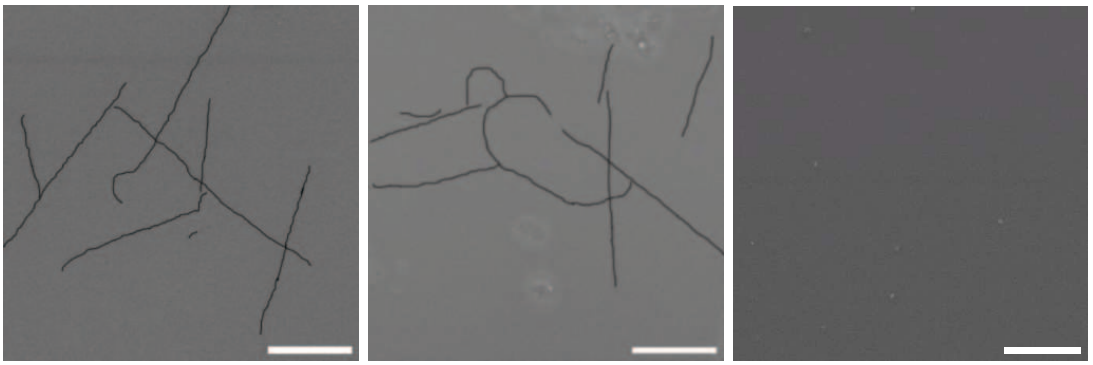

(a) (b) (c)

FIGURE 4.8: Scanning electron microscope image of CNTs synthesized from Cu catalyst dispersed on a SiO_2 support at three dilutions; (a) 1 mM, (b) 2 mM and (c) 4 mM. Scale bar corresponds to 500 nm. CNTs were grown at the optimum growth condition, H_2 pretreatment at 1000 °C for 10 minutes, followed by the CNT growth step for 20 minutes at 850 °C in a mixture of H_2 and CH_4 (1 : 3 gas ratio). CNTs have been highlighted for clarity.

homogeneous coverage across the sample. The 2 mM Cu nitrate solution sample, shown in Figure 4.8(b), also showed a reasonable density of CNTs and a fairly homogeneous coverage across the sample (1.3 ± 0.9 μm in length/μm^2). Finally, the no CNTs were detected in the 4 mM Cu nitrate solution sample, shown in Figure 4.8(c).

As with the Au nanoparticles, it is believed that the reason for the relatively higher CNT yield from the 1 mM Cu nitrate solution sample is due to a higher initial nanoparticle density. In addition, the particle size distribution of this sample after pretreatment in H_2 may be more conducive for CNT formation.

4.3.3 Effect of Catalyst Pretreatment

Figure 4.9 shows SEM images of the 1 mM Cu nitrate solution catalyst on a SiO_2 support after a CNT growth step at 900 °C in a mixture of H_2 and CH_4. Neither sample was subjected to a pretreatment in H_2 prior to the CNT growth step. Figure 4.9(a) shows the topography of a sample after a nitrate reduction anneal in air prior to the CNT growth step. In this representative image, there are two types of nanostructures present; the thin, long and straight fibres, believed to be CNTs and a high density of shorter, thicker fibres which have been found to be amorphous silicon oxide (SiO_x) nanowires in similar experiments. These nanostructures have been labelled for clarity. This is significantly different to the images shown in Figure 4.8(a) due to the existence of the SiO_x nanowires. This difference is attributed to the reduced amount of residual contaminants (amorphous carbon, unreduced nitrate, etc) in the samples subjected to the nitrate reduction anneal. Indeed, Li et al. [284] have reported that the mechanism of formation of the SiO_x nanowires is carbon assisted. Additionally, Lee et al. [340] argued that the SiO_x nanowires were catalysed by graphitic fragments, supported by

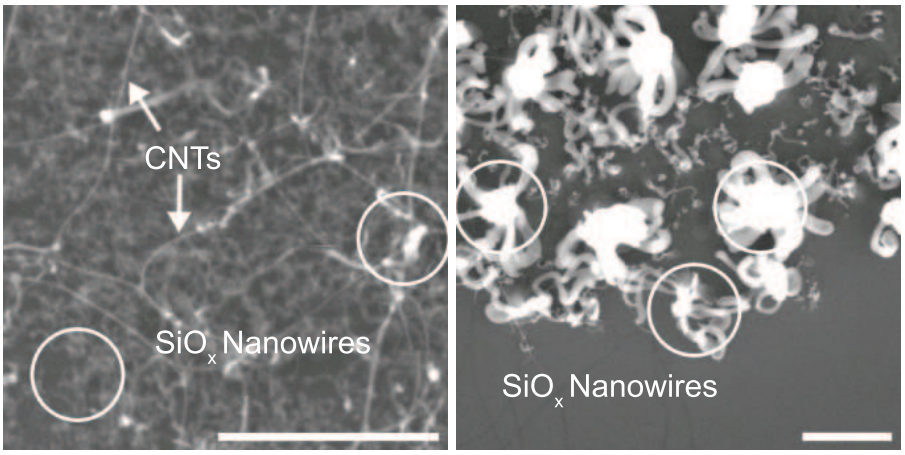

(a) (b)

FIGURE 4.9: Scanning electron microscope image of CNT growth on a SiO_2 support from 1 mM Cu catalyst, (a) with and (b) without a catalyst preparation anneal in air (400 °C for 10 minutes). The CNT growth step was 900 °C in a mixture of H_2 and CH_4 (1 : 3 gas ratio) for 20 minutes in both cases. The samples were not given a H_2 pretreatment prior to the CNT growth step. Scale bar corresponds to 500 nm.

TEM images. The formation mechanism was later determined to be the solid state transformation of SiO_2 films, catalysed by graphitic fragments [285]. Figure 4.9(b) shows the topography of a sample without the nitrate reduction anneal in air. The morphology of this sample is significantly different to that shown in Figure 4.9(a), the Cu catalyst was found to be segregated into islands and the uniformity of the sample was poor. Additionally, the SiO_x nanostructures were larger in diameter and shorter in length. These results illustrate the importance of the nitrate reduction anneal in air. Takagi et al. [3] presented XPS measurements demonstrating that a catalyst anneal in air was essential to remove the contaminant over-layer from the nanoparticles, in order to ensure a good yield of SWNTs. It was also argued that this step might contribute to preventing nanoparticle aggregation and islanding, which is seen clearly in Figure 4.9(b).

Figure 4.10 shows SEM images of the 1 mM Cu catalyst on a SiO_2 support after a 850 °C growth step following a catalyst pretreatment anneal in H_2 at various temperatures for 10 minutes. All samples were subjected to the nitrate reduction anneal in air prior to the H_2 pretreatment. The pretreatment anneal temperatures shown in Figure 4.10(a)-(d) are 1000, 950, 900 and 850 °C, respectively. These images establish the optimal growth condition of the Cu catalyst and provide an insight to the importance of the catalyst pretreatment anneal. Figure 4.10(a) shows a typical sample after pretreatment at 1000 °C, this sample showed a good density of CNTs (2.1 ± 1.1 μm in length/μm^2) and a fairly homogeneous coverage across the sample. Figure 4.4(b) shows a typical sample after pretreatment at 950 °C, this sample showed a slightly lower density of CNTs, 1.9 ± 0.9 μm in length/μm^2. After pretreatment at 900 °C, shown in Figure 4.4(c), there was an even lower density of CNTs, 0.5 ± 1.2 μm in length/μm^2 and the coverage of CNTs across the sample was not as uniform as for the higher pretreatment temperatures. Finally, a

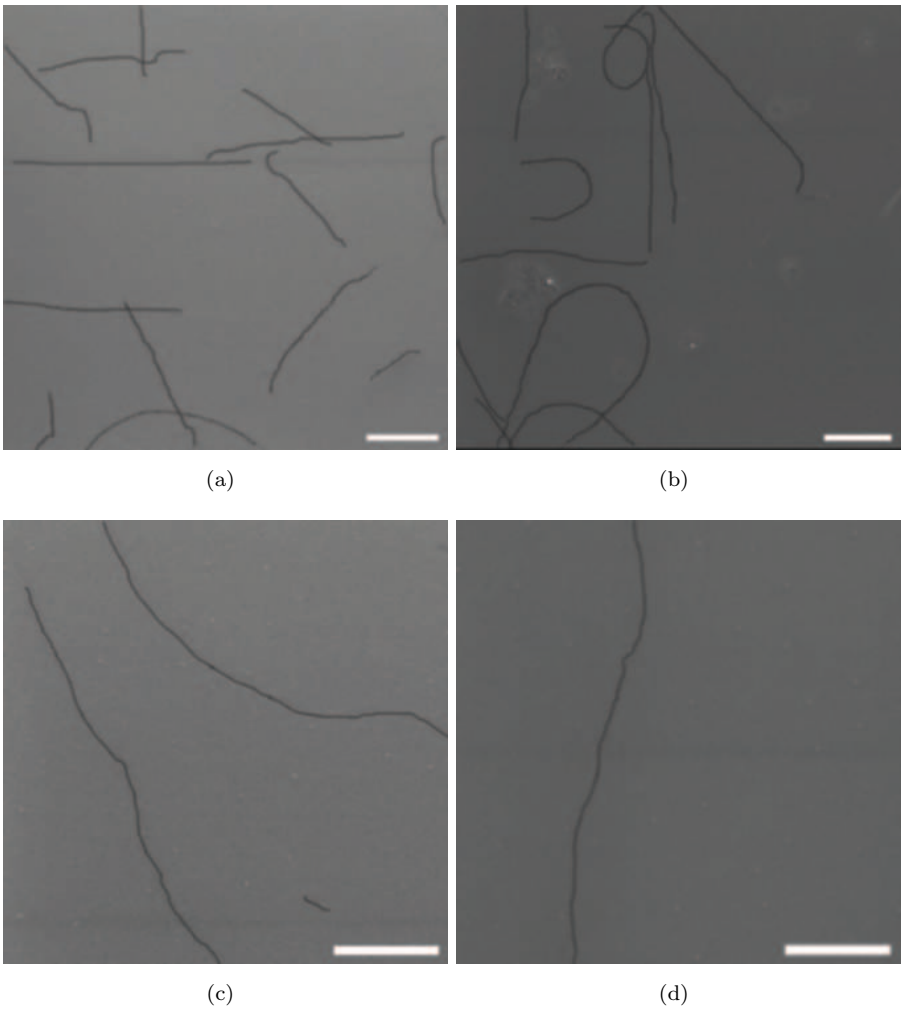

FIGURE 4.10: Scanning electron microscope image of CNT growth on a SiO_2 support from 1 mM Cu catalyst, at four different pretreatment temperatures; (a) 1000 °C, (b) 950 °C, (c) 900 °C and (d) 850 °C. The samples were pretreated in H_2 for 10 minutes. The subsequent CNT growth step was kept constant at at 850 °C in a mixture of H_2 and CH_4 (1 : 3 gas ratio) for 20 minutes. Scale bar corresponds to 500 nm. CNTs have been highlighted for clarity.

density of 0.3 ± 0.7 μm in length/μm^2 was found at the lowest pretreatment temperature, 850 °C. In these measurements, there is not a statistically significant change in CNT yield as pretreatment temperatures increase. However, one can infer that the uniformity of CNTs across the sample is improving with an increase in pretreatment temperature, suggesting that the H_2 pretreatment does play role in modifying the catalyst. The effect of pretreatment on catalyst morphology will be discussed in detail in Section 4.3.4.

As with the Au nanoparticles, in order to confirm that the CNT growth is catalysed by the Cu nanoparticles and not any systematic contaminant, a control sample was fabricated at the optimum growth condition. The control sample was subjected to the same deposition and cleaning process as the Cu nitrate samples, however no Au nanoparticles were deposited. This sample was pretreated at 1000 °C in H_2 for 10

minutes and exposed to the CNT growth step at 850 °C in a mixture of CH_4 and H_2 (3 : 1 ratio). No CNTs were found in this sample. Additionally, EDS analysis has been undertaken in all the sample regions which showed CNTs, and regions which showed contaminants were discarded from subsequent analysis.

4.3.4 Evolution of the Catalyst

The results presented in the previous section suggest that the H_2 pretreatment step has an effect on the yield of the process. The different CNT area densities observed for each pretreatment temperature, shown in Figure 4.10 are assumed to be due to a change in the nature of the catalyst during the pretreatment step. In order to understand the effect this has on the morphology of the catalyst, AFM characterisation of the 1 mM Cu nitrate catalyst samples have been undertaken for the range of pretreatment temperatures discussed in in Section 4.3.3.

From typical AFM images on samples after a pretreatment step at temperatures between 1000 and 850 °C, the mean density of particles has been determined. The initial particle density of 180 ± 27 (mean $\pm$ standard deviation) particles/μm^2 is reduced to 110 ± 16, 95 ± 13, 89 ± 15 and 81 ± 10 particles/μm^2 after pretreatment at 850 °C, 900 °C, 950 °C and 1000 °C respectively. Although not statistically significant, an increase in pretreatment temperature appears to result in an associated reduction in nanoparticle density. It is likely that the reduction in nanoparticle density is due to nanoparticle evaporation or ripening.

Figure 4.11(a)–(d) show the particle height distribution for samples pretreated in H_2 for 10 minutes at 1000 °C, 950 °C, 900 °C and 850 °C respectively. Each distribution has been fitted with a non-centred, normalised Gaussian. Figure 4.11(e) shows a normalised overlay of each fitted Gaussian curve for comparison. The particle height distribution for a sample pretreated at 1000 °C is shown in Figure 4.11(a). This distribution showed an excellent fit with a non-centred Gaussian and has a modal height of 2.8 nm with a standard deviation of 1.1 nm. After pretreatment at 950 °C (Figure 4.11(b)), the distribution has a modal height of 3.4 nm and a standard deviation of 1.2 nm. The particle height distribution for the sample pretreated at 900 °C is shown in Figure 4.11(c) and has a modal height of 4.6 nm and a standard deviation of 2.27 nm. Finally, after pretreatment at 850 °C (Figure 4.5(d)), the distribution has a modal height of 4.9 nm and a standard deviation of 2.52 nm. This information is summarised in Table 4.2.

This data shows that there is a decrease in the modal height of the particles as the pretreatment temperature increases. There is also a narrowing of the distribution as the pretreatment temperature increases, shown by the increasing standard deviations and Figure 4.11(e). As pretreatment temperatures increase, the distributions show a reduction in the number of large particles and a decrease in the mean particle size.

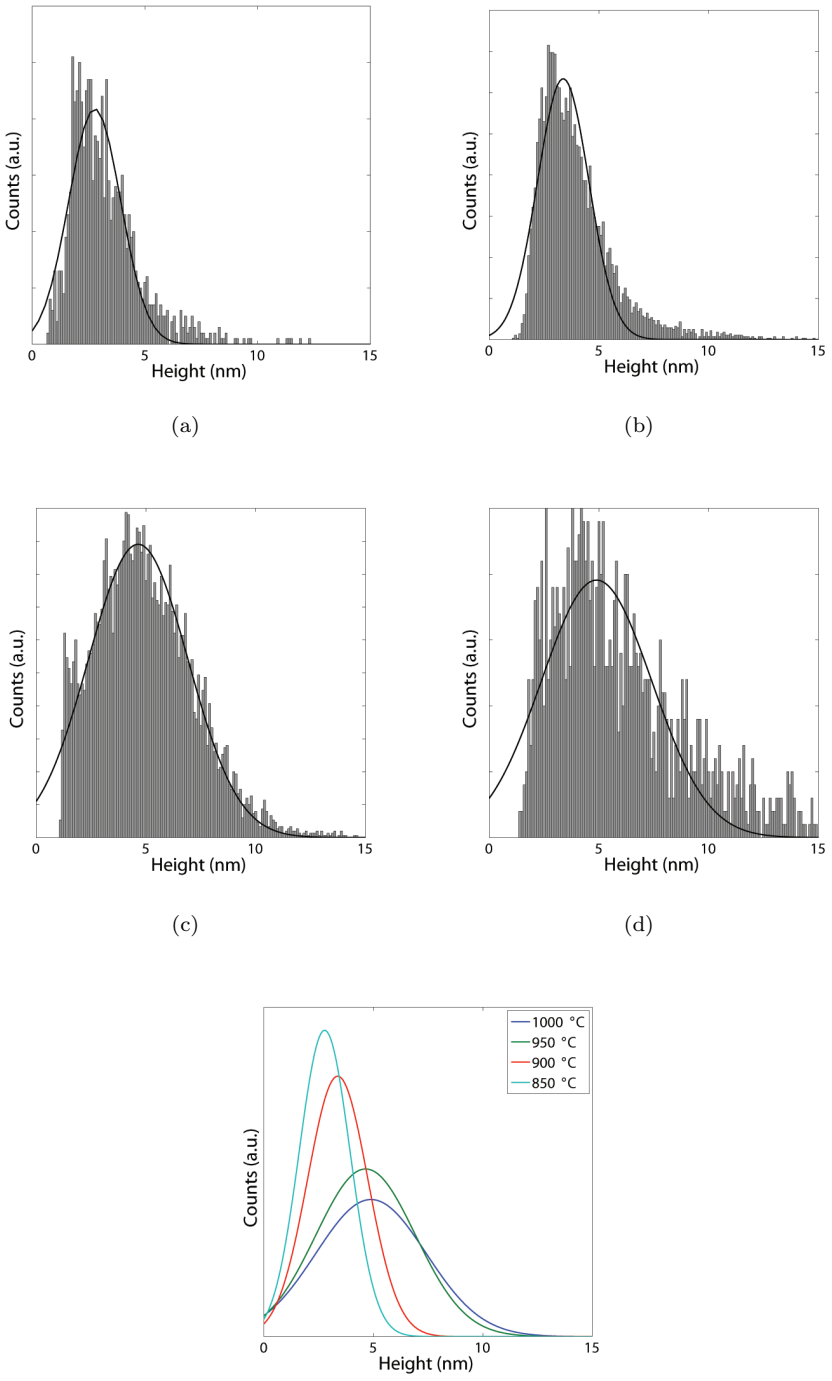

FIGURE 4.11: Particle size distribution for 1 *m*M Cu catalyst dispersed on a SiO_2 support after pretreatment in H_2 for 10 minutes at; (a) 1000 °C, (b) 950 °C, (c) 900 °C and (d) 850 °C. Particle size distributions have been fitted with a non-centred, normalised Gaussian. (e) Normalised particle size distribution Gaussian curve fits for each pretreatment temperature.

Pretreatment		Distribution Statistics		Nanoparticle Density
Temperature (°C)	Time (min)	Mode (nm)	R_2	(particles/μm^2)
1000	10	2.8 ± 1.15	0.951	81 ± 10
950	10	3.4 ± 1.17	0.967	89 ± 15
900	10	4.6 ± 2.27	0.953	95 ± 13
850	10	4.9 ± 2.52	0.890	110 ± 16

TABLE 4.2: Particle size distribution fit parameters and nanoparticle densities for 1 mM Cu catalyst dispersed on a SiO_2 support after pretreatment in H_2 at various temperatures.

The change in the particle size distributions shows a preferential reduction of larger nanoparticles, and an increase in the number of smaller nanoparticles. This behaviour suggests that breakup and redispersion of larger particles is taking place. This behaviour is in sharp contrast with that of the Au nanoparticles, seen in Section 4.2.4. However, the behaviour of supported particles is severely complicated by interactions with the substrate. Under certain conditions, the mobility of metal particles along the surface of a support has been frequently observed at elevated temperatures [341, 342]. The particle motion can result in coagulation of colliding nanoparticles (sintering). There are, however, circumstances under which the rupture of large nanoparticles into smaller ones can occur (redispersion) [343]. Redispersion happens in the case of a strong interaction between the catalyst and the support material, resulting in wetting along the support surface. In the case of the Cu nanoparticles and the support utilised, SiO_2, there is a weak interaction between the two materials due to a net repulsion arising from the Cu $4s$ electron and the empty 3s orbitals of Si (in a vacuum) [344]. This interaction is part of an overall trend toward weakening of the metal-oxide bond when passing from early to late transition metals [345]. However, it should be noted that the strength of the metal-support interaction can be altered by the gas environment, and it may be possible that an H_2 environment increases the strength of this interaction. A more likely possibility, however, is that the H_2 pretreatment at higher temperatures leads to a more complete reduction of the CuO formed during the nitrate reduction anneal in air, resulting in an overall reduction in nanoparticle size. Indeed, the particles are thought to be composed of two phases prior to H_2 pretreatment, an oxidised free surface and a metal core.

The results presented in this section demonstrate that the size of the Cu nanoparticle catalyst after pretreatment is within the possible range to seed CNT growth. There was a significantly higher CNT yield in samples pretreated at 1000 and 950 °C than those pretreated at lower temperatures. The particle size distributions showed that there was an increase in the proportion of nanoparticles in the range of $1-5$ nm, which is considered optimum for CNT synthesis, in the samples pretreated at higher temperatures. Although there was a small reduction in nanoparticle density, there were more nanoparticles in

the desired range in the higher pretreatment temperature samples. Another possibility is that pretreatment at higher temperatures were more effective at removing residual contaminants and reducing the nanoparticles to a metallic state, which is also thought to increase the yield of the process.

4.3.5 Raman Spectroscopy

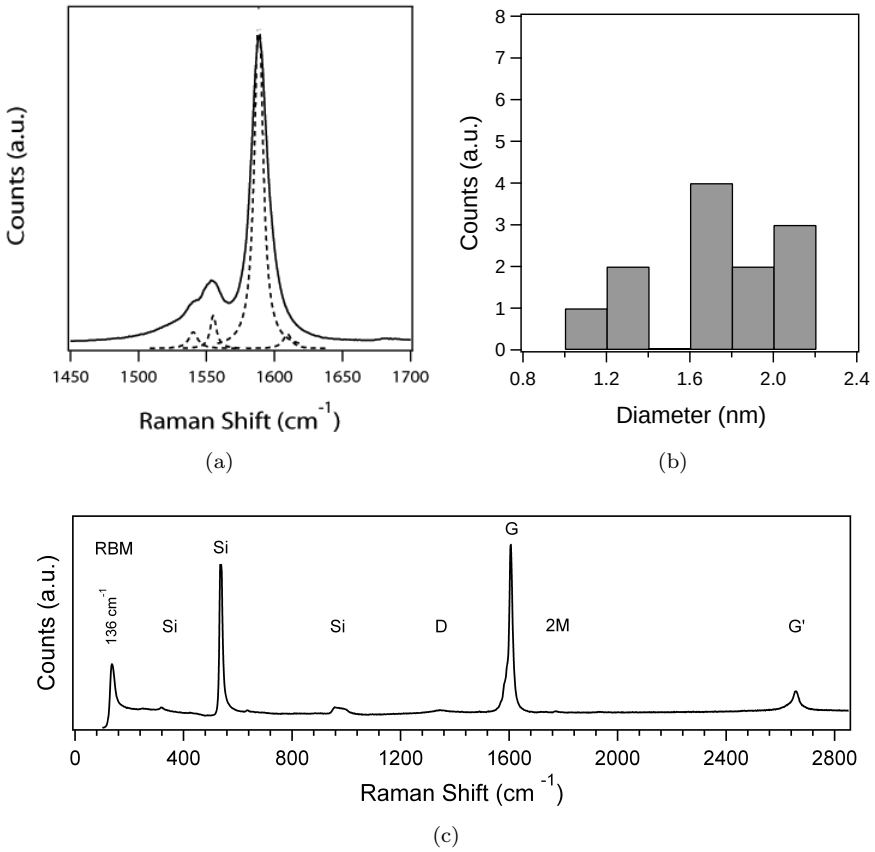

FIGURE 4.12: Raman spectra for the carbon nanotubes synthesized using 1 mM diluted Cu catalyst dispersed on a SiO_2 support after pretreatment in H_2 for 10 minutes at 1000 °C, followed by a growth step at 850 °C in a mixture of H_2 and CH_4 (1 : 3 gas ratio) for 20 minutes. (a) Typical G-band characteristic, fitted with four Lorentzian curves. (b) Histogram of the SWNT diameters obtained via RBM. (c) Typical Raman spectra of the synthesized nanotubes.

In Figure 4.12, representative Raman spectra are shown from samples synthesized using a 1 mM Cu catalyst dispersed on a SiO_2 support. The measured CNTs were grown using a pretreatment in H_2 for 10 minutes at 1000 °C, followed by a growth step at 850 °C in a mixture of H_2 and CH_4 (1 : 3 gas ratio) for 20 minutes. The Raman measurements were undertaken utilising a Renishaw in-Via system, as in Section 4.2.5. It should be noted that the frequency cut-off was a shift of approximately 110 cm^{-1}, as a result SWNTs with diameters larger than 2.3 nm were not detected.

The Raman spectra obtained from areas of relatively high CNT area density typically exhibited an asymmetric double peak at approximately 1590 cm^{-1} (Figure 4.12(a)). This double peak can be attributed to the Raman-allowed tangential mode of CNTs, G-band. In the representative spectrum shown in Figure 4.12(a), this feature could be fitted with four Lorentzian oscillators located at 1539, 1555, 1589 and 1608 cm^{-1}. Due to the lineshape and location of the four Lorentzian components of this feature, it is believed to be characteristic of a semiconducting tube. Indeed, assuming that the signal originates from a single, isolated nanotube, we can determine the signal to originate from a semiconducting tube of 1.15 nm diameter (using the relation $\Delta\omega_G = \omega_{G^+} - \omega_{G^-}$, as described in Section 2.4.5).

Figure 4.12(c) shows a typical Raman spectrum obtained from the Cu catalyst sample. This spectrum shows five characteristic features of CNTs; the RBM, D-band, G-band, 2M band and G' mode. The G-band feature in this spectrum is similar to that shown in in Figure 4.12(a). In general, the measured spectra showed a good intensity ratio between the disorder induced D-band and the Raman allowed G-band ($I_D/I_G = 0.002$) indicating that the nanotubes are of a high quality in terms of structure and graphitisation. This spectrum shows an overtone of the D-band, the G' mode at approximately 2650 cm^{-1}. Additionally, there is a combination mode present, the 2M mode which results from the G-band and the RBM. Finally, in many cases spectra exhibiting peaks in the region between 110 to 250 cm^{-1} were obtained. These peaks are attributed to the RBM feature of SWNTs [125] and appear only at points from the sample from which a strong G-band feature is obtained. Therefore, it can be concluded that this spectral feature is indicative of the presence of SWNTs in the sample. In the typical spectrum shown in Figure 4.12(c), there is a low-frequency peak at 136 cm^{-1} which is attributed to a RBM. This breathing mode corresponds to a metallic nanotube of 1.86 nm diameter.

A histogram of the SWNT diameters observed in the measurements via the RBM spectral feature is shown in Figure 4.12(b). It should be noted that since the measurements were only undertaken using a 632.8 nm He-Ne excitation these results do not provide a full diameter characterisation of the sample. This histogram indicates that the majority of the SWNTs observed had a large diameter. Although no strong conclusions can be drawn from this fact, this result correlates with the particle size distributions shown in Figure 4.11(a), which showed a nanoparticle modal size of 2.8 ± 1.15 nm.

Interestingly, Zhou et al. [4] reported a higher ratio of metallic SWNTs in Cu catalysed samples, determined from Raman analysis. This characteristic was not detected in our experiments. Simulations by Yazyev and Pasquarello [270] also found that the nucleation of graphitic fragments bound to the Cu nanoparticle catalyst favours the formation of metallic nanotubes. In addition, the low melting point and low carbon diffusion barriers suggest that CVD synthesis could take place at much lower temperatures. In these conditions, the chirality preference would be further enhanced.

4.4 Silver Nanoparticle Catalysts

Metal nanoparticles have become a subject of intense interest in various fields of chemistry and physics during past decades. The interest in these particles stems from their unique optical, electronic, and catalytic properties [346], which are different from their bulk counterparts and hence may lead to various novel applications. Ag nanoparticles, in particular, have been used in sensor [347], catalysts [348], nanoelectronic devices [349], biochemical tagging reagents [350] and optical switches [351].

There are few reports in the literature of Ag nanoparticles catalysing SWNT growth. The first demonstration of CNT growth from Ag nanoparticles by Takagi et al. [3] involved the decomposition of ethanol vapour over nanoparticles supported on SiO_2. In this experiment, nanoparticles were formed by annealing an ultra-thin metal film in air at $800 - 900$ °C. To the authors knowledge, the only other report of Ag nanoparticles used to synthesize CNTs was by Kang et al. [277]. In this paper, MWNTs were formed by directly reducing C_2Cl_4 with Na at 140 °C in the presence of Ag nanocrystals. In this section, the synthesis of CNTs using Ag nanoparticles will be explored.

4.4.1 Catalyst Characterisation

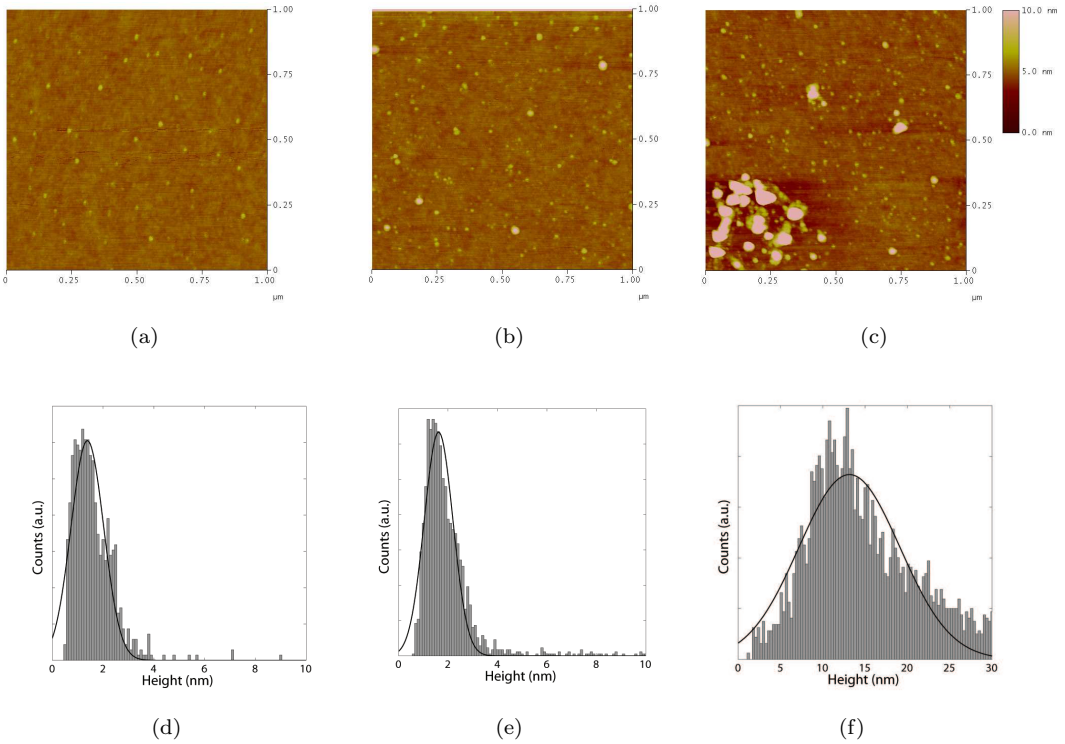

FIGURE 4.13: Atomic force microscope topography image of Ag catalyst dispersed on a SiO_2 support at three dilutions; (a) 1 mM, (b) 2 mM and (c) 4 mM. Corresponding particle size distributions are shown in (c), (d) and (e), respectively. Particle size distributions have been fitted with a non-centred, normalised Gaussian.

To determine the particle size distributions of the Ag nanoparticles, AFM analysis was performed after subjecting the dip coated samples to a O_2 plasma clean and an anneal at 400 °C in air. Figure 4.13(a)–(c) show typical AFM topography images for the 1 mM, 2 mM and 4 mM Ag nitrate solution samples, respectively. All samples showed a reasonable density of local maxima in the topography scan, and each peak is believed to be an individual particle. Figure 4.13(a) (1 mM Ag nitrate solution) showed the lowest density of nanoparticles, 70 ± 18 particles/μm^2. The 2 mM Ag nitrate solution, shown in Figure 4.13(b), showed a density of 166 ± 40 particles/μm^2. The highest concentration, 4 mM Ag nitrate solution, showed the highest density of nanoparticles, as expected. The measurements indicate a a density of 798 ± 167 particles/μm^2. The distribution of the Ag nanoparticles on the substrate is very homogeneous which indicates that dip coating is a suitable method for deposition of the catalyst on the substrate. Additionally, the density of nanoparticles on the substrate has increased as the concentration of the metal-nitrate solution increased.

Figure 4.13(d) shows the particle height distribution for several images taken from the 1 mM Ag nitrate solution sample. This distribution has been fitted with a normalised, non-centred Gaussian, which shows a modal height of 1.4 nm with a standard deviation of 0.64 nm. This curve showed a good fit, with a minimal variance ($R_2 = 0.953$, using non-linear regression). Figure 4.13(e) shows the particle height distribution for several images taken from the 2 mM Ag nitrate solution sample, also fitted with a normalised, non-centred Gaussian ($R_2 = 0.966$, using non-linear regression). This distribution shows a modal height of 1.6 nm and a standard deviation of 0.58 nm. Finally, the particle height distribution for the 4 mM Ag nitrate solution sample is shown in Figure 4.13(f), also also fitted with a normalised, non-centred Gaussian ($R_2 = 0.759$, using non-linear regression). This distribution shows a modal height of 13.2 nm and a standard deviation of 5.9 nm. As was expected, the modal height of the nanoparticles increased with increasing concentration. In addition, the standard deviation of the distributions increased monotonically with concentration indicating a larger range of nanoparticle sizes for the higher concentration samples.

4.4.2 Effect of Catalyst Concentration

Figure 4.14 shows SEM images of CNTs synthesized from the Ag catalyst solution dispersed on a SiO_2 support for each dilution. The samples subjected to a H_2 pretreatment at 1000 °C for 10 minutes, followed by a CNT growth step for 20 minutes at 850 °C in a mixture of H_2 and CH_4 (1 : 3 gas ratio). Figure 4.14(a)-(c) show representative SEM images of the 1, 2 and 4 mM Ag nitrate solution samples after the CNT growth step. In these samples no CNTs or oxide nanowires were detected. There were very few structures on the sample surfaces, and the only features which could be identified were catalyst islands, formed by agglomeration.

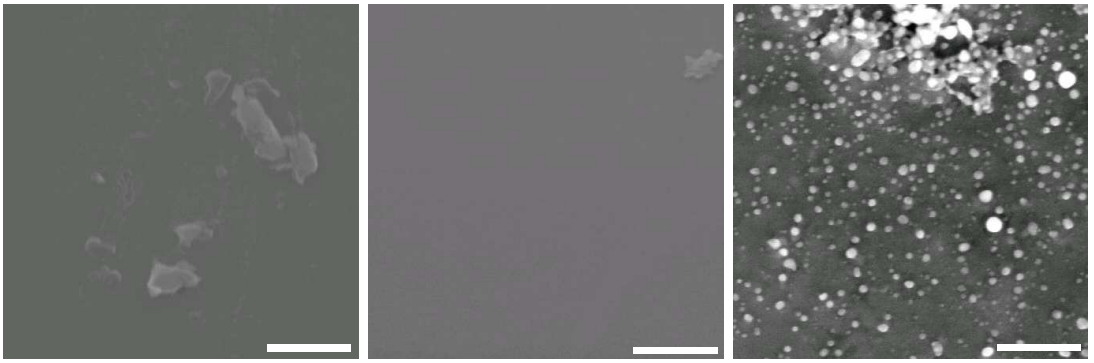

(a) (b) (c)

FIGURE 4.14: Scanning electron microscope image of CNTs synthesized from Ag catalyst dispersed on a SiO_2 support at three dilutions; (a) 1 mM, (b) 2 mM and (c) 4 mM. Scale bar corresponds to 500 nm. CNTs were grown at the optimum growth condition, H_2 pretreatment at 1000 °C for 10 minutes, followed by the CNT growth step for 20 minutes at 850 °C in a mixture of H_2 and CH_4 (1 : 3 gas ratio).

4.4.3 Effect of Catalyst Pretreatment

In order to ascertain a suitable growth condition, 2 mM Ag nitrate samples were pretreated in H_2 at a range of temperatures followed by a CNT growth step at 850 °C. These growth conditions were selected as similar experiments had resulted in CNTs. The 2 mM Ag catalyst was chosen as the initial nanoparticle density was similar to the optimum conditions for the Cu nanoparticle sample. Additionally, the particle size distribution for this catalyst was believed to be optimal for CNT synthesis.

Figure 4.15 shows SEM images of the 2 mM Ag catalyst on a SiO_2 support after a 850 °C growth step following a catalyst pretreatment anneal in H_2 at various temperatures for 10 minutes. All samples were subjected to the nitrate reduction anneal in air prior to the H_2 pretreatment. The pretreatment anneal temperatures shown in Figure 4.15(a)-(d) are 1000, 950, 900 and 850 °C, respectively. No carbon nanotubes were detected in any of the samples, regardless of pretreatment temperature.

4.4.4 Evolution of the Catalyst

In order to determine the morphology of the catalyst after pretreatment, AFM characterisation of the 2 mM Ag nitrate catalyst has been undertaken for the range of pretreatment temperatures discussed in Section 4.4.3. These measurement are expected to provide some insight as to the reasons for the lack of CNTs shown in these samples.

From typical AFM images on samples after a pretreatment step at temperatures between 1000 and 850 °C, the mean density of particles has been determined. The initial particle density of 166 ± 40 particles/μm^2 (mean $\pm$ standard deviation) is reduced to 119 ± 33, 53 ± 25, 33 ± 9 and 23 ± 5 particles/μm^2 after pretreatment at 850 °C, 900 °C, 950 °C and

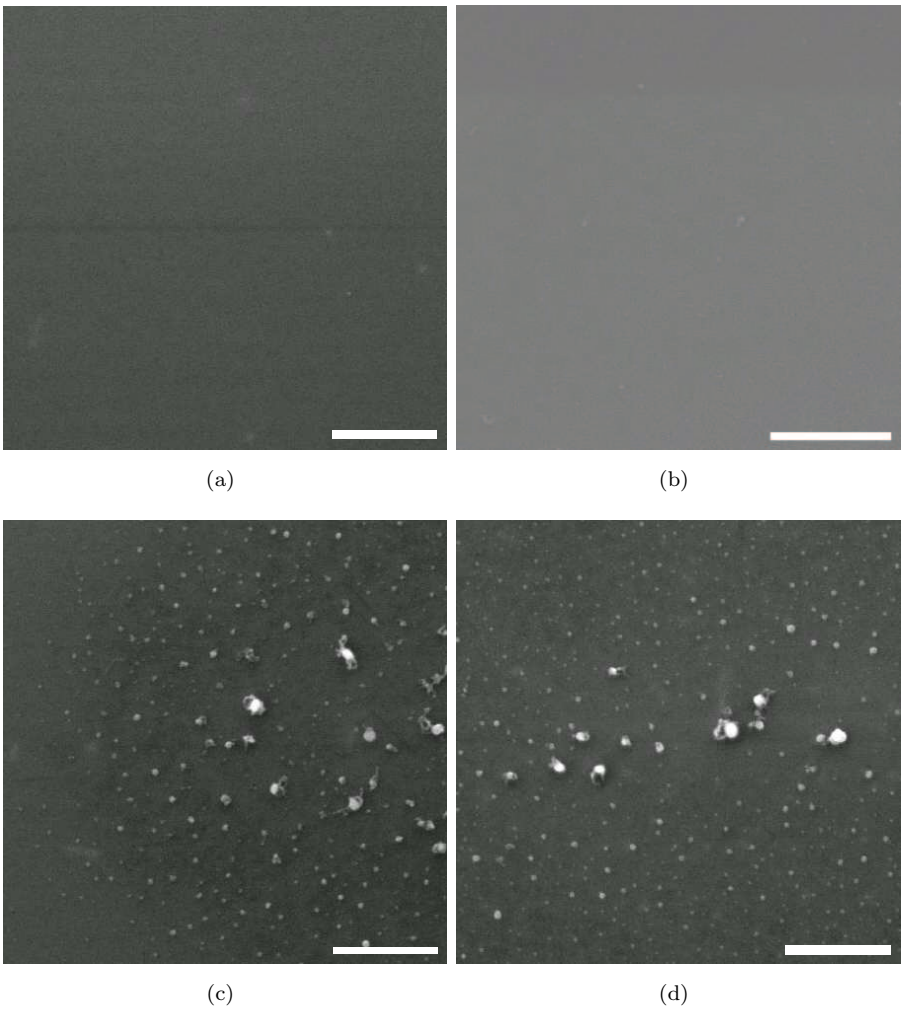

FIGURE 4.15: Scanning electron microscope image of CNT growth on a SiO_2 support from 2 *m*M Ag catalyst, at four different pretreatment temperatures; (a) 1000 °C, (b) 950 °C, (c) 900 °C and (d) 850 °C. The samples were pretreated in H_2 for 10 minutes. The subsequent CNT growth step was kept constant at at 850 °C in a mixture of H_2 and CH_4 (1 : 3 gas ratio) for 20 minutes. Scale bar corresponds to 500 nm.

1000 °C respectively. It is evident that with an increase in pretreatment temperature there is an associated reduction in nanoparticle density. It is likely that the reduction in nanoparticle density is due to nanoparticle evaporation or ripening. From these results we can deduce that the density of nanoparticles is drastically reduced, which may account for the lack of CNTs shown in these samples.

Figure 4.16(a)–(d) show the particle height distribution for samples pretreated in H_2 for 10 minutes at 1000 °C, 950 °C, 900 °C and 850 °C respectively. Each distribution has been fitted with a non-centred, normalised Gaussian. All distributions were bimodal and could be fit by a sum of two Gaussian curves. All distributions showed a close fit, with a lowest value of $R_2 = 0.897$ by non-linear regression for the sample pretreated at 1000 °C. Figure 4.16(e) shows a normalised overlay of each fitted Gaussian curve for comparison. The particle height distribution for a sample pretreated at 1000 °C is

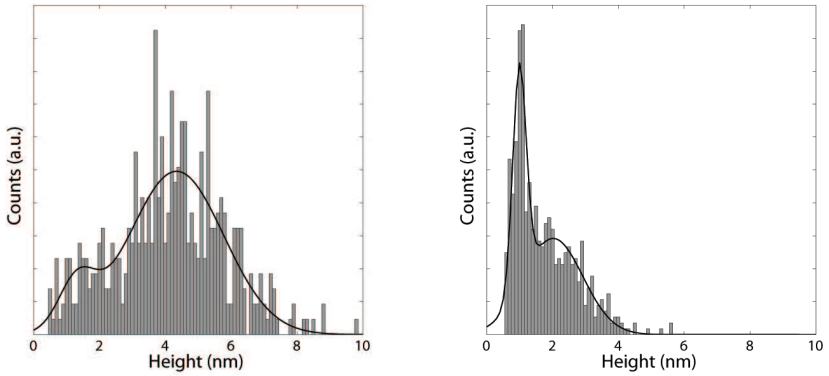

(a)

(b)

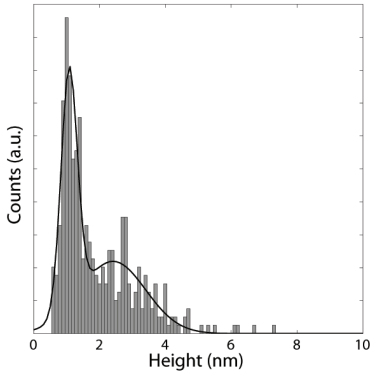

(c)

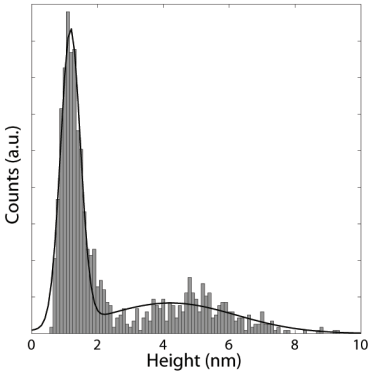

(d)

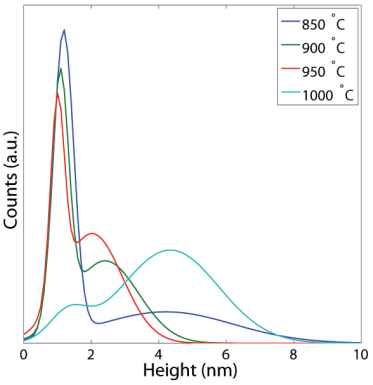

(e)

FIGURE 4.16: Particle size distribution for 2 *m*M Ag catalyst dispersed on a SiO_2 support after pretreatment in H_2 for 10 minutes at; (a) 1000 °C, (b) 950 °C, (c) 900 °C and (d) 850 °C. Particle size distributions have been fitted with a non-centred, normalised Gaussian. (e) Normalised particle size distribution Gaussian curve fits for each pretreatment temperature.

Pretreatment		Distribution Statistics			Nanoparticle Density
Temperature (°C)	Time (min)	Mode 1 (nm)	Mode 2 (nm)	R_2	(particles/μm^2)
1000	10	1.3 ± 0.55	4.3 ± 1.43	0.897	23 ± 5
950	10	1.1 ± 0.20	2.1 ± 0.95	0.964	33 ± 9
900	10	1.0 ± 0.24	2.4 ± 0.89	0.956	53 ± 25
850	10	1.1 ± 0.29	4.2 ± 1.95	0.980	119 ± 33

TABLE 4.3: Particle size distribution fit parameters and nanoparticle densities for 2 mM Ag catalyst dispersed on a SiO_2 support after pretreatment in H_2 at various temperatures.

shown in Figure 4.16(a). This distribution showed modal peaks at 1.3 ± 0.55 nm and 4.3 ± 1.43 nm. After pretreatment at 950 °C (Figure 4.16(b)), the distribution has modal peaks at 1.1 ± 0.2 nm and 2.1 ± 0.95 nm. The particle height distribution for the sample pretreated at 900 °C is shown in Figure 4.16(c) and has modal peaks at 1.0 ± 0.24 nm and 2.4 ± 0.89 nm. Finally, after pretreatment at 850 °C (Figure 4.16(d)), the distribution has modal peaks at 1.1 ± 0.29 nm and 4.2 ± 1.95 nm. This information is summarised in Table 4.3.

This data shows that there is a change in the distributions as pretreatment temperatures increase. There is a reduction in the magnitude of the smaller modal peak as pretreatment temperatures increase. This behaviour suggests the preferential reduction in the smaller nanoparticles. Additionally, there is an increase in mean particle size as pretreatment temperature increase. Excluding the particle size for samples distribution for pretreatment at 850 °, there is also a broadening of the second mode associated with an increase in pretreatment temperature. These characteristics also suggest a mechanism of phase coarsening.

The results presented in this section demonstrate that the size of the Ag nanoparticle catalyst after pretreatment is within the possible range to seed CNT growth ($1 - 5$ nm). However, the drastically reduced nanoparticle density would account for the inability to synthesize CNTs from this catalyst. This drastic reduction in nanoparticle density could be explained by a combination of evaporation and ripening of the Ag nanoparticles.

4.5 Discussion

Typically, the vapour-liquid-solid mechanism is used to explain the mechanism of carbon uptake, supersaturation and precipitation in the catalyst. However, owing to the low solubity of carbon in bulk Au, this must be reviewed for the synthesis of CNTs from Au nanoparticles. By studying the formation of carbon nanowires (CNWs) from Au catalysts, Takagi et al. [352] inferred that nanosized Au shows some carbon solubility and

that Au can form Au-C nanoalloy droplets and produce CNWs by the VLS mechanism. When the catalyst size approaches ≤ 5 nm, the carbon solubility and the nanowire nucleation energy increases dramatically, leading to a structural change in the synthesized carbon products from CNW to SWNT. This finding is in agreement with simulations by Yazyev and Pasquarello [270], who determined that monatomic carbon in Au can diffuse uniformly across the nanoparticle, even at low temperatures. However, it should be noted that no direct evidence of this effect was demonstrated and that similar studies [7] could not determine whether carbon atoms were supplied to the nanotube from the Au-C liquid phase or through surface diffusion.

It has been reported that the carbon solubility in a metallic catalyst should be in the range of $0.5 - 1.5$ wt% carbon in order to efficiently form CNTs [274]. Therefore, it is surprising that Cu can be catalytically active, as its carbon solubility is extremely low. However, Zhou et al. [4] argue that the low solubility of carbon in Cu results in an increased rate of carbon precipitation. Additionally, Cu has a lower catalytic ability for the dissociation of alkanes than traditional catalysts, resulting in a slower supply of carbon in the CVD process. Thus, matching the supply of carbon to the formation rate of nanotubes will result in the production of high quality SWNTs [183]. This argument is supported by Yazyev and Pasquarello [270], who state that the stability and the diffusion barriers of diatomic carbon on Cu allow one to restrict the diffusion pathways to the nanoparticle surface by choosing an appropriate gas-phase carbon source, resulting in the preferred formation of high quality SWNTs.

Metal catalysts with no *d*-vacancies, such as Cu and Au, do not offer sites to dissolve carbon, such that neither saturation nor precipitation is possible. However, despite the low carbon solubility, these catalysts have demonstrated an ability to catalyse CNT formation. Additionally, catalysts with a high melting point such as Al_2O_3 or ZrO_2 are thought to be solid at CNT synthesis temperatures. However, if nanoparticles of these metals are small enough (≤ 5 nm), the increasing fraction of low-coordinated atoms may lead to surface saturation followed by carbon precipitation, as reported by Takagi et al. [3]. Considering that carbon penetration inside small nanoparticles is unlikely [293], the growth of CNTs is most likely a process primarily controlled by surface diffusion [294, 295]. Indeed, it is believed by several groups that the rate-limiting factor in CNT synthesis is the surface diffusion of carbon across the catalyst [269]. Additionally, this factor could explain the influence of the carbon source on the ability of a catalyst to synthesize CNTs. Yazyev and Pasquarello [270] reported different activation energies for the surface diffusion of C dimers and adatoms on noble metal catalysts, and argued that appropriate choice of a diatomic or monatomic carbon gas-phase source could significantly accelerate diffusion.

The successful CNT growths from Au and Cu catalysts imply that hydrocarbon dissociation ability is not essential in a catalyst. It should be noted that the catalytic behaviour of Cu and Au may be explained by electron donation to the support [299],

creating *d*-vacancies which may cause hydrocarbon dissociation. However, Reilly and Whitten [176] argue that a more likely scenario is that a free radical condensate (FRC) provides carbon species through a leaving group, such as hydrogen (or oxygen). FRCs naturally form during hydrocarbon pyrolysis by the breaking of carbon-hydrogen or carbon-carbon bonds with each fragment keeping one electron to form two radicals. The presence of a radical in a hydrocarbon molecule permits rapid rearrangement of carbon bonds. In this case, the role of the catalyst particle is to provide an interface where carbon rearrangement can occur and act as a template for growth.

4.6 Conclusions

In this chapter, SWNT growth catalysed by noble metal nanoparticles has been studied. Au and Cu nanoparticles have been shown to be adequate catalysts for CNT growth and extensive characterisation is presented of each step of the growth process. The results presented show that the commonly utilised model of carbon filament growth is inadequate to describe SWNT growth from non traditional catalysts. A new interpretation of the role of the catalyst was presented where only a nanoscale curvature is necessary to grow CNTs. A mechanism for SWNT growth was suggested where the surface saturation and diffusion of C on the catalyst nanoparticle lead to the formation of a graphitic cap followed by the further incorporation of C into a growing nanotube.

Au nanoparticles, synthesized by *Nanoprobes Inc*, were used as a catalyst. Three dilutions were prepared and deposited on a SiO_2 support by spin coating. This produced samples with nanoparticle densities of 2500 ± 790, 1100 ± 400 and 210 ± 96 particles/μm^2 for the 0.03 mM, 0.006 mM and 0.003 mM dilutions, respectively. The deposited nanoparticles showed a narrow particle size distribution, with a single centred at 1.4 ± 0.2 nm. This closely matched the supplier specifications. However, at the highest dilution, AFM analysis showed that the nanoparticles had a modal height of 0.7 nm. This is most likely due to the shape of the scanning probe tip, the nanoparticles may not have been sufficiently dispersed to allow for an accurate measurement of nanoparticle height.

The results indicate that SWNT growth is only possible on a silicon dioxide support using the 0.03 mM dilution. This is due to a drastic loss of nanoparticles upon anneal, most likely due to evaporation. The 0.03 mM dilution showed a reduction from 2500 ± 790 to 213 ± 170 particles/μm^2 upon pretreatment at the optimum condition. In contrast, the lowest dilution (0.003 mM) showed a reduction from 210 ± 96 to 7 ± 4 particles/μm^2 which is most likely too low a density to support CNT growth. H_2 pretreatment was shown to be crucial for the growth of SWNT, no CNTs were found in samples which had not been pretreated. SEM analyses indicated that CNTs were possible after pretreatment in H_2 at a range of temperatures between $900 - 1050$ °C. The optimum pretreatment condition was determined to be a 10 minute anneal in H_2 at 1000 °C. It is believed

that the pretreatment step is necessary to generate contaminant free nanoparticles, by reducing the residual shell of gold oxides or gold chlorides. However, there is also a change in morphology upon pretreatment. Upon anneal there is a broadening of the nanoparticle size distribution and an increase in the modal height, attributed to phase coarsening. Interestingly, at the lowest pretreatment temperature (850 °C), the modal nanoparticle height is 0.9 nm, which is significantly lower than the initial value determined by AFM. This suggests that there must be a competing loss mechanism occurring to account for the reduction of nanoparticle size from the initial, specified size. This is thought to be nanoparticle evaporation, or diffusion into the substrate due to the temperatures involved. The synthesized CNTs were found to be of a good quality in terms of graphitisation and structure from Raman analysis. The presence of the RBM mode also indicates that there are SWNT present in the sample after growth.

Cu nanoparticles were formed by the thermal decomposition of copper nitrate in air at 400 °C. Three concentrations of metal nitrate solution were prepared, and CNT growth was shown to be possible from Cu nanoparticles prepared from 1 mM and 2 mM dilutions. As was the case with the Au nanoparticles, CNT growth was only possible after pretreatment in H_2 at temperatures between $850 - 1000$ °C. AFM analysis after pretreatment showed a change in morphology upon anneal. The 1 mM Cu catalyst showed a reduction from an initial nanoparticle density of 180 ± 27 particles/μm^2 to 81 ± 10 particles/μm^2 after pretreatment at 1000 °C in H_2 for 10 minutes. The particle size distribution also showed significant changes, from a bimodal distribution to a a single mode of 2.8 ± 1.15 nm in height after anneal at 1000 °C. From analysis of the uniformity of the samples, it was observed that the yield improves with an increase in pretreatment temperature. This is due to an increase in the proportion of particles in the range of $1 - 5$ nm, which are considered optimum for CNT synthesis. This suggests that the H_2 pretreatment is key to the formation of CNTs using a Cu catalyst. The synthesized CNTs were found to be of a good quality in terms of graphitisation and structure from Raman analysis. The presence of the RBM mode also indicates that there are SWNT present in the sample after growth.

Finally, Ag nanoparticles were shown to be unable to catalyse CNT formation. Three concentrations of metal nitrate solution were prepared, 1, 2, and 4 mM. Experiments on all three dilutions showed a drastic loss of nanoparticles upon heating. Upon pretreatment, the initial nanoparticle density of 166 ± 40 particles/μm^2 for the 2 mM Ag catalyst is reduced to 23 ± 5 particles/μm^2 upon pretreatment at 1000 °C. This is most likely too low a density to support CNT growth. The drastic reduction in nanoparticle density of this catalyst compared with Cu and Au is most likely due to the lower melting point of Ag compared with Cu and Au. Additionally, there is a reduction in the proportion of smaller nanoparticles in the range of $1 - 5$ nm believed to be due to evaporation.

Chapter 5

Growth of SWNTs Using Ge Nanocrystals Formed by Implantation

Results presented in the previous chapter demonstrate that hydrocarbon dissociation and the ability to catalyse the formation of graphite may not be essential in a catalyst to synthesize CNTs. This leads to a new interpretation of the role of the catalyst particle in CNT growth, where only a nanoscale curvature is needed to act as a template for nanotube formation. This assertion is supported by the reports of CNT formation from semiconductor nanoparticles [10, 11, 13], from which no catalytic functions were expected.

The first reports of CNT growth from semiconducting catalysts were by Uchino et al. [10]. In this experiment, carbon-doped SiGe islands deposited by CVD on Si, form nanoscale clusters through segregation of Ge during an oxidation step which act as seeds for SWNT growth. These results were supported by the work of Takagi et al. [11], who showed that CNT growth from Ge, Si and SiC nanoparticles was possible. More recently, there have been various reports of CNT growth from SiO_2 nanoparticles [282], which are thought to be promising catalysts owing to their ability to maintain a narrow size distribution at CNT growth temperatures.

In this section, research on the use of germanium for carbon nanotube growth is presented. This chapter presents a novel complementary metal oxide semiconductor compatible method for the chemical vapour deposition of single-walled carbon nanotubes. The method uses Ge implantation into a SiO_2 layer to create Ge nanocrystals, which are then used to create SWNTs. The results of atomic force microscopy and scanning electron microscopy analyses indicate that Ge implantation provides good control of particle size and delivers a well-controlled SWNT growth process. The SWNT area density of 4.1 ± 1.2 μm in lenght/μm^2 obtained from the Ge nanocrystals is comparable to that

obtained from metal-catalyst-based methods used to fabricate SWNT field-effect transistors. A carbon implantation after Ge nanocrystal formation significantly enhances the process operating window for the growth of the SWNTs and increases the area density.

5.1 Experimental Details

Ge nanocrystals were formed by implanting Ge into a SiO_2 layer and annealing in a N_2 atmosphere [353]. Silicon 4 inch wafers (p-type, $< 001 >$, $17 - 33\ \Omega\cdot$ cm) were employed as a starting material. A 30 nm thick oxide layer was thermally grown after a fuming nitric acid clean. Subsequently, the oxide layers were implanted with Ge at a dose of 5×10^{15} cm^{-2} and an energy of 20 keV. Then the wafers were annealed in N_2 atmosphere at either 600, 800 or 1000 °C for 40 minuted to create Ge nanocrystals of different sizes. This step was followed by a HF vapour etch to remove the SiO_2 and expose the Ge nanocrystals formed during the N_2 anneal. Selected wafers were implanted with carbon at a dose of 3×10^{16} cm^{-2} and a energy of 30 keV after HF vapour etching because earlier experiments [10] showed that a carbon implantation was necessary for the growth of CNTs from SiGe islands. All substrates were prepared under clean room conditions.

CNTs were grown using a two step-growth process. The first step was a H_2 pretreatment anneal and the second step was CNT growth by thermal CVD perfomed in a hot-wall reactor at atmospheric pressure. The wafers were cut into 10×10 mm pieces to suit a one-inch diameter furnace tube. The CNT growth step was carried out using a mixture of methane (1000 sccm) and hydrogen (300 sccm) immediately following the H_2 (1000 sccm) pretreatment step. The pretreatment was performed at a temperature between 850 and 1100 °C for either 5 or 10 minutes. The growth step was carried out a temperature between 850 and 1000 °C for 20 minutes. A quartz furnace tube was used exclusively for this work to avoid metal contamination.

The Ge nanocrystals were characterised using a Veeco Multi-Mode atomic force microscope, using super sharp Si cantilevers (typical tip radius of 2 nm). Particle height distributions for each sample were determined using a minimum of ten 1 μm^2 AFM images utilising the Veeco Nanoscope software package. Images were first flattened using a three point levelling technique, and a threshold height of 0.5 nm was set in the particle detection software. The synthesized CNTs were observed by field-emission scanning electron microscope (JEOL 6500F) and transmission electron microscope (JEOL 3050 and JEOL 4000HR). Transmission electron microscopy sample preparation consisted of scraping the sample surface with a surgical blade and transference onto a carbon-coated Cu grid. The chemical compositions of SEM samples were analysed by energy-dispersive X-ray spectroscopy (Oxford Instruments INCA Microanalysis System). The area densities of CNTs were evaluated using FE-SEM images using ImageJ to determine the total contour length of CNTs [315]. For quantitative analysis, several images taken from the

same sample were used, with overlapping regions being discarded. Raman spectra were obtained using a Renishaw micro-Raman system with He-Ne (632.8 nm) laser excitation with a power of 12 mW and a spot size of 1 μm.

5.2 Nanocrystal Characterisation

To characterise the fabricated Ge nanocrystals, scanning electron microscopy, atomic force microscopy and photoluminescence spectroscopy were employed. Additionally, the repeatability of the process was also investigated as a second process batch was commissioned.

5.2.1 Nanocrystal Morphology

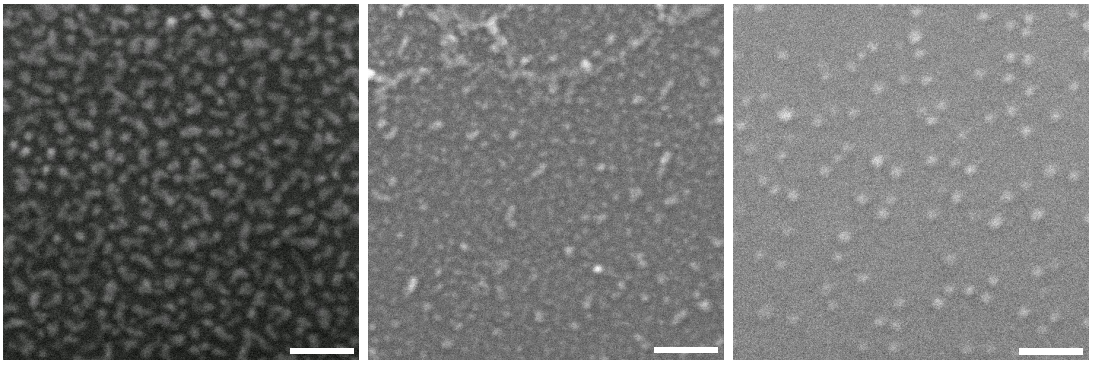

(a) (b) (c)

FIGURE 5.1: Scanning electron microscope image of Ge nanocrystals produced by ion implantation (20 keV, 5×10^{15} cm^{-2}) into a 30 nm SiO_2 layer and postanneal at (a) 600 °C, (b) 800 °C and (c) 1000 °C followed by a HF vapour etch to expose the nanocrystals. Scale bar corresponds to 100 nm.

Figure 5.1 show field emission scanning electron microscope images of Ge nanocrystals produced by ion implantation and subsequent annealing at various temperatures. The FE-SEM image for the nanocrystals formed by a N_2 anneal at 600 °C (Figure 5.1(a)) shows a high density of Ge nanocrystals of different sizes. The FE-SEM images for the nanocrystals formed by N_2 anneals at 800 °C (Figure 5.1(b)) and 1000 °C (Figure 5.1(c)) show a continual reduction in the density of nanoparticles. The nanoparticle size appears to be increasing with increasing anneal temperatures, however it is not possible to make a reliable quantitative assessment due to the resolution of the instrument.

Figure 5.2(a)-(c) shows typical atomic force microscopy images of the Ge nanocrystals formed by ion implantation and subsequent annealing at (a) 600 °C, (b) 800 °C and (c) 1000 °C followed by a HF vapour etch to expose the nanocrystals. Figure 5.2(a) showed a high density of particles of different sizes with a mean particle density of 460 ± 30

particles/μm^2. The nanocrystals annealed at 800 °C, shown in Figure 5.2(b), had a mean particle density of 280 ± 15 particles/μm^2. As shown in Figure 5.2(c), the nanocrystals annealed at 1000 °C had a mean particle density of 150 ± 17 particles/μm^2. These measurements showed a reduction in the density of nanoparticles as the post-anneal temperature increased, in agreement with the FE-SEM images presented.

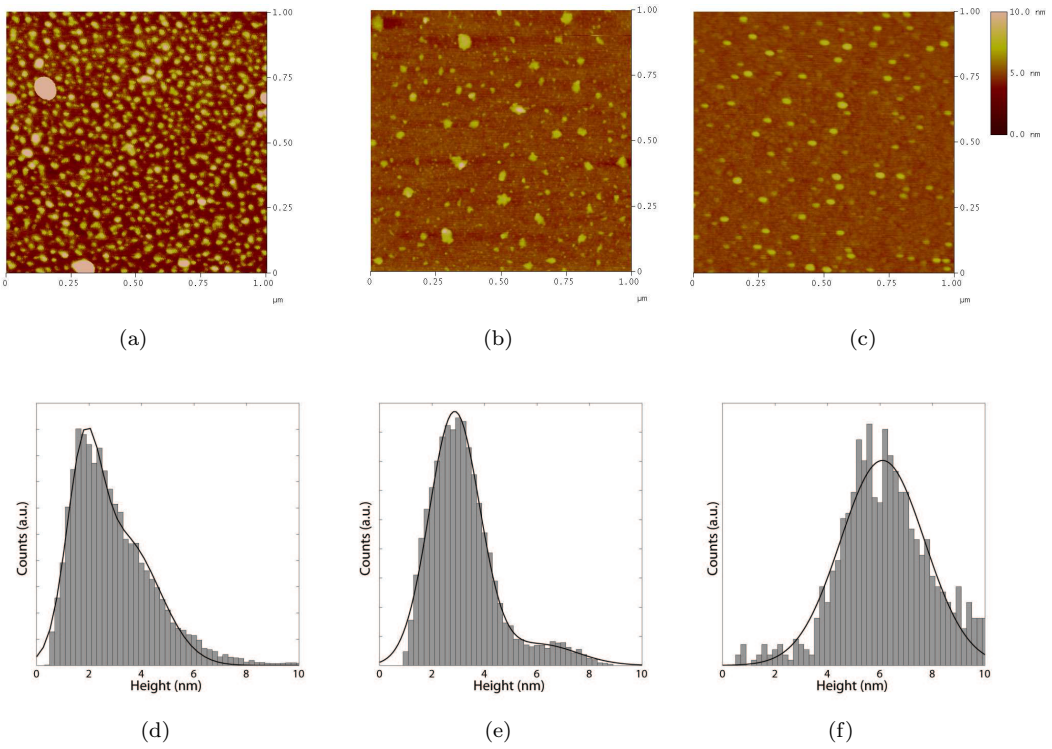

FIGURE 5.2: Atomic force microscope topography image of Ge nanocrystals produced by ion implantation (20 keV, 5×10^{15} cm^{-2}) into a 30 nm SiO_2 layer and postanneal at (a) 600 °C, (b) 800 °C and (c) 1000 °C followed by a HF vapour etch to expose the nanocrystals. Corresponding particle height distributions are shown in (d), (e) and (f), respectively. Distributions have been fitted with non-centred, normalised Gaussians.

Figure 5.2(d) shows a particle height distribution for the Ge nanocrystals formed by a 600 °C anneal in N_2. This distribution was obtained by analysing several images taken from the same sample. This result shows that the half-maximum counts of the particle height lie between 1.3 and 2.9 nm. This result agrees with others in the literature, for instance, Min et al. [353] reported the formation of Ge nanocrystals, by a similar process, with an average size of 1.9 ± 0.8 nm. This distribution, and the AFM image shown in Figure 5.2(a), indicate that some of the nanocrystals are considerably larger than 2 nm, indicating aggregation of the nanocrystals into larger clusters. The particle height distribution exhibited a bimodal character and has been fitted with two normalised, non-centred Gaussian curves ($R_2 = 0.994$). These modes are centred at 1.8 ± 0.7 nm and 3.4 ± 1.3 nm.

The particle height for the Ge nanocrystals formed by a 800 °C anneal in N_2 are shown in Figure 5.2(e). This exhibits a bimodal distribution, with modes centred at 2.9 ± 0.9

nm and 6.1 ± 1.4 nm. This distribution has been fitted by two normalised, non-centred Gaussian curves ($R_2 = 0.996$). The distribution for the nanocrystals formed by the 1000 °C anneal in N_2 is shown in Figure 5.2(f). Unlike the other two anneal temperatures, this sample exhibited a mono-modal distribution. This mode was centred at 6.1 ± 1.6 nm, and could be fitted by a normalised, non-centred Gaussian ($R_2 = 0.974$).

This data data shows that there is an increase in the modal height of the particles as the anneal temperature increases. There is also a broadening of the distribution as the pretreatment temperature increases, shown by the increasing standard deviations. Additionally there is a proportional reduction in the number of smaller nanoparticles, which suggests that the formation mechanism is likely to be some form of phase coarsening. The bimodal particle size distributions, seen in the 600 °C and 800 °C annealed samples, usually suggest a formation mechanism usually resulting from two different generation processes: the smaller mode is a result of molecular condensation, while the larger one is a result of breakup or redispersion [335]. However, the shape of the distributions closely match that of multiparticle diffusion simulations modelling Ostwald ripening [323, 324]. Indeed, this seems to be the most likely formation mechanism of the nanocrystals, considering the initial conditions and the processing undertaken [353, 354].

5.2.2 Photolumiscence of Ge Nanocrystals

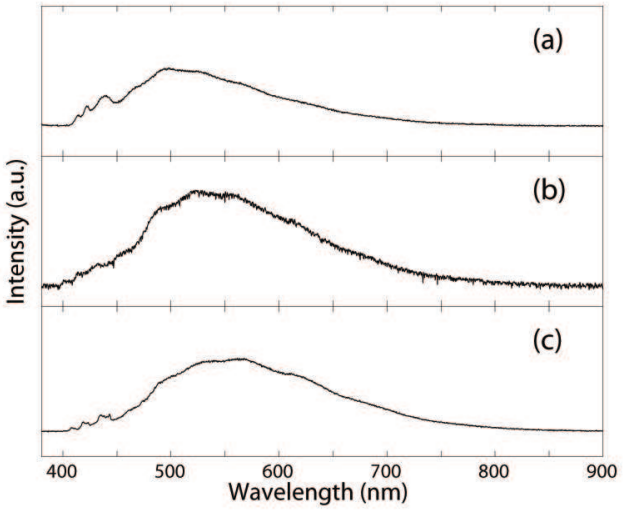

FIGURE 5.3: Photoluminescence spectra of Ge nanocrystals produced by ion implantation (20 keV, 5×10^{15} cm^{-2}) into a 30 nm SiO_2 layer and postanneal at (a) 600 °C, (b) 800 °C and (c) 1000 °C followed by a HF vapour etch to expose the nanocrystals. Measurements were undertaken using a 364 nm Ar-ion laser excitation with a power of 50 mW.

In semiconductor nanocrystals (or zero-dimensional quantum dots), the band gap increases with the decreasing diameter of nanocrystals [355], and electronic states become

discrete with high oscillator strength [356]. Quantum confinement effects play an essential role in optical absorption and luminescence processes in nanocrystals. In the case of Si, the emission wavelength does not show the dependence on size expected from simple quantum confinement models [357]. With large surface-to-volume ratios, surface electronic states affect the luminescence properties of Si nanocrystals [358]. However, bulk Ge, has a larger dielectric constant and smaller carrier masses compared to bulk Si. Moreover, the direct band-gap ($E_0 \approx 0.88$ eV) is close to the indirect band gap ($E_g \approx 0.75$ eV) [359]. Then, it is considered that quantum confinement effects would appear more pronounced in Ge than Si, and Ge nanocrystals would exhibit a direct-gap semiconductor nature [360, 361].

Visible luminescence at around 2.2 eV (560 nm) from nanocrystalline Ge in a SiO_2 matrix, fabricated by the rf co-sputtering deposition technique, was first reported by Maeda [362], and was explained by quantum confinement of the charge carriers in the system by simultaneous, high resolution TEM, XPS, Raman and PL measurements. Takeoka et al. [363] reported a blue-shift in the emission energy with a decrease in size of the particles in a similar system, indicating that the recombination of confined electron-hole pairs as the origin of PL in nanocrystalline Ge.

The photoluminescence of Ge nanocrystals fabricated by ion implantation and a postanneal at 600, 800 and 1000 °C followed by a HF vapour etch to expose the nanocrystals is shown in Figure 5.3(a)-(c), respectively. A theoretical calculation [360] shows that the band-gap energy of 4 nm Ge nanocrystals is approximately 540 nm (2.3 eV), which is similar to the peak energy of the PL spectra presented and the dimensions of the nanoparticles. Additionally, with a decrease in the nanocrystal size there is a blue shift in the luminescence peak energy. This is also in agreement with the theoretical calculations presented in [360], and shows that the indirect band-gap energy of Ge nanocrystals is very sensitive to the size of the nanocrystals. For all three spectra, the luminescence is broad indicating the presence of nanocrystals of varying sizes, matching the particle height distributions presented earlier.

5.2.3 Batch Uniformity

In order to investigate the repeatability of the process, a second process batch was commissioned. The processing conditions were exactly as those outlined in Section 5.1. To determine the size of the synthesized Ge nanocrystals, atomic force microscopy analysis was undertaken. Figure 5.4 shows particle height distributions, obtained over several AFM images, for samples in the second process batch. The particle height distribution for Ge nanocrystals formed by a 600 °C anneal in N_2 is shown in Figure 5.4(a). This distribution is significantly different from that obtained in the first experimental batch; the distribution is much sharper, the modal peak is smaller and exhibits only one mode.

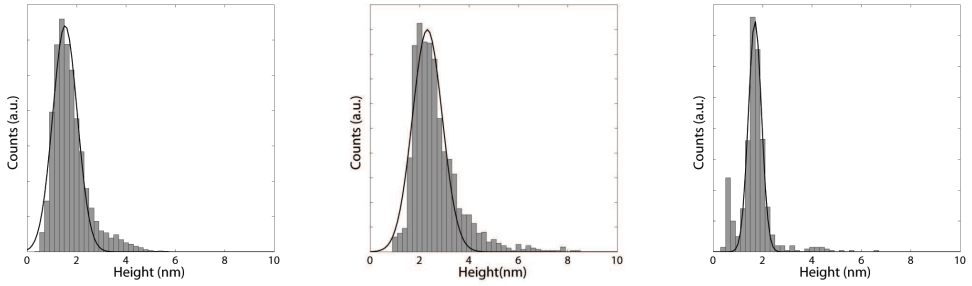

(a) (b) (c)

FIGURE 5.4: Particle size distributions derived from atomic force microscope topography images of Ge nanocrystals produced in the second process batch. The batch conditions were, Ge ion implantation (20 keV, 5×10^{15} cm^{-2}) into a 30 nm SiO_2 layer and postanneal at (a) 600 °C, (b) 800 °C and (c) 1000 °C followed by a HF vapour etch to expose the nanocrystals. Particle size distributions have been fitted with a non-centred, normalised Gaussian.

This was fit with a normalised Gaussian, centred on 1.5 ± 0.5 nm ($R_2 = 0.987$). Figure 5.4(b) shows the particle height distribution for Ge nanocrystals formed by a 800 °C anneal in N_2. This distribution was much sharper than that obtained in the first experimental batch and could be closely fit by a single Gaussian ($R_2 = 0.972$). The distribution was mono-modal, with the single mode centred at 2.3 ± 0.6 nm. Finally, the particle height distribution for the Ge nanocrystals formed by a 1000 °C anneal is shown in Figure 5.4(c). There was great variability between the first and second experimental batches for the nanocrystals annealed at this temperature. The particle height distribution showed a single, sharp mode centred at 1.7 ± 0.3 nm, which is approximately a four-fold reduction in modal particle size.

It is believed that the cause for this variability in nanocrystal size in this process was introduced by the HF vapour etch. The fabrication of Ge nanocrystals by this process is dependent on four main factors; the growth of a high quality SiO_2 matrix, Ge ion implantation, N_2 anneal temperature and the HF vapour etch. The thermal growth of SiO_2, N_2 anneal and ion implantation are crucial techniques in complementary metal-oxide semiconductor fabrication and are highly repeatable. After each of these process step, the batches were verified and showed little variance. However, due to availability the HF vapour etch was performed in non-standard equipment and as such, there were few control measures available. Typically, this is undertaken in a dedicated cell with an electronic control unit to regulate the flow of etchant into the cell. In this case, the etch was performed in a laboratory beaker with the sample suspended over liquid HF, which was heated by a hot plate. As a result, etch rates were not closely reproducible. Additionally, due to safety concerns over the crude etching process, the samples were dipped in deionised water after etching. This step could have introduced further variability in the process.

The second process batch was discarded and all further experiments were undertaken utilising the initial batch.

5.3 Effect of Nanocrystal Size

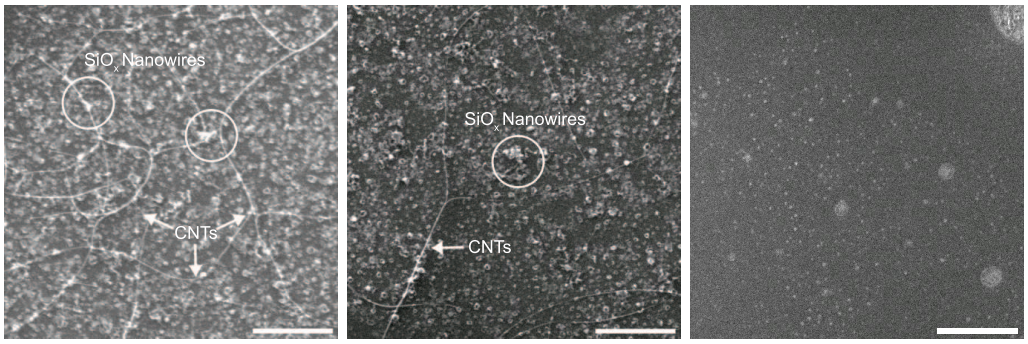

(a) (b) (c)

FIGURE 5.5: Scanning electron microscope images of CNT growth using Ge nanocrystals fabricated by ion implantation (20 keV, 5×10^{15} cm^{-2}) into a 30 nm SiO_2 layer and postanneal at (a) 600 °C, (b) 800 °C and (c) 1000 °C followed by a HF vapour etch to expose the nanocrystals. The CNTs were grown using a preanneal of 10 minutes at 900 °C and a CNT growth step of 20 minutes at 850 °C. Scale bar corresponds to 500 nm.

Figure 5.5 shows FE-SEM images of CNTs synthesized from the Ge nanocrystals formed by ion implantation for each N_2 anneal temperatures. The samples were fabricated at the optimum growth condition for the catalyst, H_2 pretreatment at 900 °C for 10 minutes, followed by the CNT growth step for 20 minutes at 850 °C in a mixture of H_2 and CH_4 (1 : 3 gas ratio). Figure 5.5(a) and Figure 5.5(b) show representative FE-SEM images of the Ge nanocrystals formed by a 600 °C and 800 °C anneal in N_2 samples after the CNT growth step, respectively. Both images show that the presence of CNTs correlates with the region where Ge nanocrystals are present. No CNTs were seen in regions of the sample where there were no nanocrystals present. There are also many short nanofibres seen in the region where Ge nanocrystals are present. Similar nanofibres were seen in comparable experiments and were composed mainly of amorphous silicon oxide (SiO_x). These can be easily removed with a HF etch. Figure 5.5(c) shows a FE-SEM image of the Ge nanocrystals formed by a 1000 °C anneal in N_2 sample after the CNT growth step. For nanocrystals formed at this anneal temperature, no CNTs were found, regardless of the pretreatment or CNT growth temperature.

The highest yield of CNTs was seen from the Ge nanocrystals formed by an anneal in N_2 at 600 °C. For the growth conditions shown in Figure 5.5, this was 3.5 ± 1.0 μm in length/μm^2. The CNT yield from the Ge nanocrystals formed by an anneal in N_2 at 800 °C was significantly lower, 1.7 ± 0.3 μm in length/μm^2. It is believed that the reason for the relatively higher CNT yield from the nanocrystals annealed at 600 °C

is due to a higher initial nanoparticle density. The particle size distribution of both successful samples are in the expected range for CNTs, however it could be argued that the distribution for the nanocrystals annealed at 600 °C may be slightly more conducive for CNT formation. This is in contrast to the nanocrystals formed by an anneal at 1000 °C, which exhibited nanoparticles which are arguably considered too large for CNT formation.

5.4 Effect of Catalyst Pretreatment

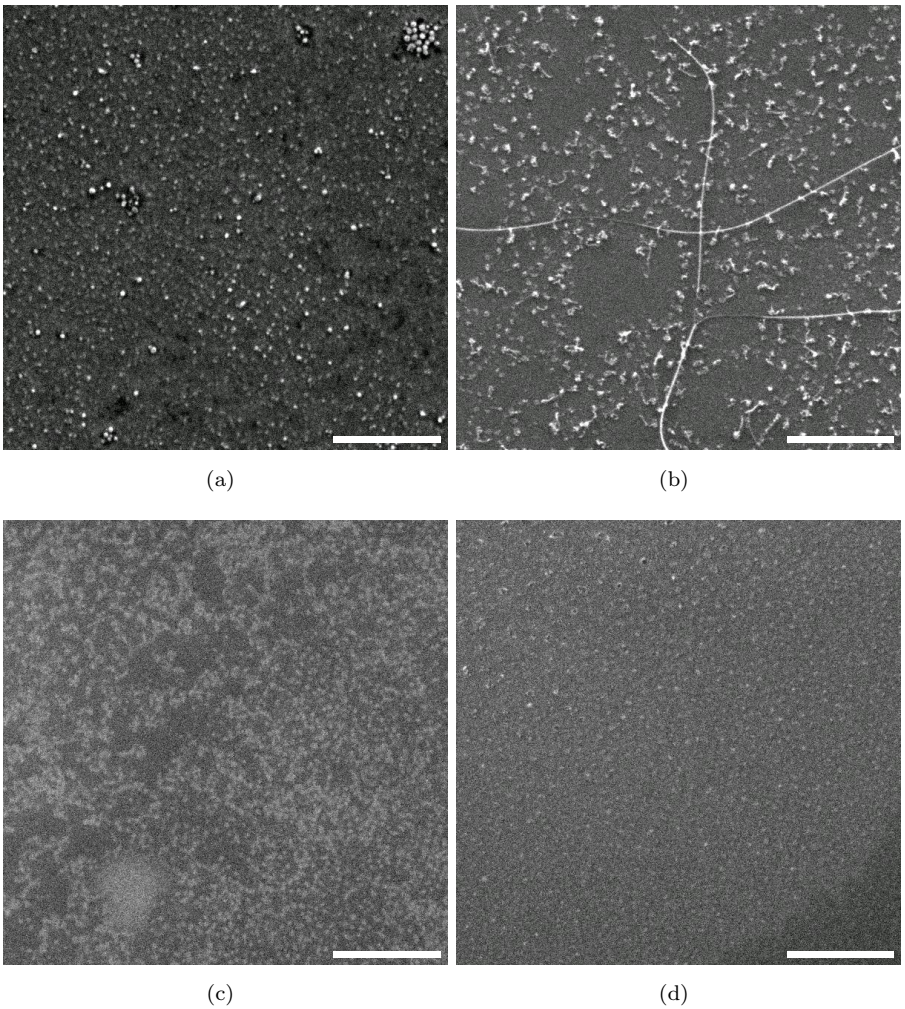

FIGURE 5.6: Scanning electron microscope image of CNT growth using Ge nanocrystals fabricated by ion implantation and a postanneal at 600 °C. The CNTs were grown at (a) 1000, (b) 950, (c)900 and (d) 850 °C in a mixture of H_2 and CH_4 (1 : 3 gas ratio) for 20 minutes. Scale bar corresponds to 500 nm.

Figure 5.6 shows FE-SEM images of CNT growth at various temperatures using Ge nanocrystals fabricated by ion implantation and a post-anneal in N_2 at 600 °C. The CNT growth temperatures shown in Figure 5.6(a)-(d) are 1000, 950, 900 and 850 °C, respectively. These images establish that only at one growth temperature, 950 °C, CNTs

are found. In Figure 5.6(b), a density of 1.6 ± 0.5 (μm in length/μm^2) CNTs are found. The presence of CNTs correlate with the regions where Ge nanocrystals are present. No CNTs were seen in regions of the sample where there were no nanocrystals present. There are also a few short nanofibres seen in the region where Ge nanocrystals present, for the samples subjected to CNT growth at 1000 and 950 °C. Similar nanofibres were seen in comparable experiments and were composed mainly of amorphous silicon oxide (SiO_x). Interestingly, no nanofibres were found in the samples subjected to a lower CNT growth temperature (850 and 900 °), indicating that the formation mechanism of these fibres requires a high temperature.

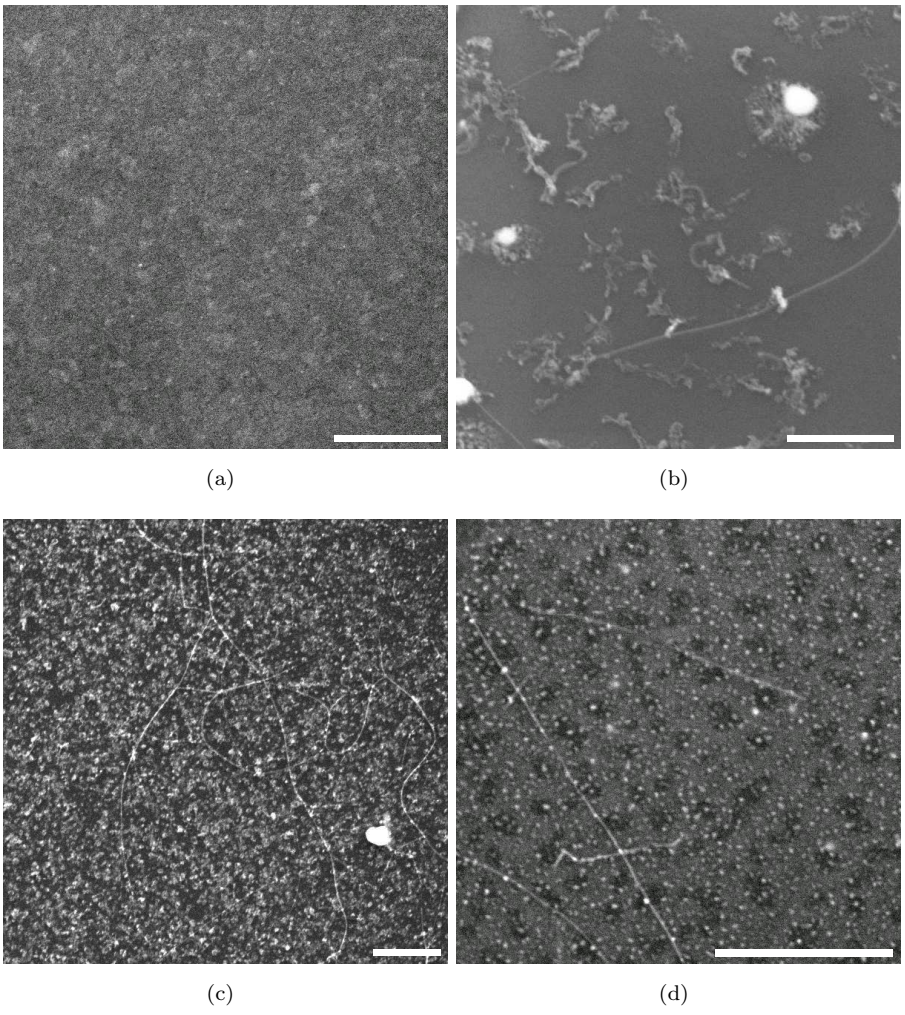

FIGURE 5.7: Scanning electron microscope image of CNT growth using Ge nanocrystals fabricated by ion implantation and post-anneal at 600 °C. The CNTs were pretreated at four different pretreatment temperatures; (a) 1000 °C, (b) 950 °C, (c) 900 °C and (d) 850 °C in H_2 for 10 minutes. The subsequent CNT growth step was kept constant at 850 °C in a mixture of H_2 and CH_4 (1 : 3 gas ratio) for 20 minutes. Scale bar corresponds to 500 nm..

Figure 5.7 shows FE-SEM images of the Ge nanocrystals fabricated by ion implantation and a post-anneal in N_2 at 600 °C after a 850 °C CNT growth step following a catalyst pretreatment anneal in H_2 at various temperatures for 10 minutes. The pretreatment

temperatures shown in Figure 5.7(a)-(d) are 1000, 950, 900 and 850 °C, respectively. These images establish the optimum growth conditions for the Ge nanocrystal catalyst and provides an insight to the importance of the catalyst pretreatment step. Figure 5.7(b) shows a typical sample after pretreatment at 950 °C, which showed density of 0.6 ± 0.2 (μm in length/μm^2) CNTs and a fairly homogeneous coverage across the sample. Figure 5.7(c) shows a typical sample after pretreatment at 900 °C. This sample showed a significantly higher CNT density of 3.5 ± 1.0 μm in length/μm^2. This area density is more than a two-fold improvement on the highest yield sample without H_2 pretreatment. After pretreatment at 850 °C, shown in Figure 5.7(d), there was a slightly lower density of CNTs, 1.3 ± 0.1 μm in length/μm^2 and a highly uniform coverage across the sample. Finally, no CNTs were found at the highest pretreatment temperature of 1000 °C, shown in Figure 5.7(a). SEM images showed a very sparse surface topography, indicating that the pretreatment temperature may have been too high and the nanocrystals may have evaporated.

CNTs were found in samples pretreated at a temperature in the range from 850 °C to 950 °C, with the highest area density found in the samples pretreated at 900 °C, as shown in Figure 5.7(c). For all samples pretreated in this temperature range we see both CNTs and the presence of amorphous silicon oxide nanowires. At pretreatment temperatures higher than 950 °C, very few features are present in the FE-SEM images and it is believed that this is due to loss of the catalyst due to evaporation. However, there may be well-dispersed smaller Ge nanocrystals present in these samples although due to the resolution of the FE-SEM these may not be visible. These results indicate that a H_2 pretreatment allows a wider process window and an improvement in the yield of the process. The CNT area densities for different pretreatment temperatures and CNT growth temperatures are summarised in Table 5.1.

The hydrogen pretreatment is effective in increasing the CNT area density and is critical for CNT growth from semiconductor nanoparticles. We believe that the hydrogen pretreatment step is required to reduce the oxide on the surface of the nanocrystals. While a chemical or thermal oxidation was not deliberately carried out before CNT growth, there would undoubtedly have been a native oxide present on the surface of the Si substrate and the Ge nanocrystals, as indicated by the presence of silica nanofibers and an oxide peak in the EDS spectra (not shown). This technique does not require oxidation in air to active the semiconductor nanoparticles, where as Takagi et al. [11] imply that this step is a key requirement for CNT growth from semiconductor nanoparticles. It is highly likely that in the case of Takagi et al. [11], the oxidation step was necessary solely to reduce residual contaminants introduced via their nanoparticle synthesis process.

In order to confirm that the CNT growth is catalysed by the Ge nanoparticles and not any systematic contaminant, a control sample was fabricated at the optimum growth condition. The control sample was subjected to the same deposition and cleaning process as the Ge nanocrystal samples, however no Ge was implanted. This sample was

Pretreatment		CNT growth		CNT area density (μm in length/μm^2)	
Temperature (°C)	Time (min)	Temperature (°C)	Time (min)	Without C+	With C+
N/A	N/A	1000	20	No CNTs	No CNTs
N/A	N/A	950	20	1.6 ± 0.5	3.2 ± 2.6
N/A	N/A	900	20	No CNTs	0.4 ± 0.1
N/A	N/A	850	20	No CNTs	No CNTs
850	10	850	20	1.3 ± 0.1	1.2 ± 0.3
900	10	850	20	3.5 ± 1.0	4.1 ± 1.2
950	10	850	20	0.6 ± 0.2	2.0 ± 0.6
1000	10	850	20	No CNTs	1.5 ± 1.0
1000	5	850	20	No CNTs	2.7 ± 0.8
1050	5	850	20	No CNTs	0.6 ± 0.1
1100	5	850	20	No CNTs	No CNTs

TABLE 5.1: CNT area densities for different pretreatment temperatures and CNT growth temperatures. Samples were grown using Ge nanocrystals fabricated by ion implantation and post-anneal at 600 °C.

pretreated at 900 °C in H_2 for 10 minutes and exposed to the CNT growth step at 850 °C in a mixture of CH_4 and H_2 (3 : 1 ratio). No CNTs were found in this sample. Additionally, EDS analysis has been undertaken in all the sample regions which showed CNTs, and regions which showed contaminants were discarded from subsequent analysis. However, it should be noted that at this scale, the sensitivity of EDS is low.

5.5 Effect of Carbon Implant

In our earlier growth method using SiGe islands [10], a carbon implantation was found to be necessary for the growth of CNTs. Selected wafers were implanted with carbon at a dose of 3×10^{16} cm^{-2} and a energy of 30 keV after Ge nanocrystal formation and HF vapour etching to expose the nanocrystals. A typical AFM image of the Ge nanocrystals, formed after a 600 °C anneal in N_2 and subjected to a carbon implantation, is shown in Figure 5.8(a). These samples showed a lower particle density than those without the carbon implantation, in this case 64 ± 18 particles/μm^2. It is believed that the carbon ions sputter the Ge nanocrystals from the surface, thereby lowering their density. Line analyses also show that the surface the Si substrate is rougher in carbon-implanted samples than in non-implanted samples. The associated particle height distribution is shown in Figure 5.8(b). This distribution was closely fit by two non-centred, normalised Gaussian ($R_2 = 0.990$), with modes centred at a height of 1.0 ± 0.25 nm and 1.8 ± 0.75 nm. This distribution is much narrower than the non-implanted samples and showed a

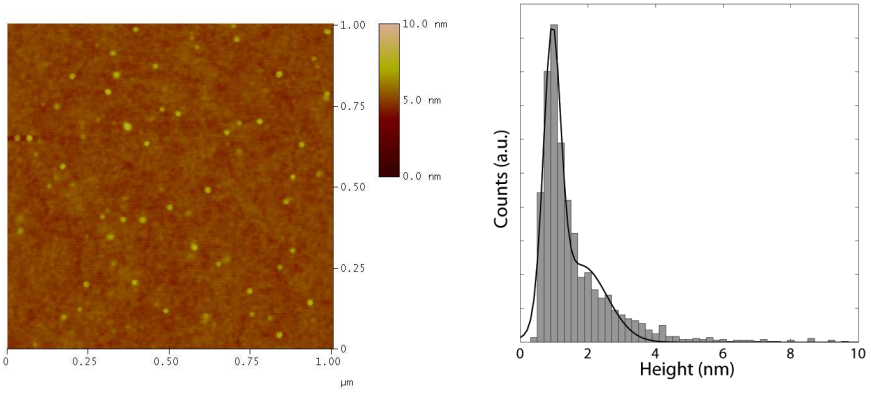

(a) (b)

FIGURE 5.8: (a) Atomic force microscope image and (b) particle height distribution of Ge nanocrystals produced by Ge implantation (20 keV, 5×10^{15} cm^{-2}) into a 30 nm SiO_2 layer and post-anneal at 600 °C followed by a HF vapour etch to expose the nanocrystals. Samples were then given a carbon implantation (30 keV, 3×10^{16} cm^{-2})

smaller modal height. This reduction in size is also believed to be due to the sputtering effect caused by the carbon implantation.

Figure 5.9 shows FE-SEM images of CNT growth at various temperatures using Ge nanocrystals fabricated by ion implantation and a post-anneal in N_2 at 600 °C in N_2 and subjected to a carbon implantation. The CNT growth temperatures shown in Figure 5.9(a)-(d) are 1000, 950, 900 and 850 °C, respectively. These images establish that only at two growth temperatures, 900 and 950 °C, CNTs are found. In Figure 5.9(b), a density of 3.5 ± 1.0 (μm in length/μm^2) CNTs are found. In Figure 5.9(c), a CNT density of 0.4 ± 0.1 μm in length/μm^2 was found. The presence of CNTs correlate with the regions where Ge nanocrystals are present. No CNTs were seen in regions of the sample where there were no nanocrystals present. Compared to the non-implanted samples, the process window is wider and the yield is higher.

Figure 5.10 shows FE-SEM images of the Ge nanocrystals fabricated by a post-anneal in N_2 at 600 °C and subjected to carbon implantation, after a 850 °C CNT growth step following a catalyst pretreatment anneal in H_2 at various temperatures for 10 minutes. The pretreatment temperatures shown in Figure 5.10(a)-(d) are 1000, 950, 900 and 850 °C, respectively. These images establish the optimum growth conditions for the Ge nanocrystal catalyst and provides an insight to the importance of the catalyst pretreatment step. Unlike the non-implanted samples, CNTs were found for all of the pretreatment temperatures, indicating a wider process window. Additionally, the area density of CNTs was significantly higher for all samples.

Table 5.1 summarises the CNT area densities for a range of pretreatment and CNT growth temperatures for samples with and without carbon implantation. The highest CNT density, for both implanted and non-implanted samples, is obtained by preanneling

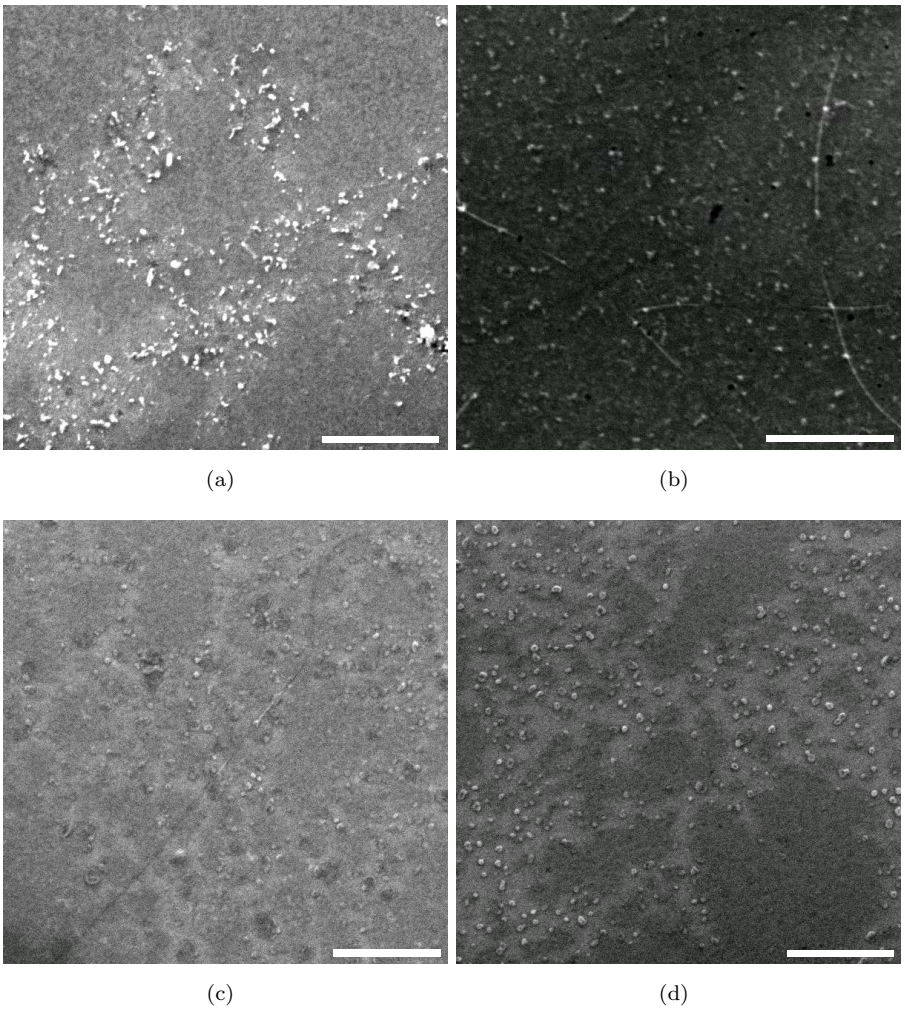

FIGURE 5.9: Scanning electron microscope image of CNT growth using Ge nanocrystals fabricated by ion implantation (20 keV, 5×10^{15} cm^{-2}) into a 30 nm SiO_2 layer and postanneal at 600 °C followed by a HF vapour etch to expose the nanocrystals. Samples were then given a carbon implantation (30 keV, 3×10^{16} cm^{-2}). The CNTs were grown at (a) 1000, (b) 950, (c)900 and (d) 1000 °C in a mixture of H_2 and CH_4 (1 : 3 gas ratio) for 20 minutes. Scale bar corresponds to 500 nm.

at 900 °C followed by a CNT growth at 850 °C. For these growth conditions, there is no statistically significant advantage to the carbon implantation in terms of area density. However, the results show that successful CNT growth is achieved for a wider range of growth conditions, particularly higher growth temperatures. If higher growth temperatures are used, successful growth can be attained without the pretreatment step.

To investigate the role of pretreatment in the growth process, AFM images of samples with and without carbon implantation were recorded immediately after a pretreatment step. Table 5.2 summarizes the key findings. Samples without carbon implantation show a drastic reduction in Ge nanocrystal density as the pretreatment temperature increases and almost no Ge nanocrystals are present after pretreatment at 1000 °C. Typical FE-SEM images after pretreatment are presented in Figure 5.11 for samples without carbon

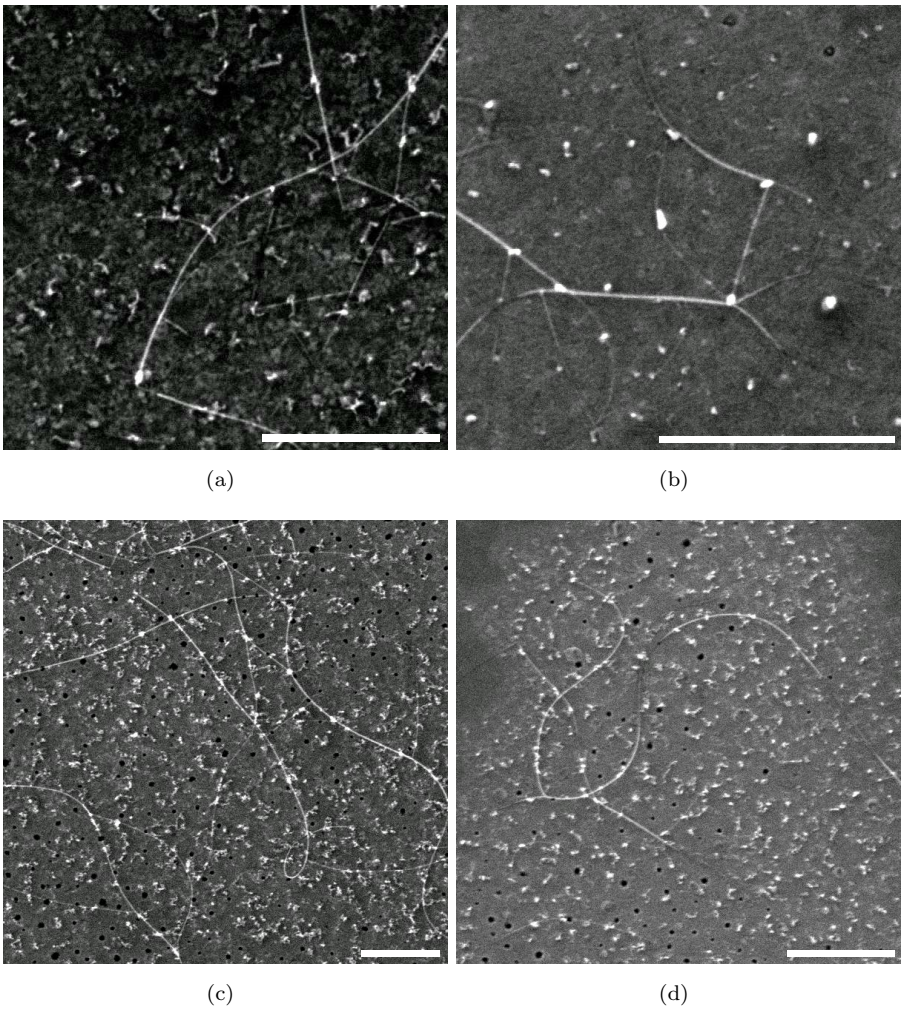

(a) (b)

(c) (d)

FIGURE 5.10: Scanning electron microscope image of CNT growth using Ge nanocrystals fabricated by ion implantation (20 keV, 5×10^{15} cm^{-2}) into a 30 nm SiO_2 layer and post-anneal at 600 °C followed by a HF vapour etch to expose the nanocrystals. Samples were then given a carbon implantation (30 keV, 3×10^{16} cm^{-2}). The CNTs were pretreated at four different pretreatment temperatures; (a) 1000 °C, (b) 950 °C, (c) 900 °C and (d) 850 °C in H_2 for 10 minutes. The subsequent CNT growth step was kept constant at at 850 °C in a mixture of H_2 and CH_4 (1 : 3 gas ratio) for 20 minutes. Scale bar corresponds to 500 nm..

implantation and show the reduction in Ge nanocrystal density on increasing the pretreatment temperature from 900 to 950 °C. The reduction in Ge nanocrystal density at high pretreatment temperatures is most likely related to the melting point of Ge (937 °C). The reduction in the Ge nanocrystal density is also associated with a reduction in the proportion of larger nanocrystals (larger than 2 nm in diameter). AFM results show that the particle size distributions for samples with and without carbon implantation and annealed at 900 and 950 °C are similar. The pretreatment has much less effect on carbon-implanted samples, which show little change in density and particle size distribution as the pretreatment temperature is increased from 900 to 1000 °C.

Table 5.2 also shows a well-defined process window for CNT growth. The CNT area

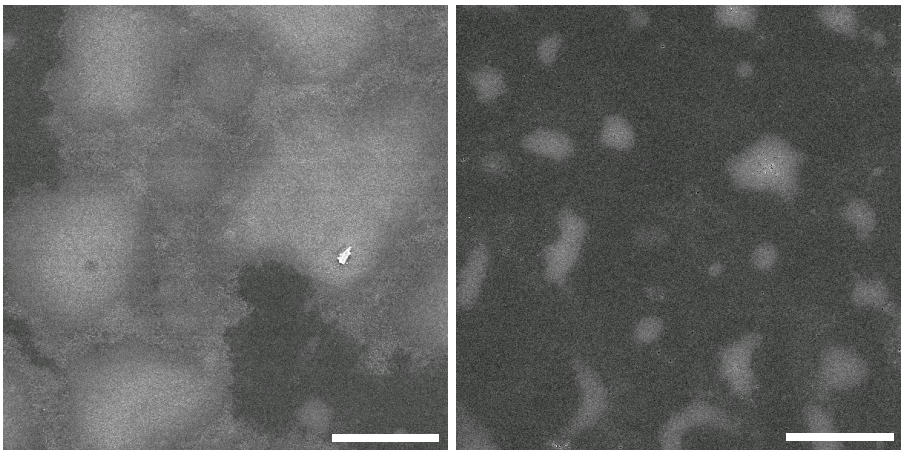

(a) (b)

FIGURE 5.11: Field emission scanning electron microscope images immediately following 10 minute H_2 pretreatment step at (a) 900 and (b) 950 °C for non carbon implanted Ge nanocrystals produced by implantation and post-anneal in N_2 at 600 °C. Scale bar corresponds to 5 μm.

density is directly proportional to the Ge nanoparticle density at high pretreatment temperatures for samples both with and without carbon implantation. This result suggests that Ge nanoparticles are the nucleation sites for the CNT growth. Almost all Ge nanoparticles are expected to have melted into liquid droplets over 900 °C due to the melting-point reduction in nanoparticles [364] and CNTs are synthesized from Ge droplets which have adsorbed atomic carbon.

In our earlier growth method using SiGe islands, carbon implantation was a prerequisite for CNT growth [10], whereas for implanted Ge nanocrystals CNT growth is possible without carbon implantation (Table 5.1). This result suggests that the Ge implantation into SiO_2 and N_2 anneal is a more successful method of producing nanocrystals of a size suitable for CNT growth. Nevertheless, the carbon implantation is very beneficial to CNT growth as it significantly broadens the process window for successful CNT growth and increases the CNT area density. In particular, it enables a pretreatment up to temperatures as high as 1050 °C. For the carbon implanted samples there is little reduction in Ge nanocrystal density as the pretreatment temperature increases, in sharp contrast with samples without carbon implantation (Table 5.2). This suggest that the carbon implantation might increase the melting point through the formation of a $Ge_{1-y}C_y$ alloy. This hypothesis is supported by the phase diagram of the the Ge-C system presented by Scace and Slack [365], which indicated that the presence of a small percentage of carbon has a string effect on raising the melting point of Ge. Furthermore Kanzawa et al. [366] demonstrated that the $Ge_{1-y}C_y$ alloys can be successfully formed by carbon implantation into Ge. An alternative, albeit less likely explanation may be that the role of the carbon implantation in suppressing the agglomeration of Ge nanocrystals

is physical. The lower initial nanocrystal density and the higher surface roughness cause by ion implantation may act to reduce agglomeration [167].

Pretreatment Temperature (°C)	Nanocrystal density (particles/μm^2)		CNT area density (μm in length/μm^2)	
	Without C+	With C+	Without C+	With C+
As Formed	460 ± 30	64 ± 18	N/A	N/A
900	30 ± 6	57 ± 8	3.5 ± 1.0	4.1 ± 1.2
950	16 ± 7	40 ± 4	0.6 ± 0.2	2.0 ± 0.6
1000	3.6 ± 1.6	38 ± 8	No CNTs	1.5 ± 1.0

TABLE 5.2: Comparison of Ge nanocrystal densities immediately after pretreatment in H_2 for 10 minutes and CNT area densities for samples with and without carbon implantation. The CNTs were grown at 850 °C for 20 minutes after pretreatment. The nanocrystals used were fabricated using ion implantation and a post-anneal at 600 °C.

The CNT area density of 4.1 ± 1.2 μm in length/μm^2 shown in Table 5.1 is comparable to densities reported for CNT-FET fabrication. For example, many groups have reported experimental CNT-FETs fabricated with SWNT area densities of less than 1.5 μm in length/μm^2 [367, 368]. The CNT density achieved in this work is satisfactory for CNT-FET based applications in sensors, logic, and memory devices. However, for application as SWNT via interconnects, much lower process temperature and higher CNT densities are required. The use of techniques already developed to reduce the growth temperature of CNTs using a Fe catalyst, e.g. use of C_2H_2 thermal CVD or oxygen-assisted plasma enhanced CVD may well allow the maximum temperature to reduce toward the upper limit of 400 °C required for via interconnects [369]. However, it is unlikely that the high CNT densities required will be achievable with a Ge catalyst. However, with Fe catalysts, densities vary strongly with growth conditions and as such further research is needed to investigate this.

5.6 Evolution of the Catalyst

In order to determine the morphology of the Ge catalyst after pretreatment, AFM characterisation of the samples without and with a carbon implantation has been undertaken for a range of pretreatment temperatures. These measurements are expected to complement the discussion in Section 5.5 and provide some insight into the behaviour of the catalyst after pretreatment.

From typical AFM images on samples after a pretreatment step at temperatures between 1000 and 900 °C, the mean density of particles has been determined. The results are summarised in Table 5.2 for Ge nanocrystals without and with a carbon implantation.

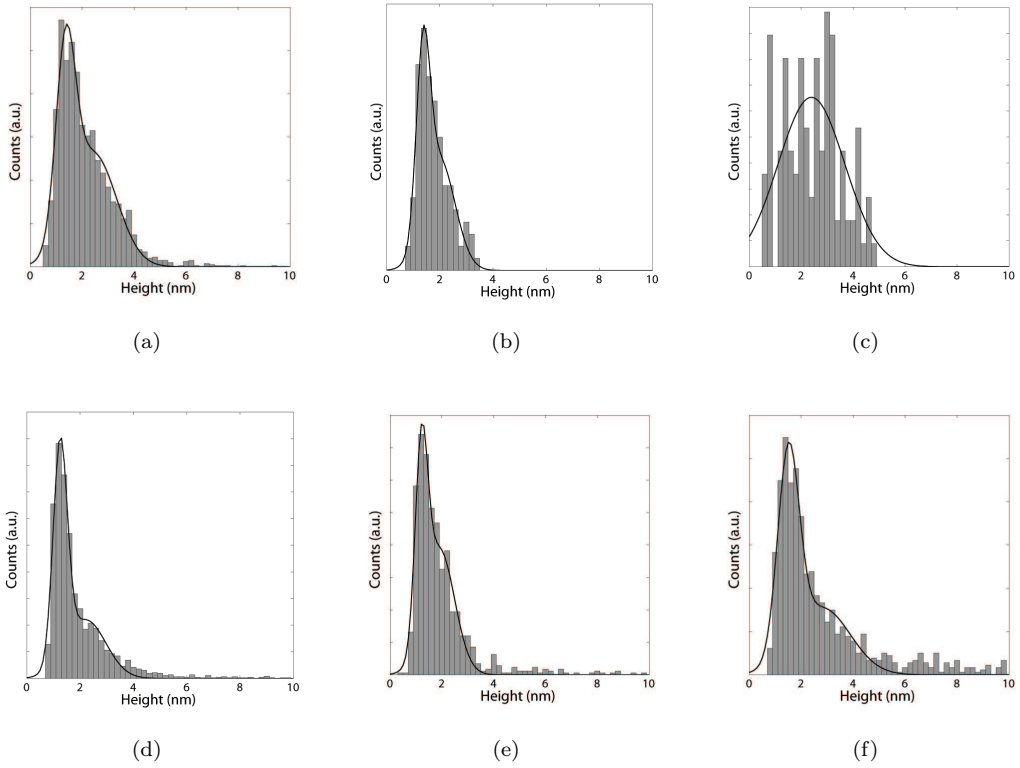

FIGURE 5.12: Particle size distribution of of Ge nanocrystals produced by Ge implantation and post-anneal in N_2 at 600 °C. Samples were pretreated in H_2 for 10 minutes at (a) 900 °C, (b) 950 °C and (c) 1000 °C. Samples subjected to a carbon implantation prior to H_2 pretreatment at 900 °C, 950 °C and 1000 °C are shown in (c), (d) and (e), respectively. All distributions have been fitted with non-centred, normalised Gaussians.

This table demonstrates a drastic reduction in nanoparticle density with increasing pretreatment temperatures for Ge nanocrystals without a carbon implantation. The initial particle density of 460 ± 30 particles/μm^2 is reduced to 30 ± 6, 16 ± 7 and 3.6 ± 1.6 particles/μm^2 after pretreatment at 900, 950 and 1000 °C respectively. The reduction in nanoparticle density for samples subjected to a carbon implantation is far less drastic. The initial density of 64 ± 18 particles/μm^2 is reduced to 57 ± 8, 40 ± 4 and 38 ± 8 particles/μm^2 after pretreatment at 900, 950 and 1000 °C respectively. As discussed in Section 5.5, it is likely that the reduction in Ge nanocrystal density is related to the melting point of Ge (937 °C). The disparity between the rate of nanoparticle reduction with respect to pretreatment temperature between Ge nanocrystals without and with a carbon implantation is most likely due to an increase in melting point via the formation of a $Ge_{1-y}C_y$ alloy.

Figure 5.12(a)–(c) show the particle size distribution for Ge nanocrystals pretreated in H_2 for 10 minutes at 900, 950 and 1000 °C respectively. Each distribution has been fitted with non-centred, normalised Gaussian curves. The distribution for Ge nanocrystals pretreated at 900 °C, shown in Figure 5.12(a), resembles the initial distribution (Figure 5.2(d)). However, there is a noticeable reduction in the modal heights and a

narrowing of the distribution profile. Additionally, there is a proportional reduction in the number of larger nanoparticles (larger than 2 nm in diameter). This behaviour, when considered in conjuction with the reduction in nanoparticle density is indicative of a loss mechanism, most likely evaporation. As pretreatment temperatures increase, there is a slight increase in the modal height of the nanoparticles and a broadening of the distribution. This behaviour suggests phase coarsening, which occurs at the expense of small particles within a system. However, due to the very low density of nanoparticles after pretreatment at higher temperatures, the accuracy of the measurement is questionable and much care is required when drawing conclusions.

The particle size distributions for Ge nanocrystals subjected to a carbon implantation are shown in Figure 5.12(d)–(f) for pretreatment in H_2 for 10 minutes at 900, 950 and 1000 °C respectively. All distributions were bimodal and could be closely fit by a sum of two Gaussian curves, with a lowest value of $R_2 = 0.980$ for samples pretreated at 1000 °C. As was the case with the samples without a carbon implantation, the distribution for Ge nanocrystals pretreated at 900 °C, shown in Figure 5.12(d), closely resembles the initial distribution (Figure 5.8(b)). Although not statistically significant, there is a slight increase in the modal height of the nanoparticles upon pretreatment. The results presented in Figure 5.12 show that the particle size distributions for samples with and without carbon implantation and annealed at 900 and 950 °C are similar. As with the samples without a carbon implantation pretreated at the same temperatures, there is a narrowing of the distribution profile and there appears to be a proportional reduction in the density of larger nanoparticles (larger than 2 nm diameter). However at the highest pretreatment temperature, 1000 °C, there is no statistically significant broadening of the the distribution profile or increase in the modal height. This is in sharp contrast to the samples without a carbon implant, which showed a drastic change in the distribution profile. This behaviour can be explained by the increase in melting point via the formation of a $Ge_{1-y}C_y$ alloy during carbon implantation (Section 5.5).

Pretreatment Temperature (°C)	Without C+			With C+		
	Mode 1 (nm)	Mode 2 (nm)	R_2	Mode 1 (nm)	Mode 2 (nm)	R_2
As Formed	1.8 ± 0.7	3.4 ± 1.3	0.994	1.0 ± 0.3	1.8 ± 0.8	0.990
900	1.3 ± 0.4	2.5 ± 0.9	0.991	1.3 ± 0.3	2.2 ± 0.8	0.991
950	1.4 ± 0.3	2.0 ± 0.6	0.991	1.2 ± 0.2	1.9 ± 0.6	0.989
1000	2.4 ± 1.3	N/A	0.844	1.5 ± 0.4	2.8 ± 1.0	0.980

TABLE 5.3: Comparison of Ge nanocrystal particle size distribution fit parameters immediately after pretreatment in H_2 for 10 minutes. The nanocrystals used were fabricated using ion implantation and a post-anneal at 600 °C.

Table 5.3 summarises the Ge nanocrystal particle size distribution fit parameters immediately after pretreatment for samples without and with a carbon implantation. The

highest CNT density, for both implanted and non-implanted samples, is obtained by pretreating at 900 °C followed by a CNT growth step at 850 °C. For these growth conditions, there is no statistically significant advantage to the carbon implantation in terms of CNT area density. Indeed, the particle size distribution profiles and the density of nanoparticles are similar. However, the results have shown that successful CNT growth is achieved for a wider range of growth conditions. The pretreatment has much less effect on carbon-implanted samples, which show little change in density and particle size distribution as the pretreatment temperature is increased from 900 to 1000 °C.

5.7 Characterisation of Synthesized CNTs

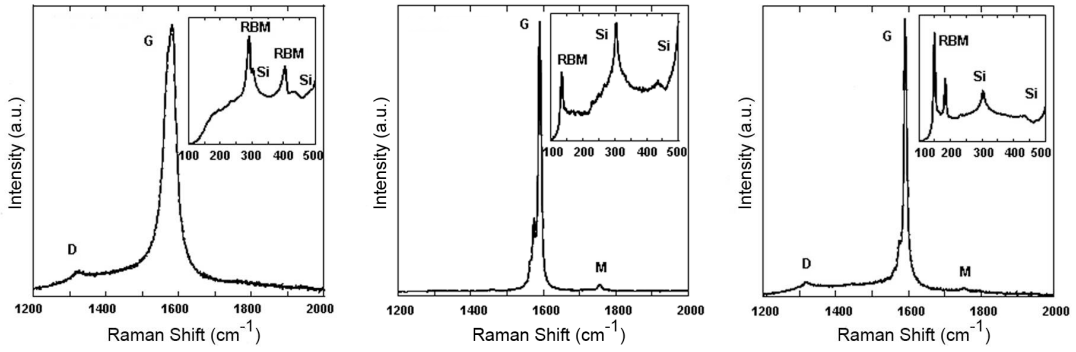

FIGURE 5.13: Raman spectra of CNTs grown from Ge nanocrystals fabricated by ion implantation (20 keV, 5×10^{15} cm^{-2}) into a 30 nm SiO_2 layer and post-anneal at 600 °C (a) without a subsequent carbon implantation, and (b) with a carbon implantation. (c) Raman spectra of CNTs grown from Ge nanocrystals fabricated by ion implantation and post-anneal at 800 °C. Inset shows the radial breathing mode feature. The CNTs were grown at 850 °C after a pretreatment in H_2 at 900 °C

In Figure 5.13, representative Raman spectra are presented for CNTs grown from Ge nanocrystals fabricated by ion implantation and a post-anneal at 600 °C, with and without carbon implantation, and post-anneal at 800 °C without carbon implanatation. The measured CNTs were grown using a pretreatment step in H_2 at 900 ° for 10 minutes and a CNT growth step at 850 °C for 20 minutes. All samples (insets) clearly show the RBM indicating that SWNTs are present. For CNTs grown from Ge nanocrystals formed at 600 °C without carbon implantation, shown in Figure 5.13(a), a small D-band peak is visible around 1320 cm^{-1}, which can be attributed to disorder in the CNTs. Figure 5.13(c) shows the Raman spectra for CNTs grown from Ge nanocrystals formed at 800 °C, in which a small D-band peak at 1320 cm^{-1} is also visible. In contrast, the CNTs grown from carbon-implanted Ge nanocrystals show no D-band peak (Figure 5.13(b)). This indicates that the SWNTs synthesized have a low defect density and are thus of a high quality. RBM peaks with a large number of different Raman shifts within the range of 408 cm^{-1} to the lower limit of 110 cm^{-1} imposed by our Raman notch filter

have been observed. Assuming a standard formula for converting RBM Raman shift to diameter, this indicates that the CNTs observed by Raman scattering have diameters in the range of $0.6 - 2.3$ nm.

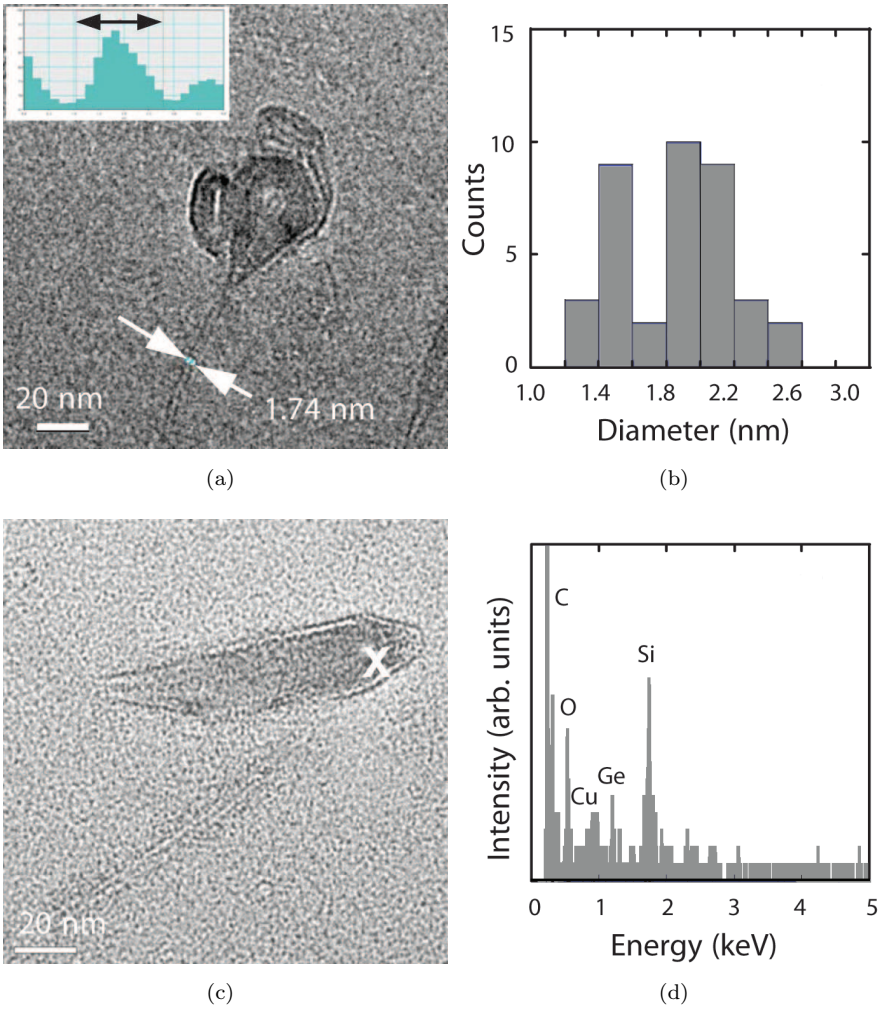

FIGURE 5.14: (a) Transmission electron microscope image of SWNTs and carbon implanted Ge nanocrystals using a pretreated at 900 °C and a CNT growth step at 850 °C. The inset shows line profile of the SWNT used to determine the diameter distribution. (b) Histogram of the diameter distribution of SWNTs. (c) TEM image of the SWNT and the carbon-implanted Ge nanocrystals for EDS analysis. (d) EDS spectra of the carbon implanted Ge nanocrystal

The Raman measurements are supported by TEM measurements on a total of 38 CNTs synthesized from Ge nanocrystals formed at 600 °C and given a carbon implantation. Representative TEM images and a histogram of the diameter distribution determined by analysing the TEM images are shown in Figure 5.14. In all cases, the CNTs appeared as SWNTs. TEM measurements show a range of diameters varying from 1.2 to 2.5 nm. This compares to a range of $1.7 - 2.0$ nm obtained from Raman measurements on the samples given a carbon implantation. These measurements indicate that the low frequency cut-off of the Raman notch filter prevent thicker CNTs from being observed and that the true maximum diameter is 2.5 nm. Often, as shown in Figure 5.14, the

TEM images show CNTs attached to particles with a size of tens of nanometres, although we have not been able to determine if the CNTs originate from any specific features on these particles. EDS spectra show the presence of Ge and oxide in the nanoparticles. Other peaks of carbon and Cu come from the carbon-coated Cu grid and a peak of Si originates from the Si substrate. No contamination from transition metals has been found.

5.8 Conclusions

In this chapter, research on the use of Ge nanocrystals for SWNT growth was presented. A technique of producing a good density of CNTs compatible with complementary metal oxide semiconductor processing was demonstrated. The results indicate that Ge implantation into a SiO_2 layer provides good control over the morphology of the nanoparticles and delivers a well-controlled CNT growth process. A SWNT area density of 4.1 ± 1.2 μm in length/μm^2 was obtained from the Ge nanocrystals under the optimum growth conditions.

FE-SEM and AFM analyses show that good control over nanocrystal size and density is possible with this technique. Three sizes of nanocrystal were fabricated by annealing a 30 nm SiO_2 layer subjected to Ge ion implantation (20 keV, 5×10^{15} cm^{-2}) at 600 °C, 800 °C or 1000 °C. The size of the nanocrystals fabricated were 1.8 ± 0.7, 2.9 ± 0.9 and 6.1 ± 1.4 nm, respectively. It is strongly believed that these nanocrystals are formed by Ostwald ripening, considering the initial conditions and processing undertaken [353, 354]. Photoluminescence measurements confirmed the presence of nanocrystals of varying sizes, and demonstrated a blue shift in luminescence energy as the nanocrystal formation anneal temperature decreased. This behaviour is in agreement with theoretical calculations presented in [360], and shows that the indirect band-gap energy of Ge nanocrystals is very sensitive to the size of the nanocrystals.

The uniformity of nanocrystal fabrication process was investigated, and found great variability between experimental batches. It is believed that this was variability was introduced during the HF etching step due to poor control over the flow of etchant. This problem could be overcome by a more rigorous approach to this step achieved by the use of a standardised HF vapour etching cell.

Following a CNT growth step, the Ge nanocrystals fabricated by annealing at 600 and 800 °C were able to catalyse the formation of CNTs. The nanocrystals fabricated by annealing at 1000 °C failed to produce any CNTs, most likely due to the size of the nanocrystals being too large. A higher CNT yield was obtained for the nanocrystals annealed at 600 °C owing to the high initial nanocrystal density. It could also be argued that the morphology of the nanocrystals fabricated at this anneal temperature is more conducive to CNT formation, however further experimentation is required to prove this.

It was determined that a hydrogen pretreatment step is effective in increasing the CNT area density and is critical for CNT growth from semiconductor nanoparticles. Without a hydrogen pretreatment step, CNT growth was only possible at one temperature, 950 °C, and the yield was low. In contrast, CNTs were found in samples pretreated at a temperature in the range from 850 °C to 950 °C. Pretreatment in hydrogen increased the yield of the process by a factor of three. It is believed that the hydrogen pretreatment step is required to reduce the oxide on the surface of the nanocrystals.

Selected wafers were implanted with carbon at a dose of 3×10^{16} cm^2 and a energy of 30 keV after Ge nanocrystal formation (at 600 °C) and HF vapour etching to expose the nanocrystals. Unlike the non-implanted samples, CNTs were found for all of the pretreatment temperatures, indicating a wider process window. Additionally, the area density of CNTs was significantly higher for all samples. The highest CNT density, for both implanted and non-implanted samples, is obtained by pretreatment in hydrogen at 900 °C followed by a CNT growth at 850 °C. For these growth conditions, there is no statistically significant advantage to the carbon implantation in terms of area density. However, the results show that successful CNT growth is achieved for a wider range of growth conditions, particularly higher growth temperatures. If higher growth temperatures are used, successful growth can be attained without the pretreatment step. AFM measurements show that samples without a carbon implantation show a drastic reduction in nanoparticle density as pretreatment temperatures increase, with almost no Ge nanocrystals present after pretreatment at 1000 °C. In contrast, the samples with a carbon implantation show little reduction in Ge nanocrystal density as pretreatment temperatures increase. This improvement is believed to be due to an increase in melting point via the formation of a $Ge_{1-y}C_y$ alloy and is responsible for the wider process window.

The CNT area density of 4.1 ± 1.2 μm in length/μm^2 is comparable to densities reported for CNT-FET fabrication. For example, many groups have reported experimental CNT-FETs fabricated with SWNT area densities of less than 1.5 μm in length/μm^2 [367, 368]. The CNT density achieved in this work is satisfactory for CNT-FET based applications in sensors, logic, and memory devices.

Chapter 6

Colloidal Ge Nanoparticle Catalyst for CNT Synthesis

Presently, at least five different non-metallic materials have been shown to enable the formation of SWNTs. The first of these is SiC, which has has been shown to work both in the form of macroscopic flat substrates and nanoparticles [265, 266, 266]. The second material shown to produce CNTs was carbon nanoparticles [267, 268]. While bundles of SWNTs have been produced using carbon nanoparticles, Raman spectra suggest that the SWNTs are structurally defective and that the bundles of nanotubes produced in this way may not be suitable for many electronics applications. Both of these methods differ from more standard metal catalysed-growth in that the source of carbon for the formation of SWNTs is the catalyst material itself, rather than a carbon containing gas. Our group has previously published a method for growing SWNTs on SiGe islands or Stranski-Krastanow Ge dots using a standard CVD process with growth temperatures down to 850 °C [10, 283]. This work has been supported by the results of Takagi et al. [11] on the growth of SWNTs from Si and Ge nanoparticles on SiC substrates.

In this chapter, a second novel approach for the growth of CNTs using Ge nanoparticles is presented. The nanoparticles were synthesized from solution by means of an inverse micelle technique, and suspended in tryoctylamine. The colloidal Ge nanoparticle catalyst is found to be a viable catalyst for the synthesis of SWNTs from a silicon dioxide support. The results indicate that the inverse micelle technique provides good control over the morphology of the nanoparticles and delivers a well-controlled CNT growth process. A SWNT area density of 5.2 ± 0.7 μm in length/μm^2 was obtained from the colloidal Ge nanoparticles under the optimum growth condition. This process has the advantage of being amenable to large-scale manufacturing by means of a floating catalyst approach and offers the possibility of CNT synthesis on a variety of support materials.

6.1 Experimental Details

Ge nanoparticles were synthesized in solution by means of an inverse micelle method by Dr. B. M. Mazumder from the School of Chemistry in the University of Southampton. The synthesis of a $Ge[N(SiCH_3)_2]_2$ precursor for the formation of Ge nanocrystals was based on the works of Lessing et al. [370, 371], with some minor modifications. The precursor (50mg) was dissolved in 7 ml of trioctylamine and injected into hot (340 °C), molten hexadecylamine (HDA, 1g). The injection method was inspired by various publications and has been standardised for this purpose [372, and references therein]. The residue was then dissolved in toluene, re-precipitated with methanol and suspended in trioctylamine. Four concentrations were prepared, 4 mM, 3 mM, 2 mM and 1 mM. This process yielded nanoparticles with a narrow size distribution, shown in Section 6.2.1.

$< 001 >$ oriented, p-type silicon ($17 - 33$ Ωcm resistivity) with a 300 nm SiO_2 layer were used as substrates. In selected experiments, R-cut sapphire wafers (r-Al_2O_3, supplied by IDB Technologies) were utilised. All supports were cut to 10×10 mm pieces to suit a one-inch diameter furnace tube. The Ge catalyst was deposited by spin-coating 40 μL of the Ge solution at a rotation speed of 4000 RPM for 45s. Samples were then subjected to a 100W O_2 plasma for 30 minutes to remove any residual organic left from deposition. All substrates were prepared under clean room conditions.

CNTs were grown using a two step-growth process. The first step was a H_2 pretreatment anneal and the second step was CNT growth by thermal CVD perfomed in a hot-wall reactor at atmospheric pressure. The wafers were cut into 10×10 mm pieces to suit a one-inch diameter furnace tube. The CNT growth step was carried out using a mixture of methane (1000 sccm) and hydrogen (300 sccm) immediately following the H_2 (1000 sccm) pretreatment step. The pretreatment was performed at a temperature between 850 and 1100 °C for 2 to 10 minutes. The growth step was carried out a temperature between 850 and 1000 °C for 20 minutes. A quartz furnace tube was used exclusively for this work to avoid metal contamination.

The Ge nanoparticles were characterised using a Veeco Multi-Mode atomic force microscope, using super sharp Si cantilevers (typical tip radius of 2 nm). Particle height distributions for each sample were determined using a minimum of ten 1 μm^2 AFM images utilising the Veeco Nanoscope software package. Images were first flattened using a three point levelling technique, and a threshold height of 0.5 nm was set in the particle detection software. The synthesized CNTs were observed by field-emission scanning electron microscope (JEOL 6500F) and transmission electron microscope (JEOL 3050 and JEOL 4000HR). Transmission electron microscopy sample preparation consisted of scraping the sample surface with a surgical blade and transference onto a carbon-coated Cu grid. The chemical compositions of SEM samples were analysed by energy-dispersive

X-ray spectroscopy (Oxford Instruments INCA Microanalysis System). The area densities of CNTs were evaluated using FE-SEM images using ImageJ to determine the total contour length of CNTs [315]. For quantitative analysis, several images taken from the same sample were used, with overlapping regions being discarded. Raman spectra were obtained using a Renishaw micro-Raman system with three laser excitation energies (532, 632.8 and 785 nm) with a power of 12 mW.

6.2 Catalyst Characterisation

To characterise the Ge nanoparticles; transmission electron microscopy, atomic force microscopy and photoluminescence spectroscopy were undertaken. A study of the nanoparticle size distribution was performed using both TEM and AFM in order to characterise and optimise the synthesis process.

6.2.1 Catalyst Morphology

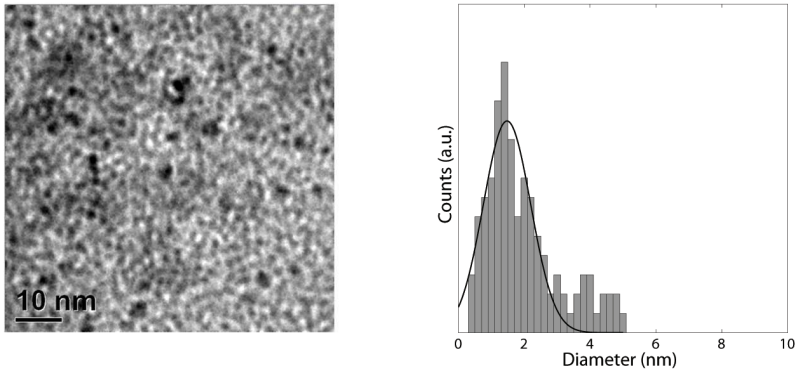

(a) (b)

FIGURE 6.1: (a) Transmission electron microscope image of the as synthesized Ge colloid powder suspended in trioctylamine and drop casted onto a carbon coated Cu grid. Scale bar corresponds to 10 nm. (b) Histogram of the diameter distribution of the nanoparticles, generated from 8 images.

Figure 6.1 shows a transmission electron microscopy image of Ge nanoparticles produced by an inverse micelle technique method and an associated particle size distribution, generated from 8 TEM images. In order to obtain these images, a very low dilution of the colloidal Ge nanoparticle solution was drop casted onto a carbon-coated Cu grid. The required dilution was determined by an empirical serial dilution of the colloidal nanoparticle solution. The TEM image shown in Figure 6.1(a) shows several dark spots, in which EDS analysis indicated high levels of Ge present, which were assumed to be the Ge colloidal nanoparticles. Figure 6.1(b) shows the particle size distribution the

the colloidal Ge nanoparticles. This result shows that the half-maximum counts of the particle size lie between 0.7 and 2.1 nm. This range of nanoparticle sizes was as expected, as the partial separation of the halide salt and reductant into hydrophilic and hydrophobic regions of the inverse micelles permits some control over size distribution [373]. This distribution indicates that some of the nanoparticles are considerably larger than 3 nm, indicating aggregation of the nanoparticles into larger clusters. This is most likely due to the deposition onto the carbon-coated Cu grids as opposed to poor control over the nanoparticle synthesis. The distribution shown in Figure 6.1(b) exhibited a single mode and has been fitted with a normalised, Gaussian curve ($R_2 = 0.916$) centred at 1.4 ± 0.7 nm.

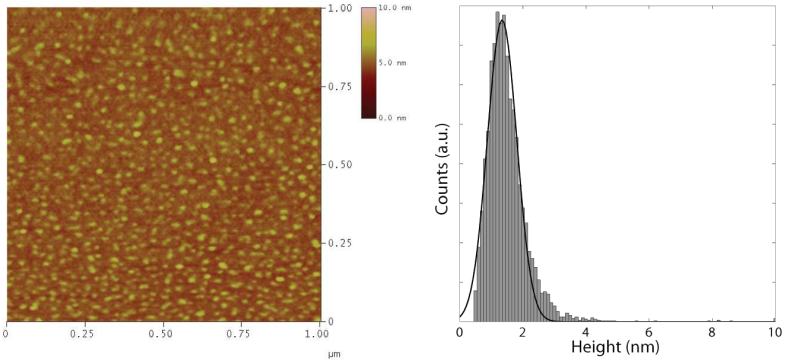

(a) (b)

FIGURE 6.2: (a) Atomic force miscroscope image and (b) particle height distribution of Ge nanoparticles dispersed on a SiO_2 support at 1 mM dilution. Particle size distribution has been fitted with a non-centred, normalised Gaussian.

To verify the particle size distribution of the colloidal Ge nanoparticles, AFM analysis was performed after spin coating and O_2 plasma treatment of 1 mM diluted solution on SiO_2 substrates. Figure 6.2(a) shows a typical AFM topography image of the Ge nanoparticles fabricated by an inverse micelle technique. This image shows a high density of local maxima in the topography scan, and each peak is believed to be an individual nanoparticle. The measurements indicate a density of 530 ± 60 (mean $\pm$ standard deviation) particles/μm^2, which corresponds to an interparticle separation of 43 ± 3 nm. Figure 6.2(b) shows the particle height distribution for several images taken from the 1 mM Ge nanoparticle sample. This distribution has been fitted with a normalised, non-centred Gaussian ($R_2 = 0.990$), which shows a modal height of 1.4 nm and a standard deviation of 0.5 nm, matching the results obtained by TEM. Due to the higher number of nanoparticles observed in this technique, this distribution is considered to be more accurate than that derived from TEM images.

6.2.2 Optical Properties of Colloidal Ge Nanoparticles

The reaction carried out by the method outlined in the experimental section produced Ge colloids at different molar concentrations. It was found that the stability of the Ge colloid has the following tendency. For lower concentrations (1 mM), after a fraction has flocculated, the colloid remained stable and in suspension for a few weeks. At higher concentrations (10 mM), the colloids coagulate within a few days. Qualitatively, the colloids synthesized are transparent, but they turn whitish when the Ge particles have flocculated. In general, Ge colloids obtained by this method are kinetically unstable [374]. This instability is due to the high reactivity of Ge nanoparticles.

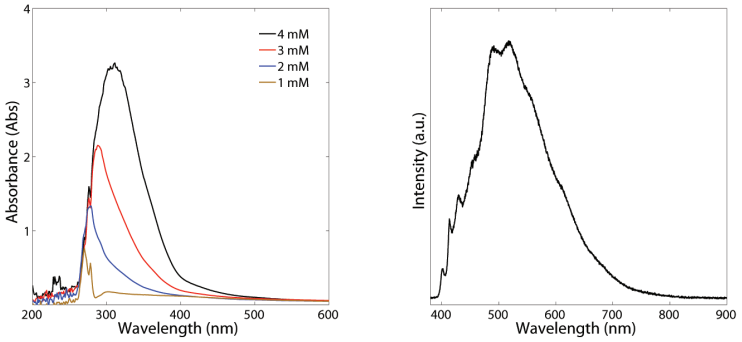

(a) (b)

FIGURE 6.3: (a) UV-Visible Absorption spectra of Ge nanoparticles synthesized by inverse micelle method and suspended in trioctylamine at three dilutions 1 mM, 2 mM, 3 mM and 4 mM. (b) Room temperature photoluminescence spectra of Ge nanoparticles dispersed on a SiO_2 support at 1 mM dilution. PL measurements were undertaken using a 364 nm Ar-ion laser excitation with a power of 50 mW with a spot size of 3 μm.

Figure 6.3(a) shows the absorption spectra of the Ge colloid at four concentrations, exposed to the air, in the $200-600$ nm range. For the UV-Visible absorption study, 0.01 ml of each concentration of the colloidal solution was diluted in hexane (3 ml) to decrease the high absorption and prevent the particle agglomeration. The diluted colloid was placed in a a rectangular quartz cell of of 1 cm of optical path length and analysed in a Spectronic Genesis 2 Spectrophotometer. A blank of pure hexane was examined before every sample to eliminate solvent absorption. The spectra shows a change in absorbance as the concentration of the colloid is decreased, as was expected. However, the spectra for the higher concentration colloidal solutions show a broader characteristic, with the onset of absorbance occurring at longer wavelengths. This suggests that the higher concentrations have a broader range of nanoparticle sizes, resulting in a shift toward lower energy values [375]. This is most likely due to aggregation of colloidal nanoparticles. The nanoparticles measured absorb strongly in the ultraviolet region ($250-300$ nm) allowing us to suggest that these Ge nanoparticles are quantum confined. Although the UV-Vis spectra in this figure are not presented as measurements of band-gaps, the

absorption onset seen in this figure are of similar energy [373] and are expected to scale inversely with mean particle size in accordance with quantum confinement models.

The spectra in Figure 6.3(b) demonstrates luminescence in the blue-to-violet region of the spectrum. The shift in energy of the PL maxima is over 2 eV. This large shift is reproducible and consistent between samples of similar mean size. While some of the shift may be a result of surface effects, it is primarily because of quantum confinement. Ge nanoparticles $2 - 4$ nm in diameter prepared in inverse micelles using $LiAlH_4$ as a reductant show a similar shift in PL spectra [376]. Recent X-ray absorption measurements of butyl-terminated Ge nanoparticles prepared by the Zintl salt metathesis also showed approximately a 2 eV shift of the conduction band [377].

6.3 Catalyst Deposition

Figure 6.4(a)–(d) shows scanning electron microscope images of the topography of Ge colloidal particles deposited by various techniques. The SEM image of the colloidal particles drop-casted onto the substrate in Figure 6.4(c) shows a high density of Ge particles with little dispersion. This particle aggregation is most likely due to attractive lateral capillary forces and convective particle flux caused by solvent evaporation [37, 378]. Figure 6.4(a) shows Ge particles deposited by dipping the substrate in the colloidal solution. This technique showed better dispersion of particles in comparison to the drop-casting method. Figure 6.4(b) shows Ge particles deposited by dipping the substrate in the colloidal suspension and rinsing in deionised water. This technique shows a lower density of particles, however there are larger aggregation sites. The best dispersion of particles was obtained by spin coating the substrate with the colloidal solution, as is shown in Figure 6.4(d). This result is in agreement with the literature. Jeong et al. [153, 379] reported that the deposition of the catalyst by spin coating prevented particle aggregation. Moreover, it has been reported that by using a viscous solution it is possible to obtain uniform particle distribution without agglomeration when spin coating [380].

6.4 Effect of Catalyst Dilution

Figure 6.5 shows SEM images of CNTs synthesized from the Ge colloidal nanoparticles dispersed on a SiO_2 support for each dilution. The samples were fabricated at the optimum condition for the catalyst; H_2 pretreatment at 1000 °C for 2 minutes, followed by the CNT growth step for 20 minutes at 850 °C in a mixture of H_2 and CH_4 ($1 : 3$ gas ratio). Figure 6.5(a) and Figure 6.5(b) show a representative SEM image of the 4 mM and 3 mM concentrated solution samples after the CNT growth step, respectively. In these samples, no CNTs were detected and the catalyst appeared to have agglomerated into a film. There is one type of nanostructure present in these samples; short, thick

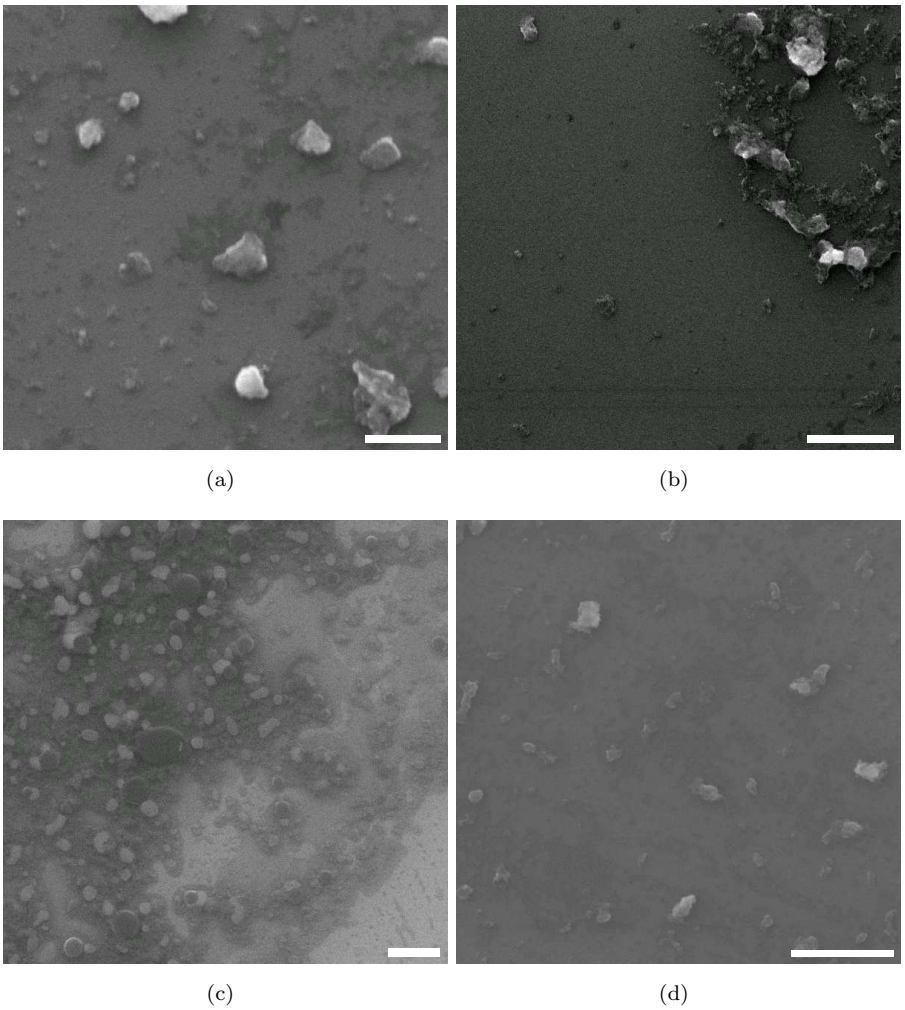

FIGURE 6.4: Scanning electron microscope images of Ge nanoparticles deposited on a SiO_2 support at 4 mM dilution by various techniques; (a) dip coated, (b) dip coated and rinsed in H_2O, (c) drop-casted and (d) spin coated. Scale bar corresponds to 500 nm.

fibres, approximately 20 nm in diameter and 0.5 μm in length. These fibres are present after the pretreatment step for all concentrations of the Ge colloidal nanoparticles, and PL and TEM measurements have shown that these are composed of amorphous silicon oxide (Section 6.7). Figure 6.5(c) shows an SEM image of the 2 mM concentrated solution sample after the CNT growth step. This sample showed a good density of CNTs, 3.6 ± 1.2 μm in length/μm^2 and a fairly homogeneous coverage across the sample. The 1 mM Ge colloidal nanoparticle solution sample, shown in Figure 6.5(d) showed the highest yield of CNTs and excellent uniformity across the sample, 5.2 ± 0.7 μm in length/μm^2. It is believed that lower concentrations of the Ge colloidal nanoparticle solution were more successful in synthesizing CNTs due to a larger interparticle separation, preventing agglomeration upon anneal.

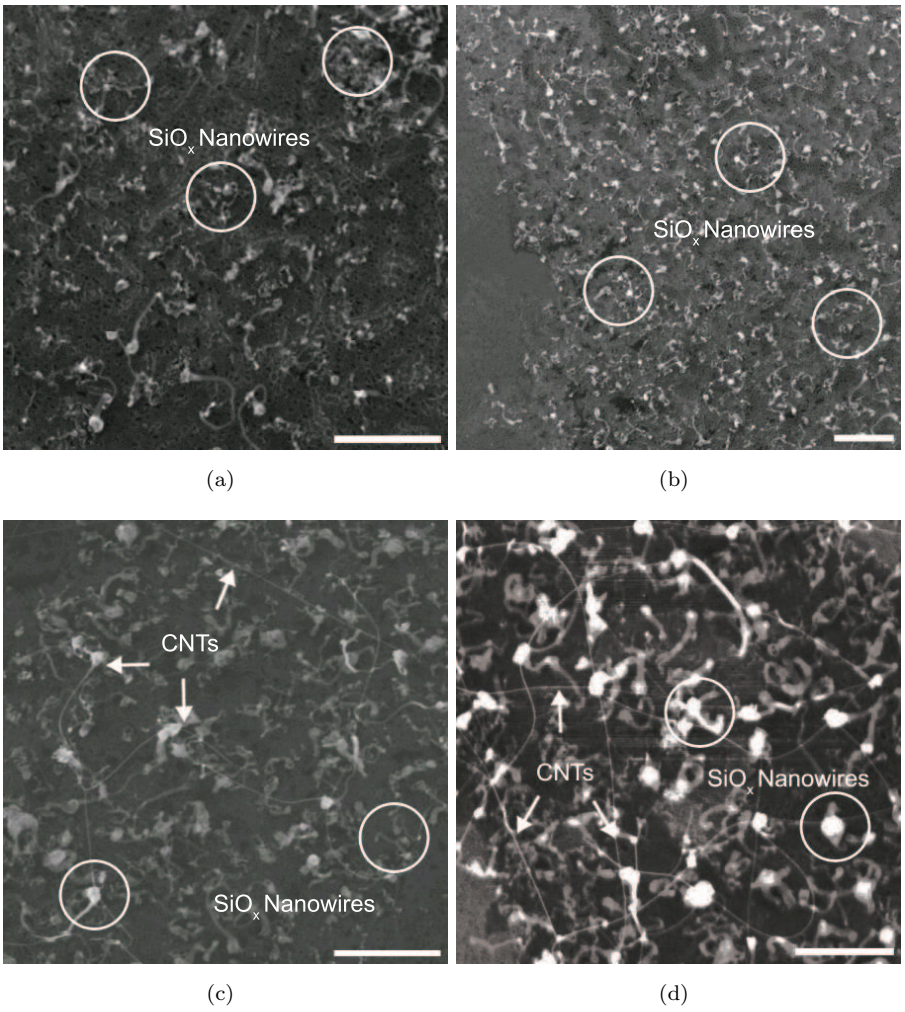

FIGURE 6.5: Scanning electron microscope images of CNTs synthesized from colloidal Ge nanoparticles dispersed on a SiO_2 support at four dilutions; (a) 4 mM, (b) 3 mM, (c) 2 mM and (d) 1 mM. Scale bar corresponds to 250 nm. CNTs were grown at the optimum growth condition, H_2 pretreatment at 1000 °C for 2 minutes, followed by the CNT growth step for 20 minutes at 850 °C in a mixture of H_2 and CH_4 (1:3 gas ratio).

6.5 Effect of Catalyst Pretreatment

Figure 6.6 shows FE-SEM images of CNT growth at various temperatures using a 1 mM Ge nanoparticle colloidal solution dispersed on a SiO_2 support. The growth temperatures shown in Figure 6.6(a)–(d) are 1000, 950, 900 and 850 °C, respectively. These images show aggregation of the catalyst into large clusters, and no presence of CNTs. Additionally, no SiO_x nanowires were detected.

Figure 6.7 shows FE-SEM images of the 1 mM Ge nanoparticle colloidal solution dispersed on a SiO_2 support after a 850 °C CNT growth step. Figure 6.7(a) shows the topography of a sample without a catalyst preparation anneal prior to growth. This image shows large aggregations of Ge particles throughout the sample surface. This sample showed no evidence of CNTs. Figure 6.7(b) shows the topography of a sample subjected

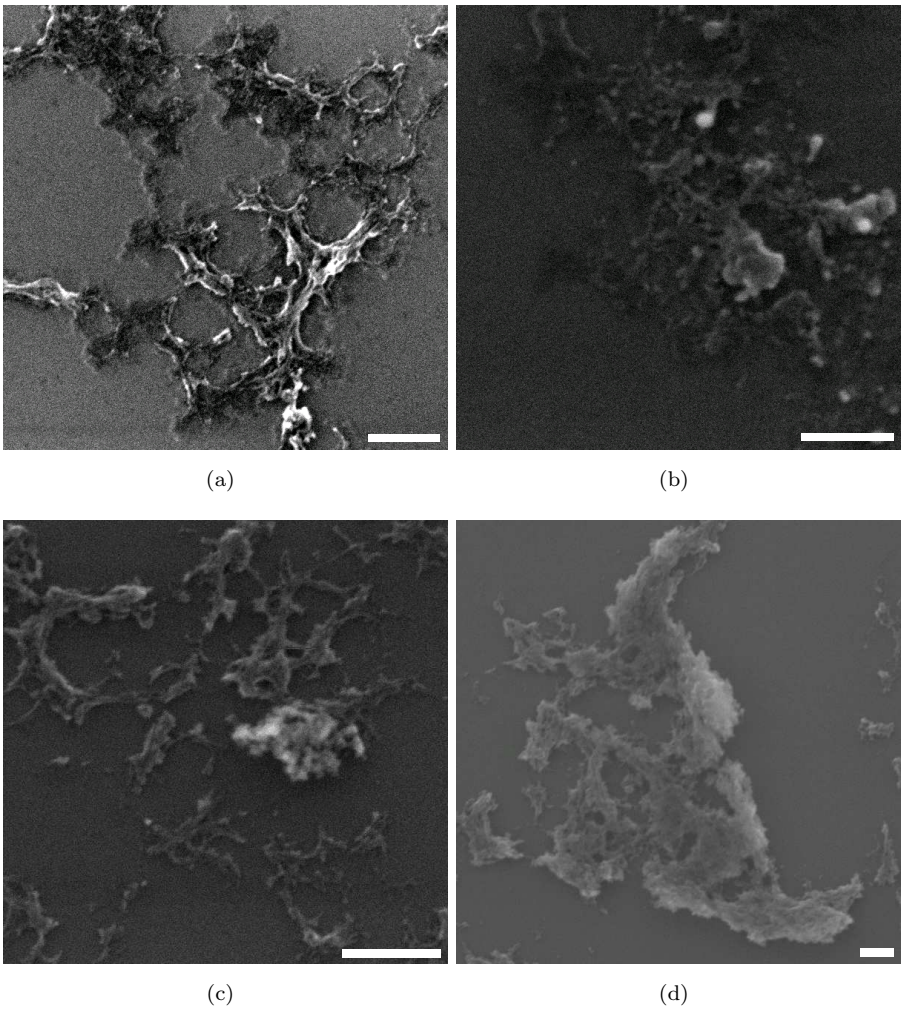

FIGURE 6.6: Scanning electron microscope images of CNTs synthesized from colloidal Ge nanoparticles dispersed on a SiO_2 support at a 1 mM dilution. The CNTs were grown at (a) 1000 °C, (b) 900 °C, (c) 950 °C and (a) 850 °C in a mixture of H_2 and CH_4 (1:3 gas ratio) for 20 minutes. Scale bar corresponds to 250 nm.

to a 1000 °C pre-anneal in H_2 prior to growth. This sample showed a good density of CNTs (shown in Figure 6.5(d)), in addition to some SiO_x nanowires. Additionally, the Ge particles on the surface appear re-dispersed (in comparison to the topography of the sample prior to growth, shown in Figure 6.4(d)), indicating that a catalyst preparation anneal is necessary to reduce the catalyst particles. Reports from the literature state that this particle-size reduction may be due to evaporation during thermal annealing [379]. The results presented in this work suggest that the catalyst pretreatment step also affects the morphology of the supported catalyst. A study of the effect of pretreatment on catalyst morphology will be discussed in further detail below.

Figure 6.8 shows FE-SEM images of the 1 mM Ge nanoparticle colloidal solution dispersed on a SiO_2 support after a 850 °C CNT growth step following a catalyst pretreatment anneal in H_2 at at various temperatures. The samples shown in Figure 6.8(a)–(c) were pretreated at 1000 °C for 2 minutes, 5 minutes and 10 minutes, respectively. The

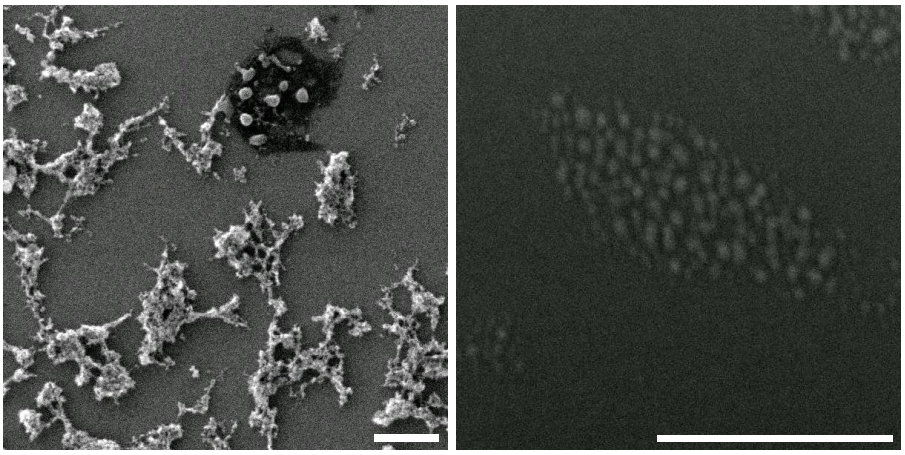

(a) (b)

FIGURE 6.7: Scanning electron microscope images of Ge nanoparticle aggregation and redispersion after CNT growth. Ge nanoparticles were dispersed on a SiO_2 support at a 1 mM dilution and subjected to a CNT growth step at 850 °C; (a) without a catalyst pretreatment anneal (b) with a 1000 °C pretreatment in H_2 prior to the growth step. Scale bar corresponds to 250 nm.

pretreatment temperatures shown in Figure 6.8(d)–(f) are 950, 900 and 850 °C for 10 minutes, respectively. These images establish the optimum growth conditions for the colloidal Ge nanoparticle catalyst and provide an insight to the importance of the catalyst pretreatment step. CNTs and SiO_x nanowires were found in all samples, with the highest CNT area density found in the samples pretreated at 1000 °C for 2 minutes, shown in Figure 6.8(a). All images show that the presence of CNTs correlates with the regions where Ge nanoparticles are present. No CNTs were found in regions of the sample where no nanoparticles were present. These results indicate that a H_2 pretreatment is essential for CNT formation and allows a wide process window. The CNT area densities for different pretreatment temperatures are summarised in Table 6.1.

The hydrogen pretreatment is effective in increasing the CNT area density and is critical for CNT growth from semiconductor nanoparticles. As is the case with the Ge nanocrystals formed by implantation, we believe that the hydrogen pretreatment step is required to remove residual contaminants on the surface of the nanoparticles. While the nanoparticles were subjected to a 100W O_2 plasma for 30 minutes to remove any residual organic left from deposition, there would undoubtedly have been some residual contaminants (i.e. oxide or solvent) present on the surface of the Ge nanocrystals.

In order to confirm that the CNT growth is catalysed by the Ge nanoparticles and not any systematic contaminant, a control sample was fabricated at the optimum growth condition. The control sample was subjected to the same deposition and cleaning process as the Ge particle samples, however no Ge was suspended in the solvent. This sample was pretreated at 1000 °C in H_2 for 2 minutes and exposed to the CNT growth step at 850 °C in a mixture of CH_4 and H_2 (3 : 1 ratio). No CNTs were found in this sample.

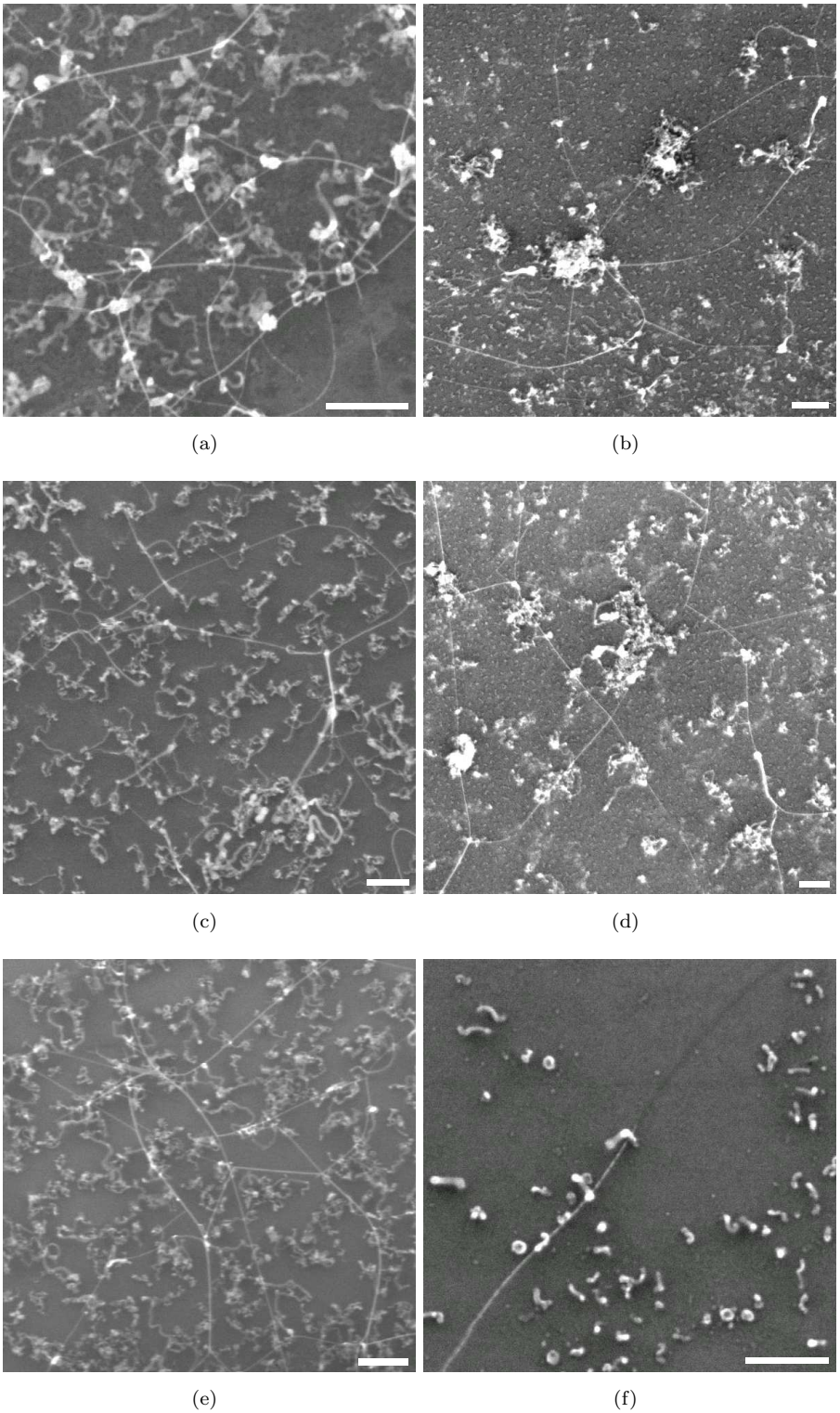

(a) (b)

(c) (d)

(e) (f)

FIGURE 6.8: Scanning electron microscope image of CNT growth using colloidal Ge nanoparticles dispersed on a SiO_2 support at 1 mM dilution. The CNTs were pretreated at four different temperatures; 1000 ^{c}ircC for (a) 2 minutes, (b) 5 minutes, (c) 10 minutes, (d) 950 °C, (e) 900 °C and (f) 850 °C in H_2 for 10 minutes. The subsequent CNT growth step was kept constant at 850 °C in a mixture of H_2 and CH_4 (1 : 3 gas ratio) for 20 minutes. Scale bar corresponds to 250 nm.

Pretreatment		CNT Growth		CNT area density
Temperature (°C)	Time (min)	Temperature (°C)	Time (min)	(μm in length/μm^2)
N/A	N/A	1000	20	No CNTs
N/A	N/A	950	20	No CNTs
N/A	N/A	900	20	No CNTs
N/A	N/A	850	20	No CNTs
850	10	850	20	1.3 ± 0.6
900	10	850	20	2.2 ± 0.9
950	10	850	20	4.4 ± 1.1
1000	10	850	20	3.8 ± 1.2
1000	5	850	20	4.3 ± 0.5
1000	2	850	20	5.2 ± 0.7

TABLE 6.1: CNT area densities for different pretreatment temperatures and CNT growth temperaures. Samples were grown using 1 mM Ge nanoparticle colloidal solution dispersed on a SiO_2 support.

Additionally, EDS analysis has been undertaken in all the sample regions which showed CNTs, and regions which showed contaminants were discarded from subsequent analysis. However, it should be noted that at this scale, the sensitivity of EDS is low.

The results summarised in Table 6.1 suggest that the H_2 pretreatment step has a strong effect on the yield of the process. The different area densities observed for each pretreatment temperature are assumed to be due to a change in the nature of the catalyst upon pretreatment. In order to determine the morphology of the catalyst after pretreatment, AFM characterisation of the 1 mM colloidal Ge nanoparticle catalyst has been undertaken for the range of pretreatment temperatures discussed in Section 6.5.

From typical AFM images on samples after pretreatment temperatures between 1000 and 850 °C, the mean density of particles has been determined. The initial particle density of 530 ± 60 (mean $\pm$ standard deviation) particles/μm^2 is reduced to 405 ± 28, 370 ± 22, 348 ± 53 and 322 ± 77 particles/μm^2 after pretreatment at 850, 900, 950 and 1000 °C respectively. It is evident that with an increase in pretreatment temperature there is an associated reduction in nanoparticle density. It is likely that this reduction in due to nanoparticle evaporation or ripening. It should be noted that the reduction in nanoparticle density is far less pronounced than that which occurred with the Ge nanocrystals formed by implantation (discussed in Chapter 5). This difference is most likely due to the differences in surface termination of the colloidal nanoparticles. The issue of surface termination is often overlooked because most of the interesting properties of nanoparticles depend primarily on their size. However, particles from $2 - 10$ nm in diameter, which is the size range of interest for quantum confined nanoparticles, have enormous surface areas. They also oxidise more rapidly than bulk material due to a

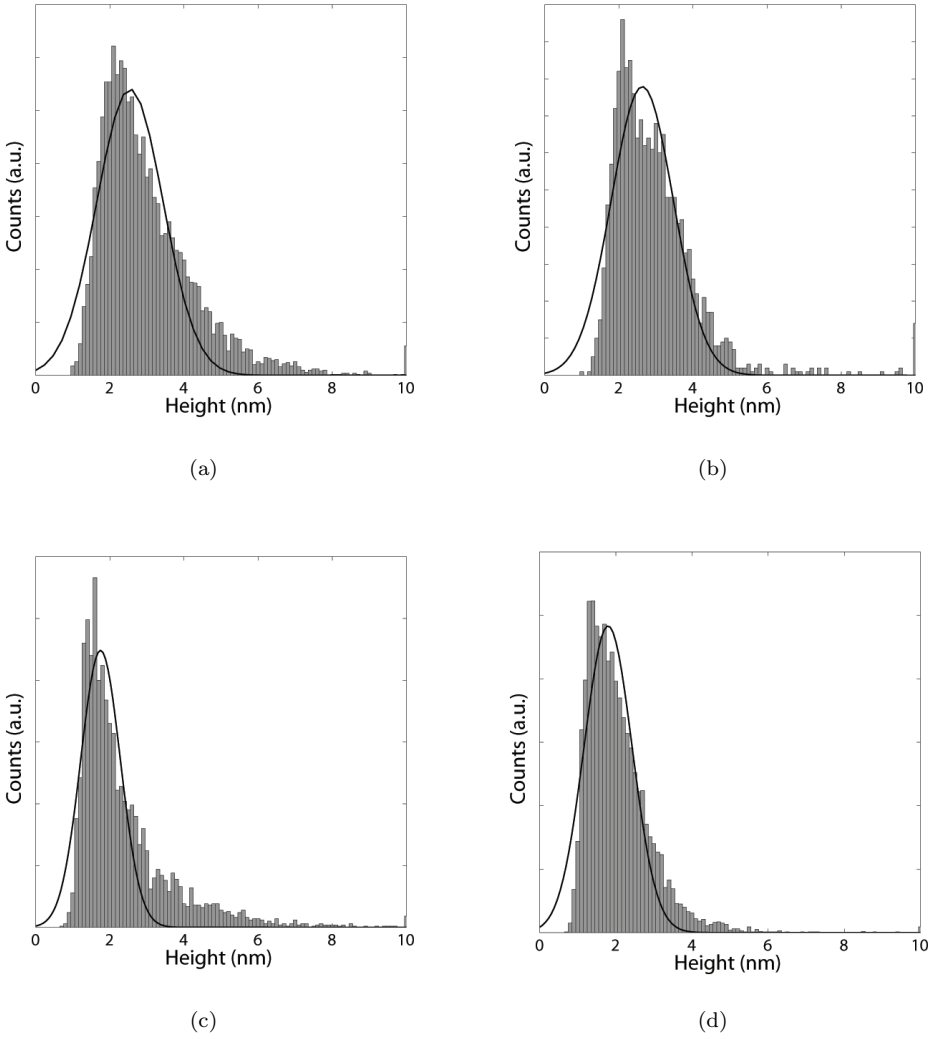

FIGURE 6.9: Particle size distribution for 1 mM diluted colloidal Ge catalyst dispersed on a SiO_2 support after pretreatment in H_2 for 10 minutes at; (a) 1000 °C, (b) 950 °C, (c) 900 °C and (d) 850 °C. Particle size distributions have been fitted with a non-centred, normalised Gaussian.

larger proportion of surface-bound atoms. Additionally, unlike Si nanoparticles, the surface oxide of Ge does not effectively passivate the nanoparticle surface. For the Ge nanoparticles prepared by this inverse micelle technique, it is thought that due to the synthesis process they would have H-terminated surfaces [373].

Figure 6.9(a)–(d) show the particle height distribution for samples pretreated in H_2 for 10 minutes at 1000 °C, 950 °C, 900 °C and 850 °C respectively. Each distribution has been fitted with a non-centred, normalised Gaussian. Table 6.2 summarises the Ge nanoparticle size distribution parameters immediately after pretreatment. This data shows that there is an increase in the modal height of the nanoparticles as the pretreatment temperature increases. There is also a broadening of the distribution as

Pretreatment		Distribution Statistics			Nanoparticle Density
Temperature (°C)	Time (min)	Mode (nm)	Mean (nm)	R_2 (nm)	(particles/μm^2)
850	10	1.4 ± 0.6	2.0	0.961	405 ± 28
900	10	1.6 ± 0.7	2.4	0.933	370 ± 22
950	10	2.4 ± 0.8	3.0	0.955	348 ± 53
1000	10	2.5 ± 0.9	3.1	0.953	322 ± 77

TABLE 6.2: Particle size distribution fit parameters and nanoparticle densities for 1 mM colloidal Ge nanoparticle catalyst dispersed on a SiO_2 support after pretreatment at various temperatures.

the pretreatment temperatures increase, clearly shown by the increasing standard deviations. As pretreatment temperatures increase, the distributions show a reduction in the number of small particles and an increase in the mean particle size. This behaviour suggests phase coarsening, which occurs at the expense of small particles within a system which shrink and finally disappear [321]. This is a thermodynamically-driven process occurring because larger particles are more energetically favoured than smaller particles [322]. This process accounts for the slight reduction in nanoparticle density as pretreatment temperature increases.

There is a consensus in the literature concerning the correlation between the catalyst size and the CNT diameter. Many groups have observed a direct dependence of the two quantities [150–159]. Nikolaev et al. [189] observed that the catalyst particle tends to be slightly larger than CNT diameter, suggesting a growth mechanism involving graphene cap formation. This has been supported by high-resolution in-situ TEM observation of the catalytic growth of CNTs [36, 192]. The results presented in this section demonstrate that the size of the Ge nanoparticle catalyst after pretreatment is within the possible range to seed CNT growth. However, these results do not allow us to determine the reason for the higher CNT yield in samples pretreated at 1000 °C. One possibility may be that the slightly larger nanoparticles are more efficient at forming the graphene cap required to seed a CNT. Yet it is more likely that pretreatment at higher temperatures are more effective at removing residual contaminants or reducing the nanoparticles.

6.6 Characterisation of Synthesized CNTs

In Figure 6.10, representative Raman spectra are shown from samples synthesized using a 1 mM colloidal Ge catalyst dispersed on a SiO_2 support. The measured CNTs were grown using a pretreatment in H_2 for 2 minutes at 1000 °C, followed by a growth step at 850 °C in a mixture of H_2 and CH_4 (1 : 3 gas ratio) for 20 minutes. The Raman measurements were undertaken utilising a Renishaw in-Via system, consisting

of an Olympus Microscope, a monochromator with a 1200 groves/mm grating, a Peltier cooled CCD, holographic notch filter and a He-Ne (632.8 nm) laser excitation. The signal is collected via a backscatter geometry, with the holographic notch filter tuned so that the frequency cut-off was a shift of approximately 110 cm^{-1}. For this reason, the system is not able to detect RBMs from CNTs with diameters larger than 2.3 nm.

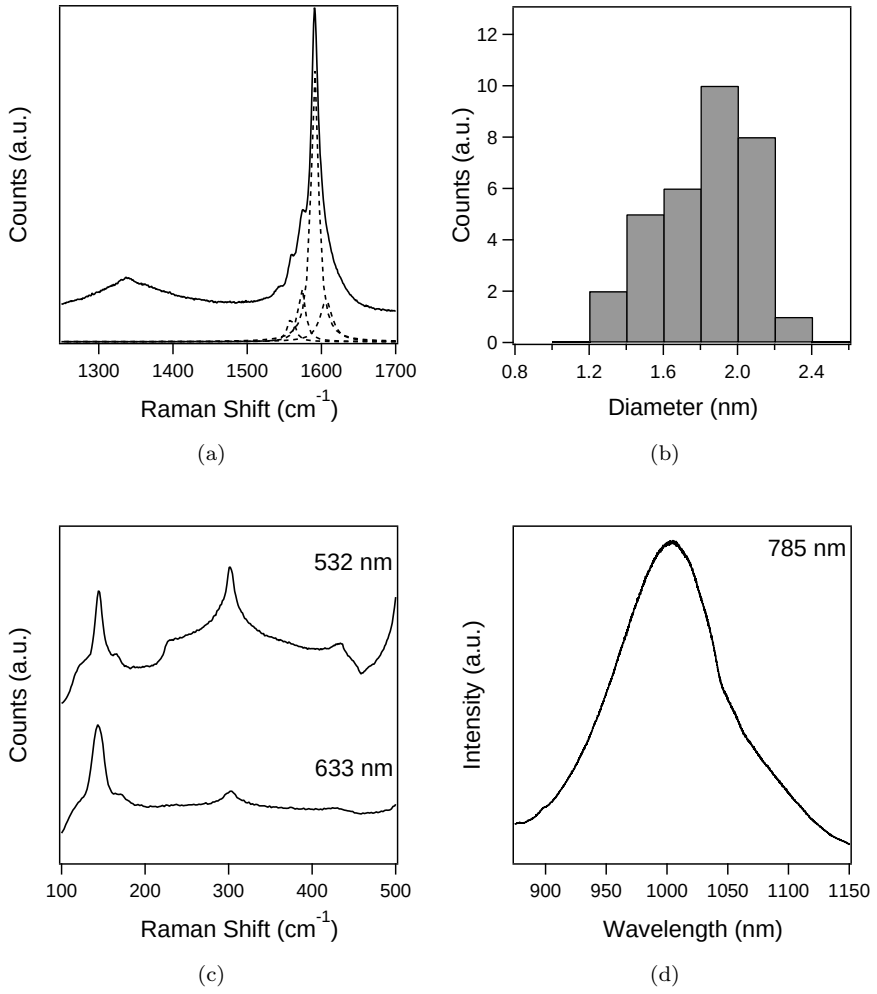

FIGURE 6.10: Raman spectra for the carbon nanotubes synthesized using 1 mM diluted colloidal Ge catalyst dispersed on a SiO_2 support after pretreatment in H_2 for 2 minutes at 1000 °C, followed by a growth step at 850 °C in a mixture of H_2 and CH_4 (1 : 3 gas ratio) for 20 minutes. (a) Typical G-band characteristic detected with 532 nm laser excitation, fitted with four Lorentzian curves. (b) Histogram of the SWNT diameters obtained via RBM. (c) Typical RBM modes detected with 532 and 633 nm laser excitation lines. (d) Broad luminescence exhibited when samples excited with 785 nm laser line.

The Raman spectra obtained from areas of relatively high CNT area density typically exhibited an asymmetric double peak at approximately 1590 cm^{-1} (Figure 6.10(a)). This double peak can be attributed to the Raman-allowed tangential mode of CNTs, G-band. In the representative spectrum shown in Figure 6.10(a), this feature could be fitted with four Lorentzian oscillators located at 1559, 1573, 1591 and 1606 cm^{-1}.

Group theory predicts that there are six Raman-active modes within the tangential G-band spectral region (1600 cm^{-1}) for general chiral SWNTs [112, 325]. The symmetry assignments used to fit the four Lorentzian features have been reported [112, 325], and are believed to be characteristic of a semiconducting tube. Indeed, assuming that the signal originates from a single, isolated nanotube, we can determine the signal to originate from a semiconducting tube of 1.62 nm diameter (using the relation $\Delta\omega_G = \omega_{G^+} - \omega_{G^-}$, as described in Section 2.4.5). This spectrum also exhibits a small D-band peak around 1320 cm^{-1}, which can be attributed to disorder in the CNTs. The ratio between the disorder induced D-band and the Raman allowed G-band (I_D/I_G)is approximately 0.1, suggesting that the nanotube is of a good quality in terms of structure and graphitisation.

Figure 6.10(c) shows typical spectra obtained in the region of $100 - 500$ cm^{-1} by two laser excitation lines, 532 nm and 633 nm at different sample locations. Due to a broad luminescence, shown in full in Figure 6.10(d), it was not possible to obtain Raman measurements in this region using a 785 nm laser excitation line. It is believed that this luminescence is caused by SiO_2 nanoparticles, arising from defects in the support used in these experiments [363, 381]. Figure 6.10(c) clearly shows the RBM feature, indicating the presence of SWNTs. In most cases, the RBM feature was detected in the region of $110 - 210$ cm^{-1}. Assuming the standard formula for converting Raman shift to CNT diameter, $\omega_{RBM} = 248/d_t$ as described in Section 2.4.4, this indicates that the CNTs observed by Raman scattering have diameters in the range of $1.2 - 2.3$ nm. A histogram of the SWNT diameters observed in the measurements via the RBM spectral feature is shown in Figure 6.10(b). It should be noted that since the measurements were only undertaken using two laser excitation lines these results do not provide a full diameter characterisation of the sample. The histogram indicates that the SWNT diameters observed have a modal peak of approximately 1.8 nm and appears to show a Gaussian distribution profile. Although no strong conclusions can be drawn from this fact, the nanotube diameters detected are of similar sizes to the particle size distributions shown in Figure 6.9, which showed a nanoparticle modal size of 2.5 ± 0.9 nm.

The Raman measurements are supported by transmission electron microscope measurements on a total of 5 CNTs synthesized from colloidal Ge nanoparticles dispersed on a SiO_2 support. Representative TEM images of these nanotubes are shown in Figure 6.11. In all cases, the CNTs appeared as SWNTs. TEM measurements show a range of diameters varying from 1.2 to 2.2 nm, which match the range of diameters obtained from Raman measurements. In most cases, the CNTs originated from a cluster of particles with a size of tens of nanometres, although it was not possible to determine if the CNTs originated from any specific feature in these particles. This is most likely due to the TEM sample preparation technique used, which consisted of scraping the sample with a surgical blade and transference onto a carbon-coated Cu grid.

As is demonstrated in Figure 6.11(a), the tip structure of the nanotubes measured showed a cone shape, with no nanoparticles present. This is indicative of a base-growth,

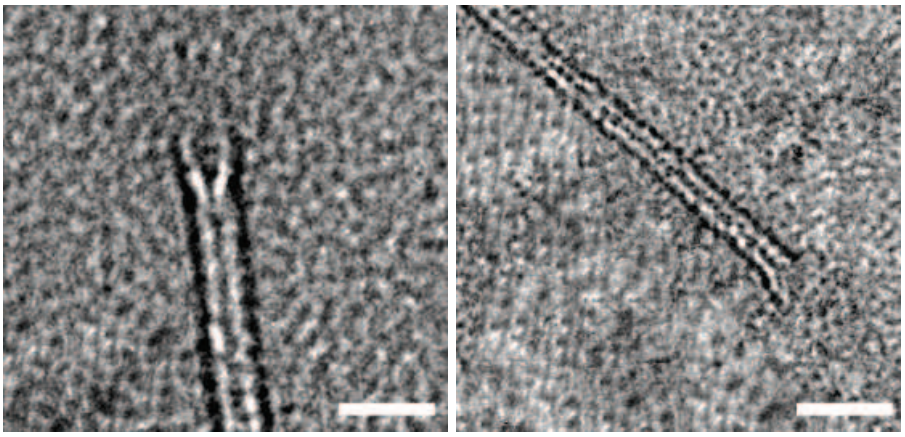

(a) (b)

FIGURE 6.11: Transmission electron microscope images of SWNTs synthesized from colloidal Ge nanoparticles dispersed on a SiO_2 support. CNTs were synthesized with a 1000 °C pretreatment in H_2 for 2 minutes, followed by a CNT growth step at 850 °C in a mixture of H_2 and CH_4 (1 : 3 gas ratio) for 20 minutes. Scale bar corresponds to 5 nm.

which supports a growth mechanism involving the formation of a graphene cap. Due to the size of the catalyst nanoparticles, the increasing fraction of low-coordinated atoms may lead to surface saturation followed by carbon precipitation, as reported by Takagi et al. [3]. Considering that carbon penetration inside small nanoparticles is unlikely [293], the growth of CNTs is most likely a process primarily controlled by surface diffusion [294, 295]. Indeed, it is believed by several groups that the rate-limiting factor in CNT synthesis is the surface diffusion of carbon across the catalyst [269].

Due to their nanometer dimensions, the mechanics of growth of nanotubes on nanoparticles are markedly different from the growth of carbon filaments. Other mechanisms are therefore required to explain the nucleation of CNTs from nanoparticle catalysts. One such model is the Yarmulke mechanism proposed by Dai et al. [188]. In the Yarmulke mechanism, a graphene cap is assembled on the particle surface with its edges strongly chemisorbed to the catalyst. The graphene cap acts to reduce the high total surface energy of the particle caused by its high curvature, owing to the fact that the basal plane of graphite has an extremely low surface energy. As additional carbon atoms are added, the hemifullerene cap formed on the particle surface lifts off, creating a hollow tube with constant diameter which grows away from the particle [189]. This model was supported by molecular dynamics simulations by Shibuta and Maruyama [190]. Recent works in high-resolution *in-situ* TEM observation of the catalytic growth of CNTs have verified this mechanism on nickel nanoparticles [36, 192]. These studies have also shown that cap stabilisation and nanotube growth involve reshaping of the catalyst nanoparticle.

6.7 Characterisation of SiO_x Nanowires

SiO_x nanowires were synthesized as a by-product of the growth process in several of the experiments conducted in this thesis. One dimensional SiO_x have recently attracted considerable research attention due to their unique optical properties and promising applications [382]. The stable and bright blue emission of SiO_x nanowires make them potential sources of high intensity light, near-field optical probes, waveguides, etc. However, the nanowire formation mechanism is unclear. The majority of reported fabrication methods are catalyst-based methods. To date, several different types of catalyst have been used, such as Au [383], Fe [384], Co [385], Ni [386] and Ge [387]. In most cases, the formation of SiO_x nanowires has been attributed to a vapour-liquid-solid mechanism (VLS) [47]. In this regime, a nanocluster serves as the critical point for nucleation and the addition of reactants from the vapour phase allows the formation of a nanowire underneath the catalyst cluster.

In this section, characterisation of the SiO_x nanowires synthesized using Ge colloidal nanoparticles is undertaken. Referring to the data presented throughout this thesis, a mechanism for nanowire formation is suggested. The results show that the possible growth mechanism for nanowire formation is the solid-liquid-solid (SLS) process.

Figure 6.12(a) shows a representative HR-TEM image of a SiO_x nanowire, synthesized as a by-product of the CNT synthesis process. In this case, the growth process was a pretreatment step in H_2 for 10 minutes at 1000 °C followed by the CNT growth step at 850 °C for 20 minutes in a mixture of CH_4 (1000 sccm) and H_2 (300 sccm). It should be noted that in all CNT growth experiments conducted in this thesis, no SiO_x nanowires were detected prior to the introduction of CH_4 in the growth step. There is no evidence of Ge nanoparticles or metal catalyst particles either at the tip or the base of the nanowires. All of the nanowires were isolated and did not form bundles. The diameter of the representative nanowire shown is approximately 10 nm; the complete diameter range observed by TEM was between 10 and 20 nm. EDS analysis of this nanowire revealed the presence of silicon and oxygen, in high concentrations. As expected due to the synthesis process, there was also the presence of a small carbon peak. Calculated compositions of the nanowire from the EDS analysis revealed the formation of an oxygen deficient silica phase (SiO_{2-x}).

The PL spectrum of SiO_x nanowires was measured using a 364 nm Ar-ion laser excitation with a power of 50 mW. Figure 6.12(b) shows the PL spectra of nanowires fabricated using a a pretreatment step in H_2 for 10 minutes at 1000 °C followed by the CNT growth step at 850 °C for 20 minutes in a mixture of CH_4 (1000 sccm) and H_2 (300 sccm). The PL spectra shows three distinguishable peaks at 415 nm (3.0 eV), 440 nm (2.8 eV) and 460 (2.2 eV). Repeated measurements were made in different regions of the sample and the same peaks were consistently seen in areas containing high density of nanowires, but not seen in areas where no nanowires were present. These bands are analogous to

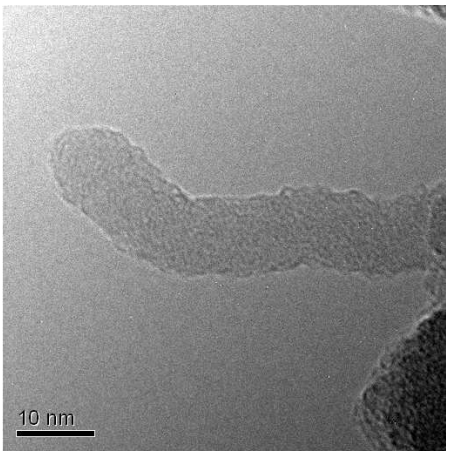

(a)

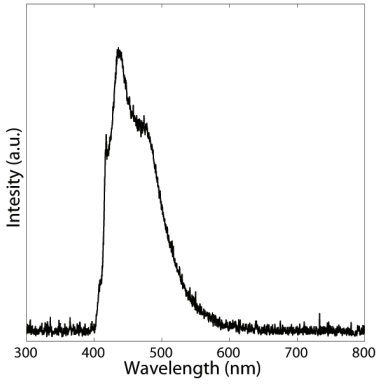

(b)

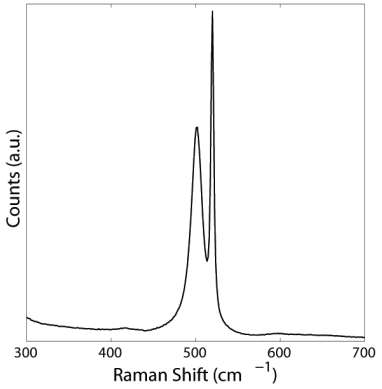

(c)

FIGURE 6.12: (a) Transmission electron microscope image of SiO_x nanowire, synthesized as a by-product of the CNT synthesis process. (b) Room temperature photoluminescence spectra of SiO_x nanowires undertaken using a 364 nm Ar-ion laser excitation with a power of 50 mW. (c) Raman spectra of SiO_x nanowires undertaken using a 532 nm laser excitation.

the PL spectrum bands usually observed in amorphous silica nanowires [340, 384]. For amorphous silica, the 2.7 eV band is ascribed to a neutral oxygen vacancy (≡Si-Si≡) [388], and the 3.1 eV band is due to a twofold coordinated silicon lone pair centres (O-Si-O) [389]. These defects are clearly induced by high oxygen deficiency in silica, as is expected with the high hydrogen content during the growth step from both H_2 gas and radicals from the decomposition of CH_4.

Figure 6.12(c) shows the Raman spectrum of SiO_x nanowires taken using a 532 nm laser excitation with a power of 12 mW. The spectrum demonstrates a sharp peak around 505 cm^{-1} in addition to the first order Raman peak at 520 cm^{-1} of crystalline Si. The FWHM of this peak is also considerably broader than that of crystalline Si, 17 cm^{-1} compared with 4 cm^{-1}. Similar peaks around 505 cm^{-1} have been reported in the literature for silica nanowires [383, 384, 390]. Indeed, Wang et al. [390] reported a shift in the first-order optical phonon to 505 cm^{-1} from 520 cm^{-1} when comparing a 10 nm

SiO_x nanowire with crystalline Si. This shift from the first order peak of crystalline Si is reported to be due to phonon confinement effects, which become more pronounced when the nanowire diameter is less than 22 nm [390].

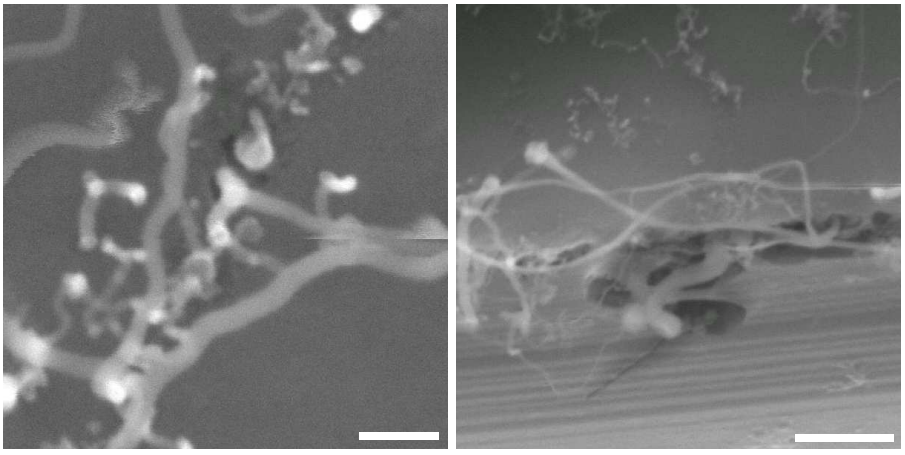

(a) (b)

FIGURE 6.13: Scanning electron microscope images of SiO_x nanowires, synthesized as a by-product of the CNT synthesis process. Colloidal Ge nanoparticles were dispersed on a SiO_2 support at 1 mM dilution, pretreated at 1000 °C in H_2 for 10 minutes and subjected to a CNT growth step at 850 °C in a mixture of H_2 and CH_4 (1 : 3 gas ratio) for 20 minutes. Scale bar corresponds to 1 μm. (a) Representative and (b) cross-sectional showing image showing pitting at the base of the nanowire.

Figure 6.13(a) shows a SEM image of the nanowires fabricated as described above. The SEM image shows that pits are created in the SiO_2 support surface. Indeed after the removal of the nanowires via a HF vapour etch, AFM line analyses showed pitting in the regions of high nanowire density. To confirm these observations, cross-sectional SEM images were undertaken. The samples were prepared using a Zeiss Focussed Ion Beam (FIB) with a liquid-metal Ga ion source to mill out a section of the support medium in an area of high SiO_x nanowire density. A representative cross-sectional image is shown in Figure 6.13(b). This image shows a highly undulated interface between the nanowire layer and the substrate. Although the quality of the interfacial layer cannot be quantitatively determined, the randomness and size of the voids suggest that the crystalline quality of the top layer of the support is substantially deteriorated. This result is consistent with Figure 6.13(a), suggesting that nanowire growth is always associated with pit formation. Additionally, this demonstrates that the growth mechanism is not a VLS process, as no pits are expected for the VLS process.

From the results presented in this thesis, the main observations with regard to SiO_x nanowires can be summarised as follows: (1) Carbon appears to be the source for promoting the formation of SiO_x nanowires as no nanowires were detected prior to the introduction of CH_4 in the growth step. (2) The formation of SiO_x nanowires required a catalyst layer, as no nanowires were detected in any of the control samples. (3) The

synthesized nanowires show a round or elliptical tip, with no catalyst nanoparticles detected in the tip structure, suggesting that the growth of the nanowire begins from a melt. From these observations and the conclusions drawn from Figure 6.13, evidence points to a solid-liquid-solid (SLS) growth mechanism. Indeed, Paulose et al. [391] reported that the formation of Au-SiO_x composite nanowires under similar conditions was due to a SLS growth mechanism: Si atoms diffused to the Au-Si liquid alloy to form nanowires.

The role that the catalyst may play is to create a highly stressed Si surface layer for pitting to occur. One possible mechanism for the SiO_x nanowire growth could be the carbothermal reduction of SiO_2 [284, 319] at the catalyst-support interface. Li et al. [284] report that the presence of carbon radicals will increase the rate of SiO_x nanowire formation due to the formation of local temperature gradients at the support-catalyst interface. An alternate mechanism by which SiO_x nanowires could grow from an oxide layer is that reported by LeGoues et al. [392] who showed that Ge has a catalytic effect on the oxidation of Si at high temperatures over 800 °C. When a Si substrate and GeO_2 (from the colloidal Ge nanoparticles) are close to each other, Ge atoms are replaced by Si atoms to form SiO_2. A continuous supply of both Si and O sources from the support would then provide the feedstock needed for the SiO_x nanowire growth [393].

6.8 Effect of Support Material

In order to determine the role of the support in the synthesis of CNTs from Ge colloidal nanoparticles, an alternate support was used. In this section, Al_2O_3 was used as a support medium and processed as described in Section 6.1. These measurements are expected to complement the discussion presented in this chapter and provide some insight into the catalyst-support interactions that occur in this growth methodology.

Figure 6.14 shows FE-SEM images of the 1 mM Ge nanoparticle colloidal solution dispersed on a Al_2O_3 support after a 850 °C CNT growth step following a catalyst pretreatment anneal in H_2 at various temperatures for 10 minutes. The pretreatment temperatures shown in Figure 6.14(a)–(d) are 1000, 950, 900 and 850 °C, respectively. Figure 6.14(a) shows a typical sample after pretreatment at 1000 °C, which showed a high density of thick fibres. These fibres had an approximate diameter of 20 nm and a typical length of 1 μm. EDS measurements showed the presence of Al, O and a strong C peak; indicating these are C nanofibres. The uniformity of this layer was high and showed a homogeneous coverage across the sample. After pretreatment at 950 °C, shown in Figure 6.14(b), there was a high density of long, thin fibres which were found to be CNTs. This layer showed a density of 1.8 ± 0.4 μm in length/μm^2, and a highly homogeneous coverage across the sample. Finally, no nanostructures were found in the samples pretreated at the two lowest temperatures, 900 °C and 850 °C. This may indicate that

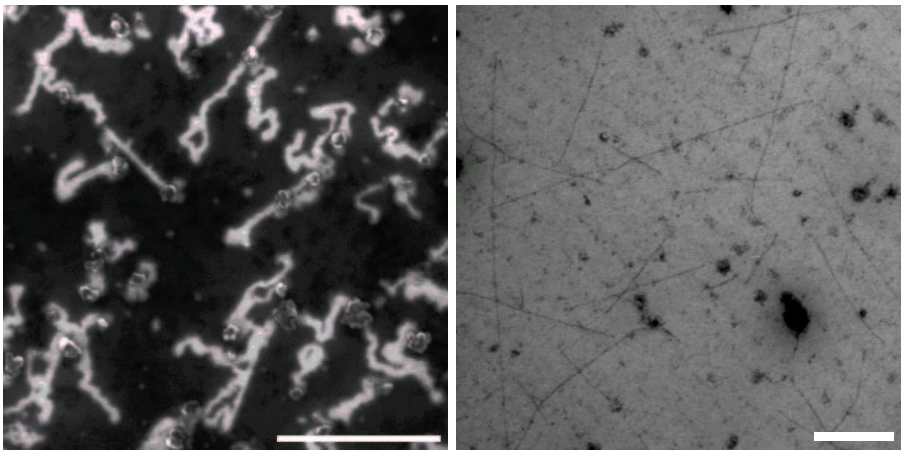

(a) (b)

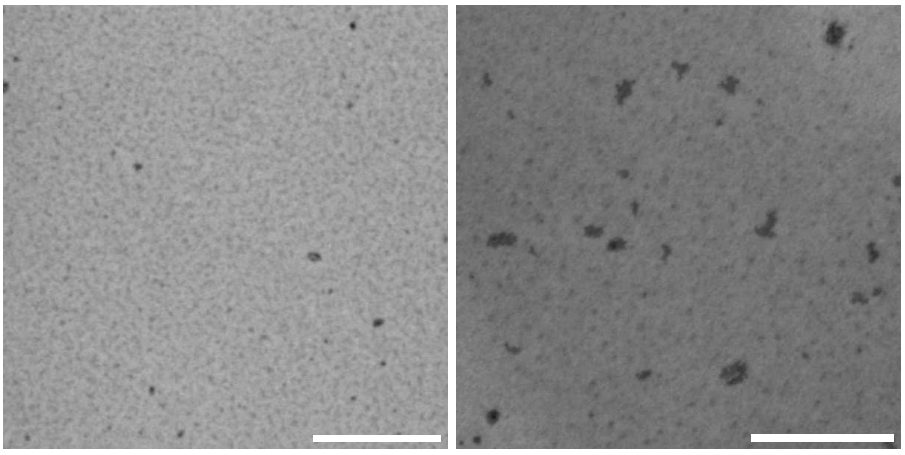

(c) (d)

FIGURE 6.14: Scanning electron microscope image of CNT growth using colloidal Ge nanoparticles dispersed on a Al_2O_3 support at 1 mM dilution. The CNTs were pretreated at four different temperatures; (a) 1000 ^{c}ircC (b) 950 °C, (c) 900 °C and (d) 850 °C in H_2 for 10 minutes. The subsequent CNT growth step was kept constant at 850 °C in a mixture of H_2 and CH_4 (1 : 3 gas ratio) for 20 minutes. Scale bar corresponds to 1 μnm.

the activation temperature for this catalyst-support combination is higher than that witnessed for the Ge-SiO_2 catalyst-support system.

The results presented in Figure 6.14 suggest that the behaviour of the Ge-Al_2O_3 catalyst-support system is significantly different than that seen in Section 6.5. In order to investigate the effect the support has on the CNT synthesis process, AFM characterisation of the 1 mM colloidal Ge nanoparticles dispersed on Al_2O_3 has been undertaken for the range of pretreatment temperatures discussed above.

From typical AFM images on samples after a pretreatment step at temperatures between 1000 and 850 °C, the mean density of particles has been determined. The results are summarised in Table 6.3. This table demonstrates a drastic reduction in nanoparticle density as pretreatment temperatures are increased. The initial nanoparticle density

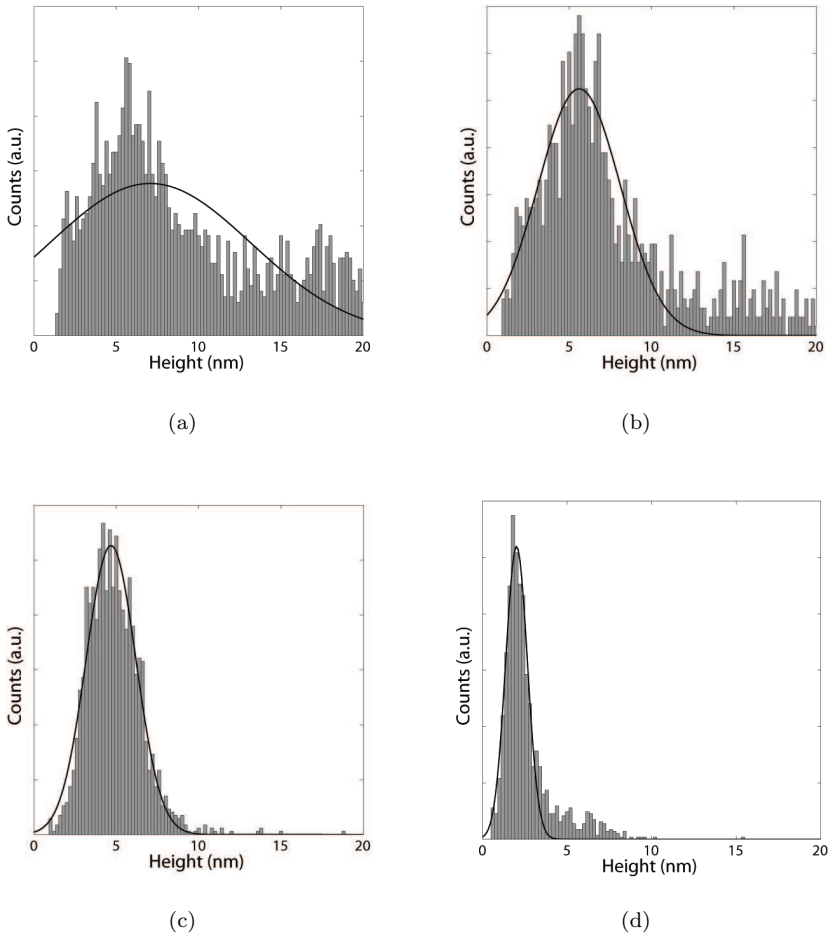

FIGURE 6.15: Particle size distribution for 1 mM diluted colloidal Ge catalyst dispersed on a Al_2O_3 support after pretreatment in H_2 for 10 minutes at; (a) 1000 °C, (b) 950 °C, (c) 900 °C and (d) 850 °C. Particle size distributions have been fitted with a non-centred, normalised Gaussian.

is reduced from 530 ± 60 particles/μm^2 is reduced to 303 ± 35, 170 ± 24, 85 ± 6 and 18 ± 8 particles/μm^2 after pretreatment at 850, 900, 950 and 1000 °C, respectively. The reduction in nanoparticle density is far more pronounced in the Ge-Al_2O_3 catalyst-support system than that seen in the Ge-SiO_2 system.

Figure 6.15(a)–(d) show the particle size distribution for colloidal Ge nanoparticles dispersed on a Al_2O_3 support pretreated in H_2 for 10 minutes at 1000, 950, 900 and 850 °C, respectively. Each distribution has been fitted with non-centred, normalised Gaussian curves. The distribution for Ge nanoparticles pretreated at 850 °C, shown in Figure 6.15(d), resembles the initial distribution (shown in Figure 6.2(b)). However, there is a noticeable increase in the modal height and a broadening of the distribution profile. As pretreatment temperatures increase, there is a large increase in the modal height of the nanoparticles and a broadening of the distribution. Additionally, there is a proportional increase in the number of larger nanoparticles (larger than 2 nm in

diameter). The statistics of the distributions shown are summarised in Table 6.3. This behaviour, when considered in conjuction with the reduction in nanoparticle density is indicative of phase coarsening, which occurs at the expense of small particles within a system. However, due to the very low density of nanoparticles after pretreatment at higher temperatures, the accuracy of the measurement is questionable and much care is required when drawing conclusions.

Pretreatment		Distribution Statistics		Nanoparticle Density
Temperature (°C)	Time (min)	Mode (nm)	R_2 (nm)	(particles/μm^2)
850	10	2.0 ± 0.6	0.978	303 ± 35
900	10	4.7 ± 1.5	0.985	170 ± 24
950	10	5.6 ± 2.6	0.908	85 ± 6
1000	10	7.1 ± 6.1	0.626	18 ± 8

TABLE 6.3: Particle size distribution fit parameters and nanoparticle densities for 1 mM colloidal Ge nanoparticle catalyst dispersed on a Al_2O_3 support after pretreatment at various temperatures.

When compared with the Ge-SiO_2 catalyst support system, these results show that phase coarsening is occurring at a much higher rate in the Ge-Al_2O_3 catalyst support system. This is indicative of a weaker support-catalyst interaction. The data suggests that a clean Al_2O_3 surface does not provide strong enough adhesive force for higher coverages of Ge. Even though Ge is thought to interact with the Al_2O_3 quite strongly at lower coverage [394], the stronger cohesion results in clustering and agglomeration at higher surface coverages with concomitant loss of surface area of the catalyst and its reactivity for catalytic processes.

In order to characterise the CNTs formed using this catalyst-support combination, Raman analysis was undertaken. Figure 6.16 shows the Raman spectrum for the carbon nanotubes synthesized using 1 mM diluted colloidal Ge catalyst dispersed on a Al_2O_3 support after pretreatment in H_2 for 10 minutes at 950 °C, followed by a growth step at 850 °C in a mixture of H_2 and CH_4 (1 : 3 gas ratio) for 20 minutes. The spectrum shows two distinct peaks, at 1347 cm^{-1} and 1582 cm^{-1}, these peaks can be attributed to the D-band and the G-band of crystalline carbon. The shape of the G-band feature is broad and asymmetric with a FWHM of approximately 75 cm^{-1}. This spectra is characteristic of of MWNTs, which exhibit an asymmetric G-band peak located at approximately 1582 cm^{-1} [395]. Additionally, no spectral features were detected in the RBM region in any location of this sample.

The synthesis of MWNTs with the Ge-Al_2O_3 catalyst-support system is most likely due to the agglomeration of Ge nanoparticles into clusters too large to catalyse SWNT formation. Additionally, it is reported that nanoparticles of Al_2O_3 are capable of promoting ordered carbon growth [278]. Rummeli et al. [278] attributed this to the presence

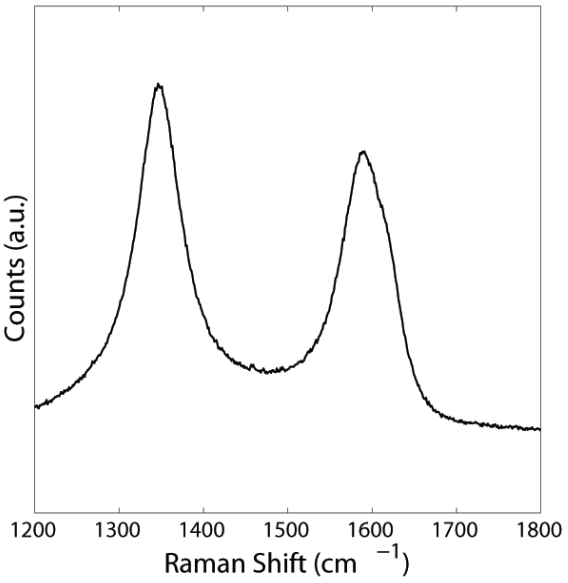

FIGURE 6.16: Raman spectra for the carbon nanotubes synthesized using 1 mM diluted colloidal Ge catalyst dispersed on a Al_2O_3 support after pretreatment in H_2 for 10 minutes at 950 °C, followed by a growth step at 850 °C in a mixture of H_2 and CH_4 (1 : 3 gas ratio) for 20 minutes.

of surface defects on the nanoparticle oxides. However, the interface between the catalyst nanoparticle and the support is thought to act as a annular defect site. This would indicate that the nature of the support-nanoparticle interface may be very important to the behaviour of the catalyst. The higher propensity for ordered carbon formation and the larger nanoparticle sizes obtained due to agglomeration may have resulted in the catalysis of MWNTs.

6.9 Conclusions

In this chapter, research on the use of colloidal Ge nanoparticles fabricated by an inverse micelle technique as a catalyst for CNT growth was presented. The colloidal Ge nanoparticle catalyst was shown to be a viable catalyst for the synthesis of SWNTs on a SiO_2 support. The results indicate that the inverse micelle technique provides good control over the morphology of the nanoparticles and delivers a well-controlled CNT growth process. A SWNT area density of 5.2 ± 0.7 μm in length/μm^2 was obtained from the colloidal Ge nanoparticles under the optimum growth condition.

TEM and AFM analyses show that good control over nanoparticle size and concentration is possible with the inverse micelle technique. The colloidal Ge nanoparticles were synthesized at various concentrations with a particle size of 1.4 ± 0.5 nm. PL analysis of the synthesized colloidal solutions showed that higher concentrations colloidal

solutions showed a broad luminescence compared with the lower concentrations, with the onset of absorbance occurring at longer wavelengths. This suggests that the higher concentrations have a broader range of nanoparticle sizes, as indicated by a shift toward lower energy values [375]. Additionally, the lower concentrations of colloidal solutions are stable for longer periods of time, with coagulation of the nanoparticles after a few weeks. This was determined qualitatively by a change in colloid colour, from a transparent solution to whitish, indicating flocculation of the nanoparticles. PL measurements indicated that the synthesized nanoparticles were most likely quantum confined.

Following a CNT growth step, the colloidal Ge nanoparticle solutions were able to catalyse the formation of CNTs at two concentrations; 1 and 2 mM. Higher concentrations of the colloidal nanoparticle solutions failed to produce any CNTs, most likely due to agglomeration upon annealing. The highest yield was obtained for the 1 mM concentration of the colloidal Ge nanoparticles owing to a larger initial interparticle separation. It could also be argued that the particle size distribution of the nanoparticles fabricated at this concentration is more conducive to CNT formation, however further experimentation is required to prove this.

In order to obtain CNTs, a pretreatment anneal in hydrogen was required. SEM analyses indicated that the hydrogen pretreatment step prevented agglomeration and resulted in redispersion of the nanoparticles, possibly due to evaporation of the catalyst. SEM images from samples following a CNT growth step showed that CNT growth was possible in samples pretreated at a temperature in the range of $1000 - 850$ °C . The highest yield was obtained for a pretreatment at 1000 °C for 2 minutes. It is believed that the hydrogen pretreatment step is required to remove residual contaminants on the surface of the nanoparticles. AFM analyses of the Ge nanoparticles after pretreatment showed that there is an associated reduction in nanoparticle density as pretreatment temperatures increase. However, the reduction in nanoparticle density was less pronounced than that shown in Chapter 5 for non-implanted samples. This difference is most likely due to a difference in surface termination; it is believed that the Ge nanoparticles synthesized by this process have H-terminated surfaces which is more effective in passivating the nanoparticle surface compared to the Ge surface oxide. There is also an increase in modal height of the nanoparticles and a broadening of the size distributions as pretreatment temperatures increase most likely due to phase coarsening.

The synthesized CNTs were characterised by Raman spectroscopy and were shown to be of a good quality in terms of graphitisation and structure. The RBM feature was frequently detected, indicated that presence of SWNTs. Although a full diameter characterisation was not undertaken, the histogram of the SWNT diameters obtained by RBM correlates with the particle size distributions obtained by AFM. TEM measurements confirmed the presence of SWNTs, with diameters in the range of $1.2 - 2.2$ nm. Additionally, the tip structure of the nanotubes measured showed a cone shape, with

no nanoparticles present. This is indicative of a base-growth mechanism. A new interpretation of the role of the catalyst was presented where only a nanoscale curvature is necessary to grow CNTs. It was argued that the growth mechanism of the SWNTs most likely involves the formation of a graphene cap, as carbon penetration inside small nanoparticles is unlikely [293]. The Yarmulke mechanism, first proposed by Dai et al. [188], was used to explain the nucleation of CNTs from the Ge nanoparticle catalyst. In this mechanism, a graphene cap is assembled on the particle surface with its edges strongly chemisorbed to the catalyst. The graphene cap acts to reduce the high total surface energy of the particle caused by its high curvature, owing to the fact that the basal plane of graphite has an extremely low surface energy. As additional carbon atoms are added, the hemifullerene cap formed on the particle surface lifts off, creating a hollow tube with constant diameter which grows away from the particle [189].

In order to determine the role of the support in the synthesis of CNTs from Ge colloidal nanoparticles, Al_2O_3 was used as a support medium and the CNT growth process was examined. SEM measurements showed that two types of carbon nanostructures were synthesized using this catalyst-support system after pretreatment at 1000 and 950 °C. After pretreatment at 1000 °C, carbon nanofibres were synthesized. Following a pretreatment at 900 °C, a homogeneous coverage of MWNTs (as determined by Raman spectroscopy) was synthesized. This was attributed to a weaker catalyst-support interaction compared with Ge-SiO_2, which led to increased clustering and aggregation of nanoparticles. This hypothesis was confirmed by AFM measurements on the nanoparticles after pretreatment. Additionally, Al_2O_3 is reported to have a high propensity for ordered carbon formation [278], which in conjuction with the larger nanoparticles sizes obtained due to agglomeration may have led to the catalysis of MWNTs instead of SWNTs.

Finally, the nanowires synthesized as a byproduct of the growth process was investigated. Raman, PL and TEM measurements confirmed the synthesized nanostructures as SiO_x nanowires. TEM images showed that the nanowires had a typical diameter in the range of $10-20$ nm, and EDS measurements indicated that the nanowires were oxygen deficient. This hypothesis was confirmed by the PL spectrum, which showed a neutral oxygen vacancy and twofold coordinated silicon lone pair centres. The Raman spectra showed a peak at 505 cm^{-1}, which is attributed to a shift in the first-order optical phonon of silicon (520 cm^{-1}) due to phonon confinement effects in the nanowire. SEM measurements showed pitting in the substrate at the base of the nanowires, indicating that nanowire formation is most likely due to a SLS growth mechanism. It is suggested that this occurs due to carbothermal reduction of the SiO_2 support.

The results presented show that the commonly utilised model of carbon filament growth is inadequate to describe SWNT growth from non traditional catalysts. A new interpretation of the role of the catalyst was presented where only a nanoscale curvature is necessary to grow CNTs.

Chapter 7

Support-Catalyst Interactions in SWNT Synthesis

The role played by the support in the CVD of CNTs is not yet fully understood. The simplistic view that the support only plays a catalytically passive role in the formation of CNTs requires examination. The work of Rummeli et al. [278] demonstrated that under typical CVD growth conditions, nanoparticles of difficult-to-reduce metal oxides were capable of promoting ordered carbon growth. The authors attributed this to the presence of surface defect sites on the nanoparticle oxides. However, the interface between the catalyst nanoparticle and the support is thought to act as a annular defect site. This would indicate that the nature of the support-nanoparticle interface may be very important to the behaviour of the catalyst.

In the supported catalyst method of metal catalysed carbon nanotube synthesis, the support can interact both chemically and physically with the catalyst nanoparticle [308–312]. The support can control the size of the catalyst nanoparticle by affecting the kinetics of nanoparticle formation. The support can also act to disperse the metal catalyst particles formed upon decomposition of metal salt precursors by physically holding the particle in place [299]. Additionally, the support can interact chemically with the catalyst nanoparticle and dramatically affect its catalytic ability. For instance, acquisition of negative charge by the catalyst nanoparticle from the support can enhance its catalytic activity by strengthening back donation of electron density into anti-bonding orbitals of the adsorbate [299, 396]. This electron sharing between the catalyst and adsorbate sufficiently weakens the bonding within the adsorbate, resulting in its dissociation [311, 312].

The catalyst nanoparticle can acquire negative charge through the interaction between either the metal cation or oxygen anion sites in the support [309–312]. A strong interaction between the catalyst nanoparticle and the cationic sites on the support is known as strong-metal support interaction (SMSI). SMSI arises from partial reduction of the

oxide, which enables the metal cation of the support to donate partial negative charge to the supported metal nanoparticle [299]. For support oxides that are not readily reduced, another interaction involves the catalyst nanoparticle and an exposed oxygen anion sites on the support [309, 310]. The anions can act as Lewis base sites donating negative charge to the metal nanoparticle. In a similar manner, the partial negative charge it does accept from the oxide can enhance its catalytic activity.

In addition to these site-specific interactions, other processes such as Ostwald ripening and sintering can also occur during the metal nanoparticle formation steps [313, 314]. For instance, dramatic structural changes occur when metals supported on TiO_2 are heated in H_2 to 500 °C. The oxide becomes partially reduced to Ti_4O_7 and the metal assumes the form of hexagonal plates. In other systems, a compound may form between the support and metal nanoparticle [314]. Changes in the phase and crystalline structure of the support may also affect the nature of its interaction with the catalyst [299]. Consequently, the physical and electronic structure of the supported catalyst nanoparticle will also be affected.

In this chapter, the factors affecting the activity of a metal catalyst-support system are investigated. To explore these interactions, combinations of catalyst metals and support mediums are tested. Three metals, Fe, Co and Ni, of moderate to high catalytic ability were chosen for comparison on three different support media, SiO_2, Al_2O_3 and HfO_2. AFM characterisation of the catalyst following deposition and nanoparticle formation steps provide an insight to the effects of the support on the nanoparticle formation kinetics. Additionally, the effect of pretreatment on catalyst morphology is also investigated for each support medium used. These results provide novel insights on the how interactions between catalyst and support affect morphology. The yield of CNT growth on each support is investigated by SEM, and this data is used to ascertain the chemical effects of the support on CNT synthesis. The synthesized nanotubes are also characterised and compared by Raman spectroscopy.

Finally, Ge nanoparticles are used as a catalyst promoter to passivate the effects of the support and allow carbon nanotubes to be grown directly on HfO_2 for the first time.

7.1 Experimental Details

A metal nitrate catalyst solution was prepared by mixing highly pure metal nitrate salt (99.995%) and isopropyl alcohol (Chromasolv, absolute, 99.9% from Sigma-Aldrich) at a concentration of 1 mM and sonicated for 20 minutes. The metal nitrate salts used for these experiments were iron(III) nitrate nonahydrate, cobalt(II) nitrate hexahydrate and nickel(II) nitrate hexahydrate from Sigma Aldrich. The catalyst solution was deposited by dip-coating the supports in the solution at a speed of 3 mm/s. Samples were then subjected to a 100W O_2 plasma for 10 minutes to remove any residual organic left from

deposition. The samples were then annealed in air at 400 °C for 30 minutes to thermally decompose the deposited metal nitrate.

The support media used in these experiments were SiO_2, Al_2O_3 and HfO_2. For the SiO_2 support, $< 001 >$ oriented, *p*-type silicon ($17 - 33$ Ωcm resistivity) with a 300 nm SiO_2 layer was purchased from IDB Technologies. For the Al_2O_3 support, $< 001 >$ oriented, *p*-type silicon ($17 - 33$ Ωcm resistivity) with a 100 nm Al_2O_3 layer deposited by sputtering was prepared. Finally, for the HfO_2 support, $< 001 >$ oriented, *p*-type silicon ($17 - 33$ Ωcm resistivity) with a 20 nm HfO_2 layer deposited by atomic layer deposition was used. All supports were cut to 10×10 mm pieces to suit a one-inch diameter furnace tube.

Carbon nanotubes were grown in a one-inch tube furnace using a two step process. The first step was a hydrogen pretreatment performed at a temperature of 900 °C for 10 minutes and the second step was a CNT growth step by thermal CVD in a hot-wall reactor at atmospheric pressure. The CNT growth step was carried out using a mixture of methane (1000 sccm) and hydrogen (300 sccm) at a temperature of 900 °C. A new quartz tube was used exclusively for this work to avoid contamination.

The metal catalyst was characterised using a Veeco Multi-Mode atomic force microscope, using super sharp Si cantilevers (typical tip radius of 2 nm). Particle height distributions for each sample were determined using a minimum of 10 1 μm^2 AFM images utilising the Veeco Nanoscope software package. Images were first flattened using a three point levelling technique, and a threshold height of 0.5 nm was set in the particle detection software. The synthesized CNTs were observed by field-emission scanning electron microscope (JEOL 6500F). The chemical compositions of SEM samples were analysed by energy-dispersive X-ray spectroscopy (Oxford Instruments INCA Microanalysis System). The area densities of CNTs were evaluated using FE-SEM images using ImageJ to determine the total contour length of CNTs [315]. For quantitative analysis, several images taken from the same sample were used, with overlapping regions being discarded. The Raman measurements were undertaken utilising a Renishaw in-Via system, consisting of an Olympus Microscope, a monochromator with a 1200 groves/mm grating, a Peltier cooled CCD, holographic notch filter and a He-Ne (632.8 nm) laser excitation. The signal is collected via a backscatter geometry, with the holographic notch filter tuned so that the frequency cut-off was a shift of approximately 110 cm^{-1}. For this reason, the system is not able to detect RBMs from CNTs with diameters larger than 2.3 nm. Raman spectra was taken using two laser excitation energies (532 and 632.8 nm) with a power of 12 mW.

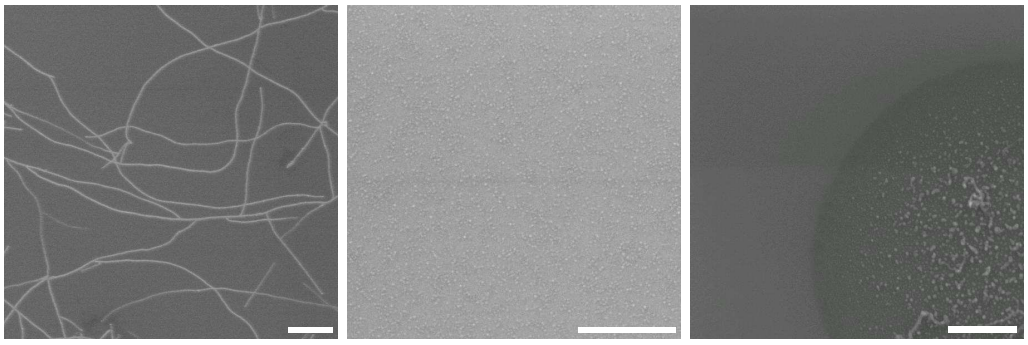

(a) (b) (c)

FIGURE 7.1: Scanning electron microscope images of CNTs synthesized from three transition metal catalysts; (a) Fe, (b) Co and (c) Ni, dispersed on a SiO_2 support. The CNTs were grown by depositing 1 mM of a metal-nitrate salt by dip coating, followed by a nitrate reduction anneal in air at 400 °C for 20 minutes prior to the CNT growth step at 900 °C in a mixture of H_2 and CH_4 (1 : 3 gas ratio) for 20 minutes. Scale bar corresponds to 500 nm.

7.2 Interactions between Catalyst and SiO_2 Support

Figure 7.1 shows SEM images of CNTs synthesized on a SiO_2 support from three transition metal catalysts; (a) Fe, (b) Co and (c) Ni. From the SEM images it is evident that only the Fe-SiO_2 catalyst-support system yielded CNTs, with a area density of 3.5 ± 0.2 μm in length/μm^2. The Co-SiO_2 and Ni-SiO_2 catalyst-support systems showed the presence of much larger nanoparticles after growth, indicating significant agglomeration of the nanoparticle catalyst upon anneal.

In order to investigate this effect, AFM analysis of the catalysts supported on SiO_2 was undertaken. Figure 7.2 show particle size distributions for each catalyst after the nitrate decomposition anneal, and following an anneal in H_2 at 900 °C for 10 minutes. From typical AFM images the mean density of particles before and after pretreatment in H_2 at 900 °C has also been determined. The Fe-SiO_2 catalyst-support system showed an initial density of 495 ± 23 particles/μm^2, which after pretreatment in H_2 was been reduced to 422 ± 37 particles/μm^2. The reduction in nanoparticle particle density upon pretreatment is more pronounced in the case of the Ni-SiO_2 and Co-SiO_2 catalyst-support systems. The Co catalyst showed a reduction from 530 ± 27 to 125 ± 84 particles/μm^2, while the Ni catalyst density was reduced from 340 ± 96 to 180 ± 48 particles/μm^2. The reduction in nanoparticle density was associated with an increase in nanoparticle modal height and broadening of the nanoparticle distribution. The Fe catalyst showed a slight increase in modal height from 1.2 ± 0.4 to 2.7 ± 1.2 nm. In the case of Co and Ni catalysts the increase was greater, with Co showing an increase in modal height from 1.9 ± 0.8 to 7.3 ± 1.8 and Ni showing an increase from 1.0 ± 0.2 to 3.7 ± 1.4 nm.

This difference can be explained by the adsorption energy between the catalyst metal to the silica surface. Ma et al. [344] reported a periodic trend in absorption energy of

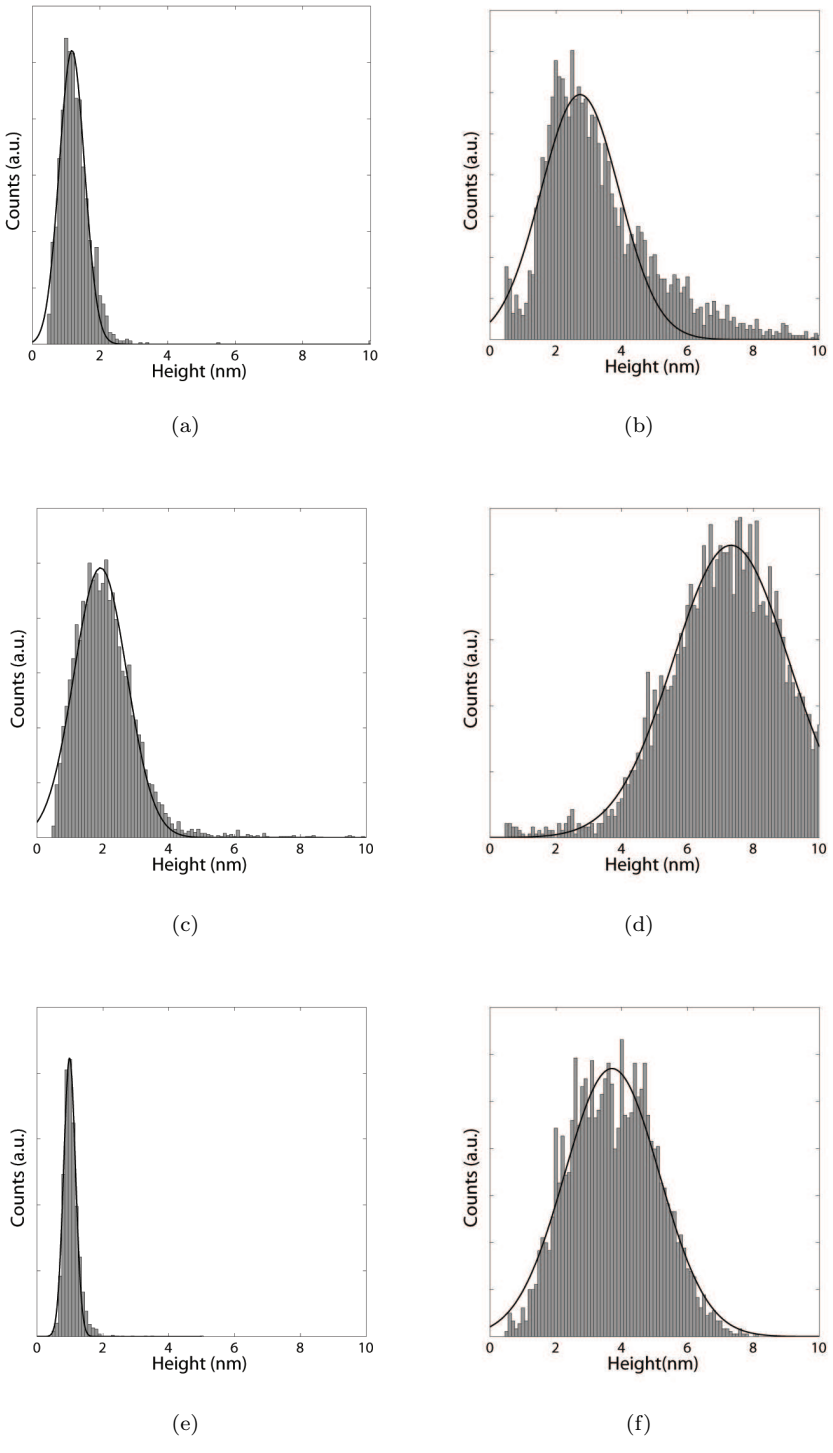

FIGURE 7.2: Particle size distribution for 1 mM transition metal catalysts dispersed on a SiO_2 support before and after anneal in H_2 for 10 minutes. (a) Fe catalyst as deposited. (b) Fe catalyst after anneal at 900. (c) Co catalyst as deposited. (d) Co catalyst after anneal at 900 °C. (e) Ni catalyst as deposited. (f) Ni catalyst after anneal at 900 °C. Particle size distributions have been fitted with a non-centred, normalised Gaussian.

first-row transition metals with the silica surface. Adsorption energies and inter-atomic distances of $3d^n4s^{1-2}$ metal atoms on silicon dioxide surface exhibit a periodic double-hump pattern determined primarily by the $3d^n$ subshell. There is an overall trend toward weakening of the metal-oxide bond when passing from early to late transition metals. Molecular dynamics calculations suggest that a clean siloxane surface of silica does not provide a strong enough adhesive force for higher coverages of Co and Ni metals [397]. Even though these metals interact with the silica support fairly strongly ($1-2$ eV/atom) at lower coverage, the stronger cohesion ($3-4$ eV/atom) results in clustering and further agglomeration at higher metal coverages [345]. Co and Ni both have a weaker interaction with the silica surface than that of Fe, which at higher coverages results in higher clustering and agglomeration.

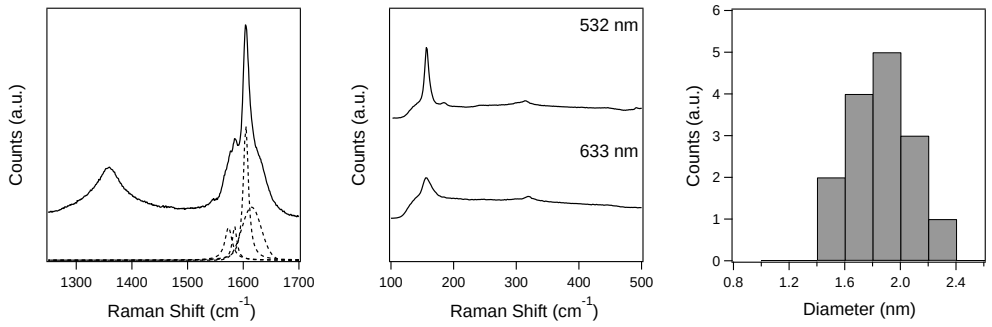

FIGURE 7.3: Raman spectra for the carbon nanotubes synthesized using 1 mM Fe catalyst dispersed on a SiO_2 support. The CNTs were grown using a nitrate reduction anneal in air at 400 °C for 20 minutes prior to the CNT growth step at 900 °C in a mixture of H_2 and CH_4 (1 : 3 gas ratio) for 20 minutes. (a) Typical G-band characteristic detected with 532 nm laser excitation, fitted with four Lorentzian curves. (b) Typical RBM modes detected with 532 and 633 nm laser excitation lines. (c) Histogram of the SWNT diameters obtained via RBM.

The Raman spectra obtained from areas of relatively high CNT area density typically exhibited an asymmetric double peak at approximately 1590 cm^{-1} (Figure 7.3(a)). This double peak can be attributed to the Raman allowed tangential mode of CNTs, G-band. In the representative spectrum shown in Figure 7.3(a), this feature could be fitted with four Lorentzian oscillators located at 1573, 1584, 1605, 1614 cm^{-1}. The spectra shown in Figure 7.3(a) shows a strong D-band feature, located at 1360 $cm^{-}1$, which can be attributed to disorder in the CNT. The ratio between the disorder induced D-band and the Raman allowed G-band (I_D/I_G)is approximately 0.25, suggesting a moderate defect density. Figure 7.3(b) shows the spectral region of $100-500$ cm^{-1} by two laser excitation lines, 532 nm and 633 nm at different sample locations. Due to a broad luminescence, it was not possible to obtain Raman measurements in this region using a 785 nm laser excitation line. This figure clearly shows the RBM feature, indicating the presence of SWNTs. In most cases, the RBM feature was detected in the region of $110-180$ cm^{-1}. Assuming the standard formula for converting Raman shift to CNT

diameter, $\omega_{RBM} = 248/d_t$ as described in Section 2.4.4, this indicates that the CNTs observed by Raman scattering have diameters in the range of $1.4 - 2.3$ nm. A histogram of the SWNT diameters observed in the measurements via the RBM spectral feature is shown in Figure 7.3(c). It should be noted that since the measurements were only undertaken using two laser excitation lines these results do not provide a full diameter characterisation of the sample. The histogram indicates that the SWNT diameters observed have a modal peak of approximately 1.8 nm and appears to show a Gaussian distribution profile. Although no strong conclusions can be drawn from this fact, this result correlates with the particle size distributions shown in Figure 7.2(b), which showed a nanoparticle modal size of 2.7 ± 1.2 nm.

7.3 Interactions between Catalyst and Al_2O_3 Support

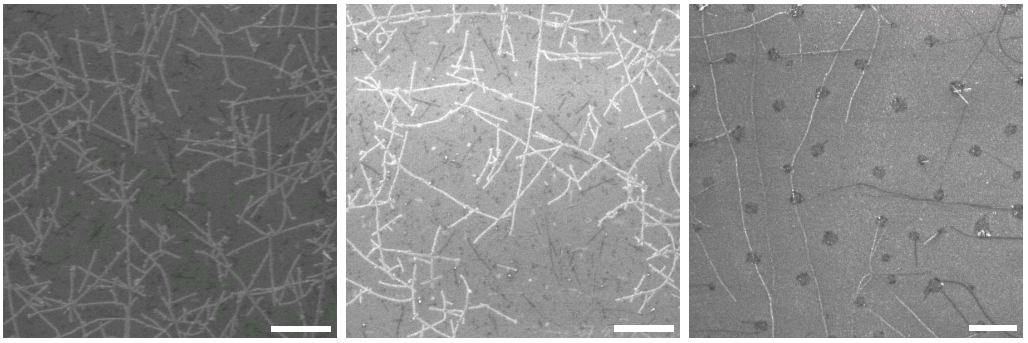

(a) (b) (c)

FIGURE 7.4: Scanning electron microscope images of CNTs synthesized from three transition metal catalysts; (a) Fe, (b) Co and (c) Ni, dispersed on a Al_2O_3 support. The CNTs were grown by depositing 1 mM of a metal-nitrate salt by dip coating, followed by a nitrate reduction anneal in air at 400 °C for 20 minutes prior to the CNT growth step at 900 °C in a mixture of H_2 and CH_4 (1 : 3 gas ratio) for 20 minutes. Scale bar corresponds to 500 nm.

Figure 7.4 shows SEM images of CNTs synthesized on a Al_2O_3 support from three transition metal catalysts; (a) Fe, (b) Co and (c) Ni. Unlike with the SiO_2 support, the SEM images indicate that all three catalyst-support systems yield CNTs. The highest area density achieved was that of the Fe-Al_2O_3, with an area density of 7.6 ± 0.8 μm in length/μm^2. The Co-SiO_2 and Ni-SiO_2 catalyst-support systems achieved slightly lower densities, 5.5 ± 1.1 and 3.8 ± 0.6 μm in length/μm^2, respectively. This increase in yield compared with SiO_2 as a support medium was expected. Indeed, there have been several reports in the literature of higher rates of CNT formation obtained on Al_2O_3. Su et al. [398] and Colomer et al. [223] both reported higher CNT yields on Al_2O_3 compared with SiO_2. Experiments by Kukovecz et al. [399] showed that Ni-Al_2O_3 was very catalytically active, whereas Ni-SiO_2 is poorly active.

In order to determine the morphology of the catalyst supported on Al_2O_3, AFM characterisation of the samples has been undertaken for Fe, Co and Ni catalysts before and after pretreatment at 900 °C in H_2 for 10 minutes. Figure 7.5 shows the particle size distributions derived from a minimum of 15 AFM images for each catalyst supported on Al_2O_3. The mean density of the Fe-Al_2O_3 catalyst-support system showed an initial density of 580±66 particles/μm^2, which after pretreatment in H_2 was reduced to 390±55 particles/μm^2. The reduction in nanoparticle particle density upon pretreatment is similar in the case of the Ni-SiO_2 and Co-SiO_2 catalyst-support systems. The Co catalyst showed a reduction from 504±34 to 446±47 particles/μm^2, while the Ni catalyst density was reduced from 521 ± 48 to 468 ± 54 particles/μm^2. The particle size distributions showed little change after pretreatment, unlike with SiO_2 as a support medium. The Fe catalyst showed a slight reduction (although not statistically significant) in modal height from 1.2 ± 0.4 to 1.1 ± 0.3 nm. In the case of Co and Ni there was a slight increase in the modal height and slight broadening of the nanoparticle distribution, although again this was not statistically significant. The Co catalyst showed an increase in modal height from 0.9 ± 0.3 nm to 1.6 ± 0.6, while the Ni catalyst showed an increase from 1.4 ± 0.4 nm to 1.9 ± 0.6 nm. The shape of the particle size distribution for the Ni catalyst after pretreatment remained very similar to the initial distribution, with a only a very slight increase in modal height which could be attributed to the measurement accuracy. However, in the case of Fe and Ni, the distributions showed a slight increase in the proportion of larger particles, which is shown as a pedestal to the right of the main mode. This behaviour is indicative of a coarsening mechanism.

The difference in the behaviour of the catalyst when supported by Al_2O_3 compared with SiO_2 can be explained by a stronger interaction between the catalyst and support. Hofmann et al. [396] reported the formation of stronger Fe oxide signatures by XPS analysis for Al_2O_3-supported Fe, which could be explained by interfacial bonding [400, 401]. This was shown to result in a narrower Fe particle size distribution during the pretreatment compared with Fe on SiO_2, resulting in a higher density of CNTs [401]. In the case of a metal and its silica support, a direct redox reaction is thermodynamically predicted only for metals with electronegativities less than 1.5 on the Pauling scale [402]. This behaviour pattern can be related to the oxide free energy of formation per O atom [403], which increases (negatively) as the metal work function decreases. Fe, the most electropositive metal studied in this work, shows a very weak oxidation signature on SiO_2, which indicates that it does not reduce the SiO_2 support. This indicates that the interaction strength at the metal-oxide interface determines the metal wetting. Indeed, in the case of Ni, it is reported that the reduction of Ni oxide leads to a physical dewetting of the Ni catalyst from the SiO_2 support [396]. This effect is seen in Figure 7.2(f) and is consistent with the weak-metal support interaction seen for Ni catalysts on SiO_2 supports [404]. The as-formed Ni nanoparticles coarsen with increasing temperatures and process time, reflecting the higher surface free energies of metal facets [405] compared with the oxide support, and also the low adhesion energy of Ni [406].

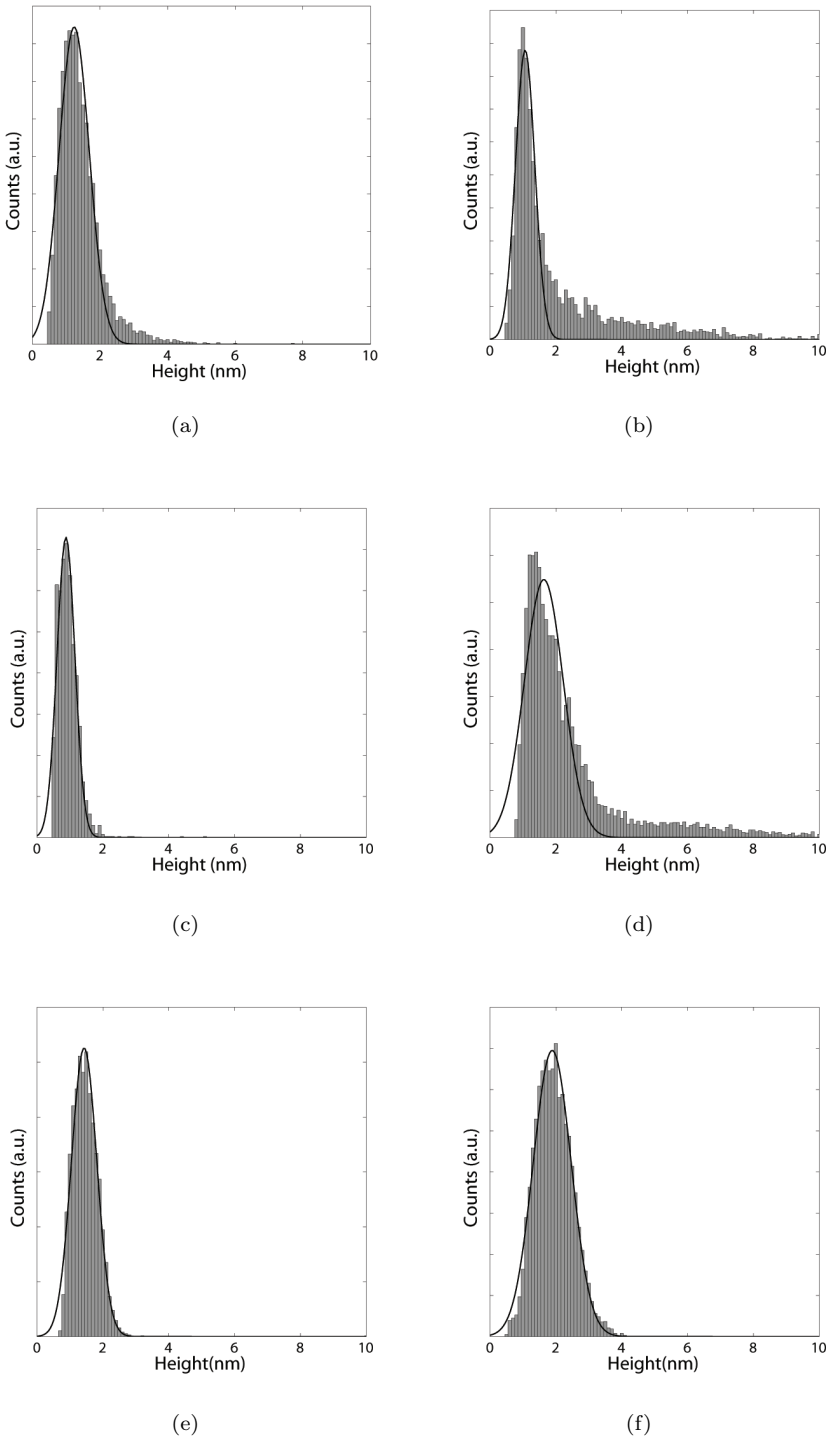

FIGURE 7.5: Particle size distribution for 1 mM transition metal catalysts dispersed on a Al_2O_3 support before and after anneal in H_2 for 10 minutes. (a) Fe catalyst as deposited. (b) Fe catalyst after anneal at 900. (c) Co catalyst as deposited. (d) Co catalyst after anneal at 900 °C. (e) Ni catalyst as deposited. (f) Ni catalyst after anneal at 900 °C. Particle size distributions have been fitted with a non-centred, normalised Gaussian.

Molecular dynamics simulations by Ma et al. [407] of Co and Ni on Al_2O_3 attempt to describe the orbital nature of the metal-support interactions. Their results indicated that a significant contribution to the metal-support interaction is due to the ligand field splitting of partially occupied $3d$ orbitals screened by the bonding orbital involving the $4s$ electron in a threefold oxygen site. This is thought to result in surface reconstruction of the Al_2O_3 surface, as unsaturated surface bonds result in surface levels which will affect the surface geometry and electronic properties. However, it should be noted that the authors reach the conclusion that the adsorption energy of Co and Ni atoms on Al_2O_3 is significantly smaller compared to Co and Ni atoms on SiO_2. This is in direct opposition to the experimental results obtained in this section, which show a strong interaction between the catalyst and the support.

Figure 7.6 shows Raman spectra for carbon nanotubes synthesized using Fe, Co and Ni catalysts dispersed on a Al_2O_3 support. The Raman spectra obtained in areas with relatively high CNT density for typically exhibited an asymmetric double peak at approximately 1590 cm^{-1}, show in Figure 7.6(a), 7.6(d), 7.6(g) for the Fe, Co and Ni catalysts, respectively. This double peak can be attributed the Raman-allowed tangential mode of CNTs, G-band. In all cases shown, this feature could be fitted with four Lorentzian oscillators. The similar symmetry assignments used to fit the four Lorentzian features have been reported [112, 325], and are believed to be characteristic of a semiconducting tube. The spectra presented also shows a small D-band feature, located at 1350 cm^{-1}, which can be attributed to disorder in the CNT. The ratio between the disorder induced D-band and the Raman allowed G-band (I_D/I_G) for the Fe, Co and Ni catalysts are 0.05, 0.05 and 0.06, respectively. This suggests that the nanotubes are of a good quality in terms of structure and graphitisation. The I_D/I_G ratios obtained from CNTs synthesized on Al_2O_3 are significantly better than those obtained from CNTs synthesized on SiO_2. This result is expected, as it has been reported that Al_2O_3 has a greater propensity for promoting ordered carbon growth than SiO_2 [278].

Figure 7.6(b), 7.6(e) and 7.6(h) show the spectra region of $100 - 500$ cm^{-1} by two laser excitation lines, 532 nm and 633 nm at different locations, for nanotubes synthesized using Fe, Co and Ni catalysts, respectively. All samples clearly show the RBM feature, indicating the presence of SWNTs. For CNTs synthesized by the Fe catalyst, the RBM mode feature was typically found in the region of $110-250$ cm^{-1}. Assuming the standard formula for converting Raman shift to CNT diameter, $\omega_{RBM} = 248/d_t$, this corresponds to diameters in the range of $1.0-2.2$ nm. A histogram of the SWNT diameters observed in these measurements via the RBM spectral feature is shown in Figure 7.6(c). In the case of the Co catalyst, the RBM feature was typically found in the region of $210 - 110$ cm^{-1} corresponding to SWNT diameters of $1.2 - 2.2$ nm (histogram shown in Figure 7.6(f)). Finally, the CNTs synthesized from the Ni catalyst showed a much sharper diameter distribution, shown in Figure 7.6(i). The RBM feature was typically observed between $175 - 210$ cm^{-1}, corresponding to SWNT diameters in the range

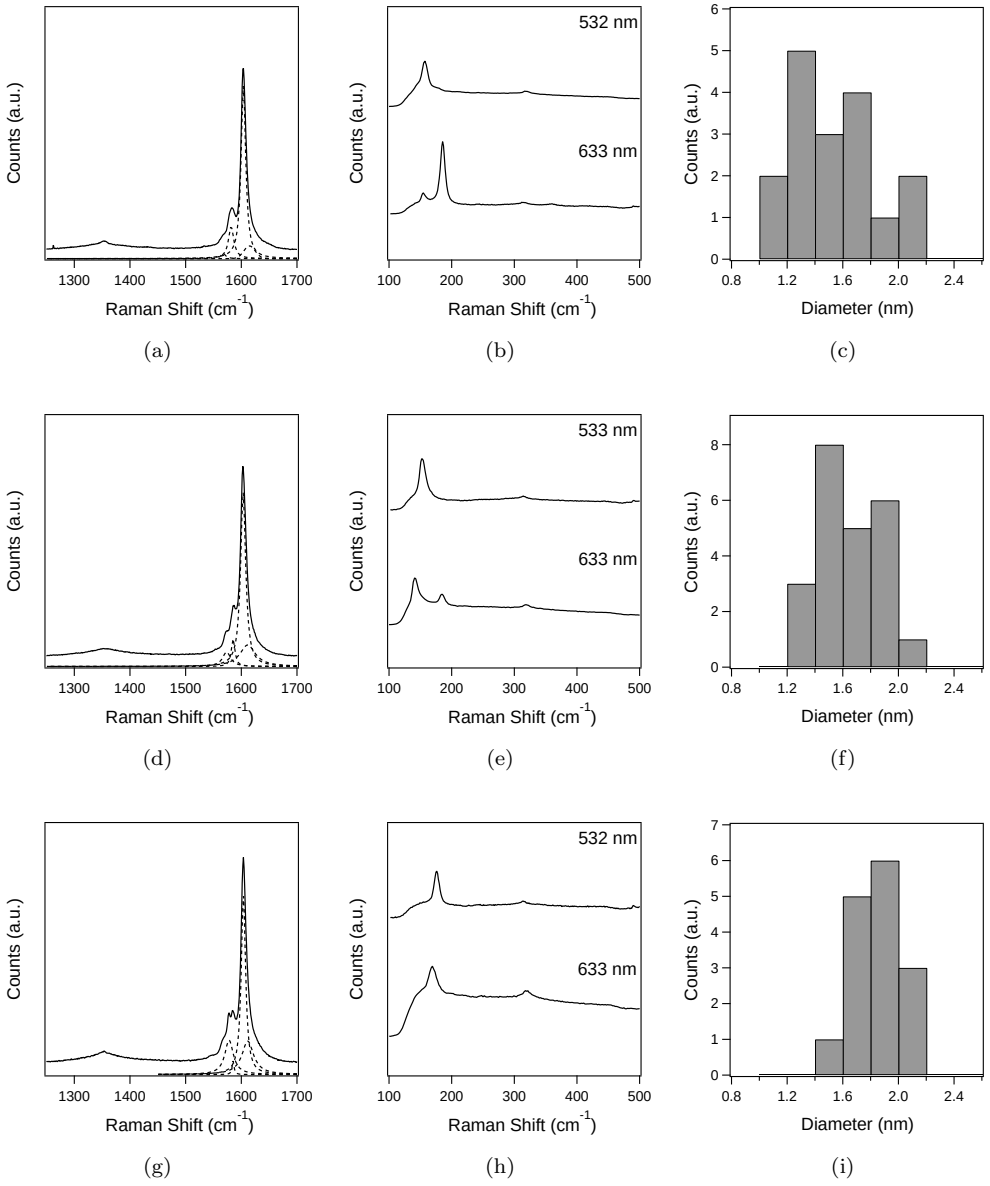

FIGURE 7.6: Raman spectra for the carbon nanotubes synthesized using 1 mM metal nitrate catalyst dispersed on a Al_2O_3 support. Typical G-band characteristic detected with 532 nm laser excitation, fitted with four Lorentzian curves for; (a) Fe, (d) Co and (g) Ni catalyst. Typical RBM modes detected with 532 and 633 nm laser excitation lines for; (b) Fe, (e) Co and (h) Ni catalyst. Histogram of the SWNT diameters obtained via RBM for; (c) Fe, (e) Co and (i) Ni catalyst. CNT growth parameters as above.

of $1.4 - 2.2$ nm. Again, it should be noted that since the measurements were only undertaken using two laser excitation lines these results do not provide a full diameter characterisation of the sample. However, from the data collected we can suggest that the histogram of SWNT diameters for the Co and Ni catalysts correlates with the particle size distributions shown in Figure 7.5. For nanotubes synthesized using the Fe catalyst this was not the case.

7.4 Interactions between Catalyst and HfO_2 Support

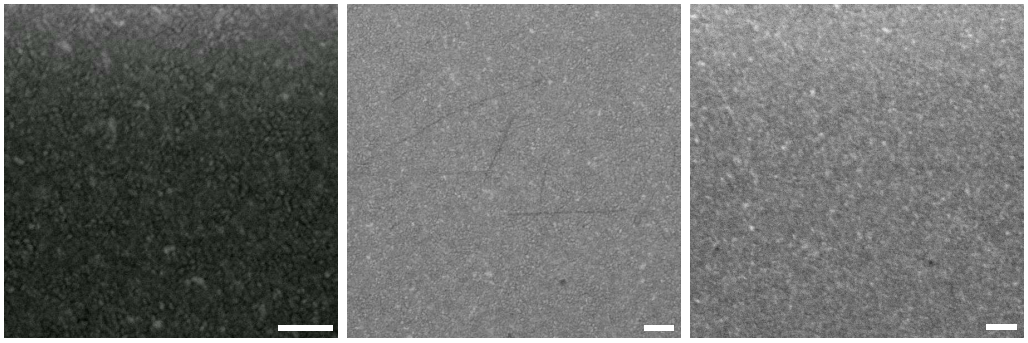

(a) (b) (c)

FIGURE 7.7: Scanning electron microscope images of CNTs synthesized from three transition metal catalysts; (a) Fe, (b) Co and (c) Ni, dispersed on a HfO_2 support. The CNTs were grown by depositing 1 mM of a metal-nitrate salt by dip coating, followed by a nitrate reduction anneal in air at 400 °C for 20 minutes prior to the CNT growth step at 900 °C in a mixture of H_2 and CH_4 (1 : 3 gas ratio) for 20 minutes. Scale bar corresponds to 250 nm.

Figure 7.7 shows SEM images of CNTs synthesized on a HfO_2 support from three transition metal catalysts; (a) Fe, (b) Co and (c) Ni. The samples were prepared using 1 mM of metal nitrate catalyst, deposited by dip coating. The samples were then subjected to a nitrate decomposition anneal in air at 400 °C for 30 minutes, followed by pretreatment in H_2 for 10 minutes and CNT growth step at 900 °C for 20 minutes in a mixture of H_2 and CH_4. From the SEM images it is evident that no CNTs were synthesized on any catalyst on this support medium. It should be noted that a small amount of nanotubes were found using the Co and Fe catalysts, however the yield was extremely low and the coverage across the sample was inhomogeneous. This growth could be attributed to a contaminant or a due to a defect in the HfO_2 capping layer. A range of growth conditions were carried out for all catalysts and in all cases, there were no statistically significant number of CNTs found. This support has shown to be inactive for CNT growth.

In order to investigate this effect, AFM analysis of the catalysts supported on HfO_2 was undertaken. Figure 7.8 show particle size distributions for each catalyst after the nitrate decomposition anneal, and following a pretreatment anneal in H_2 for 10 minutes

at 900 °C. From the typical AFM images, the mean density of particles before and after pretreatment in H_2 has also been determined. The Fe-HfO_2 catalyst-support system showed an initial density of 621 ± 59 particles/μm^2, which after pretreatment in H_2 was reduced to 420 ± 49 particles/μm^2. The initial distribution of the Fe catalyst was broad, with a modal height of 4.1 ± 1.9 nm. This is broader and the modal height is larger than that seen for the SiO_2 and Al_2O_3 support, indicating higher adsorption of Fe on HfO_2. Upon pretreatment in H_2 at 900 °C, there is a narrowing in the distribution and a slight reduction in modal height, to 3.7 ± 1.2 nm. The change in the particle size distributions shows a preferential reduction of larger nanoparticles, and an increase in the proportion of smaller nanoparticles. This behaviour suggests that breakup and redispersion of larger particles is taking place. Redispersion typically occurs when there is a strong interaction between the catalyst and the support medium, resulting in wetting along the support surface [343]. However, the relatively small change in the distribution indicates that a more likely possibility is that the H_2 pretreatment at a 900 °C leads to a reduction of the Fe_xO_y formed during the nitrate reduction anneal in air, resulting in a slight reduction in nanoparticle size. Indeed, the particles are thought to be composed of two phases prior to H_2 pretreatment; an oxidised surface and a metal core. The behaviour of the Co-HfO_2 and Ni-HfO_2 catalyst support system are markedly different. The Co-HfO_2 catalyst-support system showed no statistically significant change upon H_2 pretreatment. The nanoparticle density after H_2 pretreatment, 350 ± 41 particles/μm^2 is very similar to the initial density of 375 ± 58 particles/μm^2. The particle size distribution showed a slight narrowing upon pretreatment in H_2, showing a change in modal height from 1.6 ± 0.8 nm to 1.6 ± 0.6 nm. However, this change is too small to be considered a significant result. In the case of the Ni-HfO_2 system, the nanoparticle density after pretreatment in H_2, 405 ± 47 particles/μm^2 is also very similar to the initial density of 470 ± 54 particles/μm^2. The particle size distribution also showed little change, with the initial modal height changing from 3.2 ± 0.8 nm to 2.4 ± 0.8 nm after pretreatment.

7.5 Ge Nanocrystals as a Catalyst Promoter

Ge nanocrystals were formed on the HfO_2 substrate by a process similar to that outlined in Chapter 5. A 30 nm thick SiO_2 layer was deposited by plasma enhanced chemical vapour deposition on the HfO_2 support, and densified at 950 °C. The top SiO_2 layer was then implanted with 5×10^{15} cm^{-2}, 20 keV Ge and annealed in N_2 at 600 °C for 40 minutes to create Ge nanoparticles. The top SiO_2 layer was then removed using a HF vapour etch to expose the Ge nanocrystals and the HfO_2 layer.

Figure 7.9 shows FE-SEM images after CNT growth for samples using (a) Ge nanoparticles only and a (b) combined Fe/Ge nanoparticles. For Ge nanocrystals supported on HfO_2, shown in Figure 7.9(b), no CNTs were detected. A range of growth conditions

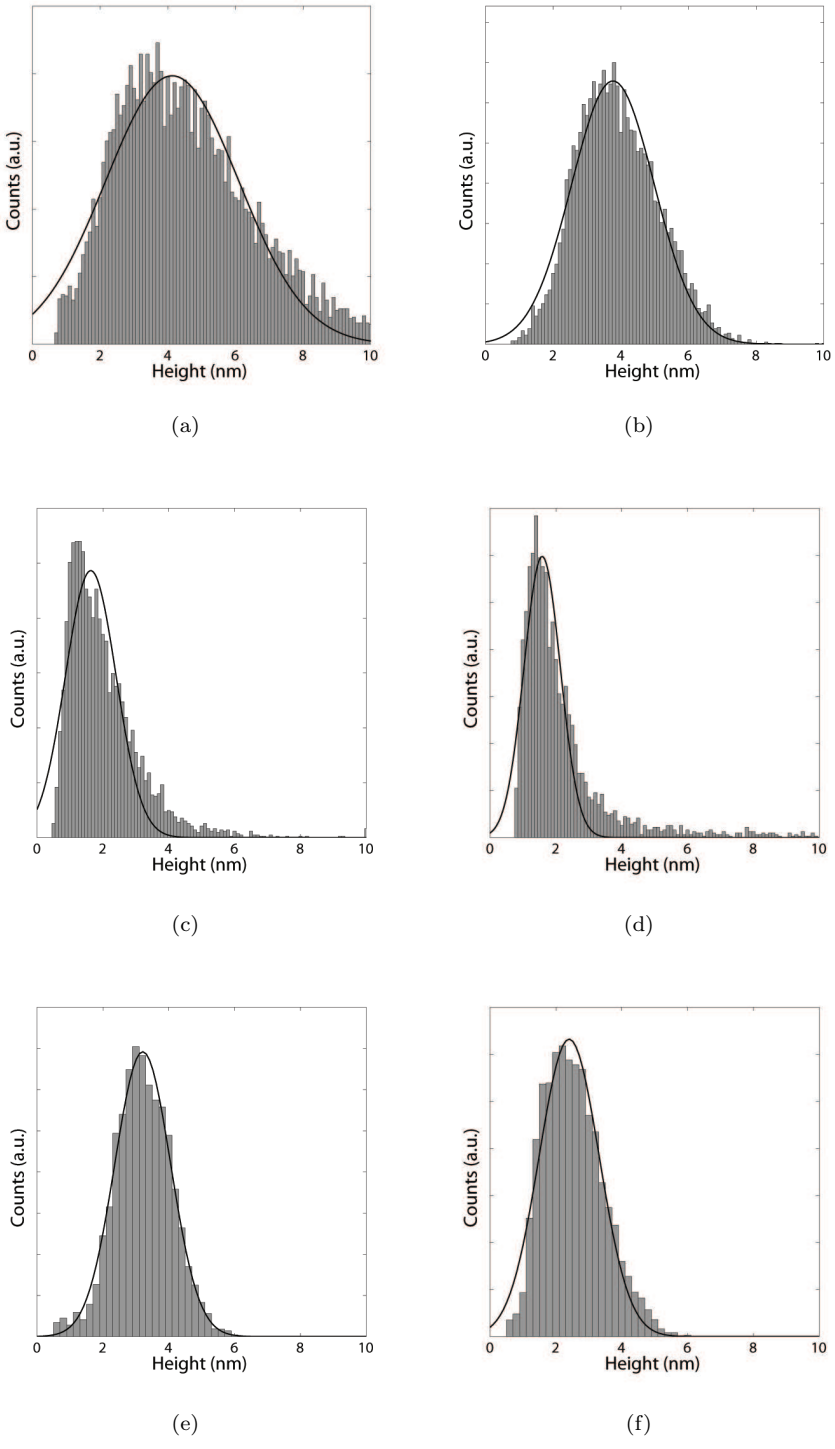

FIGURE 7.8: Particle size distribution for 1 mM transition metal catalysts dispersed on a HfO_2 support before and after anneal in H_2 for 10 minutes. (a) Fe catalyst as deposited. (b) Fe catalyst after anneal at 900. (c) Co catalyst as deposited. (d) Co catalyst after anneal at 900 °C. (e) Ni catalyst as deposited. (f) Ni catalyst after anneal at 900 °C. Particle size distributions have been fitted with a non-centred, normalised Gaussian.

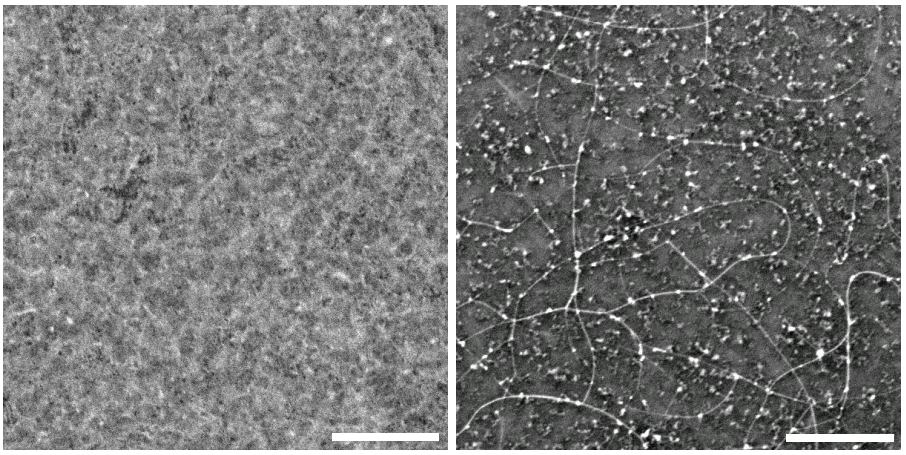

(a) (b)

FIGURE 7.9: Scanning electron microscope images of CNTs synthesized on a HfO_2 support, using (a) Ge nanocrystals only and (b) Fe-Ge nanocrystal catalyst. The CNTs were grown by depositing 1 mM of a metal-nitrate salt by dip coating, followed by a nitrate reduction anneal in air at 400 °C for 20 minutes prior to the CNT growth step at 900 °C in a mixture of H_2 and CH_4 (1 : 3 gas ratio) for 20 minutes. Scale bar corresponds to 500 nm.

was carried out for the Ge nanocrystal catalyst and in all cases, there were no statistically significant number of CNTs found. It should be noted that for Fe nanoparticles supported on HfO_2, as discussed in Section 7.4, there was also no statistically significant number of CNTs detected and only isolated CNTs are occasionally seen. In contrast, the presence of the Ge nanocrystals in conjuction with Fe nanoparticles dramatically enhances CNT growth, giving an area density of 6.2 ± 0.3 μm in length/μm^2. These results indicate that the presence of Ge nanocrystals dramatically enhances the area density of CNTs on HfO_2. Furthermore, the results suggest that selective CNT growth on HfO_2 may be possible by using photo-resist mask patterns during Ge ion implantation.

To determine the morphology of the catalyst supported on HfO_2, AFM characterisation of the samples has been undertaken for Ge and Fe-Ge catalysts before and after pretreatment at 900 °C in H_2 for 10 minutes. Figure 7.10 shows the particle size distributions derived from a minimum of 15 AFM images for the Ge and Fe-Ge catalyst supported on HfO_2. The mean density of the Ge-HfO_2 catalyst-support system showed a mean density of 157 ± 18 particles/μm^2, which after pretreatment in H_2 was reduced to 70 ± 9 particles/μm^2. It is evident that upon pretreatment, there is an associated reduction in nanoparticle density. This reduction in density is most likely due to the nanoparticle evaporation or ripening. The initial particle size distribution is shown in Figure 7.10(a) and is closely fitted with a non-centred, normalised Gaussian curve ($R_2 = 0.951$). This distribution was narrow, with a single mode at 1.3 ± 0.4 nm. After pretreatment, the distribution showed a bimodal characteristic, with modal peaks at 1.9 ± 0.7 and 12.8 ± 1.9 nm (Figure 7.10(b)). This shows that there is a significant change in the morphology of

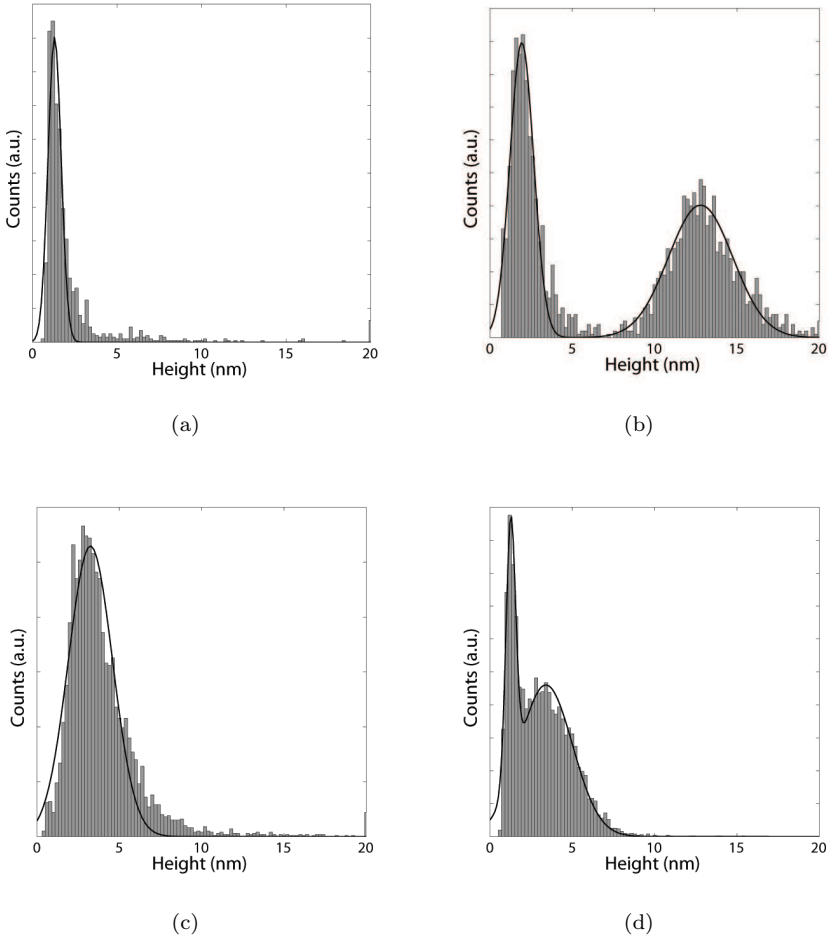

FIGURE 7.10: Particle size distribution for catalysts dispersed on a HfO_2 support before and after anneal in H_2 for 10 minutes. (a) Ge nanocrystals only, as deposited. (b) Ge nanocrystals only, after anneal at 900. (c) Fe-Ge nanocrystal catalyst as deposited. (d) Fe-Ge nanocrystal catalyst after anneal at 900 °C. Particle size distributions have been fitted with a non-centred, normalised Gaussian.

the Ge nanoparticles supported on HfO_2 upon pretreatment in H_2. There is a proportional increase in the number of larger particles, shown by the formation of the larger mode at 12.8 ± 1.9 nm. Additionally, there is also an increase in the mean size of the nanoparticles and a broadening of the distribution. This behaviour suggests a mechanism of phase coarsening, and low adsorption energy of Ge on the HfO_2 support. The initial density of the Fe-Ge-HfO_2 catalyst support was 426 ± 54 particles/μm^2. Upon pretreatment in H_2 for 10 minutes, this was reduced to 357 ± 9 particles/μm^2. The reduction in density upon H_2 pretreatment is similar in magnitude to that seen with the Ge nanoparticles. This is expected as previous experiments showed that the density of Fe nanoparticles only, supported on HfO_2 showed little change after pretreatment. The initial distribution of the Fe-Ge catalyst shows a single mode, centred at 3.2 ± 1.3 nm. After pretreatment, the distribution becomes bimodal, with modal peaks at 1.3 ± 0.3 and 3.4 ± 1.6 nm. This change is less pronounced than that seen for the Ge nanocrystals

only, the modal peaks are smaller and the distribution is narrower. This is possibly due to the strong interaction between the Fe and the HfO_2 support.

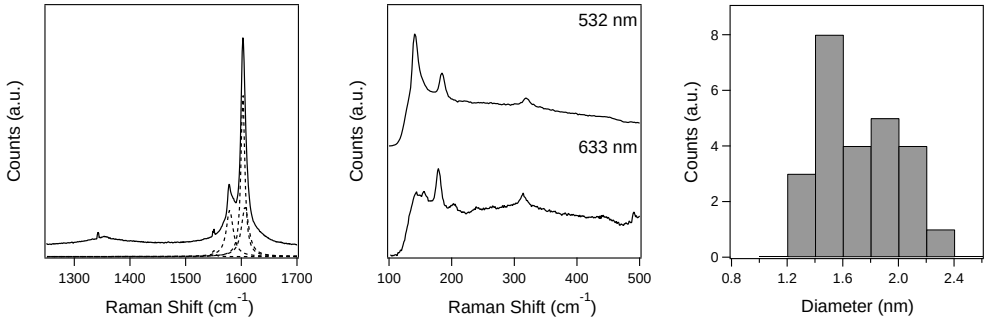

FIGURE 7.11: Raman spectra for the carbon nanotubes synthesized using a Fe - Ge nanocrystal catalyst dispersed on a HfO_2 support. The CNTs were grown using a nitrate reduction anneal in air at 400 °C for 20 minutes prior to the CNT growth step at 900 °C in a mixture of H_2 and CH_4 (1 : 3 gas ratio) for 20 minutes. (a) Typical G-band characteristic detected with 532 nm laser excitation, fitted with four Lorentzian curves. (b) Typical RBM modes detected with 532 and 633 nm laser excitation lines. (c) Histogram of the SWNT diameters obtained via RBM.

The CNTs grown from the combined Fe-Ge nanoparticles were characterised by Raman spectroscopy and the results are shown in Figure 7.11. The Raman spectra obtained from areas of relatively high CNT area density typically exhibited an asymmetric double peak at approximately 1590 cm^{-1} (Figure 7.11(a)). This double peak can be attributed to the Raman allowed tangential mode of CNTs, G-band. In the representative spectrum shown in Figure 7.11(a), this could be fitted with four Lorentzian oscillators located at 1550, 1579, 1602 and 1606 cm^{-1}. The Raman intensity ratio (I_D/I_G) of D-band to G-band was less than 0.1, indicating that synthesized SWNTs have a low defect density. All samples clearly showed the radial breathing mode, and M-band, indicating that SWNTs are present. Figure 7.11(b) shows the spectral region of $100 - 500$ cm^{-1} by two laser excitation lines, 532 nm and 633 nm at different sample locations. Due to a broad luminescence it was not possible to obtain Raman measurements in this region using a 785 nm laser excitation line. The diameter distribution of SWNTs is estimated at $1.4 - 2.3$ nm from the RBM peaks, though larger diameter SWNTs may be present due to the cut-off of the Raman notch filter. A histogram of the SWNT diameters is shown in Figure 7.11(c). It should be noted that since the measurements were only undertaken using two excitation lines these results do not provide a full diameter characterisation of the sample. The histogram indicates that the SWNTs observed had a modal peak of 1.4 nm and shows a similar profile to Figure 7.8(b).

To study the relationship between the catalyst and the synthesized CNTs, AFM characterisation of the CNTs grown from the combined Fe-Ge nanoparticles was undertaken. Figure 7.12(a) shows a typical AFM image of the sample after CNT growth. This image shows a high density of nanoparticles and CNTs. The diameter of the CNTs detected

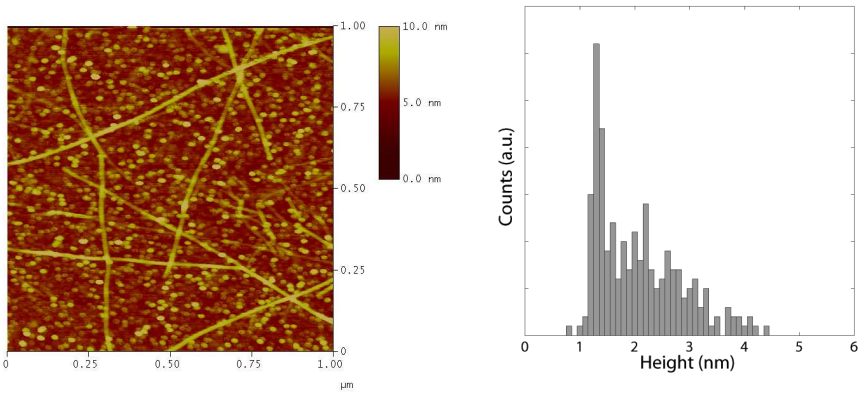

(a) (b)

FIGURE 7.12: (a) Atomic force microscope image of CNTs on a HfO_2 support using Fe-Ge nanocrystal catalyst. The CNTs were grown by depositing 1 mM of a Fe-nitrate salt by dip coating, followed by a nitrate reduction anneal in air at 400 °C for 20 minutes prior to the CNT growth step at 900 °C in a mixture of H_2 and CH_4 (1 : 3 gas ratio) for 20 minutes. (b) Histogram of the diameter distribution of the synthesized CNTs, generated from 196 nanotubes.

were measured and were found to be between $0.8 - 4.4$ nm. A histogram of the CNTs diameters measured, consisting of data from 296 CNTs, is shown in Figure 7.12(b). It should be noted that CNTs with diameters larger than 3 nm are unlikely, and that the larger diameter nanotubes measured are most likely bundles. The histogram shows a diameter distribution with two modal peaks at 1.3 and 2.2 nm. This distribution closely matches that of the Fe-Ge nanoparticles after pretreatment at 900 °C in H2, shown in Figure 7.11(c). Indeed, there is a consensus in the literature concerning the correlation between the catalyst size and the CNT diameter. Many groups have observed a direct dependence of the two quantities [150–159]. Nikolaev et al. [189] observed that the catalyst particle tends to be slightly larger than CNT diameter, suggesting a growth mechanism involving graphene cap formation. This appears to be the case in this experiment, as the modal peaks of the Fe-Ge nanoparticles after pretreatment were also slightly larger than the CNT diameters observed.

7.6 Discussion and Conclusions

The activity of a metal catalyst-support system depends upon a variety of factors ranging from the dispersion of the metal salt precursor on the support to the chemical composition and phase of the support material itself. By testing combinations of metal catalysts and support media explores the effect of different catalyst-support interactions upon CNT growth. Three metals, Fe, Co and Ni of moderate to high catalytic activity were chosen for comparison on three different support media, HfO_2, Al_2O_3 and SiO_2. Additionally, a novel growth process using a combination of Fe and Ge nanoparticles

was presented which minimises the effect of the HfO_2 support on the CNT yield. The results of these studies are summarised in Table 7.1.

However, there is still controversy for many of the suggested atomic processes during CNT growth. The active physical and chemical state of the catalyst is still debated; oxide [408], carbide [36, 409] or metallic [36] phases have been proposed for commonly used catalysts. A liquid catalyst is frequently cited as necessary to obtain SWNTs [410], by analogy to VLS theory. Additionally, the properties of a nanoscale catalyst depend strongly on their surfaces and interfaces. Therefore, bulk values do not necessarily apply and effects such as melting point reduction [411], solubility shifts [412] and higher reactivity [413] have led to much speculation.

For the catalysts examined in this study, the overall CVD growth process can be viewed as a two step process: (1) restructuring the deposited metal catalyst into catalytically active nanoparticles during pretreatment and (2) introduction of a carbon feedstock and SWNT growth. The step of catalyst formation is equivalent to the calcination step in conventional heterogeneous catalysis [396]. This step produces the active, metastable catalyst form, usually by oxidising a precursor into a defective oxide that is then carefully activated into the final catalyst form. This process is also followed here, by a combination of a nitrate reduction anneal (oxidation) and a reduction step in H_2.

When supported on SiO_2, the Fe catalyst showed good catalytic activity as observed by CNT area density. In comparison, both Ni and Co catalysts were inactive on this support medium. This difference is believed to be due to the formation of Fe nanoparticles of the preferred size for CNT formation after the reduction anneal. In the case of Ni and Co, the interaction strength between the catalyst and SiO_2 support is weaker than that of Fe, which at higher coverages results in higher clustering and agglomeration. Additionally, Hofmann et al. [396] found that due to its higher affinity to oxygen, Fe does not fully reduce by annealing in vacuum or in H_2 pressure below 4 $m$bar. Due to the lower surface free energies of metal oxide nanoparticles [414] there would be less wetting and agglomeration compared with metallic nanoparticles, resulting in a narrower size distribution. However, it should be noted that Hofmann et al. [396] also determined that FeO is not catalytically active, and that potential metal oxide phases require at least partial reduction. Fe supported on Al_2O_3 provided the highest CNT yield among the nine systems examined. This could again be attributed to the particle size distribution obtained after the reduction anneal. Fe showed a very narrow distribution after the reduction anneal, this is thought to be due to the formation of Fe 2+ and 3+ interface states when supported on Al_2O_3. The Fe-Al_2O_3 interfacial bonding restricts Fe surface mobility, resulting in a narrow catalyst size distribution which allows a high density growth of SWNTs. Additionally, Al_2O_3 is reported to have higher rates of CNT formation [223, 398]. This can be understood through Lewis base theory; a basic support may donate electron density to the catalyst, increasing its catalytic activity.

This behaviour can be observed for all catalysts supported on Al_2O_3, as CNT yield on was significantly higher on this support medium.

Co supported on SiO_2 has received great attention due to its application in Fischer-Tropsch synthesis (high-molecular weight hydrocarbon formation). Through these studies it is known that the metallic phase is the active form for most applications [414]. Although SiO_2 is considered an inert support, the interaction of the Co phase with the SiO_2 support and the formation of surface cobalt silicate or silicate-like species during the preparation of Co-SiO_2 has been reported [415–417]. The formation of silicates decreases the reducibility of the catalyst under growth conditions and reduces the surface area of the active catalyst [418, 419]. In this work Co was found inactive for CNT synthesis when supported on SiO_2. The work of Potoczna-Petru and Krajczyk [414] showed that samples with a low Co catalyst loading on SiO_2 formed Co_2SiO_4 upon anneal at 900 °C in air. Indeed, the binary phase diagram of CoO-SiO_2 shows that Co_2SiO_4 forms at temperatures higher than 900 °C [420]. It should be noted that Potoczna-Petru and Krajczyk [414] also found that following a reduction step in H_2, the crystalline phase of Co was recovered and there was a marked increase in mean particle size due to agglomeration. The particle size distributions for Co-SiO_2 shown in this chapter showed significant evidence of phase coarsening and agglomeration upon a reduction anneal, increasing the modal peak of the catalyst from 1.9 ± 0.8 nm to 7.3 ± 1.8. This behaviour is similar to that seen by Potoczna-Petru and Krajczyk [414], although it is unlikely that Co_2SiO_4 was formed due to the low temperature used in the nitrate reduction anneal in air. The coarsening of the Co catalyst upon anneal can be attributed due to the weak interactions between the support and the catalyst. The inability of this catalyst support system to synthesize CNTs is most likely due to the morphology of the catalyst after the reduction anneal in H_2. In the case of Co supported on Al_2O_3, the particle size distribution after the reduction anneal remained relatively unchanged. This possibly is due to the formation of interfacial states, as with the Fe catalyst, which restrict surface mobility.

Ni is reported to have the highest propensity for carbon nanostructure formation [299]. Vander Wal et al. [299] found that Ni is most catalytically active on supports that are capable to donate negative charge upon partial reduction initiated by the supported catalyst. Group VIIIB elements are known for their ability to catalyse H_2 decomposition [421]. On TiO_2 for instance, the resulting H-atoms are known to reduce the oxide to one with an empirical formula of Ti_4O_7 [422, 423]. The presence of H_2 in the carrier gas may further accelerate this process. In the reduced state, the Ti ion may transfer electronic charge to the supported metal catalyst. The results obtained for Ni are consistent with this process, Ni is most active on Al_2O_3 than SiO_2, which is less readily reduced [299]. Additionally, the morphology of the catalyst plays a very important part. The results shown in this chapter show that due to weak interactions between Ni and SiO_2 there is significant coarsening of the catalyst, which showed an increase in modal height from

1.0 ± 0.2 nm to 3.7 ± 1.4 nm. In contrast, on Al_2O_3, Ni showed a very slight increase in modal height, from 1.4 ± 0.4 nm to 1.9 ± 0.6 nm. This resulted in the synthesis of SWNTs, at a reasonable density. It should be noted that Ni catalysed SWNTs showed a larger diameter than Fe and Co (on Al_2O_3), similar results are also seen in the literature [396].

SWNT synthesis on a HfO_2 has shown to be very problematic. Fe, Co and Ni nanoparticles were unable to catalyse SWNTs when dispersed on this support medium. AFM analysis of the deposited metal nanoparticles showed that all catalysts were well dispersed and with a modal height adequate for SWNT synthesis. Upon pretreatment in H_2 at 900 °C, there was little reduction in nanoparticle density and the particle size distributions showed little change. From the results presented, it is evident that the interactions between the HfO_2 support and the metal catalysts are chemical. It has been reported that upon a high temperature anneal in an inert atmosphere, oxygen vacancy states in HfO_2 are formed [403]. These appear to exist in sizeable amounts in HfO_2 films [424, 425], which allow oxygen transport across the HfO_2 layer [426]. This effect is expected to be more pronounced in a reducing atmosphere such as H_2. One possibility for the difficulty in catalysing SWNTs on a HfO_2 support may be due to a transfer of the oxygen liberated from the vacancy into the metal catalyst, forming an oxide cap which is expected to be inactive. Calculations have indicated that the modified vacancy formation energy for this mechanism is too large to allow enough vacancies to have an effect in bulk metals [403]. However for nanoparticular metals, the free energy of oxide formation per O atom for bulk high work function metals (such as Fe, Co or Ni) is expected to be lower due to surface effects, and would require the formation of less oxygen vacancies.

Finally, a novel technique using a combination of Fe and Ge nanoparticles was presented which allowed carbon nanotubes to be grown directly on HfO_2 for the first time. These results were published in Uchino et al. [427]. Experiments showed that the presence of Ge nanoparticles dramatically increases the area density of CNTs. It is thought that the Ge nanoparticles act as a barrier layer, passivating the support. It is possible that this effect could also be achieved by the deposition of a thin film. However, it is likely that the higher surface area achieved by using Ge nanoparticles, compared with a Ge thin film, has an effect on the yield of the process. Further experimentation is required to investigate this issue.

Additionally, the origin of SWNTs was investigated by TEM (by Dr. Takashi Uchino), and the resulting images were also presented in [427]. The TEM images show the presence of at least two distinct nanoparticles with a diameter around 6 nm and SWNT appear to originate from these particles. The SWNTs are wrapped with amorphous carbon layers, which are probably due to the long growth time of 20 minutes. The undesirable amorphous carbon coating could be avoided by reducing the growth time. Raman measurements have shown that the SWNTs have a low intensity D-band peak

which indicates a small amount of amorphous carbon coating and defects. However, the I_D/I_G ratio was low, indicating that the nanotubes were of a good quality in terms of graphitisation and structure. To investigate the nature of the nanoparticles, EDS was carried out on the nanoparticle and showed that the atomic ratio of Fe/Ge is 3.2. As the nanoparticle is surrounded and sat on a support material into which Ge was implanted, it is likely that the nanoparticle is richer in Fe relative to Ge than this ratio implies. A lattice image of the nanoparticle was also taken, and this showed that the measured lattice spacing was 0.20 nm and the corresponding fast Fourier transfer pattern gives a lattice constant of 0.28 nm which is in reasonable agreement with the lattice constant of Fe ($a = 0.29$ nm) and quite different from the lattice constant of FeGe ($a = 0.47$ nm) [428]. In the previous chapters, we determined that CNT growth was possible from Ge nanoparticles, without the presence of a metal catalyst. However, in this work, the results indicate that CNTs were grown from the Fe nanoparticles rather than the Ge nanoparticles. In interpreting these results, it should be also noted that Figure 7.7(a) shows no significant CNT growth when only Fe nanoparticles are present. Thus, the improvement of CNT area density when Ge nanoparticles are combined with Fe nanoparticles can be attributed to a reduction in the interactions between the Fe nanoparticles and the HfO_2 layer due to the presence of the Ge nanoparticles.

Catalyst -Support	As Formed			After 900 °C Anneal			CNT Yield
	Mode (nm)	R_2 (nm)	Density (particles/μm^2)	Mode (nm)	R_2 (nm)	Density (particles/μm^2)	(μm in length/μm^2)
Fe-SiO_2	1.2 ± 0.4	0.989	495 ± 23	2.7 ± 1.2	0.941	422 ± 37	3.5 ± 0.2
Co-SiO_2	1.9 ± 0.8	0.993	530 ± 27	7.3 ± 1.8	0.989	125 ± 84	N/A
Ni-SiO_2	1.0 ± 0.2	0.994	340 ± 96	3.7 ± 1.4	0.973	180 ± 48	N/A
Fe-Al_2O_3	1.2 ± 0.4	0.984	580 ± 66	1.1 ± 0.3	0.946	390 ± 55	7.6 ± 0.8
Co-Al_2O_3	0.9 ± 0.3	0.984	504 ± 34	1.6 ± 0.6	0.942	446 ± 47	5.5 ± 1.1
Ni-Al_2O_3	1.4 ± 0.4	0.992	521 ± 48	1.9 ± 0.6	0.995	468 ± 54	3.8 ± 0.6
Fe-HfO_2	4.1 ± 1.9	0.979	621 ± 59	3.7 ± 1.2	0.991	420 ± 49	N/A
Co-HfO_2	1.6 ± 0.8	0.956	375 ± 58	1.6 ± 0.6	0.935	350 ± 41	N/A
Ni-HfO_2	3.2 ± 0.8	0.996	470 ± 54	2.4 ± 0.8	0.989	405 ± 47	N/A
Ge-HfO_2	1.3 ± 0.4	0.951	157 ± 18	1.9 ± 0.7, 12.8 ± 1.9	0.970	70 ± 9	N/A
Fe-Ge-HfO_2	3.2 ± 1.3	0.957	426 ± 54	1.3 ± 0.3, 3.4 ± 1.6	0.991	357 ± 38	6.2 ± 0.3

TABLE 7.1: Particle size distribution fit parameters for various catalyst-support systems. Shown in the table are nanoparticle densities following a nitrate decomposition anneal in air and after pretreatment in H_2 at 900 °C. CNT yield for each catalyst-support system are also shown. Samples were prepared by dip-coating 1 mM of metal-nitrate salt solution.

Chapter 8

Conclusions and Perspectives

The aim of this work was to investigate the use of non-traditional catalyst-assisted chemical vapour deposition of carbon nanotubes with a view to determine the essential role of the catalyst in nanotube growth. Initial experiments by Uchino et al. [10] at the University of Southampton showed that carbon doped SiGe islands, deposited by CVD on Si, form nanoscale clusters through various mechanisms which act as a seed for SWNT growth. These results were supported by the work of Takagi et al. [11], who showed that CNT growth from Ge, Si and SiC nanoparticles was possible. More recently, there have been various reports of CNT growth from SiO_2 nanoparticles [279, 282], which are thought to be promising catalysts owing to their ability to maintain a narrow size distribution at CNT growth temperatures.

To investigate the role of Ge nanoparticles on carbon nanotube growth, Ge nanoparticles have been directly fabricated by Ge implantation into silicon dioxide and anneal at various temperatures. Analysis by AFM showed that good control of the Ge nanoparticle size is obtained through this process, and SEM analysis showed that CNT growth from nanoparticles formed by anneal at 600 °C and 800 °C. The highest yields were obtained from the nanoparticles annealed at 600 °C, corresponding to an approximate nanoparticle size of 2.0 nm. Carbon nanotubes were grown successfully on both samples with and without carbon implantation, demonstrating that a solid source of carbon is not necessary for CNT growth on Ge nanoparticles. However, samples subjected to a carbon implant show an advantage of enabling CNT growth for a wider range of pretreatment and growth conditions. Furthermore, Raman measurements showed the presence of a disorder induced D-band peak in carbon nanotubes grown without the carbon implant, but this peak was absent in carbon implanted samples.

Ge nanoparticles were also synthesized from solution by means of an inverse micelle technique. The colloidal Ge nanoparticle catalyst was shown to be a viable catalyst for the synthesis of SWNTs from a silicon dioxide support. The results indicate that the inverse micelle technique provides good control over the morphology of the nanoparticles

and delivers a well-controlled CNT growth process. A SWNT area density of 5.2 ± 0.7 μm in length/μm^2 was obtained from the colloidal Ge nanoparticles under the optimum growth condition. This process has the advantage of being amenable to large-scale manufacturing by means of a floating catalyst approach and offers the possibility of CNT synthesis on a variety of support materials. In order to determine the role of the support in the synthesis of CNTs from Ge colloidal nanoparticles, Al_2O_3 was also used as a support medium and the CNT growth process was examined. SEM measurements showed that two types of carbon nanostructures were synthesized using this catalyst-support system after pretreatment at 1000 and 950 °C. After pretreatment at 1000 °C, carbon nanofibres were synthesized. Following a pretreatment at 900 °C, a homogeneous coverage of MWNTs (as determined by Raman spectroscopy) was synthesized. This was attributed to a weaker catalyst-support interaction compared with Ge-SiO_2, which led to increased clustering and aggregation of nanoparticles.

Both CNT synthesis techniques based on Ge nanoparticles presented in this thesis resulted in the formation of silica nanowires as a byproduct. Raman, PL and TEM measurements confirmed the synthesized nanostructures as SiO_x nanowires. TEM images showed that the nanowires had a typical diameter in the range of $10 - 20$ nm, and EDS measurements indicated that the nanowires were oxygen deficient. This hypothesis was confirmed by the PL spectrum, which showed a neutral oxygen vacancy and twofold coordinated silicon lone pair centres. The Raman spectra showed a peak at 505 cm^{-1}, which is attributed to a shift in the first-order optical phonon of silicon (520 cm^{-1}) due to phonon confinement effects in the nanowire. SEM measurements showed pitting in the substrate at the base of the nanowires, indicating that nanowire formation is most likely due to a SLS growth mechanism. It is suggested that this occurs due to carbothermal reduction of the SiO_2 support.

Additionally, SWNT growth catalysed by noble metal nanoparticles has been studied. Au and Cu nanoparticles have shown to be adequate catalysts for CNT growth and extensive characterisation has been undertaken for each step of the growth process. Au nanoparticles of 1.4 ± 0.2 nm, synthesized by *Nanoprobes Inc*, were used as a catalyst. The results indicate that SWNT growth is possible on a silicon dioxide support from dilutions of 0.3 mM, after pretreatment in H_2 at a range of temperatures between $900 - 1050$ °C. H_2 pretreatment was shown to be crucial for the growth of SWNT, as it is believed that growth is only possible from contaminant free nanoparticles, once the residual shell of gold oxides or gold chlorides have been reduced. Cu nanoparticles were formed by the thermal decomposition of copper nitrate in air at 400 °C. Three concentrations of metal nitrate solution were prepared, and CNT growth was shown to be possible from Cu nanoparticles prepared from 1 mM and 2 mM dilutions. As was the case with the Au nanoparticles, CNT growth was only possible after pretreatment in H_2 at temperatures between $850 - 1000$ °C. From analysis of the uniformity of the samples, it was observed that the yield improves with an increase in pretreatment temperature.

This suggests that the H_2 pretreatment affects the morphology of the catalyst. This hypothesis was confirmed by AFM analysis of the nanoparticles after pretreatment, which showed a reduction in nanoparticle size as pretreatment temperatures increased. Finally, Ag nanoparticles were shown to be unable to catalyse CNT formation. AFM analyses showed this to be due to a loss of nanoparticles during pretreatment. This is most likely due to the lower melting point of Ag compared with Cu and Au.

The role played by the support in the CVD of CNTs is not yet fully understood. The simplistic view that the support only plays a catalytically passive role in the formation of CNTs requires examination. By testing combinations of metal catalysts and support media, the effect of different catalyst support interactions were explored. Three metals, Fe, Co and Ni of moderate to high catalytic activity were chosen for comparison on three different support media, HfO_2, Al_2O_3 and SiO_2. Additionally, a novel growth process using a combination of Fe and Ge nanoparticles was presented which minimises the effect of the HfO_2 support on the CNT yield. The results of these studies are summarised in Table 7.1.

When supported on SiO_2, the Fe catalyst showed good catalytic activity as observed by CNT area density. In comparison, both Ni and Co catalysts were inactive on this support medium. This difference is believed to be due to the formation of Fe nanoparticles of the preferred size for CNT formation after the reduction anneal. In the case of Ni and Co, the interaction strength between the catalyst and SiO_2 support is weaker than that of Fe, which at higher coverages results in higher clustering and agglomeration. Fe supported on Al_2O_3 provided the highest CNT yield among the nine systems examined. This could again be attributed to the particle size distribution obtained after the reduction anneal. Fe showed a very narrow distribution after the reduction anneal, this is thought to be due to the formation of Fe 2+ and 3+ interface states when supported on Al_2O_3. The Fe-Al_2O_3 interfacial bonding restricts Fe surface mobility, resulting in a narrow catalyst size distribution which allows a high density growth of SWNTs.

In this work Co was found inactive for CNT synthesis when supported on SiO_2. The particle size distributions for Co-SiO_2 shown in this chapter showed significant evidence of phase coarsening and agglomeration upon a reduction anneal, increasing the modal peak of the catalyst from 1.9 ± 0.8 nm to 7.3 ± 1.8. The coarsening of the Co catalyst upon anneal can be attributed due to the weak interactions between the support and the catalyst. The inability of this catalyst support system to synthesize CNTs is most likely due to the morphology of the catalyst after the reduction anneal in H_2. In the case of Co supported on Al_2O_3, the particle size distribution after the reduction anneal remained relatively unchanged. This possibly is due to the formation of interfacial states, as with the Fe catalyst, which restrict surface mobility.

The results obtained for Ni are consistent with the fact that Ni is most catalytically active on supports that are capable to donate negative charge upon partial reduction

initiated by the supported catalyst [299]. Ni is most active on Al_2O_3 than SiO_2, which is less readily reduced [299]. Additionally, the morphology of the catalyst plays a very important part. The results shown in this chapter show that due to weak interactions between Ni and SiO_2 there is significant coarsening of the catalyst, which showed an increase in modal height from 1.0 ± 0.2 nm to 3.7 ± 1.4 nm. In contrast, on Al_2O_3, Ni showed a very slight increase in modal height, from 1.4 ± 0.4 nm to 1.9 ± 0.6 nm. This resulted in the synthesis of SWNTs, at a reasonable density. It should be noted that Ni catalysed SWNTs showed a larger diameter than Fe and Co (on Al_2O_3), similar results are also seen in the literature [396].

SWNT synthesis on a HfO_2 has shown to be very problematic. Fe, Co and Ni nanoparticles were unable to catalyse SWNTs when dispersed on this support medium. AFM analysis of the deposited metal nanoparticles showed that all catalysts were well dispersed and with a modal height adequate for SWNT synthesis. One possibility for the difficulty in catalysing SWNTs on a HfO_2 support may be due to a transfer of the oxygen liberated from the vacancy into the metal catalyst, forming an oxide cap which is expected to be inactive. A novel technique using a combination of Fe and Ge nanoparticles was presented which minimises the effect of the HfO_2 support on the CNT yield. A good yield of CNTs were fabricated using this technique.

Despite enormous strides in the synthesis of CNTs, the mechanism for growth is still a highly debated issue. As discussed previously, it is generally accepted that the model for carbon filament growth [1, 2], derived from concepts of VLS theory, also applies to CNT growth. This belief arises from the visual observation (by TEM) of catalyst particles on the ends of nanotubes, as was the case with carbon filaments. In this model, hydrocarbons adsorbed on the metal nanoparticle are catalytically decomposed resulting in atomic carbon dissolving into the liquid catalyst particle, and when a supersaturated state is reached, carbon precipitates in a tubular, crystalline form.

However, the results presented in this work suggest several inconsistencies that do not support this mechanism. Successful CNT growths from catalyst free and ceramic catalysts reported in the literature, and the results from noble metal catalysts and semiconducting catalysts shown in this thesis imply that hydrocarbon dissociation ability is not essential in a catalyst. It should be noted that the catalytic behaviour of Cu and Au may be explained by electron donation to the support [299], creating *d*-vacancies which may cause hydrocarbon dissociation. However, the ability of catalyst free and semiconducting catalysts to seed CNT growth cannot be explained by the same mechanism. Reilly and Whitten [176] argue that a more likely scenario is that a free radical condensate (FRC) provides carbon species through a leaving group, such as hydrogen (or oxygen). FRCs naturally form during hydrocarbon pyrolysis by the breaking of carbon-hydrogen or carbon-carbon bonds with each fragment keeping one electron to form two radicals. The presence of a radical in a hydrocarbon molecule permits rapid rearrangement of

carbon bonds. In this case, the catalyst particle's role is to simply provide an interface where carbon rearrangement can occur and act as a template for growth.

Typically, metal catalysts with no *d*-vacancies, such as Cu and Au, do not offer sites to dissolve carbon, such that neither saturation nor precipitation is possible. However, despite the low carbon solubility, these catalysts have demonstrated an ability to catalyse CNT formation. Additionally, catalysts with a high melting point such as Al_2O_3 or ZrO_2 are thought to be solid at CNT synthesis temperatures. However, if nanoparticles of these metals are small enough ($\leq$ 5 nm), the increasing fraction of low-coordinated atoms may lead to surface saturation followed by carbon precipitation, as reported by Takagi et al. [3]. Considering that carbon penetration inside small nanoparticles is unlikely [293], the growth of CNTs is most likely a process primarily controlled by surface diffusion [294, 295]. Indeed, it is believed by several groups that the rate-limiting factor in CNT synthesis is the surface diffusion of carbon across the catalyst [269]. Additionally, this factor could explain the influence of the carbon source on the ability of a catalyst to synthesize CNTs. Yazyev and Pasquarello [270] reported different activation energies for the surface diffusion of C dimers and adatoms on noble metal catalysts, and argued that appropriate choice of a diatomic or monatomic carbon gas-phase source could significantly accelerate diffusion.

However, due to their nanometer dimensions the mechanics of growth of nanotubes on nanoparticles are markedly different from the growth of carbon filaments. Other mechanisms are therefore required to explain the nucleation of CNTs from nanoparticle catalysts. One such model is the Yarmulke mechanism proposed by Dai et al. [188]. In the Yarmulke mechanism, a graphene cap is assembled on the particle surface with its edges strongly chemisorbed to the catalyst. The graphene cap acts to reduce the high total surface energy of the particle caused by its high curvature, owing to the fact that the basal plane of graphite has an extremely low surface energy. As additional carbon atoms are added, the hemifullerene cap formed on the particle surface lifts off, creating a hollow tube with constant diameter which grows away from the particle [189]. This model was supported by molecular dynamics simulations by Shibuta and Maruyama [190]. Recent works in high-resolution *in-situ* TEM observation of the catalytic growth of CNTs have verified this mechanism [36, 192]. These studies have also shown that cap stabilisation and nanotube growth involve reshaping of the catalyst nanoparticle.

References

[1] R. T. K. Baker, M. A. Barber, P. S. Harris, F. S. Feates, and R. J. White, "Nucleation and Growth of Carbon Deposites from the Nickel Catalyzed Decomposition of Acetylene," *J. Catal.*, vol. 26, p. 51, 1972.

[2] R. T. K. Baker, P. S. Harris, R. B. Thomas, and R. J. Waite, "Formation of Filamentous Carbon from Iron, Cobalt and Chromium Catalyzed Decomposition of Acetylene," *J. Catal.*, vol. 30, p. 86, 1973.

[3] D. Takagi, Y. Homma, H. Hibino, S. Suzuki, and Y. Kobayashi, "Single Walled Carbon Nanotube Growth from Highly Activated Metal Nanoparticles," *Nano Lett.*, vol. 6, pp. 2642–2645, 2006.

[4] W. Zhou, Z. Han, J. Wang, Y. Zhang, Z. Jin, Z. Sun, Y. Zhang, C. Yan, and Y. Li, "Copper Catalyzing Growth of Single-Walled Carbon Nanotubes on Substrates," *Nano Lett.*, vol. 6, pp. 2987–2990, 2006.

[5] D. Yuan, L. Ding, H. Chu, Y. Feng, T. P. McNicholas, and J. Liu, "Horizontally Aligned Single-Walled Carbon Nanotube on Quartz from a Large Variety of Metal Catalysts," *Nano Lett.*, vol. 8, pp. 2576–2579, 2008.

[6] S. Y. Lee, M. Yamada, and M. Miyake, "Synthesis of Carbon Nanotubes Over Gold Nanoparticle Supported Catalysts," *Carbon*, vol. 43, pp. 2654–2663, 2005.

[7] N. Yoshihara, H. Ago, and M. Tsuji, "Growth Mechanism of Carbon Nanotubes over Gold-Supported Catalysts," *Jpn. J. Appl. Phys.*, vol. 47, pp. 1944–1948, 2008.

[8] H. Liu, D. Takagi, H. Ohno, S. Chiashi, T. Chokan, and Y. Homma, "Growth of Single Walled Carbon Nanotubes from Ceramic Particles by Alcohol Chemical Vapor Deposition," *Appl. Phys. Express*, vol. 1, p. 014001, 2008.

[9] S. A. Steiner, T. F. Baumann, B. C. Bayer, R. Blume, M. A. Worsley, W. J. MoberlyChan, E. L. . Shaw, R. Schlogl, A. J. Hart, S. Hofmann, and B. L. Wardle, "Nanoscale Zirconia as a Nonmetallic Catalyst for Graphitization of Carbon and Growth of Single- and Multiwall Carbon Nanotubes," *J. Am. Chem. Soc.*, vol. 131, pp. 12 144–12 154, 2009.

[10] T. Uchino, K. N. Bourdakos, C. H. de Groot, P. Ashburn, M. E. Kiziroglou, G. D. Dilliway, and D. C. Smith, "Metal Catalyst-Free Low-Temperature Carbon Nanotube Growth on SiGe Islands," *Appl. Phys. Lett.*, vol. 86, p. 233110, 2005.

[11] D. Takagi, H. Hibino, S. Suzuki, Y. Kobayashi, and Y. Homma, "Carbon Nanotube Growth from Semiconductor Nanoparticles," *Nano Lett.*, vol. 7, pp. 2272–2275, 2007.

[12] T. Uchino, K. N. Bourdakos, G. N. Ayre, C. H. de Groot, P. Ashburn, and D. C. Smith, "CMOS Compatible Synthesis of Carbon Nanotubes," *Mater. Res. Soc. Symp. Proc.*, vol. 1081, pp. 1081–P01–09, 2008.

[13] T. Uchino, G. N. Ayre, D. C. Smith, J. L. Hutchison, C. H. de Groot, and P. Ashburn, "Growth of Single-Walled Carbon Nanotubes Using Germanium Nanocrystals Formed by Implantation," *J. Electrochem. Soc.*, vol. 156, pp. K144–K148, 2009.

[14] M. S. Dresselhaus, G. Dresselhaus, and P. C. Eklund, *Science of Fullerenes and Carbon Nanotubes.* Academic Press, 1996.

[15] K. McGuire and A. M. Rao, *Carbon Nanotubes: Science and Applications.* CRC Press, 2005, ch. V - Characterisation Techniques in Carbon Nanotube Research, pp. 117–135.

[16] R. Andrews, D. Jacques, A. R. Rao, F. Derbyshire, D. Qian, X. Fan, E. C. Dickey, and J. Chen, "Continuous Production of Aligned Carbon Nanotubes: a Step Closer to Commercial Realization," *Chem Phys. Lett.*, vol. 303, p. 467, 1999.

[17] A. Thess, R. Lee, P. Nikolaev, H. Dai, P. Petit, J. Robert, C. Xu, Y. H. Lee, S. G. Kim, G. E. S. A. G. Rinzler, D. T. Colbert, D. Tomnek, J. E. Fischer, and R. E. Smalley, "Crystalline Ropes of Metallic Carbon Nanotubes ," *Science*, vol. 273, p. 483, 1996.

[18] A. M. Rao, E. Richter, S. Bandow, P. C. Eklund, K. A. Williams, S. Fang, K. R. Subbaswamy, M. Menon, A. Thess, R. E. Smalley, G. Dresselhaus, and M. S. Dresselhaus, "Diameter-Selective Raman Scattering from Vibrational Modes in Carbon Nanotubes ," *Science*, vol. 275, p. 187, 1997.

[19] H. Kataura, Y. Kumazawa, Y. Maniwa, I. Umezu, S. Suzuki, Y. Ohtsuka, and Y. Achiba, "Optical Properties of Single-Wall Carbon Nanotubes," *Synth. Metals*, vol. 103, p. 2555, 1999.

[20] E. Obraztova, V. Yurov, V. Shevluga, R. Branovsky, V. Nalimova, V. Kuznetsov, and V. Zaikovskii, "Structured Investigations of Close-Packed Single-Wall Carbon Nanotube Material," *Nanostruct. Mater.*, vol. 1999, p. 295, 11.

[21] M. S. Dresselhaus, A. Jorio, A. G. S. Filho, G. Dresselhaus, and R. Saito, "Raman Spectroscopy on One Isolated Carbon Nanotube," *Physica B*, vol. 323, p. 15, 2002.

[22] S. Bandow, S. Asaka, Y. Saito, A. M. Rao, L. Grigorian, E. Richter, and P. C. Eklund, "Effect of the Growth Temperature on the Diameter Distribution and Chirality of Single Walled Carbon Nanotubes," *Phys. Rev. Lett.*, vol. 80, p. 3779, 1998.

[23] S. Bandow, G. Chen, U. Sumanasekera, R. Gupta, M. Yudasaka, S. Iijima, and P. C. Eklund, "Diameter Selective Resonant Raman Scattering in Double-Wall Carbon Nanotubes," *Phys. Rev. B.*, vol. 66, p. 075416, 2002.

[24] K. A. Williams, M. Tachibana, J. L. Allen, L. Grigorian, S.-C. Cheng, S. L. Fang, G. U. Sumanasekera, A. L. Loper, J. H. Williams, and P. C. Eklund, "Single-wall Carbon Nanotubes From Coal," *Chem Phys. Lett.*, vol. 310, p. 31, 1999.

[25] A. M. Rao, J. Chen, E. Richter, U. Schlecht, P. C. Eklund, R. C. Haddon, U. D. Venkateswaran, Y.-K. Kwon, and D. Tomanek, "Effect of van der Waals Interactions on the Raman Modes in Single Walled Carbon Nanotubes," *Phys. Rev. Lett.*, vol. 86, p. 3895, 2001.

[26] M. Hulman, R. Pfeiffer, and H. Kuzmandy, "Raman Spectroscopy of Small Diameter Nanotubes," *New J. Phys.*, vol. 6, p. 1, 2004.

[27] T. Belin and F. Epron, "Characterisation Methods of Carbon Nanotubes: A Review," *Mater. Sci. Eng., B*, vol. 119, pp. 105–118, 2005.

[28] A. Jorio, M. Pimenta, A. Souza-Filho, R. Saito, G. Dresselhaus, and M. Dresselhaus, "Characterizing Carbon Nanotube Samples with Resonance Raman Scattering," *New J. Phys.*, vol. 5, p. 139, 2003.

[29] J. F. Colomer, J. M. Benoit, C. Stephan, S. Lefrant, G. V. Tendeloo, and J. B.Nagy, "Characterization of Single-Wall Carbon Nanotubes Produced by CCVD Method," *Chem. Phys. Lett.*, vol. 345, p. 11, 2001.

[30] P. Bernier, W. Maser, C. Journet, A. Loiseau, M. L. D. la Chapelle, R. Lee, and J. F. Fischer, "Carbon Single Wall Nanotubes Elaboration and Properties," *Carbon*, vol. 36, p. 675, 1998.

[31] R. Bacsa, C. Laurent, A. Peigney, W. Bacsa, T. Vaugien, and A. Rousset, "High Specific Surface Area Carbon Nanotubes from Catalytic Chemical Vapor Deposition Process," *Chem Phys. Lett.*, vol. 323, p. 566, 2000.

[32] Y. Zhang, Z. Shi, Z. Gu, and S. Iijima, "Structure Modification of Single-Wall Carbon Nanotubes," *Carbon*, vol. 38, p. 2055, 2000.

[33] P. Corio, P. S. Santos, V. W. Brar, G. G. Samsonidze, S. G. Chou, and M. S. Dresselhaus, "Potential Dependent Surface Raman Spectroscopy of Single Wall Carbon Nanotube Films on Platinum Electrodes," *Chem. Phys. Lett.*, vol. 370, p. 675, 2003.

[34] Y. Park, K. Kim, H. Jeong, W. Kim, J. Moon, K. H. An, D. J. Bae, Y. Lee, and G. Park, "Low Pressure Synthesis of Single-Walled Carbon Nanotubes by Arc Discharge," *Synth. Metals*, vol. 126, p. 245, 2002.

[35] F. Ding and K. Bolton, "The Importance of Supersaturated Carbon Concetration and its Distribution in Catalytic Particles for Single-Walled Carbon Nanotube Nucleation," *Nanote*, vol. 17, p. 543, 2006.

[36] S. Hofmann, R. Sharma, C. Ducati, G. Du, C. Mattevi, C. Cepek, M. Cantoro, S. Pisana, A. Parvez, F. Cervantes-Sodi, A. C. Ferrari, R. Dunin-Borkowski, S. Lizzit, L. Petaccia, A. Goldoni, and J. Robertson, "In situ Observations of Catalyst Dynamics during Surface-Bound Carbon Nanotube Nucleation," *Nano Lett.*, vol. 7, pp. 602–608, 2007.

[37] N. D. Denkov, O. D. Velev, P. A. Kralchevsky, I. B. Ivanov, H. Yoshimura, and K. Nagayama, "Mechanism of Formation of Two-Dimensional Crystals from Latex Particles on Substrates," *Langmuir*, vol. 8, pp. 3183 – 3190, 1992.

[38] H. W. Kroto, J. R. Heath, S. C. O'Brian, R. F. Curl, and R. E. Smalley, "C-60 Buckmisterfullerene," *Nature*, vol. 381, p. 162, 1985.

[39] S. Iijima, "Helical Microtubules of Graphitic Carbon," *Nature*, vol. 354, p. 56, 1991.

[40] D. Ugarte, "Curling and Closure of Graphitic Networks Under Electron-Beam Irradiation," *Nature*, vol. 359, p. 707, 1992.

[41] S. Iijima, M. Yudasaka, R. Yamada, S. Bandow, K. Suenaga, F. Kokai, and K. Takahashi, "Nano-Aggregates of Single-Walled Graphitic Carbon Nano-Horns," *Chem Phys. Lett.*, vol. 309, p. 165, 1995.

[42] W. Marx and A. Barth, *Carbon Nanotubes.* In-Tech, 2010, ch. I - Carbon Nanotubes, A Scientometric Study, pp. 1–19.

[43] T. Guo, P. Nikolaev, A. G. Rinzler, D. Tomanek, D. T. Colbert, and R. E. Smalley, "Self-Assembly of Tubular Fullerenes," *J. Phys. Chem.*, vol. 99, p. 10694, 1995.

[44] V. Ivanov, A. Fonseca, J. B. Nagy, A. Lucas, P. Lambin, D. Bernaerts, and X. B. Zhang, "Catalytic Production and Purification of Nanotubules Having Fullerene-Scale Diameters," *Carbon*, vol. 33, p. 1727, 1995.

[45] M. Meyyappan, T. Yamada, P. Sarrazin, and J. Li, *Carbon Nanotubes: Science and Applications.* CRC Press, 2005, ch. IV - Growth: CVD and PECVD, pp. 99–116.

[46] R. T. K. Baker, "Catalytic Growth of Carbon Filaments," *Carbon*, vol. 27, p. 315, 1989.

[47] R. S. Wagner and W. C. Ellis, "Vapor-Liquid-Solid Mechanism of Single Crystal Growth," *Appl. Phys. Lett.*, vol. 4, pp. 89–90, 1964.

[48] K. Khazeni, V. H. Crespi, J. Hone, A. Zetti, and M. L. Cohen, "Metal-insulator transition in AC_{60}: RbC_{60} and KC_{60}," *Phys. Rev. B.*, vol. 56, pp. 6627–6630, 1997.

[49] L. Wang, P. S. Davids, A. Saxena, and A. R. Bishop, "Correlation Effect and Electronic Properties of Fullerenes and Carbon Nanotubes," *J. Phys. Chem. Solids*, vol. 54, pp. 1493–1496, 1993.

[50] S. Saito, A. Oshiyama, Y. Miyamoto, N. Hamada, and S. Sawada, "Electronic Structure of Fullerenes and Fullerides: Artificial Atoms and their Solids," *Nanotechnology*, vol. 3, p. 167, 1992.

[51] K. Tanaka, *The Science and Technology of Carbon Nanotubes.* Elsevier, 1999, ch. VIII - Electronic Structure of Single Walled Carbon Nanotubes, p. 76.

[52] M. S. Dresselhaus, G. Dresselhaus, and R. Saito, "Physics of Carbon Nanotubes," *Carbon*, vol. 33, p. 883, 1995.

[53] Z. K. Tang, N. Wang, X. X. Zhang, J. N. Wang, C. T. Chan, and P. Sheng, "Novel Properties of 0.4 nm Single-Walled Carbon Nanotubes Templated in the Channels of $AlPO_{4-5}$ Single Crystals," *New J. Phys.*, vol. 5, p. 146, 2003.

[54] L. C. Qin, X. Zhao, K. Hirahara, Y. Miyamoto, Y. Ando, and S. Iijima, "Materials Science: The Smallest Carbon Nanotube ," *Nature*, vol. 408, p. 50, 2000.

[55] W. Z. Liang, G. H. Chen, Z. Li, and Z. K. Tang, "Absorption Spectra and Chirality of Single-Walled 0.4 nm Carbon Nanotubes," *Appl. Phys. Lett.*, vol. 80, p. 3415, 2002.

[56] N. Sano, M. Chhowalla, D. Roy, and G. A. J. Amaratunga, "Viability of Sub-0.4-nm Diameter Carbon Nanotubes," *Phys. Rev. B*, vol. 66, p. 113403, 2002.

[57] X. Zhao, Y. Liu, S. inoue, T. Suzuki, R. O. Jones, and Y. Ando, "Smallest Carbon Nanotube Is 0.3 nm in Diameter," *Phys. Rev. Lett.*, vol. 92, pp. 125 502–1, 2004.

[58] B. K. Agrawal, S. Agrawal, and R. Srivastava, "An ab-initio Study of Optical and Raman Spectra of Heavily Li-Doped 0.4 nm Carbon Nanotubes," *J. Phys.: Condens. Matter.*, vol. 16, p. 1467, 2004.

[59] M. Machon, S. Reich, C. Thomsen, D. Shanchez-Portal, and P. Ordejon, "Ab-initio Calculations of the Optical Properties of 0.4 nm Diameter Single-Walled Nanotubes," *Phys. Rev. B*, vol. 66, p. 155410, 2002.

[60] D. B. Williams and C. B. Carter, *Transmission Electron Microscopy.* Springer, 1996.

[61] P. J. Goodhew, J. Humphreys, and R. Beanland, *Electron Microscopy and Analysis.* Taylor & Francis, 2001.

[62] T. Brintlinger, Y. Chen, T. Durkop, E. Cobas, and M. S. Fuhrer, "Rapid Imaging of Nanotubes on Insulating Substrates," *Appl. Phys. Lett.*, vol. 81, p. 2454, 2002.

[63] Y. Homma, S. Suzuki, Y. Kobayashi, M. Nagase, and D. Takagi, "Mechanism of Bright Selective Imaging of Single-Walled Carbon Nanotubes on Insulators by Scanning Electron Microscopy," *Appl. Phys. Lett.*, vol. 84, p. 1750, 2004.

[64] C. Kiang, M. Endo, K. Takeuchi, T. Furuta, and M. Dresselhaus, "Size Effects in Carbon Nanotubes," *Phys. Rev. Lett.*, vol. 81, p. 1869, 1998.

[65] A. Charlier, E. McRae, R. Heyd, M. Charlier, and D. Moretti, "Classification for Double-Walled Carbon Nanotubes," *Carbon*, vol. 37, p. 1779, 1999.

[66] R. Andrews, D. Jacques, D. Qian, and E. C. Dickey, "Purification and Structural Annealing of Multiwalled Carbon Nanotubes at Graphitization Temperatures," *Carbon*, vol. 39, p. 1681, 2001.

[67] L. Qin, "Measuring the True Helicity of Carbon Nanotubes," *Chem Phys. Lett.*, vol. 297, p. 23, 1998.

[68] J. M. Cowley, P. Nikolaev, A. Thess, and R. E. Smalley, "Electron Nano-Diffraction Study of Carbon Single-Walled Nanotube Ropes," *Chem Phys. Lett.*, vol. 265, p. 379, 1997.

[69] M. Terrones, H. Terrones, N. Grobert, W. K. Hsu, Y. Q. Zhu, J. P. Hare, H. W. Kroto, D. R. M. Walton, P. Kohler-Redlich, M. Rhle, J. P. Zhang, and A. K. Cheetham, "Efficient Route to Large Arrays of CN_x Nanofibers by Pyrolysis of Ferrocene-Melamine Mixtures," *Appl. Phys. Lett.*, vol. 75, p. 3932, 1999.

[70] B. Sadanadan, T. Savage, S. Bhattacharya, T. Tritt, A. Cassell, M. Meyyappan, Z. R. Dai, Z. Wang, R. Zidan, and A. M. Rao, "Synthesis and Thermoelectric Power of Nitrogen Doped Carbon Nanotubes," *J. of Nanosci. Nanotech.*, vol. 3, p. 99, 2003.

[71] X. Z. Liao, A. Serquis, Q. X. Jia, D. E. Peterson, Y. T. Zhu, and H. F. Xu, "Effect of Catalyst Composition on Carbon Nanotube Growth," *Appl. Phys. Lett.*, vol. 82, p. 2694, 2003.

[72] J. H. Hafner, C.-L. Cheung, T. H. Oosterkamp, and C. M. Lieber, "High-Yield Assembly of Individual Single-Walled Carbon Nanotube Tips for Scanning Probe Microscopies," *J. Phys. Chem B*, vol. 105, p. 743, 2001.

[73] J. Kong, H. T. Soh, A. M. Cassell, C. F. Quante, and H. Dai, "Synthesis of Individual Single-Walled Carbon Nanotubes on Patterned Silicon Wafers," *Nature*, vol. 385, p. 878, 1998.

[74] J. Kong, A. Morpurgo, H. T. Soh, and C. F. Quante, "Synthesis, Integration, and Electrical Properties of Individual Single-Walled Carbon Nanotubes," *Appl. Phys. A*, vol. 69, p. 305, 1999.

[75] J. Chen, A. M. Rao, S. Lyuksyutov, M. E. Itkis, M. A. Hamon, H. Hu, R. W. Cohn, P. C. Eklund, D. T. Colbert, R. E. Smalley, and R. C. Haddon, "Dissolution of Full-Length Single-Walled Carbon Nanotubes," *J. Phys. Chem. B*, vol. 105, p. 2525, 2001.

[76] D. Keller, "Envelope Reconstruction of Probe Microscope Images," *Surf. Sci.*, vol. 249, p. 409, 1993.

[77] D. Keller, "Reconstruction of STM and AFM Images Distorted by Finite Size Tips," *Surf. Sci.*, vol. 253, p. 353, 1991.

[78] C. J. Chen, *Introduction to Scanning Tunnelling Microscopy.* Oxford University Press, 1993.

[79] K. Sattler, "STM of Carbon Nanotubes and Nanocones," *Carbon*, vol. 33, p. 915, 1995.

[80] K. Ichimura, M. Osawa, K. Nomura, H. Kataura, Y. Maniwa, S. Suziki, and Y. Achiba, "Tunneling Spectroscopy on Carbon Nanotubes Using STM," *Physica B*, vol. 323, p. 230, 2002.

[81] J. Wildoer, L. Venema, A. Rinzler, R. E. Smalley, and C. Dekker, "Electronic Structure of Atomically Resolved Carbon Nanotubes ," *Nature*, vol. 391, p. 59, 1998.

[82] W. Clauss, D. Bergeron, and A. Johnson, "Atomic Resolution STM Imaging of a Twisted Single-Wall Carbon Nanotube," *Phys. Rev. B.*, vol. 58, p. R4266, 1998.

[83] N. Hamada, S. Sawada, and A. Oshiyama, "New One-Dimensional Conductors: Graphitic Microtubules," *Phys. Rev. Lett.*, vol. 68, p. 1579, 1992.

[84] J. Mintmire, B. Dunlap, and C. White, "Are Fullerene Tubules Metallic?" *Phys. Rev. Lett.*, vol. 68, p. 631, 1992.

[85] W. Lu, D. Wang, and L. Chen, "Near-Static Dielectric Polarization of Individual Carbon Nanotubes," *Nano Lett.*, vol. 7, p. 2729, 2007.

[86] W. Lu, Y. Xiong, A. Hassanien, W. Zhao, M. Zheng, and L. Chen, "A Scanning Probe Microscopy Based Assay for Single-Walled Carbon Nanotube Metallicity," *Nano Lett.*, vol. 9, p. 1668, 2009.

[87] P. Girard, "Electrostatic Force Microscopy: Principles and Some Applications to Semiconductors," *Nanotechnology*, vol. 12, p. 485, 2001.

[88] P. Cherniavskaya, L. Chen, V. Weng, L. Yuditsky, and L. E. Brus, "Quantitative Noncontact Electrostatic Force Imaging of Nanocrystal Polarizability," *J. Phys. Chem. B*, vol. 107, p. 1525, 2003.

[89] W. Lu, Y. Xiong, and L. Chen, "Length Dependent Dielectric Polarization in Metallic Single-Walled Carbon Nanotubes," *J. Phys. Chem. C*, vol. 113, p. 10337, 2009.

[90] M. S. Dresselhaus and G. Dresselhaus, "Intercalation Compounds of Graphite," *Adv. Phys.*, vol. 30, pp. 139–326, 1981.

[91] R. Saito, A. Jorio, A. G. S. Filho, A. Grueneis, M. A. Pimenta, G. Dresselhaus, and M. S. Dresselhaus, "Dispersive Raman Spectra Observed in Graphite and Single Wall Carbon Nanotubes," *Physica B*, vol. 323, p. 100, 2002.

[92] A. M. Rao, P. C. Eklund, S. Bandow, A. Thess, and R. E. Smalley, "Evidence for Charge Transfer in Doped Carbon Nanotube Bundles from Raman Scattering ," *Nature*, vol. 388, p. 257, 1997.

[93] A. G. S. Filho, A. Jorio, G. G. Samsonidze, G. Dresselhaus, M. S. Dresselhaus, A. K. Swan, M. S. Ünlü, B. B. Goldberg, R. Saito, J. H. Hafner, C. M. Lieber, and M. A. Pimenta, "Probing the Electronic Trigonal Warping Effect in Individual Single-Wall Carbon Nanotubes Using Phonon Spectra," *Chem. Phys. Lett.*, vol. 354, p. 62, 2002.

[94] L. McNeil, J. Steinbeck, L. Salamanca-Riba, and G. Dresselhaus, "Raman microscopy of intercalated graphite fibers," *Carbon*, vol. 24, p. 73, 1986.

[95] D. E. Long, *The Raman Effect: A Unified Treatment of the Theory of Raman Scattering by Molecules.* John Wiley & Sons Ltd., 2002.

[96] J. A. Konigstein, *Introduction to the Theory of the Raman Effect.* D. Reidel Publishing Company, 1972.

[97] R. M. Martin and L. M. Falicov, *Light Scattering in Solids I: Introductory Concepts*, M. Cardona, Ed. Springer-Verlag Berlin and Heidelberg GmbH & Co. K; 2nd Revised Edition, 1983.

[98] Various, *Light Scattering in Solids II: Basic Concepts and Instrumentation*, M. Cardona, Ed. Springer-Verlag Berlin and Heidelberg GmbH & Co. K; 2nd Revised Edition, 1983.

[99] D. C. Smith, "Measurements of Ultrafast Dynamics in a Superconductor and a Semiconductor," Ph.D. dissertation, University of Oxford, 1998.

[100] P. Y. Yu and M. Cardona, *Fundamentals of Semiconductors: Physics and Measurement Properties.* Springer-Verlag Berlin and Heidelberg, 1996.

[101] M. F. Lin, "Optical Spectra of Single-Wall Carbon Nanotube Bundles," *Phys. Rev. B*, vol. 62, p. 13153, 2000.

[102] I. Bozovic, N. Bozovic, and M. Damnkanovic, "Optical Dichroism in Nanotubes," *Phys. Rev. B.*, vol. 62, p. 6971, 2000.

[103] A. Grüneis, R. Saito, G. G. Samsonidze, T. Kimura, M. A. Pimenta, A. Jorio, A. G. S. Filho, G. Dresselhaus, and M. S. Dresselhaus, "Inhomogeneous Optical Absorption Around the K point in Graphite and Carbon Nanotubes," *Phys. Rev. B*, vol. 67, p. 165402, 2003.

[104] A. A. Mamedov, N. A. Kotov, M. Prato, D. M. Guldi, J. P. Wicksted, and A. Hirsch, "Molecular Design of Strong Single-Wall Carbon Nanotube/Polyelectrolyte Multilayer Composites ," *Nat. Mater.*, vol. 1, p. 190, 2002.

[105] H. Kuzmandy, B. Burger, A. Thess, and R. Smalley, "Vibrational Spectra of Single Wall Carbon Nanotubes," *Carbon*, vol. 36, p. 709, 1998.

[106] R. Jishi, L. Venkataraman, M. Dresselhaus, and G. Dresselhaus, "Phonon Modes in Carbon Nanotubes," *Chem Phys. Lett.*, vol. 209, p. 77, 1993.

[107] J. Kurti, G. Kresse, and H. Kuzmany, "First Principles Calculations of the Radial Breathing Mode of Single-Wall Carbon Nanotubes," *Phys. Rev. B*, vol. 58, p. R8869, 1998.

[108] D. Sanchez-Portal, E. Artacho, J. Soler, A. Rubio, and P. Ordejon, "Ab Initio Structural, Elastic, and Vibrational Properties of Carbon Nanotubes," *Phys. Rev. B*, vol. 59, pp. 12 678–1688, 1999.

[109] U. Venkasteswaran, A. Rao, E. Richter, M. Menon, A. Rinzler, R. E. Smalley, and P. C. Eklund, "Probing the Single-Wall Carbon Nanotube Bundle: Raman Scattering Under High Pressure," *Phys. Rev. B*, vol. 59, p. 10928, 1999.

[110] A. Jorio, C. Fantini, M. S. S. Dantas, M. A. Pimenta, A. G. S. Filho, G. G. Samsonidze, V. W. Brar, G. Dresselhaus, M. S. Dresselhaus, A. K. Swan, M. S. Ünlü, B. B. Goldberg, and R. Saito, "Linewidth of the Raman Features of Individual Single-Wall Carbon Nanotubes," *Phys. Rev. B.*, vol. 66, p. 115411, 2002.

[111] M. Milnera, J. Kürti, M. Hulman, and H. Kuzmandy, "Periodic Resonance Excitation and Intertube Interaction from Quasi-Continuous Distributed Helices in Single-Wall Carbon Nanotubes ," *Phys. Rev. Lett.*, vol. 84, p. 1324, 2000.

[112] M. S. Dresselhaus and P. C. Eklund, "Phonons in Carbon Nanotubes," *Adv. Phys.*, vol. 49, p. 705, 2000.

[113] J. Maultzsch, S. Reich, C. Thomsen, E. Dobardzic, I. Milosevic, and M. Damnjanovic, "Phonon Dispersion of Carbon Nanotubes," *Solid State Commun.*, vol. 121, p. 471, 2002.

[114] M. A. Pimenta, A. Marucci, S. Empedocles, M. Bawendi, E. B. Hanlon, A. M. Rao, P. C. Eklund, R. E. Smalley, G. Dresselhaus, and M. S. Dresselhaus, "Raman Modes of Metallic Carbon Nanotubes," *Phys. Rev. B*, vol. 58, p. R16016, 1998.

[115] S. D. M. Brown, A. Jorio, P. Corio, M. S. Dresselhaus, G. Dresselhaus, R. Saito, and K. Kneipp, "Origin of the Breit-Wigner-Fano Lineshape of the Tangential G-band Feature of Metallic Carbon Nanotubes," *Phys. Rev. B*, vol. 63, p. 155414, 2001.

[116] K. Kneipp, H. Kneipp, P. Corio, S. D. M. Brown, K. Schafer, J. Motz, L. T. Perelman, E. B. Hanlon, A. Marucci, G. Dresselhaus, and M. S. Dresselhaus, "Surface-Enhanced and Normal Stokes and Anti-Stokes Raman Spectroscopy of Single-Walled Carbon Nanotubes," *Phys. Rev. Lett.*, vol. 84, p. 3470, 2000.

[117] K. Kempa, "Gapless Plasmons in Carbon Nanotubes and their Interactions with Phonons," *Phys. Rev. B*, vol. 66, p. 195406, 2002.

[118] M. Paillet, P. Poncharal, A. Zahab, J.-L. Sauvajol, J. C. Meyer, and S. Roth, "Vanishing of the Breit-Wigner-Fano Component in Individual Single-Wall Carbon Nanotubes," *Phys. Rev. Lett.*, vol. 94, p. 237401, 2005.

[119] A. Jorio, M. A. Pimenta, A. G. Souza-Filho, G. G. Samsinidze, A. K. Swan, M. S. Ünlü, B. B. Goldberg, R. Saito, G. Dresselhaus, and M. S. Dresselhaus, "Resonance Raman Spectra of Carbon Nanotube Bundles Observed by Perpendicularly Polarised Light," *Phys. Rev. Lett.*, vol. 90, p. 107403, 2003.

[120] M. Souza, A. Jorio, C. Fantini, B. R. A. Neves, M. A. Pimenta, R. Saito, A. Ismach, E. Joselevich, V. W. Brar, G. G. Samsonidze, G. Dresselhaus, and M. S. Dresselhaus, "Single and Double Resonance Raman G-Band Processes in Carbon Nanotubes," *Phys. Rev. B*, vol. 69, p. 241403, 2004.

[121] J. Maultzsch, S. Reich, and C. Thomsen, "Raman Scattering in Carbon Nanotubes Revisited," *Phys. Rev. B*, vol. 65, p. 233402, 2002.

[122] J. Maultzsch, S. Reich, U. Schlecht, and C. Thomsen, "High-Energy Phonon Branches of an Individual Metallic Carbon Nanotube," *Phys. Rev. Lett.*, vol. 91, p. 087402, 2003.

[123] M. L. . Sanjuan, A. Anson, and M. T. Martinez, "Double Resonance Features in the Raman Spectrum of Carbon Nanotubes," *Phys. Rev. B*, vol. 70, p. 201404(R), 2004.

[124] C. Thomsen, S. Reich, and J. Maultzsch, "Resonant Raman Spectroscopy of Carbon Nanotubes," *Phil. Trans. R. Soc. Lond. A*, vol. 362, p. 2337, 2004.

[125] M. S. Dresselhaus, G. Dresselhaus, R. Sait, and A. Jorio, "Raman Spectroscopy of Carbon Nanotubes," *Phys. Rep.*, vol. 409, p. 47, 2005.

[126] R. Vidano, D. Fishbach, J. Willis, and T. Loehr, "Observation of Raman Band Shifting with Excitation Wavelength For Carbons and Graphites," *Solid State Commun.*, vol. 39, p. 341, 1981.

[127] S. Arepalli, P. Nikolaev, O. Gorelik, V. Hadjiev, W. Holmes, B. Files, and L. Yowell, "Protocol for the Characterization of Single-Wall Carbon Nanotube Material Quality," *Carbon*, vol. 42, p. 1783, 2004.

[128] S. D. M. Brown, A. Jorio, M. S. Dresselhaus, and G. Dresselhaus, "Observations of the D-band feature in the Raman spectra of carbon nanotubes," *Phys. Rev. B*, vol. 64, p. 073403, 2001.

[129] A. C. Ferrari and J. Robertson, "Interpretation of Raman Spectra of Disordered and Amorphous Carbon," *Phys. Rev. B*, vol. 61, pp. 14 095–14 107, 2000.

[130] Y. Wang and R. L. M. D. C. Alsmeyer, "Raman Spectroscopy of Carbon Materials: Structural Basis of Observed Spectra," *Chem. Mater.*, vol. 2, p. 557, 1990.

[131] M. S. Dresselhaus, A. Jorio, M. Hofmann, G. Dresselhaus, and R. Saito, "Perspectives on Carbon Nanotubes and Graphene Raman Spectroscopy," *Nano Lett.*, vol. 10, pp. 751–758, 2010.

[132] M. M. Lucchese, F. Stavale, E. H. Ferreira, C. Vilane, M. V. O. Moutinho, R. B. Capaz, C. A. Achete, and A. Jorio, "Quantifying Ion-Induced Defects and Raman Relaxation Length in Graphene," *Carbon*, vol. 48, p. 1592, 2010.

[133] M. J. O'Connell, S. M. Bachilo, C. B. Huffman, V. C. Moore, M. S. Strano, E. H. Haroz, K. L. Rialon, P. J. Boul, W. H. Noon, C. Kittrell, J. Ma, R. H. Hauge, R. B. Weisman, and R. E. Smalley, "Band Gap Fluorescence from Individual Single-Walled Carbon Nanotubes," *Science*, vol. 297, p. 593, 2003.

[134] Y. Miyauchi, S. Chiashi, Y. Murakami, Y. Hayashida, and S. Maruyama, "Fluorescence Spectroscopy of Single-Walled Carbon Nanotubes Synthesized from Alcohol," *Chem Phys. Lett.*, vol. 387, p. 198, 2004.

[135] J. S. Lauret, C. Voisin, G. Cassabois, P. Roussignol, C. Delalande, A. Filoramo, L. Capes, E. Valentin, and O. Jost, "Bandgap Photoluminescence of Semiconducting Single-Wall Carbon Nanotubes," *Physica E*, vol. 21, p. 1057, 2004.

[136] R. Droppa Jr., P. Hammer, A. C. M. Carvalho, M. C. dos Santos, and F. Alvarez, "Incorporation of Nitrogen in Carbon Nanotubes," *J. Non-Cryst. Solids*, vol. 299, p. 874, 2002.

[137] C. Pham-Huu, N. Keller, V. Roddatis, G. Mestl, R. Schlogl, and M. J. Ledoux, "Large scale synthesis of carbon nanofibers by catalytic decomposition of Ethane on Nickel Nanoclusters Decorating Carbon Nanotubes ," *Phys. Chem. Chem. Phys.*, vol. 4, p. 514, 2002.

[138] Y. S. Lee, T. H. Cho, B. K. Lee, J. S. Rho, K. H. An, and Y. H. Lee, "Surface Properties of Fluorinated Single-Walled Carbon Nanotubes," *J. Fluorine Chem.*, vol. 120, p. 99, 2003.

[139] A. Buriam, J. Koloczk, J. Dore, A. C. Hannon, J. B. Nagy, and A. Fonseca, "Radial Distribution Function Analysis of Spatial Atomic Correlations in Carbon Nanotubes," *Diam. Relat. Mater.*, vol. 13, p. 1261, 2004.

[140] P. Lambin, A. Loiseau, C. Culot, and L. P. Biro, "Structure of Carbon Nanotubes Probed by Local and Global Probes," *Carbon*, vol. 40, p. 1635, 2002.

[141] W. Z. Zhu, D. E. Miser, W. G. Chan, and M. R. Hajaligol, "Characterization of Multiwalled Carbon Nanotubes Prepared by Carbon Arc Cathode Deposit," *Mater. Chem. Phys.*, vol. 82, p. 638, 2003.

[142] S. J. Tans, A. R. M. Verschueren, and C. Dekker, "Room Temperature Transistor Based on a Single Carbon Nanotube," *Nature*, vol. 398, p. 49, 1998.

[143] A. Jarvey, J. Guo, Q. Wang, M. Lundstrom, and H. Dai, "Ballistic Carbon Nanotube Field Effect Transistors," *Nature*, vol. 424, p. 654, 2003.

[144] R. J. Luyken and F. Hofmann, "Concepts for Hybrid CMOS-Molecular Non-Volatile Memories," *Nanotechnology*, vol. 14, pp. 273–276, 2003.

[145] Y. C. Tseng, P. Xuan, A. Jarvey, R. Malloy, Q. Wang, and J. Bokor, "Monolithic Integration of Carbon Nanotube Devices with Silicon MOS Technology," *Nano Lett.*, vol. 4, pp. 123–127, 2004.

[146] A. C. Dupuis, "The catalyst in the CCVD of Carbon Nanotubes- A Review," *Progress in Materials Science*, vol. 50, pp. 929–961, 2005.

[147] H. M. Cheng, S. F. Lee, G. Pan, H. Y. Pan, L. L. He, and X. Sun, "Large Scale and and Low-Cost Synthesis of Single-Walled Carbon Nanotubes by the Catalytic Pyrolysis of Hydrocarbons," *Appl. Phys. Lett.*, vol. 72, pp. 3282–3284, 1998.

[148] K. Mukhopadhyay, K. Koshio, N. Tanaka, and H. Shinohara, "A Simple and Novel way to Synthesize Aligned Nanotube Bundles at Low Temperature," *Jpn. J. Appl. Phys.*, vol. 37, p. L1257, 1998.

[149] S. Maruyama, R. Kojima, Y. Miyauchi, S. Chiashi, and M. Kohno, "Low Temperature Synthesis of High-Purity Single Walled Carbon Nanotubes from Alcohol," *Chem. Phys. Lett.*, vol. 360, p. 229, 2002.

[150] C. L. Cheung, A. Kurtz, H. Park, and C. M. Lieber, "Diameter-Controlled Synthesis of Carbon Nanotubes," *J. Phys. Chem. B*, vol. 106, pp. 2429–2433, 2002.

[151] G. W. Ho, A. T. S. Wee, J. Lin, and W. C. Tjiu, "Synthesis of Well-aligned Multiwalled Carbon Nanotubes on Ni Catalyst Using Radio Frequency Plasma Enhanced Chemical Vapour Deposition," *Thin Solid Films*, vol. 388, pp. 73–77, 2001.

[152] Y. Homma, T. Yamashita, P. Finnie, M. Tomita, and T. Ogino, "Single-Walled Carbon Nanotube Growth on Silicon Substrates Using Nanoparticle Catalysts," *Jpn. J. Appl. Phys.*, vol. 41, p. 89, 2002.

[153] G.-H. Jeong, S. Suzuki, Y. Kobayashi, A. Yamazaki, H. Yoshimura, and Y. Homma, "Effect of Nanoparticle Density on Narrow Diameter Distribution of Carbon Nanotubes and Particle Evolution During Chemical Vapour Deposition," *J. Appl. Phys.*, vol. 98, p. 124311, 2005.

[154] D. Kondo, S. Sato, and Y. Awano, "Low-temperature Synthesis of Single-walled Carbon Nanotubes with a Narrow Diameter Distribution Using Size-classified Catalyst Nanoparticles," *Chem. Phys. Lett.*, vol. 422, pp. 481–487, 2006.

[155] E. F. Kukovitsky, S. G. L'voy, N. A. Sainov, V. A. Shustov, and L. A. Chernozatonski, "Correlation Between Metal Catalyst Particle Size and Carbon Nanotube Growth," *Chem. Phys. Lett.*, vol. 355, p. 497, 2002.

[156] C. J. Lee, S. C. Lyu, Y. R. Cho, J. H. Lee, and K. I. Cho, "Diameter-Controlled Growth of Carbon Nanotubes Using Thermal Chemical Vapour Deposition," *Chem. Phys. Lett.*, vol. 341, p. 245, 2001.

[157] Y. Li, W. Kim, Y. Zhang, M. Rolandi, D. Wang, and H. Dai, "Growth of Single-Walled Carbon Nanotubes from Discrete Catalytic Nanoparticles of Various Sizes," *J. Phys. Chem. B*, vol. 105, pp. 11 424–11 431, 2001.

[158] O. A. Nerushev, S. Dittmar, R.-E. Morjan, F. Rohmund, and E. E. B. Campbell, "Particle Size Dependence and Model for Iron-Catalyzed Growth of Carbon Nanotubes by Thermal Chemical Vapor Deposition," *J. Appl. Phys.*, vol. 93, no. 7, p. 4185, April 2003.

[159] Y. Y. Wei, G. Eres, V. I. Merlukov, and D. H. Lowndes, "Effect of Catalyst Film Thickness on Carbon Nanotube Growth by Selective Area Chemical Vapour Deposition," *Appl. Phys. Lett.*, vol. 78, p. 1394, 2001.

[160] J. B. Park, G. S. Choi, Y. S. Cho, S. Y. Hong, D. kim, S. Y. Choi, J. H. Lee, and K. I. Cho, "Characterization of Fe-catalyzed Carbon Nanotubes Grown by Thermal Chemical Vapour Deposition," *J. Cryst. Growth*, vol. 244, pp. 211–217, 2002.

[161] Y. H. Wang, J. Lin, C. H. A. Huan, and G. S. Chen, "Synthesis of Large Area Aligned Carbon Nanotube Arrays from C_2H_2 H_2 Mixture by RF Plasma-Enhanced Chemical Vapor Deposition," *Appl. Phys. Lett.*, vol. 78, p. 680, 2001.

[162] L. Delzeit, C. V. Nguyen, R. M. Stevens, J. Han, and M. Meyyappan, "Growth of Carbon Nanotubes by Thermal and Plasma Chemical Vapour Deposition Processes and Applications in Microscopy," *Nanotechnology*, vol. 13, p. 280, 2002.

[163] L. Delzeit, C. V. Nguyen, B. Chen, R. Stevens, A. Cassell, J. Han, and M. Meyyappan, "Multiwalled Carbon Nanotubes by Chemical Vapor Deposition Using Multilayered Metal Catalysts," *J. Phys. Chem. B.*, vol. 106, p. 5629, 2002.

[164] M. L. Terranova, V. Sessa, and M. Rossi, "The World of Carbon Nanotubes: An Overview of CVD Growth Methodologies," *Chem. Vap. Deposition*, vol. 12, pp. 315–325, 2006.

[165] C. Journet, W. K. Maser, P. Bernier, A. Loiseau, M. L. de la Chapelle, S. Lefrant, P. Deniard, R. Lee, and J. E. Fischer, "Large-Scale Production of Single-Walled Carbon Nanotubes by the Electric-Arc Technique," *Nature*, vol. 388, p. 756, 1997.

[166] A. M. Cassel, J. A. Raymakers, J. Kong, and H. Dai, "Large Scale CVD Synthesis of Single-Walled Carbon Nanotubes," *J. Phys. Chem. B*, vol. 103, pp. 6484–6492, 1999.

[167] L. Delzeit, B. Chen, A. Cassell, R. Stevens, C. Nguyen, and M. Meyyappa, "Multilayered Metal Catalysts for Controlling the Density of Single-Walled Carbon Nanotube Growth," *Chem. Phys. Lett.*, vol. 348, p. 368, 2001.

[168] M. Endo, R. Saito, M. S. Dresselhaus, and G. Dresselhaus, *Carbon Nanotubes: Preparation and Properties.* CRC Press, 1997, ch. II - From Carbon Fibers to Nanotubes, p. 35.

[169] L. B. Direktor, V. M. Zaichenko, I. L. Maikov, G. F. Sokol, L. Yu, L. Shekhther, and E. E. Shpil'rain, "Investigation of Pyrolysis of Methane under Conditions of Filetering Through a Heated Porous Medium," *High Temperature*, vol. 38, p. 85, 2001.

[170] T. D. Makris, L. Giorgi, R. Giorgi, N. Lisi, and E. Salernitano, "CNT Growth on Alumina Supported Nickel Catalyst by Thermal CVD," *Diamond and Related Materials*, vol. 14, p. 815, 2005.

[171] P. W. Atkins and J. de Paula, *Physical Chemistry.* Oxford University Press, 1999.

[172] R. D. Levine and R. B. Berstein, *Molecular Reaction Dynamics.* Cambridge University Press, 1991.

[173] W. J. Moore, *Physical Chemistry.* Orient Blackswan Pvt Ltd., 2004.

[174] A. Moisala, A. G. Nisbulin, and E. I. Kauppinen, "The Role of Metal Nanoparticles in the Catalytic Production of Single-Walled Carbon Nanotubes," *J. Phys. Cond. Matter.*, vol. 15, p. 3011, 2003.

[175] B. Giese, *Radicals in Organic Synthesis.* Pergamon Press, 1986.

[176] P. T. A. Reilly and W. B. Whitten, "The Role of Free Radical Condensates in the Production of Carbon Nanotubes During the Hydrocarbon CVD Process," *Carbon*, vol. 44, pp. 1653–1660, 2006.

[177] P. T. A. Reilly, R. A. Gieray, W. B. Whitten, and J. M. Ramsey, "Direct Observation of the Evolution of the Soot Carbonization Process in an Acetylene Diffusion Flame via Real-time Aerosol Mass Spectroscopy," *Combust. Flame*, vol. 122, p. 90, 2000.

[178] ——, "Fullerene Evolution in Flame-Generated Soot," *J. Am. Chem. Soc.*, vol. 122, p. 11596, 2000.

[179] R. P. Rodgers, P. T. A. Reilly, W. B. Whitten, and J. M. Ramsey, "Soot-free Synthesis of C-60," *Carbon*, vol. 41, p. 1469, 2003.

[180] C. W. Sweitzer and G. L. Heller, "The Formation of Carbon Black in Hydrocarbon Flames," *Rubber World*, vol. 134, p. 855, 1956.

[181] S. Stein and A. Fahr, "High Temperature Stabilities of Hydrocarbons," *J. Phys. Chem.*, vol. 89, p. 3714, 1985.

[182] J. H. Hafner, M. J. Bronikowski, B. R. Azamian, P. Nikolaev, A. G. Rinzler, and D. T. Colbert, "Catalytic Growth of Single Wall Carbon Nanotubes from Metal Particles," *Chem. Phys. Lett.*, vol. 296, pp. 195–202, 1998.

[183] C. Lu and J. Liu, "Controlling the Diameter of Carbon Nanotubes in Chemical Vapor Deposition Method by Carbon Feeding," *J. Phys. Chem. B*, vol. 110, p. 20254, 2006.

[184] H. Miki, K. Takeuchi, K. Ishida, and Y. Yoshihara, "Presoot and Soot Formation in HEating of Hydrocarbon Fuels," *Bull JSME*, vol. 29, p. 149, 1986.

[185] G. G. Tibbetts, "Why are Carbon Filaments Tubular?" *J. Cryst. Growth*, vol. 66, p. 632, 1984.

[186] J. Rostrup-Nielsen and D. L. Trimm, "Mechanisms of Carbon Formation on Nickel-Containing Catalysts," *J. Catal.*, vol. 48, p. 155, 1977.

[187] H. Kanzow and A. Ding, "Formation Mechanism of Single-Wall Carbon Nanotubes," *J. Phys. Chem. B*, vol. 27, p. 315, 1989.

[188] H. Dai, A. G. Rinzler, P. Nikolawv, A. Thess, D. T. Colbert, and R. E. Smalley, "Single-wall Nanotubes Produced by Metal-Catalyzed Disproportionation of Carbon Monoxide," *Chem. Phys. Lett.*, vol. 260, pp. 471–475, 1996.

[189] P. Nikolaev, M. J. Bronikowski, R. K. Bradley, F. Rohmund, D. T. Colbert, K. A. Smith, and R. E. Smalley, "Gas-Phase Catalytic Growth of Single-Walled Carbon Nanotubes from Carbon Monoxide," *Chem. Phys. Lett.*, vol. 313, pp. 91–97, 1999.

[190] Y. Shibuta and S. Maruyama, "Molecular Dynamics Simulation of Formation Process of Single-Walled Carbon Nanotubes by CCVD Method," *Chem. Phys. Lett.*, vol. 382, pp. 381–386, 2003.

[191] V. Vinciguerra, F. Buonocore, G. Panzera, and L. Occhipinti, "Growth Mechanisms in Chemical Vapour Deposited Carbon Nanotubes," *Nanotechnology*, vol. 14, p. 655, 2003.

[192] S. Helveg, C. Lopez-Cartes, J. Sehested, P. L. Hansen, B. S. Clausen, J. R. Rostrup-Nielsen, F. Abild-Pedersen, and J. K. Norskov, "Atomic-scale Imaging of Carbon Nanofibre Growth," *Nature*, vol. 427, pp. 426–429, 2004.

[193] S. S. Pan, Z. W. Wie, B. H. Chang, L. F. Sun, W. Y. Zhou, and G. Wang, "Direct Growth of Aligned Open Carbon Nanotubes by Chemical Vapour Deposition," *Chem. Phys. Lett.*, vol. 299, pp. 97–102, 1999.

[194] M. A. Ermakova, D. Y. Ermakov, A. L. Chuvilin, and G. G. Kuvshinov, "Decomposition of Methane Over Iron Catalysts at the Range of Moderate Temperatures: the Influence of Structure of Catalytic Systems and the Reaction Conditions on the Yield of Carbon and Morphology of Carbon Systems," *J. Catal.*, vol. 201, pp. 183–197, 2001.

[195] J. M. Planeix, N. Coustel, B. Coq, V. Brotons, P. S. Kumbhar, R. Dutartre, P. Geneste, P. Bernier, and P. N. Ajayan, "Application of Carbon Nanotubes as Supports in Heterogeneous Catalysts," *J. Am. Chem. Soc.*, vol. 116, p. 7935, 1994.

[196] R. Gao, C. D. Tan, and R. T. K. Baker, "Ethylene Hydroformylation on Graphite Nanofiber Supported Rhodium Catalysis," *Catal. Today*, vol. 65, p. 19, 2001.

[197] R. Viera, C. Pham-Huu, N. Keller, and M. J. Ledoux, "New Carbon Nanofiber/-Graphite Felt Composite for Use as a Catalyst Support for Hydrazine Catalytic Decomposition," *Chem. Commun.*, vol. ?, p. 954, 2002.

[198] D. Venegoni, P. Serp, R. Feurer, Y. Kihn, C. Vahlas, and P. Kalck, "Parametric Study for the Growth of Carbon Nanotubes by Catalytic Chemical Vapou Deposition in a Fluidized Bed Reactor," *Carbon*, vol. 40, p. 1799, 2002.

[199] V. Ivanov, J. B. Nagy, P. Lambin, A. Lucas, X. F. Zhang, and D. Bernaerts, "The Study of Carbon Nanotubes Produced by Catalytic Method," *Chem. Phys. Lett.*, vol. 223, pp. 329–335, 1994.

[200] K. Hernadi, A. Fonseca, J. B. Nagy, D. Bernaerts, A. Fudala, and A. A. Lucas, "Catalytic Synthesis of Carbon Nanotubes Using a Zeolite Support," *Zeolites*, vol. 17, pp. 416–423, 1996.

[201] A. Fonseca, K. Henardi, J. B. Nagy, D. Bernaerts, and A. Lucas, "Optimisation of Catalytic Production and Purification of Buckytubes," *J. Mol. Catal. A: Chem.*, vol. 107, pp. 159–168, 1996.

[202] H. Ago, T. Komatsu, S. Phshima, Y. Kuriki, and M. Yumura, "Dispersion of Metal Nanoparticles for Aligned Carbon nanotube Arrays," *Appl. Phys. Lett.*, vol. 77, p. 79, 2000.

[203] P. A. Kralchevsky and N. D. Denkov, "Capillary Forces and Structuring in Layers of Colloid Particles," *Current Opinion in Colloid & Interface Science*, vol. 6, pp. 383–401, 2001.

[204] M. Chhowalla, K. B. K. Teo, C. Ducat, N. L. Rupesinghe, G. A. J. Amaratunga, A. C. Ferrari, D. Roy, J. Robertson, and W. I. Milne, "Growth Process Conditions of Vertically Aligned Carbon Nanotubes using Plasma Enhanced Chemical Vapor Deposition," *J. Appl. Phys.*, vol. 90, p. 5308, 2001.

[205] V. I. Merkulov, D. H. Lowndes, Y. Y. Wei, G. Eres, and E. Voelkl, "Patterned Growth of Individual and Multiple Vertically Aligned Carbon Nanofibers," *Appl. Phys. Lett.*, vol. 76, p. 3555, 2000.

[206] V. I. Merkulov, M. A. Guillorn, D. H. Lowndes, M. L. Simpson, and E. Voelkl, "Shaping Carbon Nanostructures by Controlling the Synthesis Process," *Appl. Phys. Lett.*, vol. 79, p. 1178, 2001.

[207] V. I. Merkulov, A. V. Melechko, M. A. Guillorn, D. H. Lowndes, and M. L. Simpson, "Alignment Mechanism of Carbon Nanofibers Produced by Plasma-Enhanced Chemical-Vapor Deposition," *Appl. Phys. Lett.*, vol. 79, p. 2970, 2001.

[208] L. Valentini, J. M. Kenny, L. Lozzi, and S. Santucci, "Formation of Carbon Nanotubes by Plasma Enhanced Chemical Vapor Deposition: Role of Nitrogen and Catalyst Layer Thickness," *J. Appl. Phys.*, vol. 92, p. 6188, 2002.

[209] L. Delzeit, I. McAninch, B. A. Cruden, D. Hash, B. Chen, J. Han, and M. Meyyappan, "Growth of Multiwall Carbon Nanotubes in an Inductively Coupled Plasma Reactor," *J. Appl. Phys.*, vol. 91, p. 6027, 2002.

[210] H. T. Ng, B. Chen, J. E. Koehne, A. M. Cassell, J. Li, J. Han, and M. Meyyappan, "Growth of Carbon Nanotubes: A Combinatorial Method To Study the Effects of Catalysts and Underlayers," *J. Phys. Chem. B*, vol. 107, p. 8484, 2003.

[211] B. A. Cruden, A. M. Cassel, Q. Ye, and M. Meyyappan, "Reactor Design Considerations in the Hot Filament/Direct Current Plasma Synthesis of Carbon Nanofibers," *J. Appl. Phys.*, vol. 94, p. 4070, 2003.

[212] C. Bower, W. Zhu, S. Jin, and O. Zhou, "Plasma-Induced Alignment of Carbon Nanotubes," *Appl. Phys. Lett.*, vol. 77, p. 830, 2000.

[213] K. Matthews, B. Cruden, and B. R. Stoner, "Plasma Enhanced Chemical Vapor Deposition of Multiwalled Carbon Nanofibers," *J. Appl. Phys.*, vol. 2, p. 475, 2002.

[214] Z. F. Ren, Z. P. Huang, J. W. Xu, J. H. Wang, P. Bush, M. P. Siegal, and P. N. Provencio, "Synthesis of Large Arrays of Well-Aligned Carbon Nanotubes on Glass," *Science*, vol. 282, p. 1105, 1998.

[215] J. H. Han, W. S. Yang, J.-B. Yoo, and C. Y. Park, "Growth and Emission Characteristics of Vertically Well-Aligned Carbon Nanotubes Grown on Glass Substrate by Hot Filament Plasma-Enhanced Chemical Vapor Deposition," *J. Appl. Phys.*, vol. 88, p. 7363, 2000.

[216] Y. C. Choi, Y. M. Shin, S. C. Lim, Y. H. L. D. J. Bae, B. S. Lee, and D. C. Chung, "Effect of Surface Morphology of Ni Thin Film on the Growth of Aligned Carbon Nanotubes by Microwave Plasma-Enhanced Chemical Vapor Deposition," *J. Appl. Phys.*, vol. 88, p. 4898, 2000.

[217] R. Sen, A. Govindaraj, and C. N. R. Rao, "Carbon Nanotubes by the Metallocene Route," *Chem. Phys. Lett.*, vol. 267, p. 276, 1997.

[218] B. C. Satishkumar, A. Govindaraj, R. Sen, and C. N. R. Rao, "Single-Walled Nanotubes by the Pyrolysis of Acetylene-Organometallic Mixtures," *Chem. Phys. Lett.*, vol. 293, p. 47, 1998.

[219] C. E. Dateo, T. Gokcen, and M. Meyyappan, "Modeling of the HiPco Process for Carbon Nanotube Production," *J. Nanosci. Nanotech*, vol. 2, p. 523, 2002.

[220] F. J. Derbyshire, A. E. B. Presland, and D. L. Trimm, "Graphite Formation by Dissolution-Precipitation of Carbon in Cobalt, Nickel and Iron," *Carbon*, vol. 13, p. 111, 1975.

[221] Y. Zhang, Y. Li, W. Kim, D. Wang, and H. Dai, "Imaging As-Grown Single-Walled Carbon Nanotubes Originated from Isolated Catalytic Nanotubes," *Appl. Phys. A*, vol. 74, pp. 325–328, 2002.

[222] J. F. Colomer, C. Stephan, S. Lefrant, G. van Tendeloo, I. Willens, and Z. Konya, "Large-Scale Synthesis of Single-Wall Carbon Nanotubes by Catalytic Chemical Vapour Deposition Method," *Chem. Phys. Lett.*, vol. 317, pp. 83–89, 2000.

[223] J.-F. Colomer, C. Stephan, S. Lefrant, G. Van Tendeloo, I. Willems, and Z. Konya, "Synthesis of Carbon Nanotubes by Catalytic Decomposition of Hydrocarbons," *Chem. Phys. Lett.*, vol. 14, p. 1343, 1999.

[224] K. Hernadi, A. Fonseca, J. B. Bagy, A. Siska, and I. Kiricsi, "Production of Nanotubes by the Catalytic Decomposition of Different Carbon-Containing Compounds," *Appl. Catal. A*, vol. 199, pp. 245–255, 2000.

[225] C. Klinke, J. M. Bonard, and K. Kern, "Comparative Study of the Catalytic Growth of Patterned Carbon Nanotube Films," *Surf. Sci.*, vol. 492, pp. 195–201, 2001.

[226] W. B. Choi, B. Cheong, J. J. Kim, J. Chu, and E. Bae, "Selective Growth of Carbon Nanotubes for Nanoscale Transistors," *Adv. Funct. Mater.*, vol. 13, pp. 80–84, 2003.

[227] G. Maurin, I. Stepanek, P. Bernier, J. F. Colomer, J. B. Nagy, and F. Henn, "Segmented and Opened Multi-Walled Carbon Nanotubes," *Carbon*, vol. 39, p. 1273, 2001.

[228] G. S. Choi, Y. S. Cho, S. Y. Hong, J. B. Park, and D. J. Kim, "Effects of Ammonia on the Alignment of Carbon Nanotubes in Metal-Assisted Thermal Chemical Vapor Deposition," *J. Eur. Ceramic. Soc.*, vol. 39, p. 2095, 2001.

[229] G. S. Choi, Y. S. Cho, S. Y. Hong, J. B. Park, D. J. Kim, and H. J. Kim, "The role of Ammonia Treatment in the Alignment of the Carbon Nanotubes Synthesized with Ni and Fe via Thermal Chemical Vapor Deposition," *J. Kor. Phys. Soc.*, vol. 39, p. 7, 2001.

[230] G. S. Choi, Y. S. Cho, S. Y. Hong, J. B. Park, K. H. Son, and D. J. Kim, "Carbon Nanotubes Synthesized by Ni-assisted Atmospheric Pressure Thermal Chemical Vapor Deposition," *J. Appl. Phys.*, vol. 91, p. 3847, 2002.

[231] Y. Yang, Z. Hu, Y. J. Tian, , Y. N. Lu, X. Z. Wang, and Y. Chen, "High-yield Production of Quasi-aligned Carbon Nanotubes by Catalytic Decomposition of Benzene," *Nanotechnology*, vol. 14, pp. 733–737, 2003.

[232] E. Flauhaut, A. Peigney, C. Laurent, and A. Rousset, "Synthesis of Single-Walled Carbon Nanotube- Co-MgO Composite Powders and Extraction of the Nanotubes," *J. Mater. Chem*, vol. 10, pp. 249–252, 2000.

[233] Y. H. Hu and E. Ruckenstein, "High Resolution Transmission Electron Microscopy Study of Carbon Deposited on the NiO/MgO Solid Solution Catalysts," *J. Catal.*, vol. 184, pp. 298–302, 1999.

[234] B. J. Nagy, G. Bister, A. Fonseca, D. Mehn, Z. Konya, I. Kiricsi, Z. E. Horvath, and L. P. Biro, "On the Growth Mechanism of Single-Walled Carbon Nanotubes by Catalytic Chemical Vapour Deposition on Supported Metal Catalysts," *J. Nanosci. Nanotech.*, vol. 4, p. 326, 2004.

[235] W. Z. Li, J. G. Wen, M. Sennet, and Z. F. Ren, "Clean Double-Walled Carbon Nanotubes Synthesized by CVD," *Chem Phys. Lett.*, vol. 368, p. 299, 2003.

[236] P. Hu, X. Wang, Y. Liu, B. Wang, and D. Zhu, "Synthesis of Single Walled Carbon Nanotubes Using MgO as a Catalyst Support," *Synth. Metals*, vol. 135, p. 833, 2003.

[237] B. C. Liu, S. C. Lyu, T. J. Lee, S. K. Choi, S. K. Eum, C. W. Yang, C. Y. Park, and C. J. Lee, "Synthesis of Single and Double Walled Carbon Nanotubes by Catalytic Decomposition of Methane," *Chem. Phys. Lett.*, vol. 373, p. 475, 2003.

[238] S. C. Lyu, B. C. Liu, T. J. Lee, C. W. Yang, C. Y. Park, and C. J. Lee, "Synthesis of HIgh-Quality Single-Walled Carbon Nanotubes by Catalytic Decomposition of C_2H_2," *Chem. Comm.*, vol. 6, p. 734, 2003.

[239] B. C. Liu, S. C. Lyu, S. I. Jung, H. K. Kang, C.-W. Yang, J. W. Park, C. Y. Park, and C. J. Lee, "Single-Walled Carbon Nanotubes Produced by Catalytic Chemical Vapour Deposition of Acetylene over Fe-Mo/MgO Catalyst," *Chem Phys. Lett.*, vol. 383, p. 104, 2004.

[240] D. E. Resasco, W. E. Alvarez, F. Pompeo, L. Balzano, J. E. Herrera, B. Bitiyanan, and A. Borgna, "A Scalable Process for Production of Single-Walled Carbon Nanotubes by Catalytic Disproportionation of CO on a Solid Catalyst," *J. Nano. Res.*, vol. 4, p. 131, 2002.

[241] J. E. Herrera and D. E. Resasco, "Loss of Single-Walled Carbon Nanotubes Selectivity by Disruption of the Co-Mo Interaction in the Catalyst," *J. Catal.*, vol. 221, p. 354, 2004.

[242] W. E. Alvarez, B. Kitiyanan, A. Borgna, and D. E. Resasco, "Synergism of Co and Mo in the Catalytic Production of Single-Wall Carbon Nanotubes by Decomposition of CO," *Carbon*, vol. 39, p. 547, 2001.

[243] W. E. Alvarez, F. Pompeo, J. E. Herrera, L. Balzano, and D. E. Resasco, "Characterisation of Single-Walled Carbon Nanotubes Produced by Co Disproportionation on Co-Mo Catalysts," *Chem. Mater.*, vol. 14, p. 853, 2002.

[244] E. Lamouroux, P. Serp, and P. Kalck, "Catalytic Routes Towards Single Wall Carbon Nanotubes," *Catal. Rev. Sci. Eng.*, vol. 49, p. 341, 2007.

[245] A. Peigney, C. Laurent, F. Dobigeon, and A. Rousset, "Carbon Nanotubes Grown in A Novel Catalytic Method," *J. Mater. Res.*, vol. 12, p. 613, 1997.

[246] C. Laurent, A. Peigney, O. Quenard, and A. Rousset, "Synthesis and Characterisation of Alumina Matrix Nanocomposites Containing Carbon Nanotubes," *Key Eng. Mater.*, vol. 132, p. 157, 1997.

[247] A. Peigney, C. Laurent, O. Dumortier, and A. Rousset, "Carbon Nanotubes - Fe-Al_2O_3 Nanocomposites. Part I. Influence of the Fe Content on the Synthesis of Powders," *J. Eur. Ceram. Soc.*, vol. 18, p. 1995, 1998.

[248] C. Laurent, A. Peigney, O. Dumortier, and A. Rousset, "Carbon Nanotubes - Fe-Al_2O_3 Nanocomposites. Part II. Microstructure and Mechanical Properties of the Hot-Pressed Composites," *J. Eur. Ceram. Soc.*, vol. 18, p. 2005, 1998.

[249] H. J. Jeong, K. H. An, S. C. Lim, M. S. Park, J. S. Chang, S. E. Park, S. J. Eum, C. W. Yang, C. Y. Park, and Y. H. Lee, "Narrow Diameter Distribution of Singlewalled Carbon Nanotubes Grown on Ni-MgO by Thermal Chemical Vapour Deposition," *Chem Phys. Lett.*, vol. 380, p. 263, 2003.

[250] S. Lim, D. Ciuparu, C. Pak, G. Dobek, Y. Chen, D. Harding, L. Pfefferle, and G. Haller, "Synthesis and Characterisation of Highly Ordered Co-MCM-41 for Production of Aligned Single Walled Carbon Nanotubes," *J. Phys. Chem. B*, vol. 107, p. 11048, 2003.

[251] Y. Chen, D. Ciuparu, S. Lim, Y. Yang, and G. L. Haller, "Synthesis of Uniform Diameter Single-Wall Carbon Nanotubes in Co-MCM-41: Effect of the Catalyst Prereduction and Nanotube Growth Temperatures," *J. Catal.*, vol. 225, p. 453, 2004.

[252] D. Ciuparu, Y. Chen, S. Lim, and G. L. Haller, "Uniform Diameter Single-Walled Carbon Nanotubes Catalytically Grown in Cobalt-incorporated MCM-41," *J. Phys. Chem. B*, vol. 108, p. 503, 2001.

[253] P. Coquay, E. D. Grave, A. Peigney, R. E. Vanderberghe, and C. Laurent, "Carbon Nanotubes by a CVD Method. Part I: Synthesis and Characterisation of the (Mg, Fe)O Catalysts ," *J. Phys. Chem. B.*, vol. 106, p. 13186, 2002.

[254] P. Coquay, A. Peigney, E. D. Grave, R. E. Vanderberghe, and C. Laurent, "Carbon Nanotubes by a CVD Method. Part II: Formation of Nanotubes from (Mg, Fe)O Catalysts ," *J. Phys. Chem. B.*, vol. 106, p. 13199, 2002.

[255] E. Flahaut, R. Bacsa, A. Peigney, and C. Laurent, "Gram-Scale CCVD Synthesis of Double-Walled Carbon Nanotubes," *Chem. Comm.*, vol. 12, p. 1442, 2003.

[256] M. Paillet, V. Jourdain, P. Poncharal, J. L. Zahab, J. C. Meyer, S. Roth, N. Cordente, C. Amiens, and B. Chaudret, "Versatile Synthesis of Individual Single-Walled Carbon Nanotubes from Nickel Nanoparticles for the Study of their Physical Properties," *J. Phys. Chem. B*, vol. 108, p. 17112, 2004.

[257] Y. Kobayashi, H. Nakashima, D. Takagi, and Y. Homma, "CVD Growth of Single-Walled Carbon Nanotubes Using Size-Controlled Nanoparticle Catalyst," *Thin Solid Films*, vol. 464, p. 286, 2004.

[258] K. Hata, D. N. Futaba, K. M. andTatsunori Namai, M. Yumura, and S. Iijima, "Water Assisted Highly-Efficient Synthesis of Impurity-free Single Walled Carbon Nanotubes," *Science*, vol. 306, p. 1362, November 2004.

[259] H. C. Choi, S. Kundaria, D. Wang, A. Ajavey, Q. Wang, M. Rolandi, and H. Dai, "Efficient Formation of Iron Nanoparticle Catalysts on Silicon Oxide by Hydroxylamine for Carbon Nanotube Synthesis and Electronics," *Nano Lett.*, vol. 3, p. 157, 2003.

[260] X. Wang, W. Yue, M. He, M. Liu, J. Zhang, and Z. Liu, "Bimetallic Catalysts for the Efficient Growth of SWNTs on Surfaces," *Chem. Mater.*, vol. 16, p. 799, 2004.

[261] S. Huang, X. Cai, and J. Liu, "Growth of Millimter-long and Horizontally Aligned Single-Walled Carbon Nanotubes on Flat Substrate," *J. Am. Chem. Soc.*, vol. 125, p. 5636, 2003.

[262] S. Huang, M. Woodson, R. Smalley, and J. Liu, "Growth Mechanism of Oriented Long Single Walled Carbon Nanotubes Using Fast HEating Chemical Vapour Deposition Process," *Nano Lett.*, vol. 4, p. 1025, 2004.

[263] Z. Yu, S. Li, and P. J. Burke, "Synthesis of Aligned Arrays of Millimeter Long, Straight, Single-Walled Carbon Nanotubes," *Chem. Mater.*, vol. 16, p. 3414, 2004.

[264] R. Seidel, G. S. Duesberg, E. Unger, A. P. Graham, A. P. Liebau, and F. Kreupl, "Chemical Vapour Deposition Growth of Single-Walled Carbon Nanotubes at 600 °C and a Simple Growth Model," *J. Phys. Chem. B*, vol. 108, p. 1888, 2004.

[265] S. Botti, C. R. L. Asilyan, L. D. Dominicis, F. Fabbri, S. Orlanducci, and A. Fiori, "Carbon Nanotubes Grown by Laser-annealing of SiC Nano-particles," *Chem. Phys. Lett.*, vol. 400, pp. 264–267, 2004.

[266] M. Kusonoki, M. Rokkaku, and T. Suzuki, "Epitaxial Carbon Nanotube Film Self-Organised by Sublimation Decomposition of Silicon Carbide," *Appl. Phys. Lett.*, vol. 71, p. 2620, 1997.

[267] S. Botti, R. Ciardi, M. L. Terranova, S. Piccirillo, V. Sessa, M. Rossi, and M. Vittori-Antisari, "Self-Assembled Carbon Nanotubes Grown Without Catalyst From Nanosized Carbon Particles Adsorbed on Silicon," *Appl. Phys. Lett.*, vol. 80, p. 1441, 2002.

[268] A. Koshio, M. Yudasaka, and S. Iijima, "Metal-free Production of High-Quality Multi-Wall Carbon Nanotubes, in which the Innermost Nanotubes Have a Diameter of 0.4 nm," *Chem. Phys. Lett.*, vol. 356, pp. 595–600, 2002.

[269] S. Hofmann, G. Csnyi, A. C. Ferrari, M. C. Payne, and J. Robertson, "Surface Diffusion: The Low Activation Energy Path for Nanotube Growth," *Phys. Rev. Lett.*, vol. 95, p. 036101, 2005.

[270] O. V. Yazyev and A. Pasquarello, "Effect of Metal Elements in Catalytic Growth of Carbon Nanotubes," *Phys. Rev. Lett.*, vol. 100, p. 156102, 2008.

[271] S. Reich, L. Li, and J. Robertson, "Control the Chirality of Carbon Nanotubes by Epitaxial Growth," *Chem. Phys. Lett.*, vol. 421, p. 469, 2006.

[272] A. V. Melechko, V. I. Merlukov, T. E. McKnight, M. A. Guillorn, D. H. Lowndes, and M. L. Simpson, "Vertically Aligned Carbon Nanofibers and Related Structures: Controlled Synthesis and Directed Assembly," *J. Appl. Phys.*, vol. 97, p. 041301, 2005.

[273] K. Awasthi, A. Srivastava, and O. N. Srviastava, "Synthesis of Carbon Nanotubes," *J. Nanosci. Nanotechnol.*, vol. 5, pp. 1616–1636, 2005.

[274] C. P. Deck and K. Vecchio, "Prediction of Carbon Nanotube Growth Success by the Analysis of Carbon-Catalyst Binary Phase Diagrams," *Carbon*, vol. 43, pp. 2654–2663, 2006.

[275] S. Bhaviripudi, E. Mile, S. A. Steiner, A. T. Zare, M. S. Dresselhaus, A. M. Belcher, and J. Kong, "CVD Synthesis of Single-Walled Carbon Nanotubes from Gold Nanoparticle Catalysts," *J. Am. Chem. Soc.*, vol. 129, pp. 1516–1517, 2007.

[276] H. Liu, D. Takagi, H. Ohno, S. Chiashi, T. Chokan, and Y. Homma, "Effect of Ambient Gas on the Catalytic Properties of Au in Single Walled Carbon Nanotube Growth," *Jpn. J. Appl. Phys.*, vol. 47, pp. 1966–1970, 2008.

[277] Z. Kang, E. Wang, S. Lian, L. Gao, M. Jiang, C. Hu, and L. Xu, "Selected Synthesis of Carbon Nanostructures Directed by Silver Nanocrystals," *Nanotechnology*, vol. 15, p. 490, 2004.

[278] M. H. Rummeli, C. Kramberger, A. Gruneis, P. Ayala, T. Gemming, B. Buchner, and T. Pichler, "On the Graphitization Nature of Oxides for the Formation of Carbon Nanostructures," *Chemistry of Meterials*, vol. 19, pp. 4105–4107, 2007.

[279] B. Liu, W. Ren, L. Gao, S. Li, S. Pei, C. Liu, C. Jiang, and H.-M. Cheng, "Metal-Catalyst-Free Growth of Single-Walled Carbon Nanotubes," *J. Am. Chem. Soc.*, vol. 131, pp. 2082–2083, 2009.

[280] F. K. Mctaggart, "Reduction of Zirconium and Hafnium Oxides," *Nature*, vol. 191, p. 1192, 1961.

[281] L.-M. Berger, W. Gruner, E. Langholf, and S. Stolle, "On the Mechanism of Carbothermal Reduction Processes of TiO_2 and ZrO_2," *Int. J. Refract. Met. Hard Mater.*, vol. 17, pp. 235–243, 1999.

[282] S. Huang, Q. Cai, J. Chen, Y. Qian, and L. Zhang, "Metal-Catalyst-Free Growth of Single-Walled Carbon Nanotubes on Substrates," *J. Am. Chem. Soc.*, vol. 131, pp. 2094–2095, 2009.

[283] T. Uchino, K. N. Bourdakos, C. H. de Groot, P. Ashburn, M. E. Kiziroglou, G. D. Dilliway, and D. C. Smith, "Catalyst Free Low Temperature Direct Growth of Carbon Nanotubes," *Proceedings of 2005 5th IEEE Conference on Nanotechnology*, vol. 5, pp. 1–4, 2005.

[284] S.-H. Li, X.-F. Zhu, and Y.-P. Zhao, "Carbon Assisted Growth of SiO_x Nanowires," *J. Phys. Chem. B*, vol. 108, p. 17032, 2004.

[285] K.-H. Lee, H. S. Yang, K. H. Baik, J. Bang, R. R. Vanfleet, and W. Sigmund, "Direct Growth of Amorphous Silica Nanowires by Solid State Transformation of SiO_2 Films," *Chem. Phys. Lett.*, vol. 383, p. 380, 2004.

[286] D. C. Paine, C. Caragianis, and A. F. Schwartzman, "Oxidation of $Si_{1x}Ge_x$ Alloys at Atmospheric and Elevated Pressure," *J. Appl. Phys.*, vol. 70, p. 5076, 1991.

[287] H. K. Liou, P. Mei, U. Gennser, and E. S. Yang, "Effects of Ge Concentration on SiGe Oxidation Behavior," *Appl. Phys. Lett.*, vol. 59, p. 1200, 1991.

[288] T. Sass, V. Zela, A. Gustafsson, I. Pietzonka, and W. Seifert, "Oxidation and Reduction Behavior of Ge-Si Islands," *Appl. Phys. Lett.*, vol. 81, p. 3455, 2002.

[289] D. C. Paine, C. Caragianis, T. Y. Kim, Y. Shigesato, and T. Ishahara, "Visible Photoluminescence from Nanocrystalline Ge Formed by H_2 Reduction of $Si_{0.6}Ge_{0.4}O_2$," *Appl. Phys. Lett.*, vol. 62, p. 2842, 1993.

[290] U. Neuwald, A. Feltz, U. Memmert, and R. J. Behm, "Chemical Oxidation of Hydrogen Passivated Si(111) Surfaces in H_2O_2," *J. Appl. Phys.*, vol. 78, p. 4131, 1995.

[291] T. Akane, J. Tanaka, H. Okumura, and S. Matsumoto, "Preparation of High Quality Ge Substrate for MBE," *Appl. Surf. Sci.*, vol. 108, p. 303, 1997.

[292] Y. Nakamura, Y. Nagadomi, K. Sugie, N. Miyata, and M. Ichikawa, "Formation of Ultrahigh Density Ge Nanodots on Oxidized Ge/Si(111) Surfaces," *J. Appl. Phys.*, vol. 95, p. 5014, 2004.

[293] J.-Y. Raty, F. Gygi, and G. Galli, "Growth of Carbon Nanotubes on Metal Nanoparticles: A Microscopic Mechanism from *Ab-Initio* Molecular Dynamics ," *Phys. Rev. Lett.*, vol. 95, p. 096103, 2005.

[294] F. Ding, A. Rosen, and K. Bolton, "Dependence of SWNT Growth Mechanism on Temperature and Catalyst Particle Size: Bulk versus Surface Diffusion," *Carbon*, vol. 43, pp. 2215–2217, 2005.

[295] L. T. Chadderton and Y. Chen, "Nanotube Growth by Surface Diffusion," *Phys. Lett. A*, vol. 263, pp. 401–405, 1999.

[296] A. Peigney, C. Laurent, and A. Rousset, "Influence of the Composition of a H_2-CH_4 Gas Mixture on the Catalytic Synthesis of Carbon Nanotubes-Fe/Fe_3C-Al_2O_3 Nanocomposite Powders," *J. Mater. Chem.*, vol. 9, p. 1167, 1999.

[297] S. C. Lyu, B. C. Liu, S. H. Lee, C. Y. Park, H. K. Kang, C. W. Yang, and C. J. Lee, "Large-Scale Synthesis of High-Quality Double-Walled Carbon Nanotubes by Catalytic Decomposition of n-Hexane," *J. Phys. Chem. B*, vol. 108, p. 2192, 2004.

[298] G. G. Tibbetts and D. W. Gorkiewiez, "A New Reactor for Growing Carbon Fibers from Liquid and Vapour Phase Hydrocarbons," *Carbon*, vol. 31, p. 809, 1993.

[299] R. L. Vander Wal, T. M. Tichich, and V. E. Curtis, "Substrate-support Interactions in Metal-Catalyzed Carbon Nanofiber Growth," *Carbon*, vol. 39, pp. 2277–2289, 2001.

[300] M. S. Kim, N. M. Rodriguez, and R. T. K. Baker, "The Role of Interfacial Phenomena in the Structure of Carbon Deposits," *J. Catal.*, vol. 134, p. 253, 1992.

[301] P. G. de Gennes, "Wetting: Statistics and Dynamics," *Rev. Mod. Phys.*, vol. 57, p. 827, 1985.

[302] A. J. H. M. Kock, P. K. de Bokx, E. Boellaard, W. Klop, and J. W. Geus, "The Formation of Filamentous Carbon on Iron and Nickel Catalysts," *J. Catal.*, vol. 95, pp. 468–480, 1985.

[303] N. Yoshida, M. Yasutake, T. Arie, S. Akita, and Y. Nakayama, "Quantitative Analysis of the Magnetic Properties of Metal-Capped Carbon Nanotube Probe," *Jpn. J. Appl. Phys.*, vol. 41, pp. 5013–5016, 2002.

[304] K. Hernadi, A. Fonseca, J. B. Nagy, D. Bernaerts, and A. A. Lucas, "Fe Catalysed Carbon Nanotube Formation," *Carbon*, vol. 34, p. 1249, 1996.

[305] S. Heyrreyre, P. Gadelle, P. Moral, and J. M. M. Millet, "Study by Mossbauer Spectroscopy and Magnetisation Measurement of the Evolution of Iron Catalysts Used in the Disproportionation of CO," *J. Phys. Chem. Solids*, vol. 58, pp. 1539–1545, 1997.

[306] S. Fan, M. G. Chapline, N. R. Franklin, T. W. Tomblem, A. M. Cassel, and H. Dai, "Self-Oriented Regular Arrays of Carbon Nanotubes and their Field Emission Properties," *Science*, vol. 283, p. 512, 1999.

[307] J. S. Suh and J. S. Lee, "Highly Ordered Two-Dimensional Carbon Nanotube Arrays," *Appl. Phys. Lett.*, vol. 75, pp. 2047–2049, 1999.

[308] S. J. Tauster, S. C. Fung, and R. L. Garten, "Strong Metal-Support Interactions. Group 8 Noble Metals Supported on Titanium Dioxide," *J. Am. Chem. Soc.*, vol. 100, p. 170, 1978.

[309] T. Borowiecki, "Effect of the Support on the Coking of Nickel Catalysts in Hydrocarbon Steam Reforming," *Catal. Lett.*, vol. 33, p. 429, 1987.

[310] I. Yudanov, G. Pacchioni, K. Neyman, and N. Rosch, "Systematic Density Functional Study of the Adsorption of Transition Metal Atoms on the MgO(001) Surface," *J. Phys. Chem. B*, vol. 101, p. 2786, 1997.

[311] S. C. Davis and K. J. Klabunde, "Unsupported Small Metal Particles: Preparation, Reactivity, and Characterization," *Chem. Rev.*, vol. 82, p. 153, 1982.

[312] S. J. Tauster, S. C. Fung, R. T. K. Baker, and J. A. Horsley, "Strong Interactions in Supported-Metal Catalysts ," *Science*, vol. 211, p. 1121, 1981.

[313] M. Arai, T. Ishikawa, T. Nakayama, and Y. Nishiyama, "Effects of Metal-Support Interaction and Temperature on the Sintering of Pt and Ag Particles Supported on Inorganic Solids," *J. Colloid Interf. Sci.*, vol. 97, p. 254, 1984.

[314] K. Kunimori, Y. Ikeda, M. Soma, and T. Uchijima, "Metal-Support Interaction in Alumina-Supported Pt Catalysts," *J. Catal.*, vol. 79, p. 185, 1983.

[315] W. S. Rasband. (2004) ImageJ. National Institute of Health, Bethesda, Maryland, USA. http://rsb.info.nih.gov/ij/.

[316] B. Hvolbaek, T. V. W. Janssens, B. S. Clausen, H. Falsig, C. H. Christensen, and J. K. Norkov, "Catalytic Activity of Au Nanoparticles," *Nano Today*, vol. 2, pp. 14–18, 2007.

[317] J. Jia, K. Haraki, J. N. Kondo, K. Domen, and K. Tamaru, "Selective Hydrogenation of Acetylene over Au/Al_2O_3 Catalyst," *J. Phys. Chem. B*, vol. 104, pp. 1153–1156, 2000.

[318] M. Haruta, "Size- and Support-Dependency in the Catalysis of Gold," *Catal. Today*, vol. 36, pp. 156–166, 1997.

[319] P. Carter, B. Gleeson, and D. J. Young, "Rapid Growth of SiO_2 Nanofibers on Silicon-Bearing Alloys," *Oxid. Met.*, vol. 56, p. 375, 2001.

[320] K. B. K. Teo, M. Chowalla, G. A. J. Amaratunga, W. I. Milne, and G. Pirio, "Characterisation of Plasma-Enhanced Chemical Vapour Deposition Carbon Nanotubes by Auger Electron Spectroscopy," *J. Vac. Sci. Technol., B*, vol. 20, p. 116, 2002.

[321] J. A. Marqusee and J. Ross, "Theory of Ostwald Ripening: Competitive Growth and its Dependence on Volume Fraction," *J. Chem. Phys.*, vol. 80, p. 536, 1984.

[322] P. W. Voorhees and M. E. Glicksman, "Ostwald Ripening During Liquid Phase Sintering - Effect of Volume Fraction on Coarsening Kinetics," *Metall. Mater. Trans. A*, vol. 15, p. 1081, 1984.

[323] K. G. Wang, M. E. Glicksman, and K. Rajan, "Modeling and SImulation for Phase Coarsening: A Comparison with Experiment," *Phys. Rev. E.*, vol. 69, p. 061507, 2004.

[324] ——, "Length Scales in Phase Coarsening: Theory, Simulation and Experiment," *Comput. Mater. Sci.*, vol. 34, p. 235, 2005.

[325] A. Kasuya, Y. Sasaki, Y. Saito, K. Tohji, and Y. Nishina, "Evidence for Size-Dependent Discrete Dispersions in Single-Wall Nanotubes," *Phys. Rev. Lett.*, vol. 78, p. 4434, 1997.

[326] J. S. Bradley and G. Schmid, *Nanoparticles: From Theory to Application*, G. Schmid, Ed. VCH, 2004.

[327] A. Bell, "The Impact of Nanoscience on Heterogeneous Catalysis," *Science*, vol. 299, p. 1688, 2003.

[328] J. M. Thomas, B. F. G. Johnson, R. Raja, G. Sankar, and P. A. Midgley, "High-Performance Nanocatalysts for Single-Step Hydrogenations," *Acc. Chem. Res.*, vol. 36, p. 20, 2003.

[329] E. A. Karakhanov, A. L. Maximov, Y. S. Kardasheva, V. A. Skorkin, S. V. Kardashev, V. V. Pedreina, M. Y. Talanova, E. Lurie-Luke, J. A. Seeley, and S. L. Cron, "Copper Nanoparticles as Active Catalysts in Hydroxylation of Phenol by Hydrogen Peroxide," *Appl. Catal., A*, vol. 385, p. 62, 2010.

[330] S. Pande, A. Saha, S. Jana, S. Sarkar, M. Basu, M. Pradhan, A. K. Sinha, S. Saha, A. Pal, and T. Pal, "Resin-Immobilized CuO and Cu Nanocomposites for Alcohol Oxidation," *Org. Lett.*, vol. 10, p. 5179, 2008.

[331] S. Jammi, S. Sakthivel, L. Rout, T. Mukherjee, S. Mandal, R. Mitra, P. Saha, and T. Punniyamurthy, "CuO Nanoparticles Catalyzed C?N, C?O, and C?S Cross-Coupling Reactions: Scope and Mechanism," *J. Org. Chem.*, vol. 74, p. 1971, 2009.

[332] T. Ben-Moshe, I. Dror, and B. Berkowitz, "Oxidation of Organic Pollutants in Aqueous Solutions by Nanosized Copper Oxide Catalysts," *Appl. Catal., B*, vol. 85, p. 207, 2009.

[333] M. Kidwaia, V. Bansala, A. Saxenab, S. Aerryb, and S. Mozumdar, "Cu-Nanoparticles: Efficient Catalysts for the Oxidative Cyclization of Schiffs Bases ," *Tetrahedron Lett.*, vol. 47, p. 8049, 2006.

[334] W. Q. Deng, X. Xu, and W. A. G. III, "A Two-Stage Mechanism of Bimetallic Catalyzed Growth of Single-Walled Carbon Nanotubes," *Nano Lett.*, vol. 4, p. 2331, 2004.

[335] S. K. Friedlander, *Smoke, Dust, and Haze: Fundamentals of Aerosol Dynamics*, K. E. Gubbins, Ed. Oxford University Press, USA, 2000.

[336] Z. Y. Zhou, N. Tian, Z. Z. Huang, D. J. Chen, and S. G. Sun, "Nanoparticle catalysts with High Energy Surfaces and Enhanced Activity Synthesized by Electrochemical Method," *Farada Discuss.*, vol. 140, p. 81, 2008.

[337] A. K. Santra and D. W. Goodman, "Oxide-Supported Metal Clusters: Models for Heterogeneous Catalysts," *J. Phys.: Condens. Matter.*, vol. 1, p. R31, 2002.

[338] S. Yuvaraj, L. Fan-Yuan, C. Tsong-Huei, and Y. Chuin-Tih, "Thermal Decomposition of Metal Nitrates in Air and Hydrogen Environments," *J. Phys. Chem. B*, vol. 107, p. 1044, 2003.

[339] A. Bellare, D. B. Dadyburjor, and M. J. Kelley, "Evolution of Bimodal Distributions in the Sintering of Model Supported Metal Catalysts," *J. Catal.*, vol. 117, p. 78, 1989.

[340] K.-H. Lee, S.-W. Lee, R. R. Vanfleet, and W. Sigmund, "Amorphous Silica Nanowires Grown by the Vapour-Solid Mechanism," *Chem Phys. Lett.*, vol. 376, p. 498, 2003.

[341] G. W. Sears and J. B. Hudson, "Mobility of Silver Crystallites on Surfaces of MoS_2 and Graphite," *J. Chem. Phys.*, vol. 39, p. 2380, 1963.

[342] J. M. Thomas and P. L. Walker, "Mobility of Metal Particles on a Graphite Substrate," *J. Chem. Phys.*, vol. 41, p. 587, 1964.

[343] E. Ruckstein, "Role of Wetting in Sintering and Redispersion of Supported Metal Crystallites," *J. Cryst. Growth*, vol. 47, p. 666, 1979.

[344] Q. Ma, K. Klier, H. Cheng, and J. W. Mitchell, "Interaction between Catalyst and Support. 4 Periodic Trends and Patters in Interactions of First Row Transition Metals with the Silica Surface," *J. Phys. Chem. B*, vol. 106, p. 10121, 2002.

[345] Q. Ma, K. Klier, H. Cheng, J. W. Mitchel, and K. S. Hayes, "Interaction between Catalyst and Support. 3 Metal Agglomeration on the Silica Surface," *J. Phys. Chem. B*, vol. 105, p. 9230, 2001.

[346] K. L. Kelly, E. Coronado, L. L. Zhao, and G. C. Schatz, "The Optical Properties of Metal Nanoparticles: The Influence of Size, Shape and Dielectric Environment," *J. Phys. Chem. B*, vol. 107, p. 668, 2003.

[347] R. L. Whetten, M. N. Shafigullin, J. T. Khoury, T. G. Schaaff, I. Vezmar, M. M. Alvarez, and A. Wilkinson, "Crystal Structures of Molecular Gold Nanocrystal Arrays," *Acc. Chem. Res.*, vol. 32, p. 397, 1999.

[348] M. Wu, S. A. O'Neill, L. C. Brousseau, W. P. McConnel, D. A. Shultz, R. J. Linderman, and D. L. Feldheim, "Synthesis of Nanometer-Sized Hollow Polymer Capsules from Alkanethiol-coated Gold Nanoparticles," *Chem. Comm,*, vol. 9, p. 775, 2000.

[349] N. N. Greenwood and A. Earnshaw, *Chemistry of Elements.* Butterworth-Heinemann, 1997.

[350] F. Patolsky, A. Lichtenstein, and I. Willner, "Electronic Transduction of DNA Sensing Processes on Surfaces: Amplification of DNA Detection and Analysis of Single-Base Mismatches by Tagged Liposomes," *J. Am. Chem. Soc.*, vol. 123, p. 5194, 2001.

[351] S. Mandal, P. R. Selvakannan, R. Pasricha, and M. Sastry, "Keggin Ions as UV-Switchable Reducing Agents in the Synthesis of Au Core-Ag Shell Nanoparticles," *J. Am. Chem. Soc.*, vol. 125, p. 8440, 2003.

[352] D. Takagi, Y. Kobayashi, H. Hibino, S. Suzuki, and Y. Homma, "Mechanism of Gold-Catalyzed Carbon Material Growth," *Nano Lett.*, vol. 8, pp. 832–835, 2008.

[353] K. S. Min, K. V. Shcheglov, C. M. Yang, H. A. Atwater, M. L. Brongersma, and A. Polman, "The Role of Quantum-Confined Excitons vs Defects in the Visible Luminescence of SiO_2 Films Containing Ge Nanocrystals," *Appl. Phys. Lett.*, vol. 68, p. 2511, 1996.

[354] C. Bonafos, B. Garrido, M. Lopez, A. Perez-Rodrigues, J. R. Morante, Y. Kihn, G. B. Assayag, and A. Claverie, "Ostwald Ripening of Ge Precipitates Elaborated by Ion Implantation in SiO_2," *Mater. Sci. Eng., B*, vol. 69-70, pp. 380–385, 2000.

[355] S. Okamoto and Y. Kanemitsu, "Photoluminescence Properties of Surface-Oxidized Ge Nanocrystals: Surface Localization of Excitons," *Phys. Rev. B*, vol. 54, p. 16421, 1996.

[356] L. Brus, "Quantum Crystallites and Nonlinear Optics," *Appl. Phys. A*, vol. 53, p. 465, 1991.

[357] Y. Kanemitsu, "Light Emission from Porous Silicon and Related Materials," *Phys. Rep.*, vol. 263, p. 1, 1995.

[358] J. Diener, M. Ben-Chroin, D. I. Kovalev, S. D. Ganichev, and F. Koch, "Light from Porous Silicon by Multiphoton Vibronic Excitation," *Phys. Rev. B*, vol. 52, p. R8617, 1995.

[359] J. Phillips and G. Lucovsky, *Bonds and Bands in Semiconductors.* Academic Press, 1973.

[360] T. Takagahara and K. Takeda, "Theory of the Quantum Confinement Effect on Excitons in Quantum Dots of Indirect-Gap Materials," *Phys. Rev. B*, vol. 46, p. 15578, 1992.

[361] J. R. Heath, J. J. Shiang, and A. P. Alivisatos, "Germanium Quantum Dots: Optical Properties and Synthesis," *J. Chem. Phys.*, vol. 101, p. 1607, 1994.

[362] Y. Maeda, "Visible Photoluminescence from Nanocrystallite Ge Embedded in a Glassy SiO_2 Matrix: Evidence in Support of the Quantum-Confinement Mechanism," *Phys. Rev. B*, vol. 51, p. 1658, 1995.

[363] S. Takeoka, M. Fujii, S. Hayashi, and K. Yamamoto, "Size-Dependent Near-Infrared Photoluminescence from Ge Nanocrystals Embedded in SiO_2 Matrices," *Phys. Rev. B*, vol. 58, p. 7921, 1998.

[364] M. Takagi, "Electron-Diffraction Study of Liquid-Solid Transition of Thin Metal Films," *J. Phys. Soc. Jpn.*, vol. 9, p. 359, 1954.

[365] R. I. Scace and G. A. Slack, "Solubility of Carbon in Silicon and Germanium," *J. Chem. Phys.*, vol. 30, p. 1551, 1959.

[366] Y. Kanzawa, K. Katayama, K. Nozawa, T. Saitoh, and M. Kubo, "Preparation of $Ge_{1-y}C_y$ Alloys by C Implantation into Ge Crystal and Their Raman Spectra," *Jpn. J. Appl. Phys.*, vol. 40, p. 5880, 2001.

[367] L. Rispal and U. Schwalke, "Large Scale In Situ Fabrication of Voltage Programmable Dual Layer High-κ Dielectric Carbon Nanotube Memory Devices With High On/Off Ratio," *IEEE Electron Device Letters*, vol. 29, p. 1349, 2008.

[368] L. Durrer, T. Helbling, C. Zengler, A. Jungen, C. Stampfler, and C. Hierold, "SWNT Growth by CVD on Ferritin-based Iron Catalyst Nanoparticles Towards CNT Sensors," *Sens. Actuators*, vol. 132, p. 485, 2008.

[369] M. Cantoro, S. Hofmann, S. Pisana, V. Scardaci, A. Parvez, C. Ducati, A. Ferrari, A. Blackburn, K. Wand, and J. Robertson, "Catalytic Chemical Vapor Deposition of Single-Wall Carbon Nanotubes at Low Temperatures," *Nano Lett.*, vol. 6, p. 1107, 2006.

[370] J. G. V. Lessing, K. F. Fouche, and T. T. Retief, "Redox Extractions from Molten Alkali-Metal Cyanides. Part 1. Mechanism for Extractions with Liquid Zinc Alloys," *Dalton Trans.*, vol. 20, p. 2020, 1977.

[371] ——, "Redox Extractions from Molten Alkali-metal Cyanides. Part 2. Mechanism for Extractions with Liquid Tin Alloys," *Dalton Trans.*, vol. 20, p. 2004, 1977.

[372] P. S. Nair, T. Radhakrishnan, N. Revaprasadu, G. Kolawolea, and P. OBrien, "Cadmium Ethylxanthate: A Novel Single-Source Precursor for the Preparation of CdS Nanoparticles," *J. Mater. Chem.*, vol. 12, p. 2722, 2002.

[373] B. R. Taylor and L. J. Hope-Weeks, *Dekker Encyclopedia of Nanoscience and Nanotechnology*. CRC Press, 2004, ch. Colloidal Germanium Nanoparticles, p. 717.

[374] R. A. Segura, J. Reyes-Gasga, and G. Cardenas-Trivino, "Germanium Nanoparticles from Solvated Atoms: Synthesis and Characterisation," *Colloid Polym. Sci.*, vol. 283, pp. 854–861, 2005.

[375] H. Yang, R. Yang, X. Wan, and W. Wan, "Structure and Photoluminescence of Ge Nanoparticles with Different Sizes Embedded in SiO_2 Glasses Fabricated by a Sol-Gel Method," *J. Crystal Growth*, vol. 261, pp. 549–556, 2004.

[376] J. P. Wilcoxon, P. N. Provencia, and G. A. Samara, "Synthesis and Optical Properties of Colloidal Ge Nanocrystals," *Phys. Rev. B*, vol. 64, p. 035417(9), 2001.

[377] T. van Buuren, C. Bostedt, B. R. Taylor, T. M. Wiley, L. J. H.-W. ad B. Weeks, and L. J. Terminello, "X-ray Absorption Study of Colloidal Ge Quantum Dots," *SPIE Proc.*, vol. 4807, pp. 1–9, 2002.

[378] N. D. Denkov, O. D. Velev, P. A. Kralchevsky, I. B. Ivanov, H. Yoshimura, and K. Nagayama, "Two Dimensional Crystallization," *Nature*, vol. 361, p. 26, 1993.

[379] G. H. Jeong, S. Suzuki, Y. K. an A. Yamazaki, H. Yoshimura, and Y. Homma, "Size Control of Catalytic Nanoparticles by Thermal Treatment and its Application to Diameter Control of Single Walled Carbon Nanotubes," *Appl. Phys. Lett.*, vol. 90, pp. 043 108–1, 2007.

[380] Y. S. Cho, G. S. Choi, S. Y. Hong, and D. Kim, "Carbon Nanotube Synthesis Using a Magnetic Fluid via Thermal Chemical Vapor Deposition," *J. Cryst. Growth*, vol. 243, p. 224, 2002.

[381] E. Borsella, S. Botti, M. Cremona, S. Martelli, and R. M. Montereali, "Photoluminescence from Oxidised Si Nanoparticles Produced by CW CO_2 Laser Synthesis in a Continuous Flow Reactor," *J. Mater. Sci. Lett.*, vol. 16, pp. 221–223, 1997.

[382] J. Q. Hu, Y. Jiang, X. M. Meng, C. S. Lee, and S. T. Lee, "A Simple Large-Scale Synthesis of Very Long Aligned Silica Nanowires," *Chem Phys. Lett.*, vol. 367, p. 339, 2003.

[383] Y. W. Wang, C. H. Liang, G. W. Meng, X. S. Peng, and L. D. Zhang, "Synthesis and Photoluminescence Properties of Amorphous SiO_x Nanowires," *J. Mater. Chem.*, vol. 12, p. 651, 2002.

[384] D. P. Yu, Q. L. Hang, Y. Ding, H. Z. Zhang, Z. G. Bai, J. J. Wang, Y. H. Zou, W. Qian, G. C. Xiong, and S. Q. Feng, "Amorphous Silica Nanowires: Intensive Blue Light Emitters," *Appl. Phys. Lett.*, vol. 73, p. 3076, 1998.

[385] H. Takikawa, M. Yatsuki, and T. Sakakibara, "Synthesis of Silicon Oxide Nanofibers by Sublimation of SiC in Medium Vacuum with Oxygen Flow," *Jpn. J. Appl. Phys.*, vol. 38, p. L401, 1999.

[386] Z. J. Zhang, G. Ramanath, P. M. Ajayan, D. Goldberg, and Y. Bando, "Creation of Radial Patterns of Carbonated Silica Fibers on Planar Silica Substrates," *Adv. Mater.*, vol. 13, p. 197, 2001.

[387] B. Zheng, Y. Wu, P. Yang, and J. Liu, "Synthesis of Ultra-Long and Highly Oriented Silicon Oxide Nanowires from Liquid Alloys," *Adv. Mater.*, vol. 14, p. 122, 2002.

[388] H. Nishikawa, T. Shiroyama, R. Nakamura, Y. Ohki, K. Nagasawa, and Y. Hama, "Photoluminescence from Defect Centers in High-Purity Silica Glasses Observed Under 7.9-eV Excitation," *Phys. Rev. B*, vol. 45, p. 586, 1992.

[389] R.Tohmon, H. Mizuno, Y. Ohki, K. Sasagane, K. Nagasawa, and Y. Hama, "Correlation of the 5.0- and 7.6-eV Absorption Bands in SiO_2 with Oxygen Vacancy," *Phys. Rev. B*, vol. 39, p. 1337, 1989.

[390] R. P. Wang, G. W. Zhou, Y. L. Liu, S. H. Pan, H. Z. Zhang, D. P. Yu, and Z. Zhang, "Raman Spectral Study of Silicon Nanowires: High-Order Scattering and Phonon Confinement Effects," *Phys. Rev. B*, vol. 61, p. 16827, 2000.

[391] M. Paulose, O. K. Varghese, and C. A. Grimes, "Synthesis of Gold-Silica Composite Nanowires through Solid-Liquid-Solid Phase Growth," *J. Nanosci. Nanotechnol.*, vol. 3, p. 341, 2003.

[392] F. K. LeGoues, R. Rosenberg, and B. S. Meyerson, "Kinetics and Mechanism of Oxidation of SiGe: Dry Versus Wet Oxidation," *Appl. Phys. Lett.*, vol. 54, p. 644, 1988.

[393] I. Aharonovich, Y. Lifshitz, and S. Tamir, "Growth Mechanisms of Amorphous SiO_x Nanowires," *Appl. Phys. Lett.*, vol. 90, p. 263109, 2007.

[394] E. A. Chagarov and A. C. Kummel, "Molecular Dynamics Simulation Comparison of Atomic Scale Intermixing at the Amorphous Al_2O_3/Semiconductor Interface for Ge, InGaAs and InAlAs/InGaAs," *Surf. Sci.*, vol. 603, p. 3191, 2009.

[395] S. Gohil and S. Ghosh, "Surface Enhanced Raman Scattering from Multiwalled Carbon Nanotubes at Low Temperatures," *Appl. Phys. Lett.*, vol. 96, p. 143108, 2010.

[396] S. Hofmann, R. Blume, C. T. Wirth, M. Cantoro, R. Sharma, C. Ducati, M. Havecker, S. Zafeiratos, P. Schnoerch, A. Oestereich, D. Teschner, M. Albrecht, A. Knop-Gericke, R. Schlogl, and J. Robertson, "State of Transition Metal

Catalysts During Carbon Nanotube Growth," *J. Phys. Chem. C*, vol. 113, p. 1648, 2009.

[397] Q. Ma, K. Klier, H. Cheng, and J. W. Mitchel, "Interaction between Catalyst and Support. 1 Low Coverage of Co and Ni at the Silica Surface," *J. Phys. Chem. B*, vol. 104, p. 10618, 2000.

[398] M. Su, Y. Li, B. Maynor, A. Buldum, J. P. Lu, and J. Liu, "Lattice-Oriented Growth of Single-Walled Carbon Nanotubes," *J. Phys. Chem. B*, vol. 104, p. 6505, 2000.

[399] A. Kukovecz, Z. Konya, N. Nagaraju, I. Willems, A. Tamasi, and A. Fonseca, "Catalytic Synthesis of Carbon Nanotubes over Co, Fe, Ni Containing Conventional and Sol-Gel Silica-Aluminas," *Phys. Chem. Chem. Phys.*, vol. 2, p. 3071, 2000.

[400] A. Arranz, V. Perez-Dieste, and C. Palacio, "Growth, Electronic Properties and Thermal Stability of the Fe/Al_2O_3 Interface," *Surf. Sci.*, vol. 521, p. 77, 2002.

[401] C. Mattevi, C. Wirth, S. Hofmann, R. Blume, A. Knop-Gericke, C. Ducati, C. Cepek, M. Cantoro, S. Milne, C. Castellarin-Cudia, S. Dolafi, A. Goldoni, R. Schloegl, and J. Robertson, "In-Situ X-ray Photoelectron Spectroscopy Study of Catalyst-Support Interactions and Growth of Carbon Nanotube Forests," *J. Phys. Chem. C*, vol. 112, p. 12207, 2008.

[402] Q. Fu and T. Wagner, "Interaction of Nanostructured Metal Overlayers with Oxide Surfaces," *Surf. Sci.*, vol. 62, p. 431, 2007.

[403] J. Robertson, O. Sharia, and A. A. Denkov, "Fermi Level Pinning by Defects in HfO_2-Metal Gate Stacks," *Appl. Phys. Lett.*, vol. 91, p. 132912, 2007.

[404] J. C. Yang, Y. G. Shul, C. Louis, and M. Che, "In-Situ EXAFS Study of the Nucleation and Crystal Growth of Ni Particles on SiO_2," *Catal. Today*, vol. 44, p. 315, 1998.

[405] L. Vitos, A. V. Ruban, H. L. Skriver, and J. Kollar, "The Surface Energy of Metals," *Surf. Sci.*, vol. 411, p. 186, 1998.

[406] W. L. Winterbottom, "Equilibrium Shape of a Small Particle in Contact with a Foreign Substrate," *Acta Metall.*, vol. 15, p. 303, 1967.

[407] Q. Ma, K. Klier, H. Cheng, J. W. Mitchell, and K. S. Hayes, "Interactions between Catalyst and Support. 2 Low Coverage of Co and Ni at the Alumina Surface," *J. Phys. Chem. B*, vol. 105, p. 2212, 2001.

[408] T. de los Arcos, M. G. Garnier, J. W. Seo, P. Oelhafen, V. Thommen, and D. Mathys, "The Influence of Catalyst Chemical State and Morphology on Carbon Nanotube Growth," *J. Ph*, vol. 108, p. 7728, 2004.

[409] K. Nishimura, N. Okazaki, L. Pan, and Y. Nakayama, "In Situ Study of Iron Catalysts for Carbon Nanotube Growth Using X-Ray Diffraction Analysis," *Jpn. J. Appl. Phys.*, vol. 43, p. L471, 2004.

[410] A. R. Harytyuyan, T. Tokune, and E. Mora, "Liquid as a Required Catalyst Phase for Carbon Single-Walled Nanotube Growth," *Appl. Phys. Lett.*, vol. 87, p. 051919, 2005.

[411] J. R. Sambles, L. M. Skinner, and N. D. Lisgarten, "An Electron Microscope Study of Evaporating Small Particles: The Kelvin Equation for Liquid Lead and the Mean Surface Energy of Solid Silver ," *Proc. R. Soc. London, Ser. A*, vol. 318, p. 507, 1970.

[412] T. Toshihiro and S. Hara, "Thermodynamic Evaluation of Binaray Phase Diagrams of Small Particle Systems," *Zeitschrift fuer Metallkunde*, vol. 92, p. 467, 2001.

[413] M. Haruta, N. Yamada, T. Kobayashi, and S. Iijima, "Gold Catalysts Prepared by Coprecipitation fo Low-Temperature Oxidation of Hydrogen and of Carbon Monoxide," *J. Catal.*, vol. 115, p. 301, 1989.

[414] D. Potoczna-Petru and L. Krajczyk, "Spreading of Cobalt Phase and Silicate Formation in Co-SiO_2 Model Catalyst," *Catal. Lett.*, vol. 87, p. 51, 2003.

[415] H. F. J. van't Blik, D. C. Koningsberger, and R. Prins, "Characterisation of Supported Cobalt and Cobalt-Rhodium Catalysts - III. Temperature-Programmed Reduction (TPR), Oxidation (TPO), and EXAFS of Co–Rh-SiO_2," *J. Catal.*, vol. 97, p. 210, 1986.

[416] Y. Okamoto, K. Nagata, T. Adachi, T. Imanaka, K. Inamura, and T. Takyu, "Preparation and Characterization of Highly Dispersed Cobalt Oxide and Sulfide Catalysts Supported on Silica," *J. Phys. Chem.*, vol. 95, p. 310, 1991.

[417] R. C. Reuel and C. H. Bartholomew, "The Stoichiometries of H_2 and CO Adsorptions on Cobalt: Effects of Support and Preparation," *J. Catal.*, vol. 85, p. 63, 1984.

[418] I. Puskas, T. H. Fleisch, J. B. Hall, B. L. Meyers, and R. T. Roginski, "Metal-Support Interactions in Precipitated, Magnesium-Promoted Cobalt-Silica Catalysts," *J. Catal.*, vol. 134, p. 615, 1992.

[419] G. J. Haddad and J. G. Goodwin, "The Impact of Aqueous Impregnation on the Properties of Prereduced vs Precalcined Co-SiO_2," *J. Catal.*, vol. 157, p. 25, 1995.

[420] D. P. Mosse and A. Muan, "Binary Phase Diagram of CoO-SiO_2," *Trans. AIME*, vol. 233, p. 1448, 1965.

[421] G. A. Martin, R. Dutartre, and J. A. Dalmon, "Modification of the Catalytic and Chemisorptive Properties of Pt-SiO_2 Catalysts by High Temperature Reduction and Restoration by O_2-H_2 Treatments," *Catal. Lett.*, vol. 16, p. 329, 1981.

[422] J. A. Cairns, J. E. E. Baglin, G. J. Clark, and J. F. Ziegler, "Strong Metal-Support Interactions for Pt and Rh on Al_2O_3 and TiO_2 - Application of Nuclear Backscattering Spectrometry," *J. Catal.*, vol. 83, p. 301, 1983.

[423] U. Heiz, F. Vanolli, A. Sanchez, and W. D. Schneider, "Size-Dependent Molecular Dissociation on Mass-Selected, Supported Metal Clusters," *J. Am. Chem. Soc.*, vol. 120, p. 9668, 1998.

[424] E. Cartier, B. P. Linder, B. Narayana, and V. K. Paruchuri, "Fundamental Understanding and Optimization of PBTI in nFETs with SiO_2-HfO_2 Gate Stack," in *Electron Devices Meeting 2006*, 2006.

[425] S. Walsh, L. Fang, J. K. Schaeffer, E. Weisbrod, and L. J. Brillson, "Process-Dependent Defects in Si/HfO_2/Mo Gate Oxide Heterostructures," *Appl. Phys. Lett.*, vol. 90, p. 052901, 2007.

[426] R. P. Pezzo, M. Copel, M. Gordon, E. Cartier, and I. J. R. Baumvol, "Oxygen Transport and Reaction Mechanisms in Rhenium Gate Contacts on Hafnium Oxide Films on Si," *Appl. Phys. Lett.*, vol. 88, p. 243509, 2006.

[427] T. Uchino, G. N. Ayre, D. C. Smith, J. L. Hutchison, C. H. de Groot, and P. Ashburn, "Growth of Carbon Nanotubes on HfO_2 Towards Highly Sensitive Nano-Sensors," *Jpn. J. Appl. Phys.*, vol. 49, p. 04DN11, 2010.

[428] M. Richardson, "The Partial Equilibirum Diagram of the Fe-Ge System in the Range $40 - 72$ at. % Ge, and the Crystallisation of some Iron Germanides by Chemical Transport Reactions," *Acta Chem. Scand.*, vol. 21, p. 2305, 1967.